FATIGUE PERFORMANCE OF HIGH STRENGTH S690 TO S960 STEEL AND THEIR WELDED SECTIONS

CHEN WEI

PhD

The Hong Kong Polytechnic University

2026

The Hong Kong Polytechnic University

Department of Civil and Environmental Engineering

Fatigue Performance of High Strength S690 to S960 Steel and Their Welded Sections

CHEN WEI

A thesis submitted in partial fulfilment of the requirements for the degree of Doctor of Philosophy

August 2025

CERTIFICATE OF ORIGINALITY

I hereby declare that this thesis is my own work and that, to the best of my knowledge and belief, it reproduces no material previously published or written, nor material that has been accepted for the award of any other degree or diploma, except where due acknowledgement has been made in the text.

_______________________________(Signed)

__________CHEN WEI__________(Name of student)

ABSTRACT

Motivation

High strength steel (HSS) with yield strengths at 690 and 960 N/mm^2, i.e. S690 and S960 steel have been used in heavy machinery and lifting equipment for many years due to their large resistances per unit weight. Owing to their remarkable strength to self-weight ratios, structural engineers are eager to exploit their use in buildings and bridges as the cost as well as the time on fabrication, transportation and construction will be significantly reduced together with less energy consumption, when compared with those of normal strength S355 steel.

Over the past 30 years, fatigue accounts for about 80% of failure of steel bridges in the world, and damages due to fatigue in these steel bridges have caused huge traffic delay, economic loss, and in extreme cases, problems in public safety. Owing to their martensitic microstructures, HSS possess superior mechanical properties, and their fatigue performance are also expected to be better than those of S355 steel. However, up to the presence, systematic experimental investigations into fatigue performance of HSS and their welded joints are rather limited. Due to a lack of engineering data, some design specifications allow the use of fatigue methods which have been specifically developed for S355 steel to be applied to S690 steel, leading to very conservative and inefficient design. In order to promote effective use of HSS in bridges, there is an urgent need to determine their fatigue behaviour under cyclic actions, and also to develop effective design rules to assess their fatigue performance in bridges.

Objectives and scope of work

The research project aims to quantify the fatigue performance of S690 to S960 steel and their welded sections through experimental and numerical investigations. Systematic fatigue tests on coupons of various types of high strength steel, and also their welded sections have been carried out to determine their fatigue resistances, in terms of the number of cycles completed before fracture. Hence, any reduction in the fatigue resistances of the S690 and the S960 steel due to welding is readily determined. Then, systematic investigations into both welded T-joints between S690 circular hollow sections and S690 U-stiffened steel decks were also performed to provide engineering data and numerical predictions on their fatigue resistances for a direct comparison with those of the coupons of the S690 welded sections. Based on these

experimental and numerical data, applicability of various design recommendations to S690 and S960 steel and their welded sections was carefully established, and the use of stress concentration factors in typical welded T-joints was also verified.

Methodology and key findings

- **Full range S-N curves of base plates**

  In order to obtain the full range fatigue performance of S690-QT, S690-TM and S960-QT steel, a total of 39 fatigue tests have been carried out on cylindrical coupons extracted from their base plates, and these coupons are tested under symmetrical cyclic actions from ± 400 to 900 N/mm^2 over a range of 10^4 to 10^7 cycles.

  It is found that All of these test data lie significantly above the design curve for fatigue assessment on the base plates given in EN 1993, especially for those design fatigue life larger than 10^6 cycles. The fatigue limits, i.e. the threshold value of the fatigue stresses that will not cause any damage, of all these steel are found to be more than 4 times the given values in EN 1993.

- **Full range S-N curves of welded sections**

  In order to obtain the full range fatigue performance of butt-welded sections of the steel, another 39 fatigue tests have also been carried out on cylindrical coupons extracted from their welded sections, and these coupons are tested under symmetrical cyclic actions from ± 400 to 900 N/mm^2 over a range of 10^4 to 10^7 cycles. It should be noted that during welding, a heat input energy of 1.0 kJ/mm was adopted.

  It is found that the fatigue limits of S690-QT, s690-TM and S960-QT welded sections are reduced to be merely 37.2%, 21.8% and 29.1% of those of the base plates respectively due to the effects of welding. Similarly to those of the base plates mentioned above, all the test data of the welded sections lie significantly above the design curve for fatigue assessment on welded sections given in EN 1993-1-9, especially when the design fatigue life is larger than 10^6 cycles. The fatigue limits of all the welded sections are also more than 4 times the given values in EN 1993.

- **Structural behaviour of welded T-joints**

  In order to determine the structural behaviour of welded T-joints between S690 circular hollow sections under in-plane bending, a total of 10 *monotonic tests* were carried out on various configurations of S690 welded T-joints to determine local distributions of strains in the vicinity of the brace-chord junctions. An advanced measurement method of digital image correlation was adopted to determine local strain fields, and hence, hot spot stresses.

  Moreover, a total of 10 *fatigue tests* were carried out on the welded T-joints with one typical configuration to determine directly the fatigue behaviour of these welded T-joints under in-plane cyclic bending. It is found that all the experimental results lie well above the design curves given in EN 1993, CIDECT and API RP 2A for fatigue assessment of these welded T-joints. Hence, the experimental S-N curves with nominal stresses and hot spot stresses are found to be able to assess the fatigue behaviour of S690 welded T-joints with a high degree of accuracy.

- **Fatigue behaviour of U-rib stiffened steel decks**

  In order to determine the fatigue behaviour of S690 U-rib stiffened steel decks under axial compression, a total of 14 fatigue tests were carried out on the S690 rib-to-deck welded joints with one typical configuration. It is found that all the experimental results lie well above the design curves given in IIW for fatigue assessment of these S690 U-rib stiffened steel decks. Hence, the experimental S-N curves with nominal stresses and hot spot stresses are found to be able to assess the fatigue behaviour of S690 U-rib stiffened steel decks with a high degree of accuracy.

- **Advanced numerical modelling**

  In order to predict the fatigue behaviour of the welded T-joints between S690 circular hollow sections, an integrated numerical modelling approach is developed. Firstly, a thermal analysis is performed to determine thermal responses, and hence, temperature distributions induced during welding of the T-joints. Secondly, a thermomechanical analysis is then performed to determine mechanical responses, and hence, residual stress distributions induced by differential cooling in the vicinity of the welded collars of the T-joints. Thirdly, a stress analysis is then performed to determine structural responses, and hence, mechanical stress distributions throughout the T-joints under cyclic in-plane bending actions. Finally, a fatigue analysis is performed to determine the fatigue life of critical parts of the T-joints under various loading protocols. It is demonstrated that the fatigue behaviour of these welded T-joints, including the fatigue life and the locations of crack initiations, was successfully simulated through the proposed modelling approach with a satisfactory accuracy.

- **Verification on applicability of current design methods**

  EN 1993 recommends a number of S-N curves to determine fatigue life for various constructional details under a wide range of cyclic stress ranges for up to S460 steel. For those welded sections of S690 to S960 steel, and also welded joints of S690 steel covered in the present investigation, it is found that EN 1993 often gives very conservative predictions, especially in the range of high cycle fatigue. *Hot spot stress method* adopted in both CIDECT, API RP 2A and IIW assesses the fatigue life according to the critical stress which is induced by geometric variations in structural members. Through a comparison between the experimental results obtained in the present project and the design results of the recommendations, it is found that these recommendations give very conservative results, especially for S690 welded joints in the range of high cycle range.

Significance

A series of experimental and numerical investigations into the fatigue behaviour of various high strength steel and their welded sections were performed. A comprehensive database on both experimental and numerical data on the fatigue behaviour of these steel and their welded sections is established. Based on these data, the fatigue performance of these steel, their welded sections as well as those welded joints covered in the present project was demonstrated to be superior to those of the normal strength steel. Enhancements to current design recommendations are also proposed.

PUBLICATIONS

Chen, W., Hu, Y. F., Chung, K. F., Zhao, X. L., Nethercot, D. A., & Liu, H. L. (2025). Fatigue behaviour of high strength S690 steel and their welded sections under symmetric cyclic actions. Engineering Structures, 340, 120683.

Chen, W., Hu, Y. F., Chung, K. F., Zhao, X. L., Nethercot, D. A., & Liu, H. L. (2025). Fatigue performance of welded T-joints between S690 circular hollow sections under cyclic in-plane bending actions. Engineering Structures, 346, 121608.

Chen, W., Hu, Y. F., Chung, K. F., & Nethercot, D. A. (2025). Investigations into local stresses at welded T-joints between high strength S690 circular hollow sections under in-plane bending. Engineering Structures. (under review)

Chen, W., Hu, Y. F., Chung, K. F., & Nethercot, D. A. (2025). Fatigue behaviour of high strength S690 U-rib stiffened steel decks under cyclic axial compression. Engineering Structures. (under preparation)

Chen, W., Hu, Y. F., Chung, K. F., & Nethercot, D. A. (2026). Effects of welding-induced residual stresses on fatigue performance of high strength S690 welded joints. Engineering Structures. (under preparation)

ACKNOWLEDGEMENT

I would like to express my deepest gratitude to all those who have supported me throughout my PhD study.

First and foremost, I would like to thank my supervisor, Prof. Kwok-Fai Chung, for his invaluable guidance, encouragement, and patience. His profound knowledge and unwavering support have been instrumental in shaping my research and academic development.

I am grateful to the financial supports from the Research Committee and the Chinese National Engineering Research Centre for Steel Construction (Hong Kong Branch) of The Hong Kong Polytechnic University. I also appreciate the facilities and resources provided by the Hong Kong Polytechnic University and the Department of Civil and Environmental Engineering. A special thanks to Ms. Catherine E. Ng, Dr. H.C. Ho and Dr. Y.F. Hu for their advice and assistances in keeping my research progress on schedule.

I would like to thank my colleges and friends Dr. H. Jin, Dr. M.F. Zhu, Dr. Y.B Guo, Dr. P.F. Men Dr. B. Li, Mr. Y.C. Wang and Ms. T.Y. Xiao for their help in my research works. Special thanks to the laboratory technicians Mr. M.C. Ng, Mr. K. L. Cheung and Mr. C. F. Wong for their assistances in the experimental works. Grateful thanks are also extended to the other members in our research group.

Last but not least, I would like to express my heartfelt gratitude to my parents, my wife Jenny and my daughter Ally, thank you for your unconditional love and support, and for instilling in me the values of hard work and perseverance.

Thank you all for being a part of this journey !

TABLE OF CONTENTS

CERTIFICATE OF ORIGINALITY I
ABSTRACT II
PUBLICATIONS VI
ACKNOWLEDGEMENT VII
TABLE OF CONTENTS VIII
LIST OF FIGURES XII
LIST OF TABLES XVI

Chapter 1 Introduction 1
1.1 Research background 1
1.2 Objectives and scope of work 3
1.3 Methodology and key findings 4
1.4 Significance of the research project 6
1.5 Outline of the thesis 6

Chapter 2 Literature review 9
2.1 Introduction 9
2.2 High strength steel and their structural applications 10
2.2.1 Microstructures of high strength steel 11
2.2.2 Welding of high strength steel 13
2.3 Fatigue assessment approaches 15
2.4 Investigation into fatigue performance of high strength steel 17
2.4.1 High strength steel and their welded sections 17
2.4.2 Welded tubular joints 21
2.4.3 U-rib stiffened steel deck 24
2.4.4 Effects of stress concentration 25
2.4.5 Summary 27

Chapter 3 Material characterization of high strength Grades 690 & 960 steel and their welded sections 28
3.1 Introduction 28

3.2 Welding of high strength steel plates 30
3.3 S690-QT steel and their welded sections 32
3.3.1 Monotonic tensile tests 32
3.3.2 Fatigue tests 37
3.4 S690-TM steel and their welded sections 60
3.4.1 Monotonic tensile tests 60
3.4.2 Fatigue tests 63
3.5 S960-QT steel and their welded sections 69
3.5.1 Monotonic tensile tests 69
3.5.2 Fatigue tests 71
3.6 Analyses on S-N data 76
3.6.1 Formulation of S-N curves 76
3.6.2 Design rules for fatigue assessment 85
3.6.3 Comparison between test data and various design curves 90
3.6.4 Comparison with S355 S-N data 92
3.7 Conclusions 95

Chapter 4 Fatigue behaviour of S690 T-joints under in-plane bending 97
4.1 Introduction 97
4.2 Fabrication of cold-formed circular hollow sections and their T-joints 99
4.3 Monotonic in-plane bending test 105
4.3.1 Test programme 105
4.3.2 Test setup and instrumentation 105
4.3.3 Experimental results 107
4.4 Cyclic in-plane bending tests 111
4.4.1 Test programme 111
4.4.2 Test set-up and instrumentation 111
4.4.3 Test results 112
4.5 Analysis on S-N data 133
4.5.1 Formulation of S-N curves 133
4.5.2 Design rules for fatigue assessment 136
4.5.3 Comparison between test data and various design curves 137
4.6 Fatigue life prediction using fatigue tests on coupons 143

4.7 Conclusions 148

Chapter 5 Local stresses of S690 welded T-joints under in-plane bending 151
5.1 Introduction 151
5.2 Experimental investigation 153
  5.2.1 Test programme 153
  5.2.2 Test set-up and instrumentation 158
  5.2.3 Test results 160
5.3 Numerical investigation 171
  5.3.1 Finite element modelling 171
  5.3.2 Finite element results 174
  5.3.3 Parametric study and design development 180
5.4 Coupled thermomechanical modelling for welding simulation 190
  5.4.2 Welding-induced residual stresses 192
  5.4.3 Critical local stresses at the crown of T-joints 195
5.5 Conclusions 198

Chapter 6 Fatigue behaviour of S690 U-rib stiffened steel decks under axial compression. 200
6.1 Introduction 200
6.2 Fabrication of S690 U-rib stiffened steel decks 202
6.3 Monotonic test on S690 U-rib stiffened steel decks 206
  6.3.1 Test programme 206
  6.3.2 Test setup and instrumentation 206
  6.3.3 Experimental results 208
6.4 Cyclic in-plane bending tests 211
  6.4.1 Test programme 211
  6.4.2 Test set-up and instrumentation 211
  6.4.3 Test results 213
6.5 Analysis on S-N data 224
  6.5.1 Formulation of S-N curve 224
  6.5.2 Design rules for fatigue assessment 225
  6.5.3 Comparison with design curves 226
  6.5.4 Comparison with S-N data of S690 welded T-joints 228

6.5.5 Fatigue life prediction ... 229
6.6 Conclusions ... 231

Chapter 7 Conclusions and future plan ... 233
7.1 Introduction ... 233
7.2 Experimental investigations ... 233
7.3 Numerical investigations ... 236
7.4 Recommendations for future work ... 237

LIST OF FIGURES

Figure 1.1 Fatigue failure in the Tacoma Narrows Bridge (Encyclopaedia Britannica, 2024). 2
Figure 2.1 Heat treatment process on QT and TM steel (Xiong and Liew, 2020) 12
Figure 2.2 Microstructural changes of S690 steel after welding (Liu *et al.*, 2018) 14
Figure 2.3 Effects of welding onto mechanical properties of S690-QT steel (Liu *et al.*, 2018) 14
Figure 2.4 Strain – fatigue life curves of the S355 and the S690 steel (De Jesus *et al.*, 2012) 18
Figure 2.5 Strain – fatigue life curves of the S690 and the S960 steel, and their HAZ (Schubnell *et al.*, 2019).. 20
Figure 2.6 S-N data of various high strength steel (Tong *et al.*, 2021a)............................... 20
Figure 2.7 S-N data of butted welded sections of various high strength steel (Tong *et al.*, 2021b) 20
Figure 2.8 S-N data of butted welded sections of various high strength steel (Tong *et al.*, 2023) 21
Figure 2.9 Typical fatigue failure of offshore tubular steel structures 23
Figure 2.10 Typical fatigue cracks of U-rib stiffened steel deck (Abdelbaset and Zhu, 2024)25
Figure 3.1 Fabrication of test coupons 31
Figure 3.2 Dimensions of standard cylindrical coupons for tensile tests: S690-QT.............. 32
Figure 3.3 Test setup of monotonic tensile tests of S690-QT steel and its welded section.... 34
Figure 3.4 Mechanical properties of S690-QT steel and its welded section 36
Figure 3.5 Variation in hardness of S690-QT welded sections.. 37
Figure 3.6 Dimensions of cylindrical coupons for fatigue tests: S690-QT 39
Figure 3.7 40X magnification of specimen surface.. 40
Figure 3.8 Details of strain-controlled fatigue tests 41
Figure 3.9 Details of load-controlled fatigue tests 42
Figure 3.10 Tested coupons of S690-QT steel.. 44
Figure 3.11 Tested coupons of S690-QT welded sections 45
Figure 3.12 Test results of S690-QT steel and their welded sections 47
Figure 3.13 Fatigue test on Coupon QT-200-W1.. 50
Figure 3.14 Fatigue test on Coupon QT-150-W1.. 51
Figure 3.15 Deterioration of fatigue life at various levels of strength reduction................... 55

Figure 3.16 Specimens for SEM examination ... 56
Figure 3.17 Microstructure analyses on cross-sectional surfaces of S690-QT welded sections after fracture ... 58
Figure 3.18 Microstructure analyses on longitudinal surfaces of S690-QT welded sections after fracture ... 59
Figure 3.19 Dimensions of standard cylindrical coupons for tensile tests: S690-TM ... 60
Figure 3.20 Mechanical properties of S690-TM steel and its welded section ... 61
Figure 3.21 Variation in hardness of S690-TM welded sections ... 62
Figure 3.22 Dimensions of cylindrical coupons for fatigue tests: S690-TM ... 64
Figure 3.23 Typical fractured S690-TM coupons ... 65
Figure 3.24 Test results of S690-TM steel and their welded sections ... 66
Figure 3.25 Fracture surfaces of S690-TM welded sections ... 68
Figure 3.26 Test setup of monotonic tensile tests of S960-QT steel and its welded section ... 69
Figure 3.27 Engineering stress–strain curves of S960-QT steel and its welded section ... 70
Figure 3.28 Typical fractured S960-QT coupons ... 72
Figure 3.29 Test results of S960-QT steel and their welded sections ... 74
Figure 3.30 Fracture surfaces of S960-QT welded sections ... 75
Figure 3.31 S-N curves of S690-QT steel and their welded sections ... 78
Figure 3.32 S-N curves of S690-TM steel and their welded sections ... 79
Figure 3.33 S-N curves of S960-QT steel and their welded sections ... 80
Figure 3.34 S-N curves of S690 & S960 steel and their welded sections ... 84
Figure 3.35 S-N curves given in EN 1993-1-9 ... 86
Figure 3.36 Comparison with design curves ... 91
Figure 3.37 Comparison with references data of S355 ... 93
Figure 4.1 Configuration of S690 welded T-joint ... 100
Figure 4.2 Welding procedures of S690 CHS ... 101
Figure 4.3 Dimensions of curved coupons ... 103
Figure 4.4 Test setup of monotonic tensile tests on curved coupons ... 103
Figure 4.5 Stress-strain curves of curved coupons ... 104
Figure 4.6 Test setup and instrumentation ... 106
Figure 4.7 Stress distributions along the perimeter of the welded collar of Joint M-T1 ... 109
Figure 4.8 Test setup and loading protocol ... 112
Figure 4.9 Degradation in strength and stiffness during fatigue test - Joint C-T1a ... 115

Figure 4.10 Surface crack propagation during fatigue test - Joint C-T1a 118
Figure 4.11 Strength and stiffness degradation of S690 welded T-joins............................. 124
Figure 4.12 Surface crack characteristics along the weld collars of S690 welded T-joints at 5% strength reductions.. 128
Figure 4.13 Surface crack characteristics along the weld collars of S690 welded T-joints at 20% strength reductions.. 129
Figure 4.14 Crown parts of S690 welded T-joints after failure 130
Figure 4.15 Ratios of residual stiffness at various levels of strength reduction 132
Figure 4.16 Ratios of fatigue life at various levels of strength reduction 132
Figure 4.17 $(S\text{-}N)_j$ curves of S690 welded T-joints.. 135
Figure 4.18 Comparison with EN 140
Figure 4.19 Comparison with CIDECT and API 141
Figure 4.20 Various types of stresses in typical welded T-joints 143
Figure 4.21 Advanced numerical welding simulation: Residual stress distribution of Joint M-T1 144
Figure 4.22 Comparison with (S-N)c and (S-N)j.. 148
Figure 5.1 Configuration of typical welded T-joints between S690 CHS 154
Figure 5.2 Dimension and geometry of curved coupons.. 156
Figure 5.3 Measured stress-strain curves of curved coupons extracted from S690 CHS 157
Figure 5.4 Typical set-up of welded T-joints between S690 CHS under monotonic actions of in-plane bending 159
Figure 5.5 DIC system for strain measurement 159
Figure 5.6 Typical failure mode of S690 welded T-joints under in-plane bending............. 161
Figure 5.7 Failure mode of T-joints between S690 CFCHS under in-plane bending 163
Figure 5.8 Load-displacement (F-δ) curves of various T-joints.. 165
Figure 5.9 Load-displacement (F-δ) curves of various T-joints within linear elastic range. 166
Figure 5.10 Linear elastic deformations of typical joint under in-plane bending. Joint T-2b. 168
Figure 5.11 Finite element model of a welded T-joint 173
Figure 5.12 Predicted local stresses at Stations S04 and S10 near the weld toe of Joint T-2b 175
Figure 5.13 Stress distributions of Joint T-2b at Stage e_8 . Mechanical stresses with stress concentration effects. 176

Figure 5.14 Comparison on SCF obtained from Reference (Mashiri *et al.*, 2004a), FEM and CIDECT 179
Figure 5.15 SCF of various S690 welded T-joints obtained from parametric studies 182
Figure 5.16 SCF of various S690 welded T-joints 188
Figure 5.17 SCF obtained from CIDECT and proposed design formula 188
Figure 5.18 Coupled thermomechanical modelling approach 191
Figure 5.19 Residual stress distributions of Joint T-2b at Stage e_0. Initial condition. 193
Figure 5.20 Stress distributions of Joint T-2b at Stage e_8 . Total stresses 194
Figure 5.21 Critical local stresses at the weld toe of the crown of the welded T-joint 196
Figure 6.1 Configuration of S690 U-rib stiffened steel deck 202
Figure 6.2 Welding of S690 U-stiffened steel deck 203
Figure 6.3 Dimension of standard rectangular coupons for tensile tests 204
Figure 6.4 Measured engineering stress-strain curves 205
Figure 6.5 Test setup and instrumentation 207
Figure 6.6 Locations of strain gauges 208
Figure 6.7 Measured stresses at different loading stages 210
Figure 6.8 Test setup and instrumentation 212
Figure 6.9 Measured stresses at different loading stages 212
Figure 6.10 Typical fatigue cracks 214
Figure 6.11 Critical positions of S690 U-rib stiffened steel decks under cyclic actions 215
Figure 6.12 Typical test data of Specimen SD-3a & -3b 218
Figure 6.13 Local stress variations and crack characteristics of S690 U-rib stiffened steel decks under cyclic actions 223
Figure 6.14 S-N curve of S690 U-rib stiffened steel decks 224
Figure 6.15 S-N curve of S690 U-rib stiffened steel decks 227
Figure 6.16 S-N data of different S690 welded joints 229
Figure 6.17 Comparison on S690 welded sections and joints 230

LIST OF TABLES

Table 3.1 Chemical compositions (%) of high strength S690 & S960 steel plates 31
Table 3.2 Chemical compositions (%) of welding consumable 31
Table 3.3 Requirements for the strain rate of monotonic tensile test (ISO, 2019) 33
Table 3.4 Mechanical properties of S690-QT steel and its welded sections 35
Table 3.5 Test propramme of fatigue tests on S690-QT steel and their welded sections...... 38
Table 3.6 Frequency of data acquisition.. 43
Table 3.7 Test results of fatigue tests on S690-QT steel and their welded sections 47
Table 3.8 Various levels of strength reduction of S690-QT steel 53
Table 3.9 Various levels of strength reduction of S690-QT welded sections....................... 54
Table 3.10 Mechanical properties of S690-TM steel and its welded sections 62
Table 3.11 Test propramme of fatigue tests on S690-TM steel and their welded sections..... 64
Table 3.12 Test results of fatigue tests on S690-TM steel and their welded sections............ 67
Table 3.13 Mechanical properties of S960-QT steel and its welded sections 70
Table 3.14 Test propramme of fatigue tests on S960-QT steel and their welded sections...... 71
Table 3.15 Test results of fatigue tests on S960-QT steel and their welded sections 73
Table 3.16 Parameters of S-N curves of S690-QT steel and their welded sections 78
Table 3.17 Parameters of S-N curves of S690-TM steel and their welded sections............... 79
Table 3.18 Parameters of S-N curves of S960-QT steel and their welded sections 80
Table 3.19 Parameters of S-N curves of S690 & S960 steel and their welded sections......... 83
Table 3.20 Parameters of fatigue design in AISC 360-16.. 87
Table 3.21 Parameters of fatigue design in GB50017 89
Table 3.22 Comparison of fatigue stress limits 92
Table 4.1 Test programme of S690 welded T-joints 100
Table 4.2 Measured dimensions of S690 welded T-joints.. 102
Table 4.3 Mechanical properties of chord and brace 104
Table 4.4 Derived hot spot stresses σ_{hs} and SCF at the weld toe 110
Table 4.5 S-N data of S690 welded T-joints at various levels of strength reduction...........113
Table 4.6 Stiffness degradation of S690 welded T-joints at various levels of strength reduction 126
Table 4.7 Fatigue life ratios of S690 welded T-joints at various levels of strength reduction 131

Table 4.8 Parameters of S-N curves of S690 welded T-joints at various levels of strength reduction 134
Table 4.9 Comparison of fatigue stress limits given in various design codes 142
Table 5.1 Test programme of S690 welded T-joints 154
Table 5.2 Measured dimensions and properties of S690 welded T-joints 155
Table 5.3 Key mechanical properties of curved coupons 156
Table 5.4 Key test data of welded T-joints within linear elastic deformations 169
Table 5.5 Comparisons on local stresses σ_{wt} at Stage e_8 177
Table 5.6 Comparisons on SCF 178
Table 5.7 Comparisons on SCF from Reference (Mashiri *et al.*, 2004a) 179
Table 5.8 Numerical programme for parametric study 181
Table 5.9 Comparisons on SCF. Numerical and design results 183
Table 5.10 Comparison on critical local stresses σ_{wt} with residual stresses. Joint T-2b. 197
Table 6.1 Measured mechanical properties 205
Table 6.2 Test programme of S690 U-stiffened steel deck 206
Table 6.3 Derived hot spot stresses σ_{hs} of Specimen SD-M 210
Table 6.4 S-N data of S690 U-rib stiffened steel decks 213
Table 6.5 Parameters of S-N curve of S690 U-rib stiffened steel decks 225
Table 6.6 Comparison of fatigue stress limits 227
Table 6.7 Parameters of S-N curve of S690 welded joints – S-N curve_Wj 228

Chapter 1 Introduction

1.1 Research background

Structural steel with yield strengths fy at least equal to 460 N/mm2 are commonly referred as high strength steel, when compared with those normal strength steel with fy at 355 N/mm2. High strength steel (HSS) with yield strengths at 690 and 960 N/mm2, i.e. S690 and S960 steel designated according to EN 10025:6 (CEN 2019) and GB/T 1591 (CNS, 2018), have been used in heavy machinery and lifting equipment for many years due to their large resistances per unit weight, and typical plate thicknesses are 10 to 20 mm. With a rapid technological advancement in steel-making since the 2000s, their plate thicknesses were steadily increased to about 30 to 70 mm while their costs were reported to have significantly been reduced in the recent years. Owing to their remarkable strength-to-self-weight ratios, structural engineers are eager to exploit their use in buildings and structures as both the cost and the time on fabrication, transportation and site construction will be significantly reduced together with less energy consumption, when compared with those of normal strength S355 steel.

Over the past 30 years, fatigue accounted for about 80% of failure of steel bridges in the world, and structural damages due to fatigue in these steel bridges have caused huge traffic delay, economic loss, and in extreme cases, problems in public safety. In general, the fatigue performance of these steel bridges and structures was somehow problematic (Gogou, 2012). Fatigue carks in different steel bridges are shown in **Figure 1.1**, and these fatigue cracks may significantly shorten the service life of these bridges.

It is commonly believed that for high strength steel members in bridges, their stress ranges due to traffic loads are proportionally increased, when compared with those of normal strength steel.

Owing to their martensitic microstructures, HSS possess superior mechanical properties, and their fatigue performance are also expected to be better than those of S355 steel. However, up to the presence, systematic experimental investigations into the fatigue performance of HSS and their welded joints are rather limited. Due to a lack of engineering data, some design specifications can only adopt those fatigue methods which have been specifically developed for the S355 steel to be applied to the S690 steel, leading to very conservative and inefficient design. In order to promote effective use of HSS in bridges, there is an urgent need to determine their fatigue behaviour under cyclic actions, and also to develop effective design rules to assess their fatigue performance in bridges.

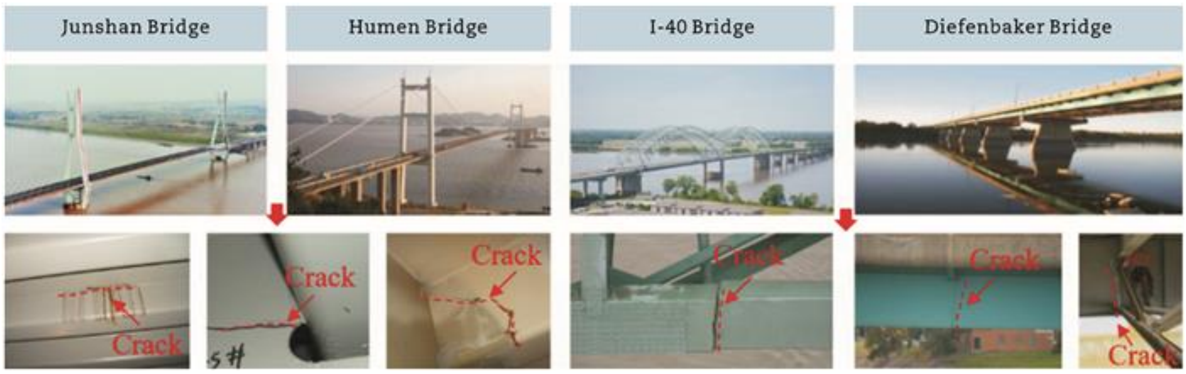

Figure 1.1 Fatigue failure in steel bridges (Encyclopaedia Britannica, 2024)

1.2 Objectives and scope of work

The research project aims to examine and appraise the fatigue performance of the S690 and the S960 steel and their welded sections through experimental and numerical investigations so that their use in steel bridges as well as offshore structures may be promoted.

In order to achieve this objective, a series of systematic fatigue tests on coupons of various types of high strength steel and also their welded sections have been carried out to determine their fatigue resistances, in terms of the number of cycles completed before fracture. Hence, any reduction in the fatigue resistances of the S690 and the S960 steel due to welding is readily determined. Then, a systematic investigation into welded T-joints between S690 circular hollow sections was also performed to provide experimental data on their fatigue resistances for a direct comparison with those of the coupons of the S690 welded sections. Comparisons among these three sets of S-N data were rigorously made to establish whether there were various relationships among the fatigue performance of the base plates and their welded sections, and that of the welded T-joints. In addition, another series of fatigue tests on S690 U-rib stiffened steel decks were carried out to provide S-N data for this practical welded joint commonly used in steel bridges. Advanced numerical models with coupled thermomechanical analyses were also developed to determine effects of welding-induced residual stresses in the brace / chord junctions of these T-joints. Based on these experimental and numerical data, various design recommendations to both the S690 and the S960 steel and their welded sections was carefully verified, and the use of stress concentration factors in typical welded T-joints was also verified.

1.3 Methodology and key findings

Both the experimental and the numerical investigations are conducted in the research project, and details are presented as follows:

- **Full range S-N curves of base plates**

  In order to obtain the full range fatigue performance of the high strength steel S690-QT, S690-TM and S960-QT steel, a total of 39 fatigue tests have been carried out on cylindrical coupons extracted from their base plates, and these coupons are tested under symmetrical cyclic actions from ± 400 to 900 N/mm^2 over a range of 10^4 to 10^7 cycles.

  It is important to obtain S-N data for all these three steels to enable direct comparison with design rules given in EN 1993, especially, the fatigue limits, i.e. the threshold value of the fatigue stresses that will not cause any damage of all these steel.

- **Full range S-N curves of welded sections**

  In order to obtain the full range fatigue performance of the butt-welded sections of the high strength S690-QT steel, another 39 fatigue tests have also been carried out on cylindrical coupons extracted from their welded sections, and these coupons are tested under symmetrical cyclic actions from ± 400 to 900 N/mm^2 over a range of 10^4 to 10^7 cycles. It should be noted that during welding, a heat input energy of 1.0 kJ/mm was adopted.

  It is important to obtain S-N data for welded sections of all these three steels to enable direct comparison with those measured data obtained from above, and also with the design rules given in EN 1993.

- **Structural behaviour of welded T-joints**

  In order to determine the structural behaviour of welded T-joints between S690 circular hollow sections under in-plane bending, a total of 10 *monotonic tests* were carried out on various configurations of S690 welded T-joints to determine local distributions of strains in the vicinity of the brace-chord junctions. An advanced measurement method of digital image correlation was adopted to determine local strain fields, and hence, hot spot stresses.

  Moreover, a total of 10 *fatigue tests* were carried out on the welded T-joints with one typical configuration to determine directly the fatigue behaviour of these welded T-joints under in-plane cyclic bending. The fatigue behaviour of both degradation in stiffness and strength, and crack propagation were examined and analysed carefully. Both the classification and the stress concentration factor approaches were adopted to assess the fatigue performance of these S690 welded T-joints.

- **Fatigue behaviour of U-rib stiffened steel decks**

  In order to determine the fatigue behaviour of S690 U-rib stiffened steel decks under axial compression, a total of 14 fatigue tests were carried out on the S690 rib-to-deck welded joints with one typical configuration. The fatigue behaviour of local stress variations and crack propagation of these S690 U-rib stiffened steel decks were examined in the entire course of the tests.

  The measured S-N data were adopted to derive a S-N curve for fatigue life prediction of these S690 U-rib stiffened steel decks.

- **Advanced numerical modelling**

  In order to predict the fatigue behaviour of the welded T-joints between S690 circular hollow sections, an integrated numerical modelling approach is developed. Firstly, a thermal analysis is performed to determine thermal responses, and hence, temperature distributions induced during welding of the T-joints. Secondly, a thermomechanical analysis is then performed to determine mechanical responses, and hence, residual stress distributions induced by differential cooling in the vicinity of the welded collars of the T-joints. Thirdly, a stress analysis is then performed to determine structural responses, and hence, mechanical stress distributions throughout the T-joints under cyclic in-plane bending actions. Finally, the combined effects of stress concentration in the presence of these welding-induced residual stresses are considered in assessing the fatigue behaviour of these T-joints.

1.4 Significance of the research project

A series of experimental and numerical investigations into the fatigue behaviour of various high strength steel and their welded sections were performed. A comprehensive database on both experimental and numerical data on the fatigue behaviour of these steel and their welded sections is established. Based on these data, the fatigue performance of these steel and their welded sections as well as those welded joints covered in the present project was demonstrated to be superior to those of the normal strength steel. Enhancements to current design recommendations are also proposed.

1.5 Outline of the thesis

- Chapter 1 Introduction

  This chapter presents an overview of the research project. The objectives and scope of work, and the methodology and the significance of the research project are also presented.

- Chapter 2 Literature Review

  This chapter presents a comprehensive review of existing research on high strength steel, including the effects of welding, fatigue assessment approaches, and experimental investigations into fatigue behaviour of high strength steel and their welded sections.

- Chapter 3 Material characterization of high strength Grades 690 & 960 steel and their welded sections

  This chapter presents an experimental investigation into fatigue behaviour of high strength Grades 690 & 960 steel, and their welded sections. Both scanning electron microscope observations and metallographic analyses were conducted on typical fractured coupons to examine micromechanics of fatigue fracture of these welded sections. A comprehensive comparison with all these test data obtained in the present project and those available in the literature is also carried out.

- Chapter 4 Fatigue behaviour of S690 T-joints under in-plane bending

  This chapter presents an experimental investigation into fatigue behaviour of welded T-joints between high strength S690 circular hollow sections (CHS) under cyclic in-plane bending. The processes of crack initiation and propagation are closely monitored throughout the tests, and measured structural responses of these T-joints are examined in details to determine their strength and stiffness degradation during the entire course of the tests. Applicability of existing design S-N curves given in EN 1993-1-9 and CIDECT-8 for fatigue assessment on S690 welded T-joints are also examined.

- Chapter 5 Local stresses of S690 welded T-joints under in-plane bending

  This chapter presents a systematic experimental and numerical investigation into local stresses of welded T-joints between high strength S690 CHS under in-plane bending. Finite element models are established to predict local stresses predict local stresses in the vicinity of the welded toes of these T-joints. After calibration against experimental results, a comprehensive parametric study on a total of 96 welded T-joints under in-plane bending is conducted to examine applicability of existing SCF formula recommended in CIDECT-8

- Chapter 6 Fatigue behaviour of S690 U-rib stiffened steel decks

This chapter presents an experimental investigation into fatigue behaviour of S690 U-rib stiffened steel decks under cyclic axial compression. The processes of crack initiation and propagation are closely monitored throughout the tests, and measured strains in the vicinity of weld toes of these U-rib stiffened steel decks during the tests are examined in details. Applicability of existing design S-N curves given in IIW for fatigue assessment on S690 U-rib stiffened steel decks are also examined.

- Chapter 7 Conclusions and future work

This chapter summarizes key findings of the research project. Recommendations for future works are also presented.

Chapter 2 Literature review

2.1 Introduction

This Chapter presents a literature review on existing research on fatigue performance of high strength steel and their welded sections. The literature review includes the followings:

- Structural applications of high strength steel, and also fatigue problems in steel structures were reviewed. Fatigue assessment approaches for steel structures, and also existing design rules of fatigue assessment on high strength steel were introduced. Effects of welding onto the high strength streel were reviewed.

- Previous experimental investigations into fatigue performance of high strength steel, their welded sections, and also their welded joints were reviewed. Existing S-N data of various normal strength steel and high strength steel were summarized systematically. Applicability of current design S-N curves given in EN 1993-1-9 for these S-N data were addressed. Research methodology and key findings of these experimental investigations were analysed to determine research gaps and significances of present project.

- Both experimental and numerical investigations into local stresses at weld toe of welded joints were reviewed. Stress concentration factor approaches for determination of local stresses at weld toe of welded joints due to geometric discontinuities were introduced.

2.2 High strength steel and their structural applications

Structural steel with yield strengths f_y at least equal to 460 N/mm^2 are commonly referred as high strength steel, when compared with those normal strength steel with f_y at 355 N/mm^2. For those high strength steel with a yield strength at 690 N/mm^2, they are designated as S690 steel according to EN 10025:6 (CEN, 2019) , and GB 1591 (CNS, 2018). These steel are primarily used by mechanical engineers for heavy lifting equipment in ports and mines since the 1980s, and typical plate thicknesses are 20 to 30 mm. With a rapid technological advancement in steel-making since the 2000s, the yield strengths of these high strength structural steel were found to have increased significantly, and their plate thicknesses were steadily increased to about 80 to 120 mm while their costs were reported to have significantly reduced.

Since the 2020s, many structural engineers become very interested to exploit effective use of these S690 steel in construction (Willms, 2009), such as heavily loaded members in bridges and buildings, due to their remarkable mechanical properties and potential economic advantages. Effective utilization of these high strength steel is widely reckoned to be able to reduce steel tonnages, leading to significant savings in material costs and other construction costs related to fabrication, welding, transportation and site operation. Additional savings in construction of foundations and supporting structures are also readily achieved because of reduced self-weights of these steel members. What’s more, as the costs of these high strength steel become readily affordable in recent years, they become highly attractive to structural engineers who are eager to exploit their use in heavily loaded members in bridges.

It should be noted that over the past 30 years, fatigue accounts for about 80% of structural failure of steel bridges in the world, and damages due to fatigue in these steel bridges have caused huge traffic delays, economic losses, and in extreme cases, collapses of bridges (Gogou, 2012). In general, the fatigue performance of these steel bridges and structures was somehow uncertain. It is commonly believed that for high strength steel members, their stress ranges are proportionally increased, when compared with those of normal strength steel under similar traffic loads. However, no increase in their fatigue strengths is permitted in current design codes, such as EN 1993-1-9 (CEN, 2005a), AISC360-10 (AISC, 2010), GB 50017 (CNS, 2017), CIDECT-8 (Zhao *et al.*, 2001), API RP 2A-WS (API, 2002) and IIW (Hobbacher, 1996), owing to a lack of sufficient test data and validated assessment methods. Hence, this poses severe restrictions to a wide use of these high strength steel in bridges.

There is a genuine need to establish the fatigue performance of these high strength steel, in particular, the S690 steel, and their welded sections in bridges, and to develop an effective assessment method to predict their fatigue resistances.

2.2.1 Microstructures of high strength steel

It should be noted that the high strength steel are produced with different methods (Willms, 2009). For examples, the S690-TM is produced with a process of thermomechanical (TM) control, and the S690-QT steel is produced with a process of quenching and tempering (QT), as shown in **Figure 2.1**. In the thermomechanical controlled process, the steel is heated to a high temperature, and then, subjected to controlled mechanical deformations, i.e. rolling, stretching and forging, at specific temperatures (Xiong and Liew, 2020). These processes aim to control microstructures of the steel by regulating its deformation temperatures and rates to achieve specific desired strength and toughness. The main constituent phases in the steel are bainite which typically exhibits in fine grains with a homogeneous microstructure.

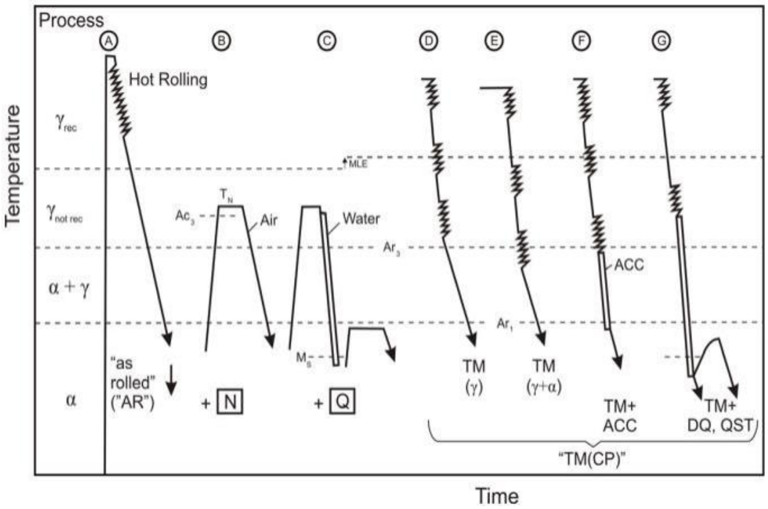

Figure 2.1 Heat treatment process on QT and TM steel (Xiong and Liew, 2020)

In the quenching process, the steel is heated to a high temperature, and then, held for a specific duration to promote grain growth. The steel is then rapidly cooled with through water or oil quenching to facilitate the formation of martensite which is a body-centered cubic structure derived from austenite through rapid cooling (Xiong and Liew, 2020; Costa *et al.*, 2016). While this martensitic microstructure is hard and brittle, and it may affect adversely toughness and processability of the steel. And hence, a tempering process is thus employed to alleviate internal stresses generated during quenching, and hence, to enhance toughness. Carbon atoms within the martensite diffuse and redistribute during the tempering process, and this transformation gives rise to a microstructure known as tempered martensite which hardness and toughness is found to perform satisfactorily. A tempered martensite exhibits better ductility and toughness, when compared with a martensite, and hence, it finds various engineering applications. In general, ductility and toughness of the QT steel are smaller than those of the TM steel, together with an enhancement in hardness, due to their different microstructures.

Owing to their excellent microstructures, high strength steel possess superior mechanical properties, and their fatigue behaviour are expected to be better than those of the S355 steel.

However, up to the presence, systematic experimental investigations into fatigue behaviour of these high strength steel and their welded sections are rather limited. Due to a lack of engineering data, some design specifications allow use of fatigue methods which have been specifically developed for the S355 steel to be applied to these high strength steel. In order to promote effective use of these high strength steel in bridges, there is an urgent need to determine their fatigue behaviour, and also to develop effective design rules to assess their fatigue behaviour under practical situations.

2.2.2 Welding of high strength steel

It is well known that welding of high strength steel may initiate phase transformation, re-crystallization and grain growth, and significant reductions in mechanical properties will take place if the welding process is not properly controlled (Liu *et al.*, 2018). Liu *et al.* (2018) reported an experimental investigation into the effects of heat input energy during welding onto the mechanical properties of high strength S690 steel plates. Due to different transient temperature history in the vicinity of fusion zones during welding, various different microstructures in heat-affected zones (HAZ) were identified as shown in **Figure 2.2**. The heat input energy q due to welding onto these S690 steel plates were specified to range from 1.0 to 5.0 kJ/mm, and monotonic tensile tests on cylindrical coupons of these welded sections were conducted to examine their mechanical properties. As shown in **Figure 2.3**, it was found that for those coupons of the welded sections with q = 1.0 kJ/mm, their mechanical properties, i.e. their strength and ductility, were almost the same as those of the base plates.

Jin *et al.* (2025) experimentally examined the mechanical properties of various sub-zones in the HAZ of S690 welded sections. Tensile tests on heat-treated coupons various heating / cooling curves were carried out, and it was found that both the maximum temperature and the cooling times from 800 °C to 500 °C , i.e. $t_{8/5}$, during welding were affected the mechanical properties in HAZ of the S690 welded sections. And there was little or even no reduction in the mechanical properties of the heat-treated coupons at specific heat treatment process.

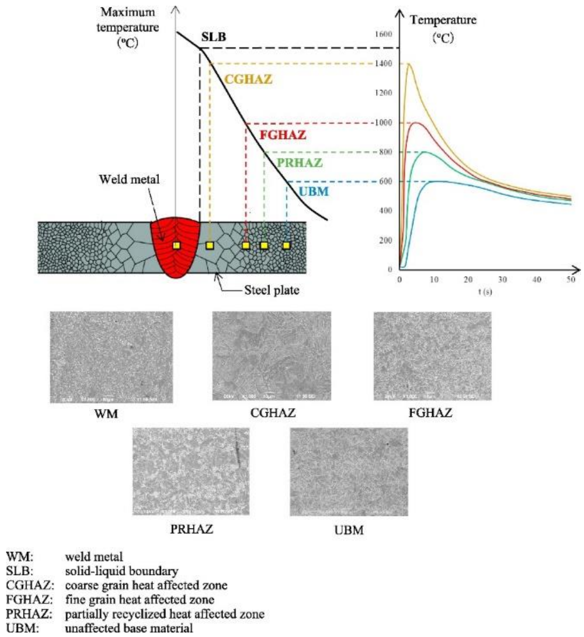

Figure 2.2 Microstructural changes of S690 steel after welding (Liu *et al.*, 2018)

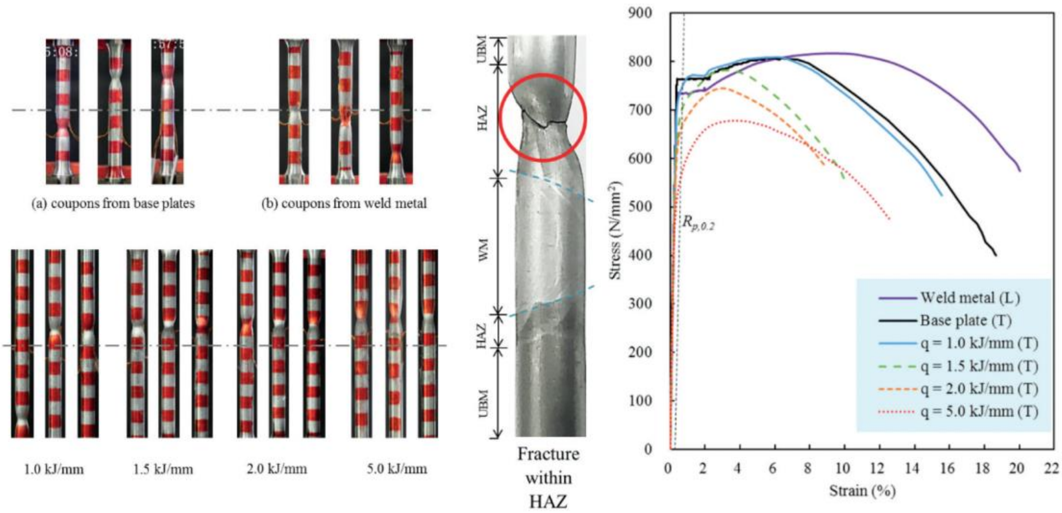

Figure 2.3 Effects of welding onto mechanical properties of S690-QT steel (Liu *et al.*, 2018)

2.3 Fatigue assessment approaches

Fatigue is the process of accumulated damage induced by repeated cyclic actions, and the accumulated damage leads to crack initiation and propagation in critical parts of steel structures. (Rolef and Barsom, 1977). At present, there are two approaches which are widely used for fatigue assessment on steel structures (CEN, 2005a; Zhao *et al.*, 2001; Morrow, 1965; Paris and Erdogan, 1963), and they are described as follows:

- S-N curve approach

  This is an experimental based approach for fatigue assessment on steel structures under long term cyclic actions, typically due to traffic, and it relates stress ranges with the fatigue life of steel structures. A S-N curve defines the number of cycles to failure, N, when a specific steel member is subjected to a given cyclic stress range, S. Through a comprehensive data statistics and analyses on extensive fatigue test results, the derived S-N curves are readily applicable to evaluate the fatigue behaviour of various steel and their sections with different structural details.

  It should be noted that effects of local stress distributions onto the fatigue behaviour of steel structures are commonly dealt with the use of stress concentration factors, i.e. SCF, and critical stresses in steel members due to stress concentrations are required to be derived experimentally and numerically for a wide range of structural details. Instead of designing to average stresses, the fatigue behaviour is evaluated according to the modified critical stresses in the vicinity of critical locations of these details.

- Fracture mechanics approach

  This approach is commonly used to assess fatigue behaviour of steel structures after crack initiation, including crack propagation, instability and fracture. Various fracture parameters are determined experimentally based on an assumption that there is always an initial defect or crack in the steel.

In general, the S-N curve approach is widely used by structural engineers to assessment fatigue performance of steel structures as stipulated in EN 1993-1-9, AISC 360-10, CIDECT-8 and API RP 2A-WSD. EN 1993-1-9 and AISC 360-10 recommends a number of S-N curves to determine fatigue life for various constructional details under a wide range of cyclic stress ranges. Hot spot stress method adopted in both CIDECT and API RP 2A assesses the fatigue life according to the critical stress which is induced by geometric variations in structural members.

However, current design S-N curves for fatigue assessment on steel members given in these design specifications were derived from extensive fatigue tests on a wide range of structural steel, and their welded and bolted joints, and also many practical structural details. It should be noted that these design S-N curves are developed with a large amount of S-N data of S235 to S460 steel, and hence, these codes recommend various S-N curves for S235 to S460 steel. However, the S-N curves are also recommended to cover the S690 steel as a conservative approach despite a lack of test data.

According to EN 1993-1-1 (CEN, 2005b) and EN 1993-1-12 (CEN, 2007), there are some additional requirements on the mechanical properties of S690 steel, in particular, ductility; however, no specific requirement on fatigue is given. In order to promote effective use of HSS in offshore structures, there is an urgent need to determine their fatigue behaviour under cyclic actions, and also to develop effective design rules to assess their fatigue performance.

2.4 Investigation into fatigue performance of high strength steel

Over the past forty years, a large number of experimental investigations have been carried out to examine the fatigue behaviour of many structural steel and their welded sections. Hence, a literature review on fatigue performance of high strength steel were presented as follows.

2.4.1 High strength steel and their welded sections

This Sections presents a review on experimental works performed on coupons of high strength steel and their welded sections. It is important to note that fatigue tests on structural members and joints of practical dimensions in bridge structures are not always feasible nor practical, while fatigue tests on small test specimens may not be able to give representative results because they may contain significantly smaller and fewer ***fatigue-sensitive imperfections*** as commonly found in those steel members and joints of practical dimensions.

Over the past 40 years, there had been many technical discussions on these issues, and diverse opinions and methods on how to address these questions may be found in the literature (Schubnell *et al.*, 2019; Tong *et al.*, 2021a; Tong *et al.*, 2021b; Costa *et al.*, 2010). However, up to the presence, a set of widely acceptable methods for preparation of test specimens (including shapes and sizes), and details of cutting and welding procedures together with specific requirements on surface roughness as well as welding details and profiles is not available yet.

De Jesus *et al.* (2012) performed strain-controlled fatigue tests on rectangular coupons of both the S355 and the S690 steel to examine their fatigue resistances. Strain ratio R was set to be -1, and strain rate was set to be 0.8% per second for these fatigue tests. The strain – fatigue life curves of both the S355 and the S690 steel are plotted in **Figure 2.4**, and it was found that the fatigue resistances in the range of 10^2 to 10^4 cycles of the S690 steel were smaller than those of the S355 steel. However, in the range of 10^4 to 10^6 cycles, the fatigue resistances of the S690 steel were significantly larger than those of the S355 steel. In addition, the crack propagation tests were conducted on both the S355 and the S690 steel, and it was found that the S690 steel performed a higher resistance to crack initiation than the S355 steel, while the resistance to crack propagation was lower than the S355 steel.

Schubnell *et al.* (2019) conducted a series of strain-controlled fatigue tests on cylindrical coupons of S690QL steel, and S960QL steel, and also their heat-treated coupons. These coupons were tested under a stress ratio R = -1. Based on the results of a rigorous data analysis, the strain – fatigue life curves of these steel and their heat-treated coupons are shown in **Figure 2.5**, the fatigue resistances of the heat-affected zones of the high strength steel are found to be very similar to those of the base metal.

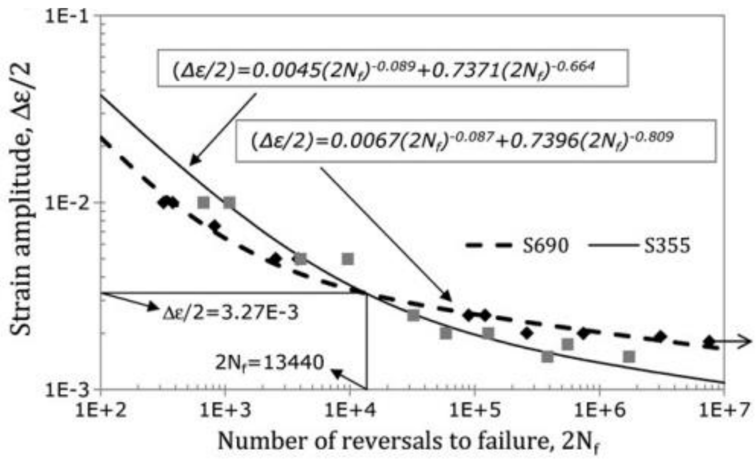

Figure 2.4 Strain – fatigue life curves of the S355 and the S690 steel (De Jesus *et al.*, 2012)

Tong *et al.* (2021a; 2021b; 2023) carried out a large number of load-controlled fatigue tests on coupons of i) high strength Q460, Q550, Q690 and Q960 steel, ii) their butted welded sections, and iii) their transverse welded sections. A stress ratio R of 0.1and a loading frequency of 15 Hz were adopted for these fatigue tests. It was found that:

- Steel plates

  As shown in **Figure 2.6**, the fatigue stress limits of these base plates increased with an increase of the steel grades, and they are found to be at least 20% higher than the codified values given in EN 1993-1-9. Hence, the current design curves for fatigue assessment on these high strength steel were demonstrated to be conservative. It is recommended to improve the current design S-N curve of Class FAT 140 to be that of Class FAT 160.

- Butted welded sections

  As shown in **Figure 2.7**, all the S-N data of these butted welded sections are found to lie above the design S-N curve given in EN 1993-1-9, i.e. FAT 112, especially for those design fatigue life larger than 10^6 cycles. In addition, the maximum fatigue stress limit was found to be 247 N/mm^2 while the minimum fatigue stress limit was found to be 126 N/mm^2 among all these welded sections. Hence, it was recommended to improve the current design S-N curve of Class FAT 112 to be that of Class FAT 125 for fatigue assessment on the butted welded sections of these high strength steel.

- Transverse welded sections

As shown in **Figure 2.8**, the S-N curve of Class FAT 92 was proposed for the fatigue assessments on the transverse welded sections of these high strength steel. And the fatigue stress limits of these transverse welded sections were found to be at least 30% greater than the codified value given in EN 1993-1-9, i.e. 80 N/mm^2. Hence, the current design S-N curve for fatigue assessment on the transverse welded sections of high strength steel were demonstrated to be conservative.

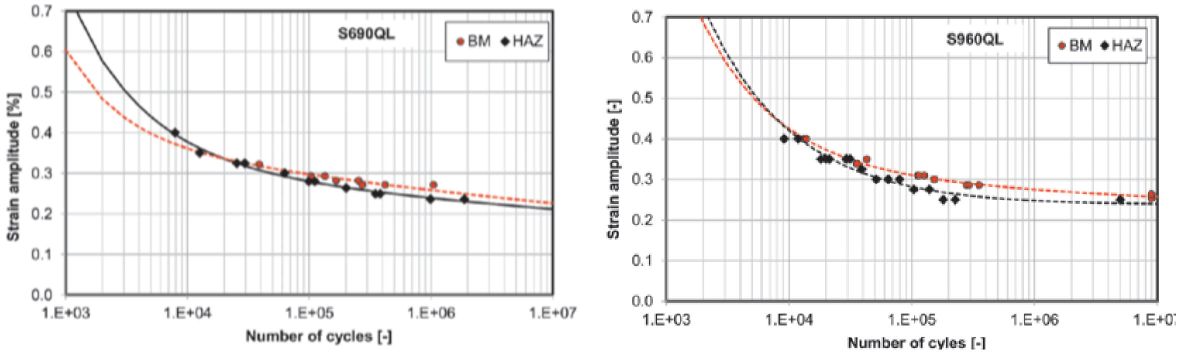

Figure 2.5 Strain – fatigue life curves of the S690 and the S960 steel, and their HAZ (Schubnell *et al.*, 2019)

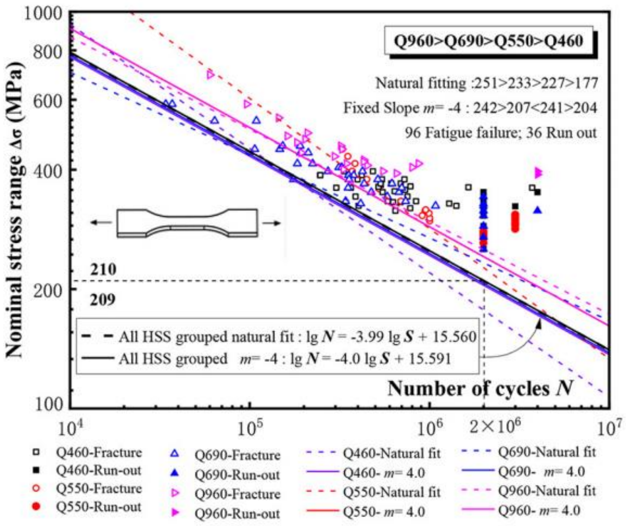

Figure 2.6 S-N data of various high strength steel (Tong *et al.*, 2021a)

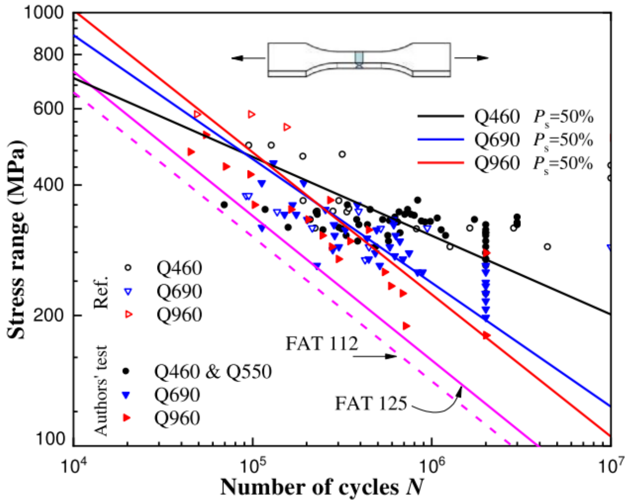

Figure 2.7 S-N data of butted welded sections of various high strength steel (Tong *et al.*, 2021b)

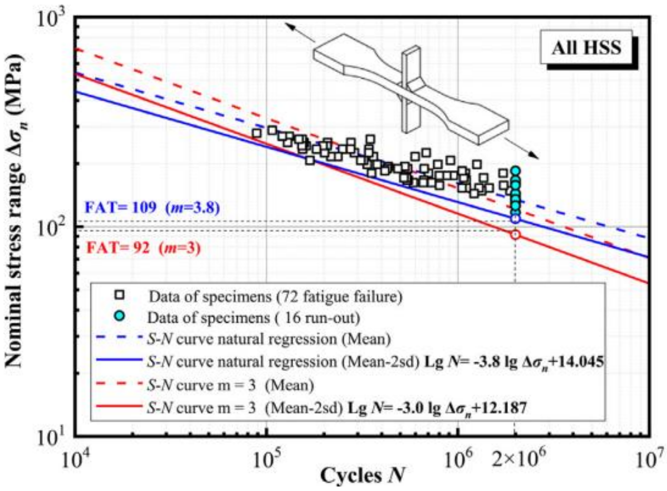

Figure 2.8 S-N data of butted welded sections of various high strength steel (Tong *et al.*, 2023)

Costa *et al.* (2010) examined the effects of welding and post-welding treatments on fatigue performance of the high strength steel, i.e. DOMEX 600 DC steel with a yield strength at 670 N/mm^2. It should be noted that a significant reduction in the fatigue resistances of the steel was identified after welding. Zong *et al.* (2015) examined experimentally the propagation rates of fatigue cracks in WNQ570 steel and their welded sections. It is found that its resistance to crack propagation is larger than those normal strength steel commonly used in bridges while the crack growth rates of these welded sections are smaller than those of the base metal.

2.4.2 Welded tubular joints

This Sections presents a review on fatigue performance of welded tubular steel joints. Tubular steel structures are widely used in offshore structures like bridges and platforms. Under long-term cyclic actions of waves, winds and vehicles, many fatigue cracks were identified in the vicinity of the welded collars of the tubular joints, and even sudden fracture of these offshore structures were found to take place due to fatigue failure at critical joints, as shown in **Figure 2.9**.

In general, fatigue performance of structural steel members and joints is heavily affected by a number of geometrical and material factors, including presence of inclusions and impurity in the steel, pores which are introduced onto the surface of the steel members during welding, and presence of a sudden change in geometry of the steel members (Ahola *et al.*, 2022; Baumgartner *et al.*, 2017; Schubnell *et al.*, 2024). Many researchers expected that the fatigue performances derived from the coupons were significantly different to those of welded steel joints (De Jesus *et al.*, 2012; Schubnell *et al.*, 2019).

In recent decades, a large number of researchers carried out experimental investigations into fatigue behaviour of welded tubular joints. Mashiri *et al.* (2004a; 2004b; 2020) experimentally examine the fatigue performance of various S355 welded T-joints, i.e. CHS-CHS, CHS-RHS, CHS-plate and RHS-plate joints, and then a series of S-N curves were proposed for the fatigue assessments on these welded joints throughout a systematic data analysis. It should be noted that most of these experimental works were performed on the welded tubular joints made of normal strength steel, while limited experimental investigation on high strength steel joints is available.

Hu *et al.* (2022) examined structural behaviour of the S690 welded T-joints under both monotonic and cyclic actions, and an advanced measurement technique of digital imaging correlation method was utilized to measure strain variations on the surfaces of these T-joints during testing. It was found that fracture occurred within the heat affected zones of the welded joints with apparent deformations, and typical values of the measured principal strains in the vicinity of the welded collars often exceeded 10% up to fracture. For those T-joints under cyclic actions with high strains and low cycles, they also failed within the heat affected zones of the welded joints with apparent deformations.

Jiao *et al.* (2013) examined experimentally the fatigue behaviour of plate joints with ultra-high strength CHS (f_y > 1350 N/mm^2) under cyclic in-plane bending actions, and it was found that the fatigue behaviour of these plate joints was significantly different with those of normal strength steel. All S-N data were found to lie above existing design S-N curves, and a higher design S-N curve was then recommended. While the thickness of these CHS was only 1.8mm, and the maximum applied load was only 4 kN, which are not commonly used in civil engineering.

Chiew *et al.* (2015) examined the fatigue behaviour of two S690 welded T-joints between RHS, and it was found that the S-N data lie above the design S-N curve given in CIDECT-8. While only two fatigue tests on the S690 welded T-joints were carried, more S-N data were needed to examine the fatigue performance of welded joints made of high strength steel. Other researchers

Figure 2.9 Typical fatigue failure of offshore tubular steel structures

2.4.3 U-rib stiffened steel deck

This Sections presents a review on fatigue performance of the U-rib stiffened steel deck. In general, orthotropic steel decks stiffened with U-shaped ribs are widely adopted in long-span steel bridge structures due to their satisfactory structural performance. While fatigue problems were found to be served in these steel bridges, typical fatigue cracks of the U-rib stiffened steel deck are shown in **Figure 2.10**. It is evident that fatigue cracks initiated and propagated along the welded joints between the U-rib and the steel deck, and also those between the U-rib and the floor beam (Abdelbaset and Zhu, 2024). Similarly, the S-N curve approach is widely used to examine the fatigue performance of the U-rib stiffened steel deck by other researchers.

Li *et al.* (2017) conducted a total of 12 fatigue tests on the U-rib stiffened steel deck with different welding penetration ratios of 15% and 75% at the welded rib-deck joints. These specimens were made of SM400 steel with yield strength and tensile strength of 281 and 424 N/mm^2 respectively. For the specimens with 15% penetration ratio, fatigue cracks were found to initiate at the weld root of the steel deck. For the specimens with 75% penetration ratio, fatigue cracks were found to initiate at the weld toe of the steel deck. And the fatigue resistances of the steel decks with a 75% welding penetration ratio were found to be greater than those with a 15% welding penetration ratio. Hence, it is demonstrated that the welding details may significantly affect the fatigue behaviour of these U-rib stiffened steel deck.

Fu *et al.* (2018) experimentally examine the fatigue performance of both the Q345 and the Q420 U-rib stiffened steel decks. The resistances to crack initiation of the Q420 U-rib stiffened steel decks were found to be grater than those of the Q345 U-rib stiffened steel decks. For most of these specimens, fatigue cracks were found to initiate at the weld root of the steel decks due to their small welding penetration ratios. And the fatigue life of the specimens with full welding penetration ratio was found to be 30% larger than those of 80% welding penetration ratio under the same cyclic actions.

Shi *et al.* (2019) performed fatigue tests on three full-scale orthotropic steel decks made of Q345 steel with a nominal yield strength of 345 N/mm^2. Based on the examined S-N data, the design S-N curve Class FAT90 given in EN 1993-1-9 was recommended to assess the fatigue performance of these steel decks. Cheng *et al.* (2017) carried out four fatigue tests on the U-rib stiffened steel decks made of Q345 steel, and it was found that obtained S-N data lie above the design S-N curve Class FAT90 given in EN 1993-1-9. The residual life after crack initiation of these steel decks were found to be about 30% of the total fatigue life.

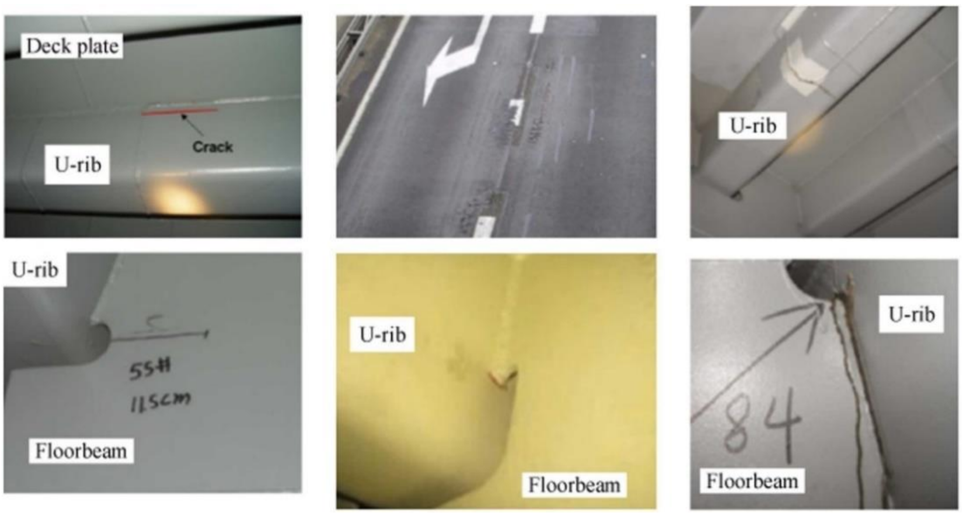

Figure 2.10 Typical fatigue cracks of U-rib stiffened steel deck (Abdelbaset and Zhu, 2024)

2.4.4 Effects of stress concentration

Due to geometrical discontinuities of the welded structures, stresses are generally found to be concentrated locally in the vicinity of the weld toe of the welded structures. Hence. the stress concentration factors (SCF) were employed to predict the stresses at the weld toe due to geometrical discontinuities, i.e. hot spot stresses σ_{hs}, for fatigue assessment on welded structures.

For welded tubular joints, many researchers experimentally and numerically determine the SCF of these welded joints. Mashiri *et al.* (2004a) measured the SCF at the crown of the welded T-joints between S355 CHS, and it was found that the SCF of these T-joints were less than 2, which were much smaller than the recommended values given by CIDECT. Mashiri *et al.* (2004b; 2006) also determined the SCF of the welded T-joints between S355 CHS and S355 RHS, and the welded T-joints between S355 CHS to plate, under in-plane bending actions. Chiew *et al.* (2015) measured the SCF of 2 welded T-joints between S690 SHS under various actions, and it was found that the differences between the measured SCF and the recommended SCF given in CIDECT were around 30%. Lan *et al.* (2021) also found that existing SCF formulae given in CIDECT overestimated the effects of stress concentration of the welded X-joints between S890 SHS under axial loadings. Finite element analyses were widely employed to carried out numerical investigations for SCF determination of various joints. Shao *et al.* (2009) numerically predicted the SCF of the welded K-joints between S355 CHS under various actions. Based on the investigation of the influence of the geometrical parameters on the stress distributions, a set of parametric equations for predicting the stress distributions of K-joints subjected to basic loadings are presented with sufficient accuracy. Tong *et al.* (2014) conducted both the experimental and the numerical investigations on the SCF of welded T-joints between Q235 SHS, and a set of SCF formulae were proposed to predict their SCF.

For welded U-rib stiffened steel decks, many researchers conducted both the experimental and the numerical investigations into the hot spot stresses of these steel decks. Cheng *et al.* (2017) experimentally and numerically examined the hot spot stresses at the weld toe along the steel decks, and also the corresponding SCF. It was found that the stress gradients within the extrapolation region near the weld toe performed a linear characteristic, and the maximum SCF of these steel decks was found to be 1.67 at the weld toe of the steel decks while the effects of stress concentration at the weld toe of the U-ribs were demonstrated to be ignored. Huang *et al.* (2019) performed fatigue tests on a total of 9 U-rib stiffened orthotropic steel decks, and the hot spot stresses at the weld toe of the steel decks were determined experimentally and numerically to evaluate the fatigue stress level of these specimens.

It should be noted that most of the investigations into the effects of stress concentration on welded structures were carried out on those made of normal strength steel, while only several literatures reported the research works on the high strength steel. Hence, it is recommended to carried out both the experimental and the numerical investigations on the effects of stress concentrations of the welded joints made of high strength steel (Liu *et al.*, 2022).

2.4.5 Summary

Existing experimental data and numerical data on the fatigue performance of the high strength steel are found to be limited in the literature. Current design S-N curves for fatigue assessment on steel structures are developed with a large amount of S-N data of S235 to S460 steel. Hence, it is necessary to carry out fatigue tests on S690 steel, their welded sections and their welded joints to provide scientific data to verify the use of these S-N curves for S690 steel.

It is also highly desirable to determine the effects of stress concentration and the welding-induced residual stresses on the fatigue performance of these welded structures, and to co-relate the fatigue behaviour of small coupons with those of large structural members and joints.

Chapter 3 Material characterization of high strength Grades 690 & 960 steel and their welded sections

3.1 Introduction

This chapter presents a comprehensive experimental investigation into fatigue behaviour of high strength Grades 690 & 960 steel, and their welded sections. The systemic fatigue tests on small standardized cylindrical coupons of the high strength S690 and S960 steel plates, and their welded sections were carried out. These coupons were then polished on their surfaces in order to eliminate micro-cracks which may affect adversely on crack initiation and propagation under cyclic actions. Both the test data and results of these fatigue tests are then analysed according to commonly adopted methods though application of these test data and results should be cautioned. Effects of stress concentration and presence of residual stresses on the fatigue performance of the structural members and joints should be considered additionally, which are presented in Chapter 4. In order to examine their fatigue behaviour, i.e. crack initiation and propagation as well as accumulative deterioration in stiffness, the following experimental works have been carried out:

Task 1 – Experimental investigation

i) S690-QT steel and their welded sections

- 2 monotonic tensile tests on standard cylindrical coupons.
- a total of 24 fatigue tests on cylindrical coupons, and a majority of them are strain-controlled cyclic tests; the cyclic strain amplitudes $\Delta\varepsilon/2$ between ±0.125% and ±0.275% are specified. The corresponding stress amplitudes $\Delta\sigma/2$ are $\pm 0.35\ f_y$ and $\pm 0.75\ f_y$, i.e. within the elastic range.

ii) S690-TM steel and their welded sections

- 2 monotonic tensile tests on standard cylindrical coupons.
- a total of 24 fatigue tests on cylindrical coupons, and all of them are load-controlled cyclic tests; the cyclic stress amplitudes $\Delta\sigma/2$ between ±0.50 f_y and ±0.70 f_y are specified.

iii) S960-QT steel and their welded sections

- 2 monotonic tensile tests on standard cylindrical coupons.
- a total of 30 fatigue tests on cylindrical coupons, and all of them are load-controlled cyclic tests; the cyclic stress amplitudes $\Delta\sigma/2$ between ±0.45 f_y and ±0.70 f_y are specified.

The measured engineering stress-strain curves under monotonic actions are adopted to provide data to facilitate selection of parameters for execution of subsequent fatigue tests, these parameters are selected to cover a wide range of practical stresses in applications. All fatigue tests were carried out under a loading frequency of at least 10 Hz according to a wide range of cyclic stress amplitudes $\Delta\sigma/2$ and cyclic strain amplitudes $\Delta\varepsilon/2$ anticipated in typical bridge structures. Key results are the numbers of cycles completed before fracture, N. Both scanning electron microscope observations and metallographic analyses were conducted on typical fractured coupons to examine micromechanics of fatigue fracture of these welded sections.

Task 2 – Analyses on S-N data and formulation of S-N curves

After data analyses, the S-N data obtained from the fatigue tests on the S690-QT, S690-TM and S960-QT steel conducted in the present project are plotted onto the same graph for comparison with codified design curves. A similar plot was also obtained for welded sections of these steel. In order to allow an effective comparison with the S355 steel, data available in the literature have also been collected. A comprehensive comparison with all these test data obtained in the present project and those available in the literature is also carried out.

3.2 Welding of high strength steel plates

As shown in **Figure 3.1a)**, a robotic welding system was adopted to perform the welding with q = 1.0 kJ/mm of both the S690-QT and S960-QT steel plates, and q = 2.5 kJ/mm of the S690-TM steel plates. The chemical compositions of these high strength steel plates given in EN 10025-6 (CEN, 2019) are summarized in **Table 3.1**, and their welding electrodes are summarized in **Table 3.2**.

Both pre-heating and post-weld heat treatment were adopted during and after welding to prevent cold cracks. It should be noted that a non-destructive inspection had then been conducted on these welded sections to identify any welding defects, and those areas with welding defects would not be used to produce test specimens. **Figure 3.1b)** shows a schematic diagram of an arrangement of various test specimens to be extracted from a welded section for both the monotonic and the cyclic tests.

Heat input energy:
q = 1.0 kJ/mm for S690-QT steel plate, t = 10 mm
q = 1.0 kJ/mm for S960-QT steel plate, t = 10 mm
q = 2.5 kJ/mm for S690-TM steel plate, t = 28 mm

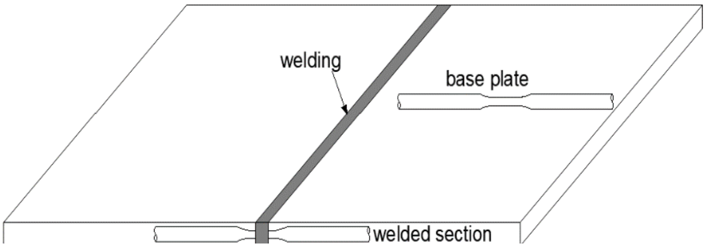

a) Robotic welding b) Arrangement of test coupons in a welded section

Figure 3.1 Fabrication of test coupons

Table 3.1 Chemical compositions (%) of high strength S690 & S960 steel plates

Material	C	Si	Mn	P	S	Cr	Cu	Mo	Nb	Ni	Ti	V
EN 10025-6	0.22	0.86	1.80	0.030	0.017	1.60	0.55	0.74	-	4.10	-	-
S690-QT	0.13	0.25	1.38	0.010	0.001	0.28	0.47	0.24	-	0.04	-	-
S690-TM	0.076	0.049	1.40	0.007	0.002	0.45	0.30	0.27	0.033	0.41	0.013	0.003
S960-QT	0.17	0.25	0.103	0.007	0.002	0.43	0.01	0.559	-	-	-	-

Table 3.2 Chemical compositions (%) of welding consumable

Material	C	Si	Mn	P	S	Cr	Cu	Mo	Nb	Ni	Ti	V
Lincoln 121K3C-H Plus for S690-QT	0.07	0.26	1.72	0.01	0.01	0.05	-	0.59	-	2.35	-	-
NSSW Y-80J for S690-TM	0.10	0.01	1.72	0.011	0.007	0.60	0.08	0.57	-	2.5	-	-
Oerlikon CARBOFIL 2NiMoCr for S960-QT	0.08	0.6	1.5	0.015	0.018	0.4	-	0.6	-	2.2	-	-

3.3 S690-QT steel and their welded sections

3.3.1 Monotonic tensile tests

- ***Test programme***

A total of 2 monotonic tensile tests were carried out to obtain full range stress-strain curves of the S690-QT and its welded sections. According to BS EN ISO 6892 (ISO, 2019), cylindrical coupons with proportional dimensions were adopted, and the diameters of the S690-QT were specified to be 5.0 mm, as shown in **Figure 3.2**.

Five times at different positions of the minimum cross sections are measured with the use of a vernier calliper. Taking the minimum measurement as the diameter of test coupon. The cross section of each coupon is a circle, and the critical diameter of the minimum cross sections is measured and then calculate the cross-sectional area.

In addition, the requirements for the strain rate are presented in the **Table 3.3**. The strain rates adopted in the tests are 0.05%/min form beginning to 1% strain, 0.2%/min for the strain range from 1% to the necking, and 0.5%/min from necking to fracture.

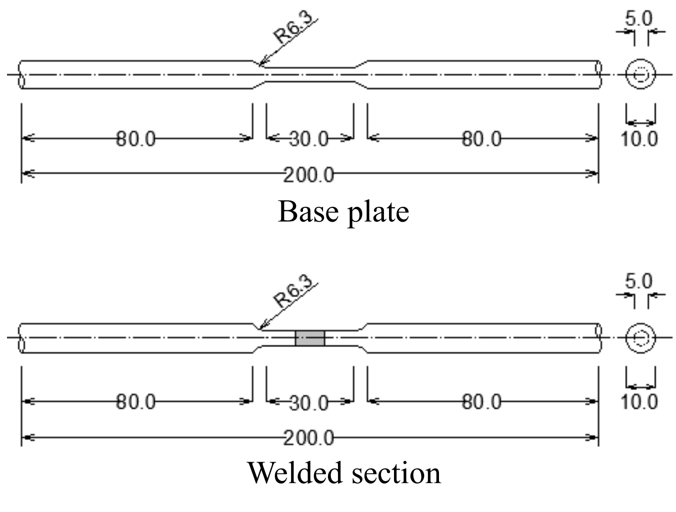

Figure 3.2 Dimensions of standard cylindrical coupons for tensile tests: S690-QT

Table 3.3 Requirements for the strain rate of monotonic tensile test (ISO, 2019)

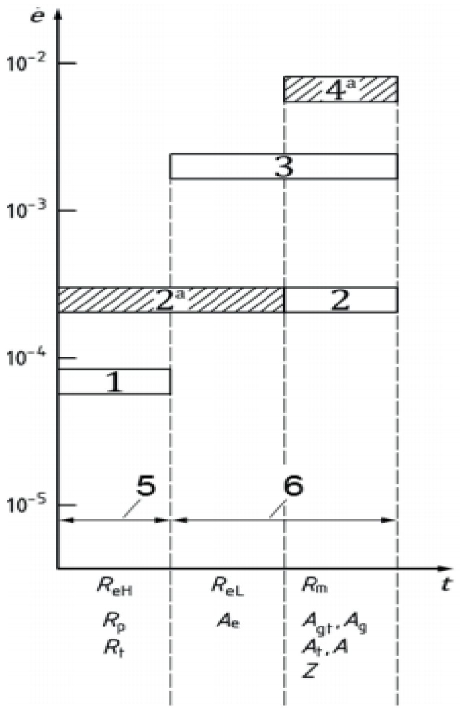

Range	Requirements of strain rate
Range 4 for determination of percentage elongation after fracture	0.00670 s^{-1} ± 20%
Range 3 for determination of tensile strength	0.00200 s^{-1} ± 20%
Range 2 for determination of lower yield strength	0.00025 s^{-1} ± 20%
Range 1 for determination of Young's modulus and higher yield strength	0.00007 s^{-1} ± 20%

- ***Test setup and instrumentation***

Figure 3.3 illustrates the test setup of the monotonic tensile tests while together with various details of the instrumentation. A "INSTRON 8803" Servo-hydraulic Controlled Testing System with a ±500kN maximum loading capacity were employed, and a high-resolution digital camera which performs 50 million pixels per frame was adopted to record the experimental phenomenon in each 30 seconds during the test.

In addition, a high precision static extensometer with a gauge length of 25.0 mm and photographic analysis technique were adopted to measure changing of strain, and the changing of load was recorded by the data logger every 0.25s.

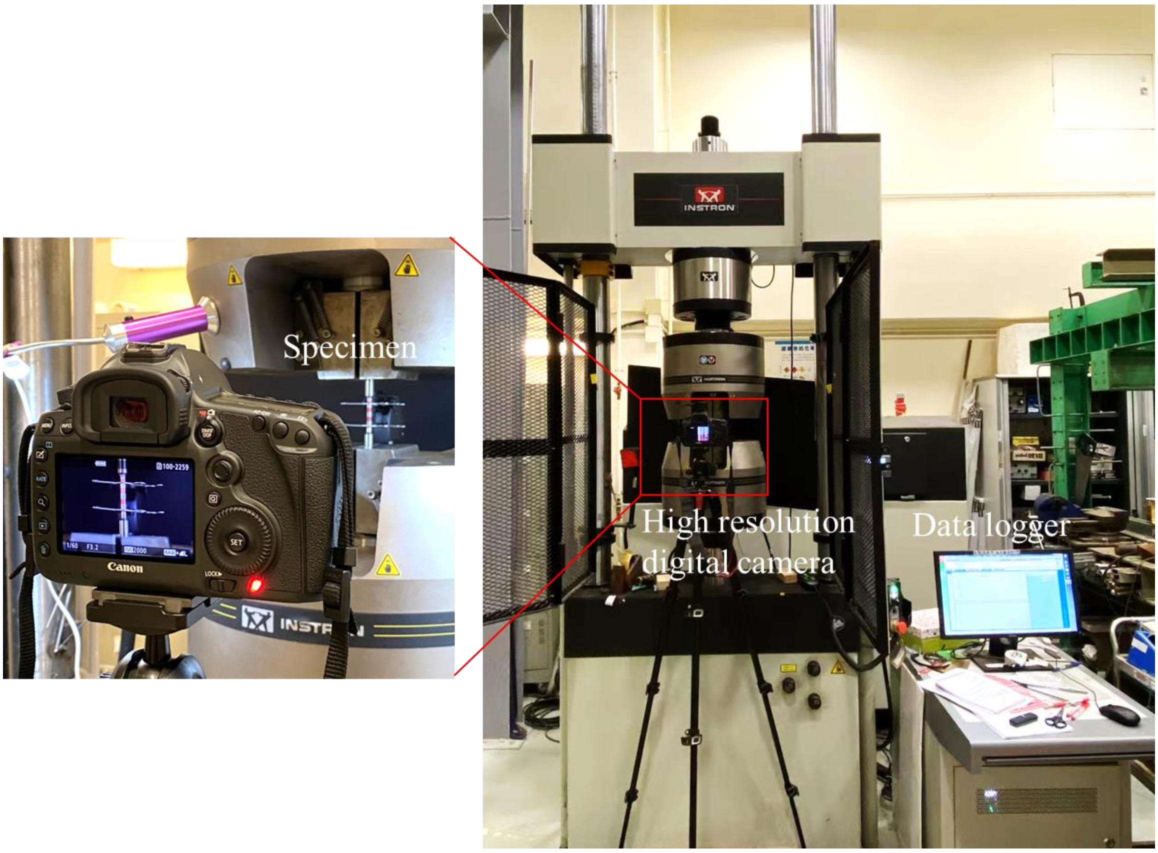

Figure 3.3 Test setup of monotonic tensile tests of S690-QT steel and its welded section

- ***Test results***

In each test, both the applied force and the elongation of the coupon at each point in time are measured and recorded continuously according to the data acquisition rates of the data logger. As shown in Equation (3-1), the engineering stress, σ_E, is determined by dividing the applied force, F, with the original cross-sectional area, A_0, of the coupon. The engineering strain, ε_E, is determined by dividing the measured elongation of coupon, Δ, with its original gauge length, L, as shown in Equation (3-2).

$$\sigma_E = \frac{F}{A_0} \tag{3-1}$$

$$\varepsilon_E = \frac{\Delta}{l} \tag{3-2}$$

According to EN 1993-1-1 (CEN, 2005b) and EN 1993-1-12 (CEN, 2007), the requirements for the mechanical properties of high strength steel are as follows:

$$\text{i) } f_y/f_u \geq 1.05 \qquad \text{ii) } \varepsilon_L \geq 10\% \qquad \text{iii) } \varepsilon_u E_s/f_y \geq 15$$

where:

f_y is the yield strength;

f_u is the tensile strength;

ε_L is the strain at fracture;

E_s is the elastic modulus; and

ε_u is the strain at tensile strength.

The engineering stress-strain curves of the S690-QT steel and its welded section are plotted in **Figure 3.4**. It should be noted that the coupon of the welded section was carefully etched before tests, the boundaries of the base plates, the heat affected zones, and the weld metal were clearly identified. In general, fracture was found to take place always within the heat affected zones of the welded section. Only small reductions in the yield and the tensile strengths were found in the welded section, when compared with those of the base plate. Key mechanical properties of the S690-QT steel and their welded section are summarized in **Table 3.4**, and these data are adopted to facilitate selections of suitable strain amplitudes in subsequent fatigue tests.

Table 3.4 Mechanical properties of S690-QT steel and its welded sections

Specimens	Young's modulus E (kN/mm^2)	Yield strength f_y (N/mm^2)	Tensile strength f_u (N/mm^2)	Strain at tensile strength ε_u (%)	Elongation at fracture ε_L (%)
S690-QT	209.4	767	811	5.9	17.2
S690-QT-WS	210.4	742	817	4.9	16.0

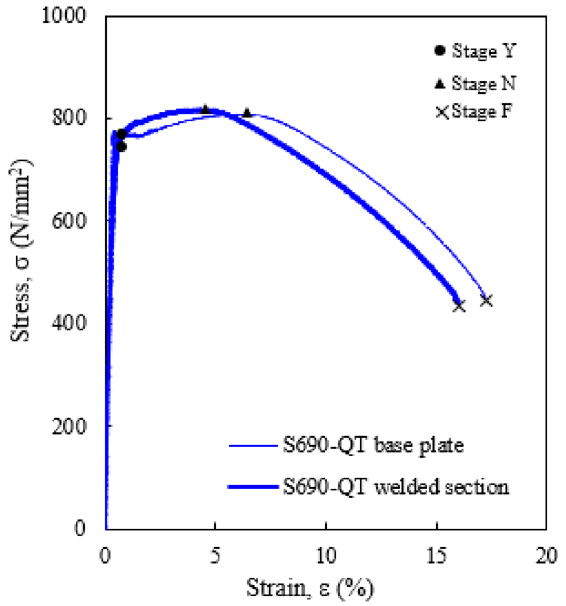

a) Engineering stress–strain curves

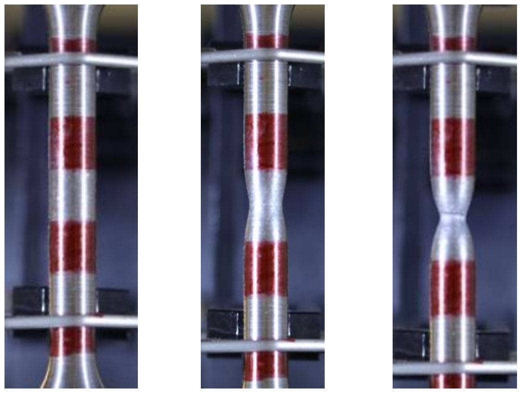

Stage Y Stage N Stage F

b) Base plate: ϕ = 5 mm

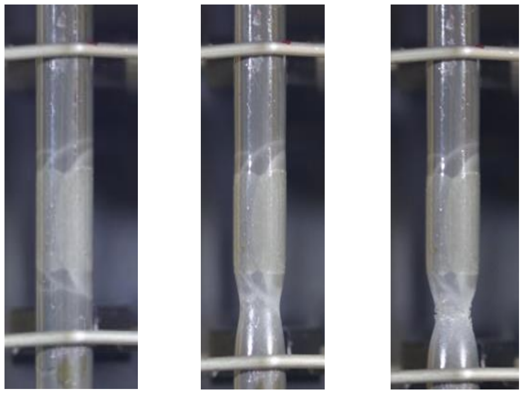

Stage Y Stage N Stage F

c) Welded section: ϕ = 5 mm

Figure 3.4 Mechanical properties of S690-QT steel and its welded section

In addition, hardness measurements were carried out on the S690-QT welded sections, the "HM-210/220 Vickers Hardness Testing Machine" was employed to do the measurements. A total of 99 points of hardness were measured on the specimens, including the upper, middle and lower sections of the cross section to detailly determine the hardness distribution along the longitudinal and transverse directions.

The results are shown in **Figure 3.5**, it is found that there is a significant variation in hardness across the welded sections, primarily due to the presence of the welding electrode which hardness is measured to be 360 HV. Significant softening is found within the fine-grained regions of the heat affected zones, and the minimum hardness is 235 HV.

As a reference, in S355 welded sections, there is normally a significant variation in hardness across the welded sections, and significant hardening is often found within the HAZ. The maximum hardness in the HAZ is typically 200 to 250 HV while the minimum hardness in the base metal is typically 150 to 180 HV (Sun *et al.*, 2019).

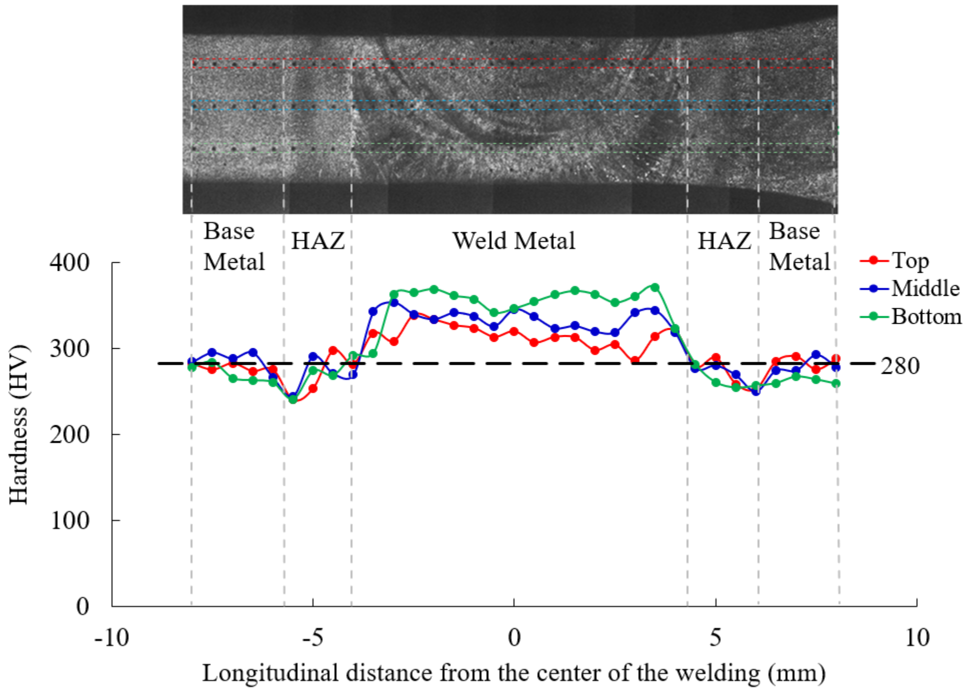

Figure 3.5 Variation in hardness of S690-QT welded sections

3.3.2 Fatigue tests

- ***Test programme***

In order to fully understand the fatigue behaviour of the S690-QT steel and their welded sections, especially, *crack initiation and propagation, and also accumulative stiffness degradation*. A total of 20 *strain-controlled* fatigue tests were carried out on the S690-QT steel and their welded sections while 4 *load-controlled* fatigue tests were also carried out as repeated tests of high cycle fatigue. It is aimed to quantify the basic fatigue performance of the S690 steel and their welded sections as reference data. Hence, the surfaces of these coupons were polished in order to eliminate micro-cracks which might affect adversely on their crack initiation and propagation under cyclic actions. Effects of stress concentration and presence of residual stresses on the fatigue performance of these structural members and joints are considered separately, as presented in Chapter 4.

It should be noted that these *strain-controlled* fatigue tests are able to provide a complete stress-strain curve for each cycle of these tests for each of these coupons, and a thorough data analysis on these curves is able to present a clear picture on the processes of stiffness degradation of these coupons under repeated cyclic actions. In general, these tests are not commonly adopted because of a high demand on the testing resources.

Table 3.5 summarise the test programme with key parameters. The dimensions and geometry of specially designed cylindrical coupons of the S690-QT steel and their welded sections for fatigue tests is shown in **Figure 3.6**, and they were designed according to ASTM E606 (ASTM, 2005). As the steel plates were 10 mm thick, the diameters of the coupons were specified to be 5.0 mm.

Table 3.5 Test propramme of fatigue tests on S690-QT steel and their welded sections

Specimens	f (Hz)	Control mode	$\Delta\varepsilon/2$ (%)	Specimens	f (Hz)	Control mode	$\Delta\varepsilon/2$ (%)
QT-275-1				QT-250-W1			
-2	10	Strain	0.275	-W2	10	Strain	0.250
-3				-W3			
QT-250-1				QT-200-W1			
-2	10	Strain	0.250	-W2	10	Strain	0.200
-3				-W3			
QT-225-1	10	Strain	0.225	QT-150-W1	10	Strain	0.150
-2				-W2			

-3	100	Load	0.614 f_y (0.225%)	-W3	100	Load	0.425 f_y (0.150%)
QT-200-1 -2	10	Strain	0.200	QT-125-W1 -W2	10	Strain	0.125
-3	100	Load	0.546 f_y (0.200%)	-W3	100	Load	0.354 f_y (0.125%)

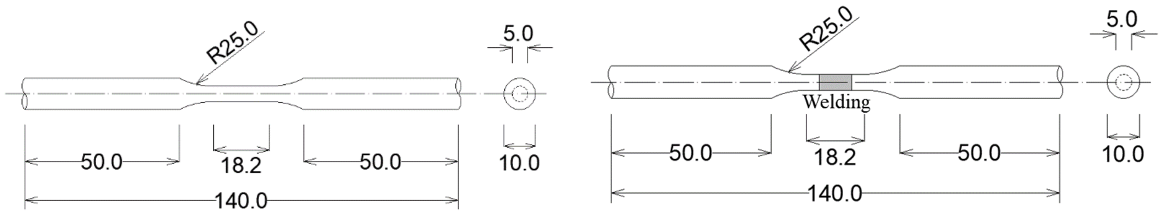

a) Base plate

b) Welded section
(nominal weld length is 5.0mm)

Figure 3.6 Dimensions of cylindrical coupons for fatigue tests: S690-QT

According to the GB T15248-2008 (CNS, 2008), the machined stripes left after polishing should not be transverse, and there should be no obvious machining on the surface of the specimen at about 20X magnification. And hence, it should be noted that the surfaces of the coupons along their gauge lengths were carefully polished to control the surface roughness to be within 0.2μm (Ra0.2) in order to avoid effects of surface roughness onto their fatigue behaviour. **Figure 3.7** shows the polished surface of specimen at both by the naked eye and under 40 times of the microscope. It can be seen that there are no transverse scratches on the surface, and only slight longitudinal polishing marks.

Figure 3.7 40X magnification of specimen surface

- ***Test setup and instrumentation***

Figure 3.8 illustrates the test setup of the *strain-controlled* fatigue tests while together with various details of the instrumentation. An "INSTRON 8803" Servo-hydraulic Controlled Fatigue Testing System with a maximum loading capacity of ±500 kN was employed, and a high-resolution digital camera with 50 million pixels per frame was employed to record cyclic responses of the coupons at 60 frames per second throughout testing.

It should be noted that a precise dynamic extensometer with a travel range 10±1.0000 mm was utilized to control the loading protocol which was a sinusoidal waveform with a constant strain amplitude $\Delta\varepsilon/2$, and a loading frequency f at 10 Hz. It should be noted that a high-resolution digital camera with 50 million pixels per frame was employed to record cyclic responses of the coupons at 60 frames per second throughout testing.

For repeated tests on selected coupons whose fatigue life were expected to exceed 10^6 cycles, only *load-controlled* fatigue tests were carried out with a loading frequency at 100 Hz on a "QBG-100" Electromagnetic Resonance High Frequency Fatigue Testing System with a maximum loading capacity at ±100kN to minimize testing resources. These load-controlled fatigue tests had been employed to investigate the fatigue behaviour of various types of structural steel and their welded sections in construction for many years by many researchers as these tests were readily completed within days or even hours. The test setup of the *load-controlled* fatigue tests is illustrated in **Figure 3.9**.

It should be noted that this loading frequency was selected according to recommendations given in the literature (ASTM, 2005; Keindorf *et al.*, 2010). It is required to ensure that the surface temperatures of the coupons should not increase by more than 2 °C throughout the tests, and the surface temperatures should be measured continuously with thermocouples. The differences of examined fatigue life under these two frequencies were approximately 10%, which falls within the acceptable range of variability of fatigue tests. It is indicated that the influences of these two loading frequencies on fatigue testing are within acceptable limits.

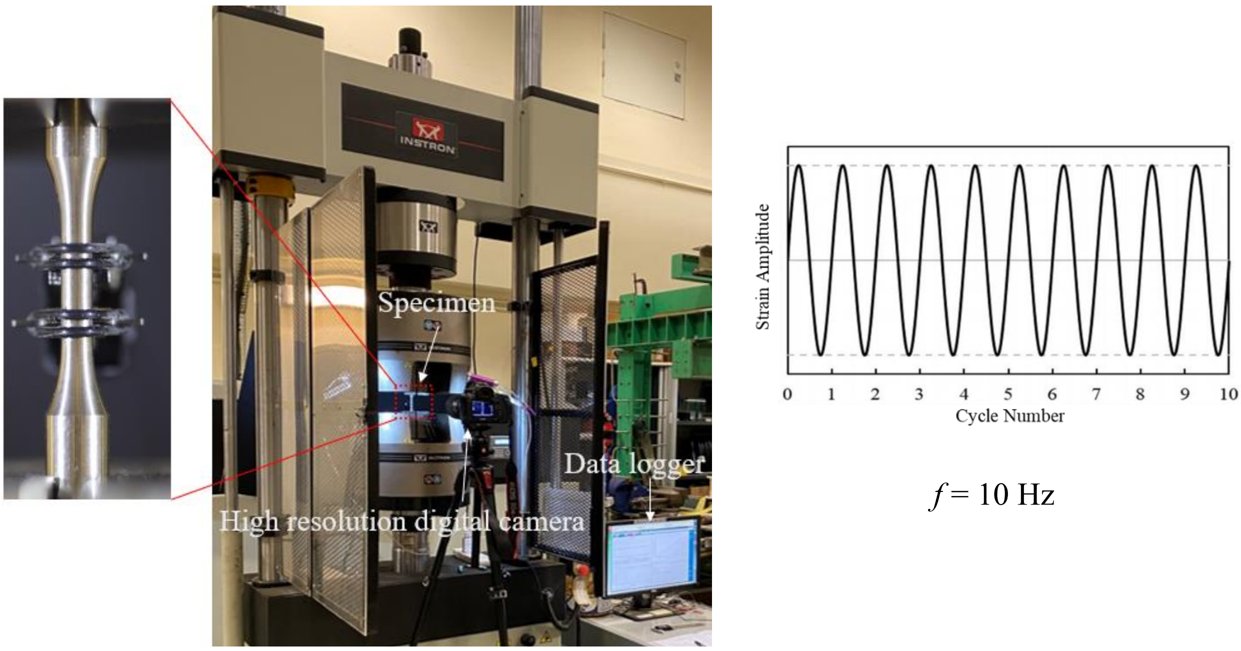

a) Test setup b) Loading protocol

Figure 3.8 Details of strain-controlled fatigue tests

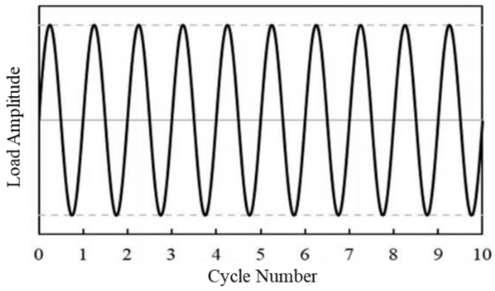

$f = 100$ Hz

a) Test setup b) Loading protocol

Figure 3.9 Details of load-controlled fatigue tests

- ***Test procedures***

All the fatigue tests were performed according to the following procedures:

a) Installation of the coupons

The coupons should be installed properly in the grooves of the grips and aligned their centre lines properly to avoid any slippage of the coupons during testing.

b) Testing

The elongation rates of the coupons along the longitudinal direction were controlled by setting various parameters in the computer program of the testing machine, and elongations of the coupons and other experimental phenomenon of the coupons were observed closely. The tests were terminated when reached the failure criterion.

c) Data acquisition

Due to the size limitation of recording files, the frequency of data acquisition of these fatigue tests is shown in **Table 3.6**.

Table 3.6 Frequency of data acquisition

Number of cycles completed	Data acquisition frequency	Recorded data point of each cycle
0 to 10,000	Each cycle	
10,000 to 1,000,000	First cycle of every 10 cycles	100
1,000,000 to 10,000,000	First cycle of every 100 cycles	

- ***Test results***

Failure modes

Figure 3.10a) shows all the tested coupons of S690-QT steel. **Figure 3.10b)** illustrates the typical failure mode of the S690-QT steel, it is found that the fracture occurred along the parallel parts within the gauge lengths of all the coupons

a) Tested coupons

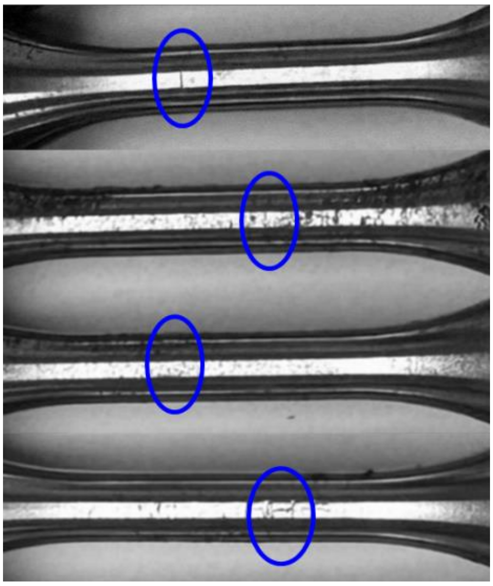

b) Typical failure mode

Figure 3.10 Tested coupons of S690-QT steel

Figure 3.11a) illustrates all the tested coupons of S690-QT welded sections after etching with a 10% nitric acid solution, and clear boundaries of the weld metal, the heat affected zones, and the base metal are readily identified. As shown in **Figure 3.11b)**, the fracture occurred typically within the weld metal.

a) Tested coupons

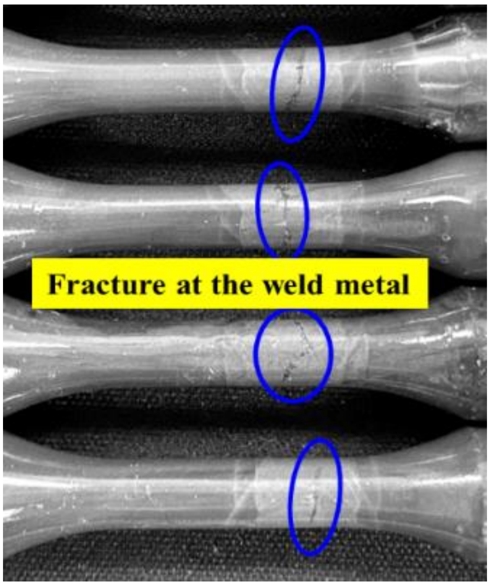

b) Typical failure mode

Figure 3.11 Tested coupons of S690-QT welded sections

S-N data

The S-N data of the fatigue tests of the S690-QT and their welded sections are summarized in **Table 3.7**. In addition, the S-N data are plotted in logarithmic coordinates as shown in **Figure 3.12**. As compared with those data of the S690 QT steel, the fatigue resistances of the welded sections are found to have a small reduction, as illustrated in **Figure 3.12**.

Hence, for those coupons examined in the current study, the effect of welding onto the fatigue life of these coupons of S690-QT steel is demonstrated to be less severe than those anticipated, as compared with those of other structural steel commonly used in constructions. It should be emphasized the welding procedures should be properly controlled so that there are no geometrical defects, such as pores and notches, in the welded components.

It should also be noted that the fatigue life of these coupons tested with strained-controlled cyclic actions at both 10 and 100 Hz are found to vary *merely* within 10%, and this is well within the acceptable range of variability. Hence, these two loading frequencies are shown to have little effects on the fatigue life of these coupons.

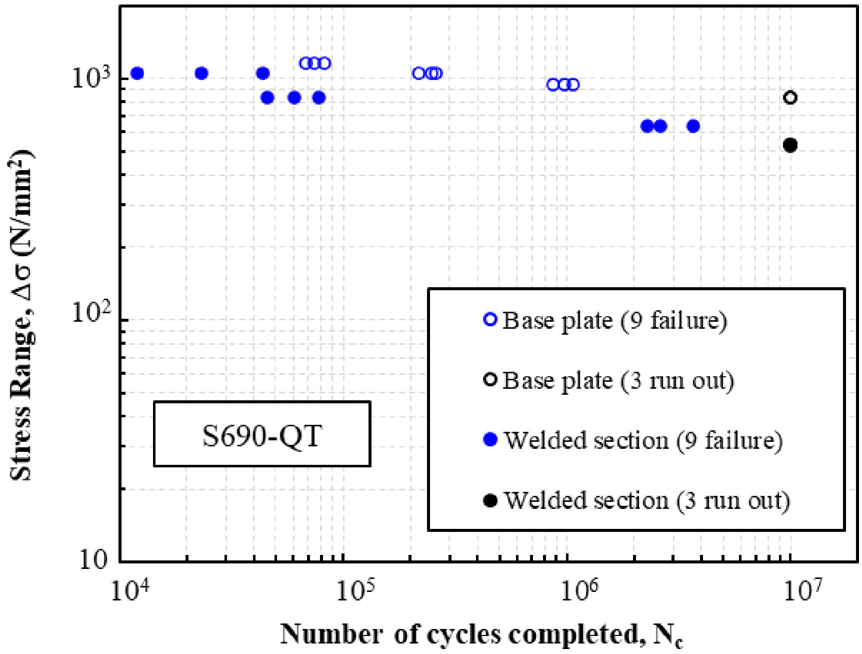

Figure 3.12 Test results of S690-QT steel and their welded sections

Table 3.7 Test results of fatigue tests on S690-QT steel and their welded sections

Specimens	f (Hz)	$\Delta\sigma$ (N/mm^2)	Number of cycles completed N_c	Specimens	f (Hz)	$\Delta\sigma$ (N/mm^2)	Number of cycles completed N_c
QT-275-1			81,912	QT-250-W1			12,090
-2	10	1151.8	74,881	-W2	10	1052.0	23,284
-3			68,139	-W3			43,505
QT-250-1			219,378	QT-200-W1			77,955
-2	10	1047.0	270,792	-W2	10	838.4	46,019
-3			253,052	-W3			60,474
QT-225-1	10		873,291	QT-150-W1	10		2,618,879
-2		942.3	1,062,436	-W2		637.9	3,660,605
-3	100		980,500	-W3	100		2,300,110
QT-200-1	10		10,000,000	QT-125-W1	10		10,000,000
-2		837.6	10,000,000	-W2		526.0	10,000,000
-3	100		10,000,000	-W3	100		10,000,000

Deterioration in stiffness

As all these fatigue tests were conducted under strain-control, additional deformation characteristics of these tests become available. A detailed consideration on these characteristics is able to reveal their accumulative degradation in their mechanical properties after thousands or even millions of cyclic actions. Two typical test results are selected to illustrate the accumulative degradation of the S690 welded sections, and they are test results of Coupons QT-200-W1 and QT-150-W1, as shown in **Figure 3.13** and **Figure 3.14** respectively.

A detailed analysis on the stress-strain curves was conducted, and key data of the fatigue test on Coupon QT-200-W1 are presented in **Figure 3.13**. It should be noted while the stress-strain curves of all cycles are plotted in **Figure 3.13a)**, the corresponding peak values are identified in **Figure 3.13b)**. The initial values of the stresses corresponding to a target strain $\pm\Delta\varepsilon/2$ at 0.2% are ±419 N/mm^2, either tensile or compressive, and this represents a stress range of 838 N/mm^2. It is evident that after 77,955 cycles, a significant softening takes place in the coupon as demonstrated in a sudden change in slope, and the modified stresses corresponding to the target strain $\pm\Delta\varepsilon/2$ at 0.2% becomes +377 and -420 N/mm^2, and this represents to a stress range at 797 N/mm^2, or a 5% reduction to the original stress range. This deformation range is referred as the *stable fatigue stage* even though a visible crack was identified on the surface of the coupon with a naked eye during a close examination on the video image. As the test continued, softening occurred quickly, and a fracture of the coupon took place suddenly after 80,714 cycles, this deformation range is referred as the *rapid fracture stage*.

Similarly, a detailed analysis on the stress-strain curves the fatigue test on Coupon QT-200-W1 was conducted, and key data are presented in **Figure 3.14.** It should be noted while the stress-strain curves of all cycles are plotted in **Figure 3.14a)**, the corresponding peak values are identified in **Figure 3.14b)**.

The initial values of the stresses corresponding to a target strain $\pm\Delta\varepsilon/2$ at 0.15% are ±319 N/mm^2, either tensile or compressive, and this corresponds to a stress range of 638 N/mm^2. It is evident that after 2,618,879 cycles, a significant softening takes place in the coupon as demonstrated in a sudden change in slope, and the modified stresses corresponding to the target strain $\pm\Delta\varepsilon/2$ at 0.15% becomes +254 and -351 N/mm^2, and this corresponds a stress range at 605 N/mm^2, i.e. a 5 % reduction to the original stress range. A visible crack was clearly identified on the surface of the coupon with a naked eye during a close examination on the video image. As the test continued, a fracture of the coupon took place suddenly after 2,653,973 cycles.

Within 5% degradation in stress ranges, this deformation range is referred as the stable fatigue stage even though a visible crack was identified on the surface of the coupon with a naked eye during a close examination on the video image. As the test continued, softening occurred quickly, and a fracture of the coupon took place suddenly, this deformation range is referred as the rapid fracture stage. A failure criterion is proposed so that the coupon is considered to have failed when its stresses under repeated cyclic strain actions are reduced by 5%, i.e. a degradation of its stress range, $\Delta\sigma$, by 5%. It should be noted that for both coupons, the number of cycles completed corresponding to various levels of strength reduction in the coupons are shown in **Figure 3.13c)** and **Figure 3.14c)**. Accuracy of the fatigue tests is demonstrated in **Figure 3.13d)** and **Figure 3.14d)** as the errors of the target strains ε_{tar} during testing is shown to lie well within the limit of $\pm2\%$ of the cyclic strain amplitudes $\pm\Delta\varepsilon/2$, according to ASTM E606.

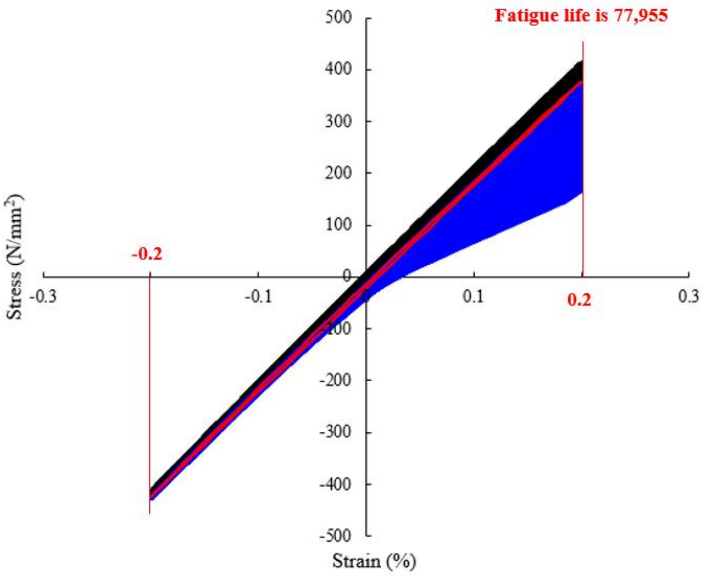

a) Cyclic stress-strain curves

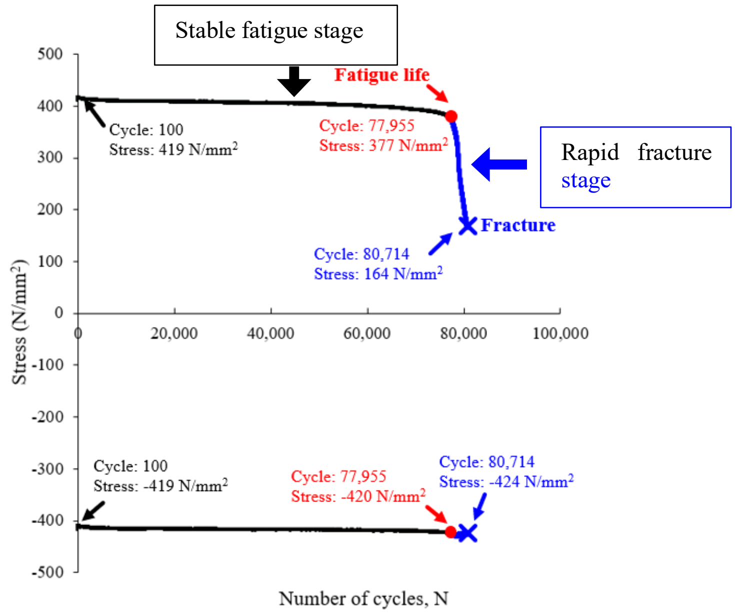

b) Peak stresses

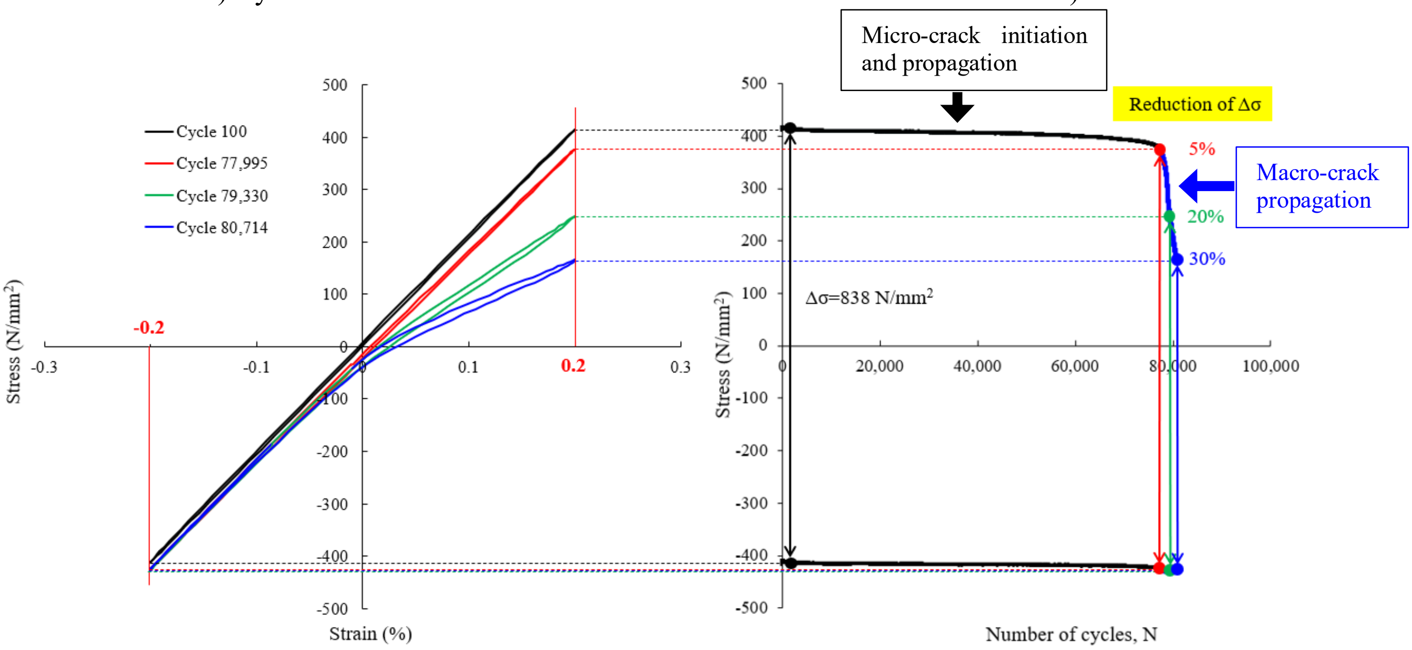

c) Stiffness degradation

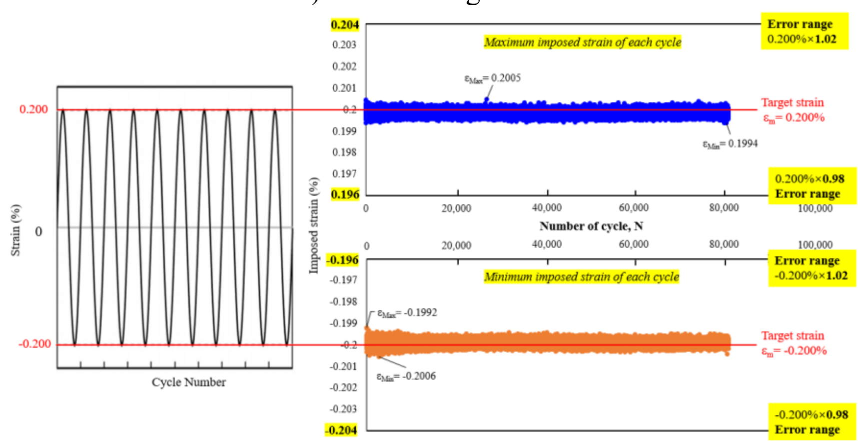

d) Accuracy of cyclic strain amplitudes $\pm\Delta\varepsilon_t/2$ imposed during testing

Figure 3.13 Fatigue test on Coupon QT-200-W1

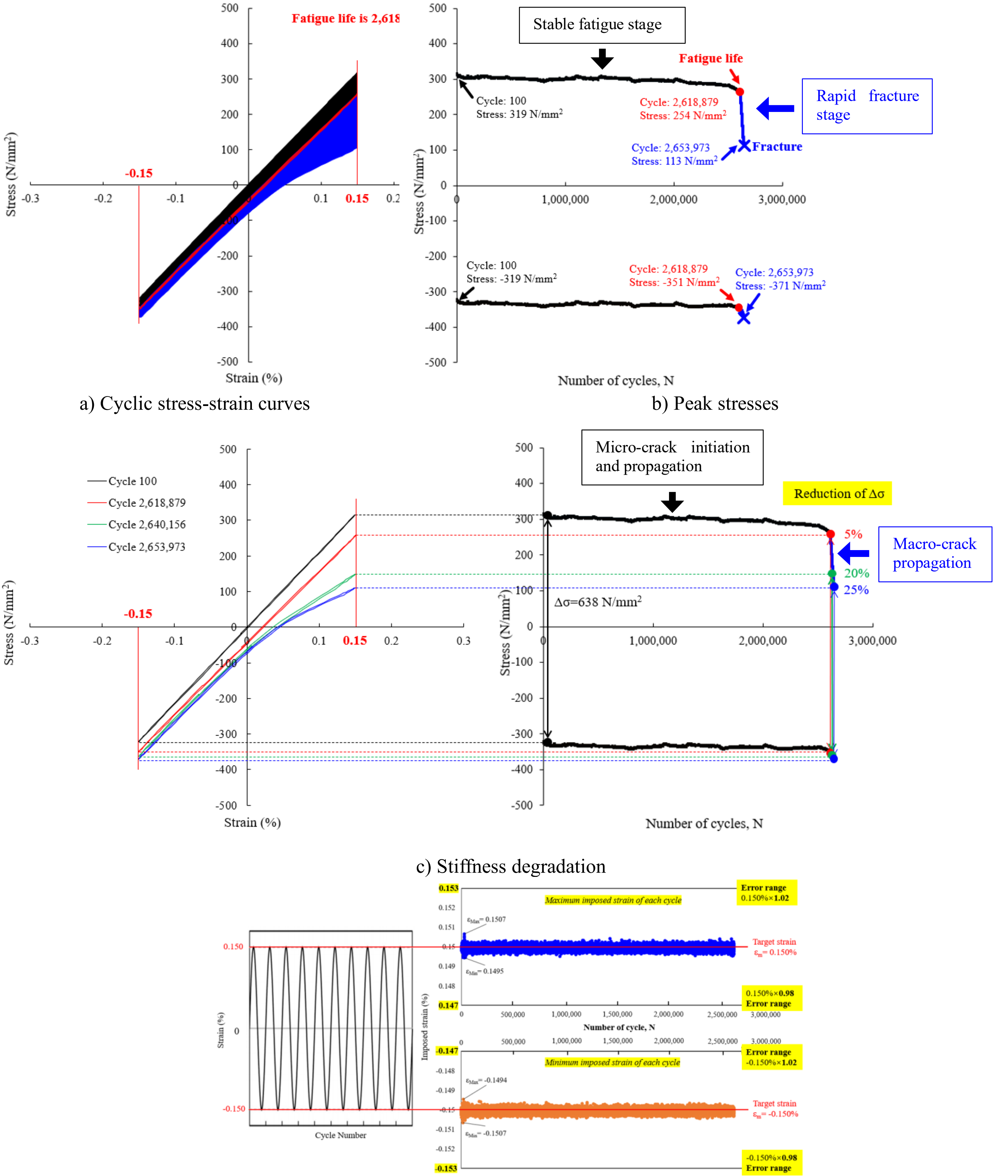

a) Cyclic stress-strain curves

b) Peak stresses

c) Stiffness degradation

d) Accuracy of cyclic strain amplitudes $\pm\Delta\varepsilon_t/2$ imposed during testing

Figure 3.14 Fatigue test on Coupon QT-150-W1

After a comprehensive data analysis, **Table 3.8** and **Table 3.9** summarize various data of the fatigue tests of both the S690-QT steel and their welded sections. These include the numbers of cycles completed before fracture at various strength reduction stages: at 1%, 2.5%, 5%, 10% and 20% reductions in $\Delta\sigma$. For ease of presentation, these data are re-presented as ratios of their respective fatigue life in **Table 3.8** and **Table 3.9**, and they are illustrated in **Figure 3.15** for easy comparison. It should be noted that:

a) For steel plates

- All coupons have completed over 90% of their fatigue life before a 1% reduction in strength.
- All coupons have completed over 95% of their fatigue life before a 5% reduction in strength.
- All coupons have completed over 97% of their fatigue life before a 10% reduction in strength.
- Fracture takes place only after a significant strength reduction in the range of 18 to 29%.

b) For welded sections

- There are significant differences in the fatigue behaviour among these coupons that the ratios of fatigue life for a 1% reduction in strength vary between 0.298 and 0.782.
- All coupons have completed over 90% of their fatigue life before a 5% reduction in strength.
- All coupons have completed over 97% of their fatigue life before a 10% reduction in strength.
- Fracture takes place only after a significant strength reduction in the range of 20 to 31%.

All these information on the fatigue behaviour of these coupons, and hence, these insights on crack initiation and propagation as well as accumulative deterioration in stiffness in these high strength S690-QT steel and their welded sections are readily obtained from strain-controlled cyclic tests.

Table 3.8 Various levels of strength reduction of S690-QT steel

Coupons	$\Delta\sigma$ (N/mm^2)	Number of completed cycles N at various strength reduction stages					
		1%	2.5%	5%	10%	20%	End of test
QT-275-1	1151.8	78,095	80,369	81,912	83,202	83,724	83,799
-2		71,021	73,829	74,881	75,863	76,312	76,351
-3		*Out of measurement range*					68,139
QT-250-1	1047.0	207,968	215,097	216,929	218,101	218,971	219,378
-2		249,527	255,880	259,587	262,836	266,961	270,793
-3		238,818	245,711	249,762	252,240	253,025	253,052
QT-225-1	942.3	853,982	867,494	873,291	880,153	-	885,339
-2		*Out of measurement range*					1,062,436
QT-200-1	837.6	---					10,000,000
-2		---					10,000,000

Coupons	$\Delta\sigma$ (N/mm^2)	Fatigue life ratios at various strength reduction stages						Reduction in $\Delta\sigma$ at N_F
		$N_{1\%}$	$N_{2.5\%}$	$N_{5\%}$	$N_{10\%}$	$N_{20\%}$	N_F	
QT-275-1	1151.8	0.932	0.959	0.978	0.993	0.999	1.000	29%
-2		0.930	0.967	0.981	0.994	0.999	1.000	25%
QT-250-1	1047.0	0.948	0.981	0.989	0.994	0.998	1.000	28%
-2		0.921	0.945	0.959	0.971	0.986	1.000	29%
-3		0.944	0.971	0.987	0.997	0.999	1.000	23%
QT-225-1	753.8	0.965	0.980	0.986	0.994	-	1.000	18%

Table 3.9 Various levels of strength reduction of S690-QT welded sections

Coupons	$\Delta\sigma$ (N/mm^2)	Number of completed cycles N at various strength reduction stages					
		1%	2.5%	5%	10%	20%	End of test
QT-250-W1		3,935	8,392	12,090	12,859	13,222	13,222
-W2	1052.0	8,662	16,776	23,284	24,323	24,913	25,099
-W3				*Out of measurement range*			68,139
QT-200-W1		59,839	76,140	77,955	78,636	79,330	80,714
-W2	838.4	17,996	34,925	46,019	46,265	46,580	47,623
-W3		42,244	54,349	60,474	61,261	62,067	62,418
QT-150-W1	637.9	2,075,777	2,452,491	2,618,879	2,625,922	2,640,156	2,653,973
-W2		2,924,164	3,426,635	3,660,605	3,735,557	3,774,545	3,426,635
QT-125-W1	420.8			---			10,000,000
-W2				---			10,000,000

Coupons	$\Delta\sigma$ (N/mm^2)	Fatigue life ratios at various strength reduction stages						Reduction in $\Delta\sigma$ at N_F
		$N_{1\%}$	$N_{2.5\%}$	$N_{5\%}$	$N_{10\%}$	$N_{20\%}$	N_F	
QT-250-W1	1052.0	0.298	0.635	0.914	0.972	1.000	1.000	20%
-W2		0.345	0.668	0.928	0.970	0.993	1.000	25%
QT-200-W1		0.741	0.943	0.966	0.974	0.983	1.000	30%
-W2	838.4	0.378	0.733	0.966	0.971	0.978	1.000	31%
-W3		0.677	0.871	0.969	0.981	0.994	1.000	27%
QT-150-W1	637.9	0.782	0.924	0.987	0.989	0.995	1.000	25%

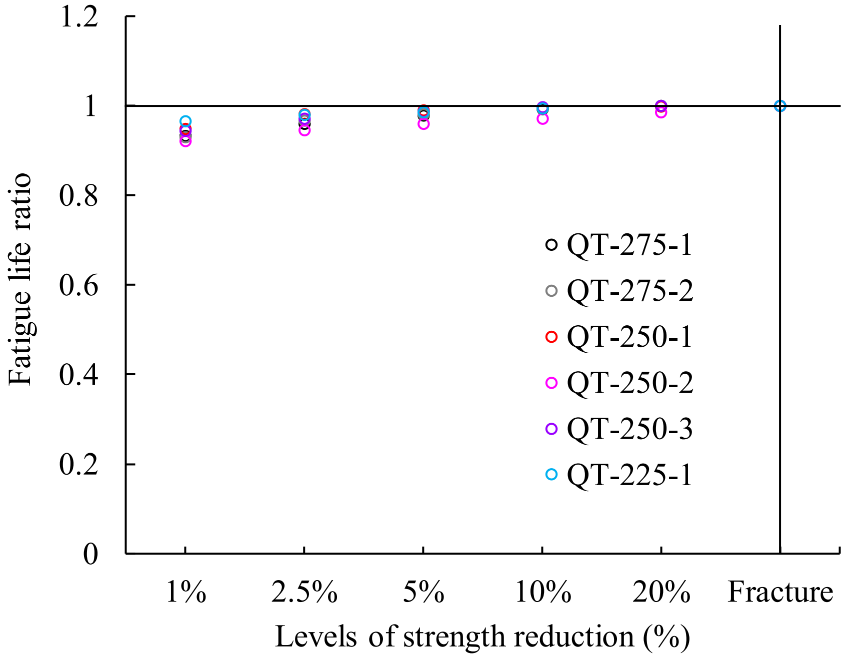

a) Base plates

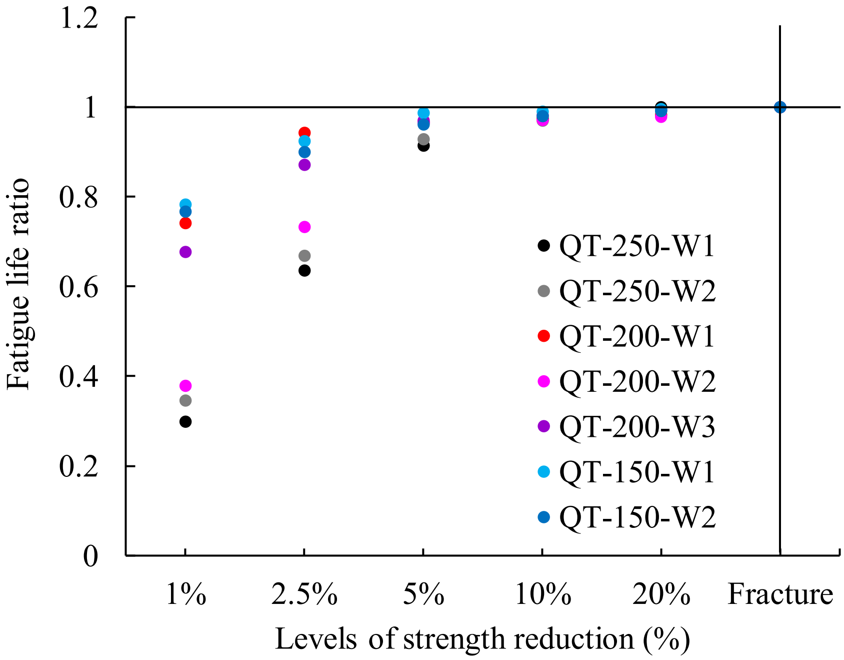

b) Welded sections

Figure 3.15 Deterioration of fatigue life at various levels of strength reduction

SEM observations on fractured coupons

A high-performance scanning electron microscope “JEOL 6490” was employed to conduct observations on the fracture surfaces of selected coupons. **Figure 3.16** shows typical preparation for SEM specimens for examination on both the cross-sectional and the longitudinal surfaces of a coupon of S690 welded sections after fracture.

Hence, a number of SEM specimens were extracted accordingly to allow for detailed SEM examination on their surfaces, and these provided insights on the micro-mechanics of crack initiation and propagation of the coupons during fatigue tests. More importantly, it was possible to correlate them broadly with accumulative degradation of the mechanical properties of these coupons.

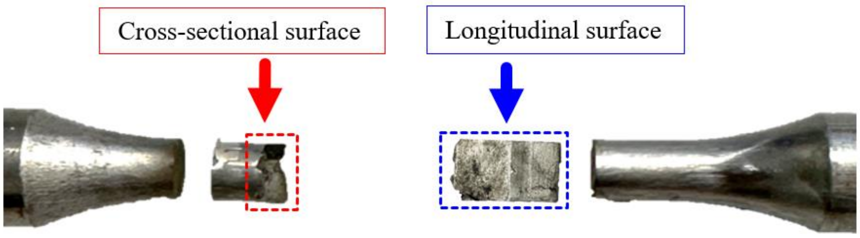

Figure 3.16 Specimens for SEM examination

Figure 3.17 illustrates the observed SEM images of the fractured cross-sectional surfaces of Coupons QT-200-W1 and QT-150-W1. It is evident that some inclusions with typical dimensions at 20 to 30 μm are found within the weld metal on these fracture surfaces, and more importantly, optical dark areas (ODA) are identified near these inclusions, i.e. within a distance of approximately 80 to 120 μm. It should be noted that the formation of ODA may probably due to the plastic deformations and the micro-cracks under repeated cyclic actions.

Owing to differential deformations with the surrounding weld metal under cyclic actions, **micro-crack initiation** takes place in the vicinity of these inclusions shortly after the commencement of the fatigue test.

As the test continues, **micro-crack propagation** develops across the cross-section gradually under repeated cyclic actions (Sun *et al.*, 2012; Yamashita and Murakami, 2016), and hence, plastic deformations in the vicinity of these inclusions, shown as optical dark areas in these SEM images, are developed. The stage of **micro-crack propagation** is readily identified in **Figure 3.13b)** and **Figure 3.14b)** for Coupons QT-200-W1 and QT-150-W1 respectively, and only minor reduction in strength of these coupons is evident.

After a substantial development of micro-crack propagation across the cross-sections, a sudden **macro-crack fracture** takes place, leading to a ductile fracture of the two coupons.

Upon a close observation of the fracture surfaces of the SEM specimens, some obvious fatigue striations and cleavage planes, also known as 'beach marks', are identified as the features of continual dislocation movement induced by repeated cyclic actions. The unevenness of these surfaces indicates that some secondary cracks may propagate along other planes. Moreover, dimples are identified as the main microscopic features representing a fracture of the weld metal with significant deformations.

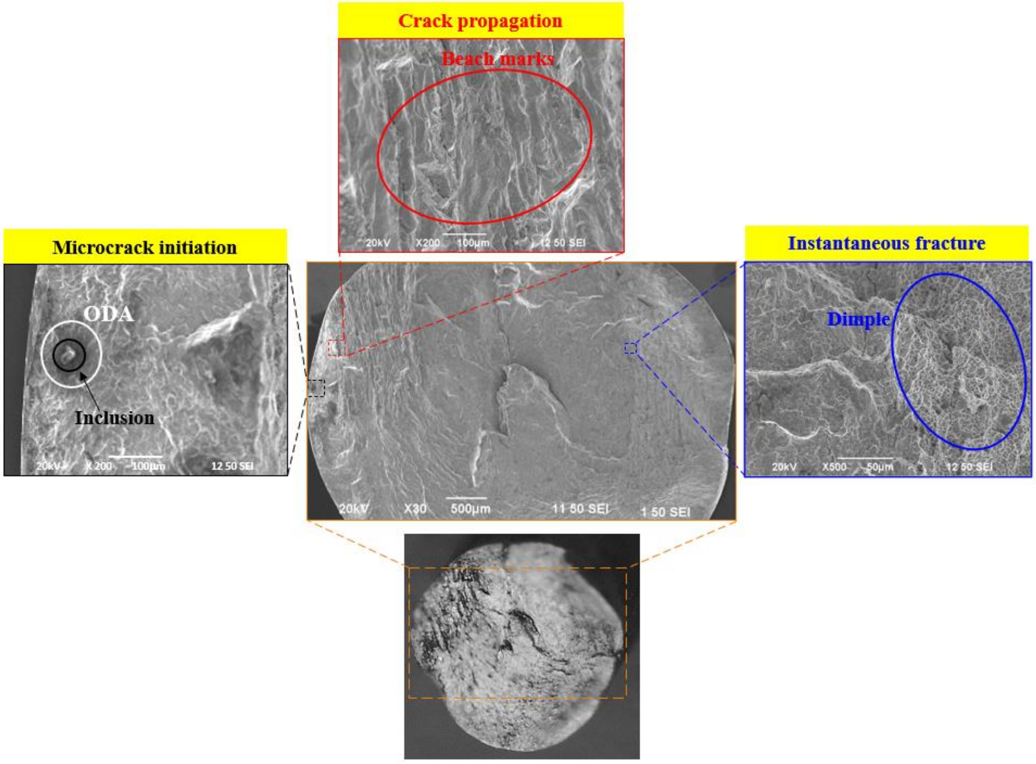

a) Coupon QT-200-W1

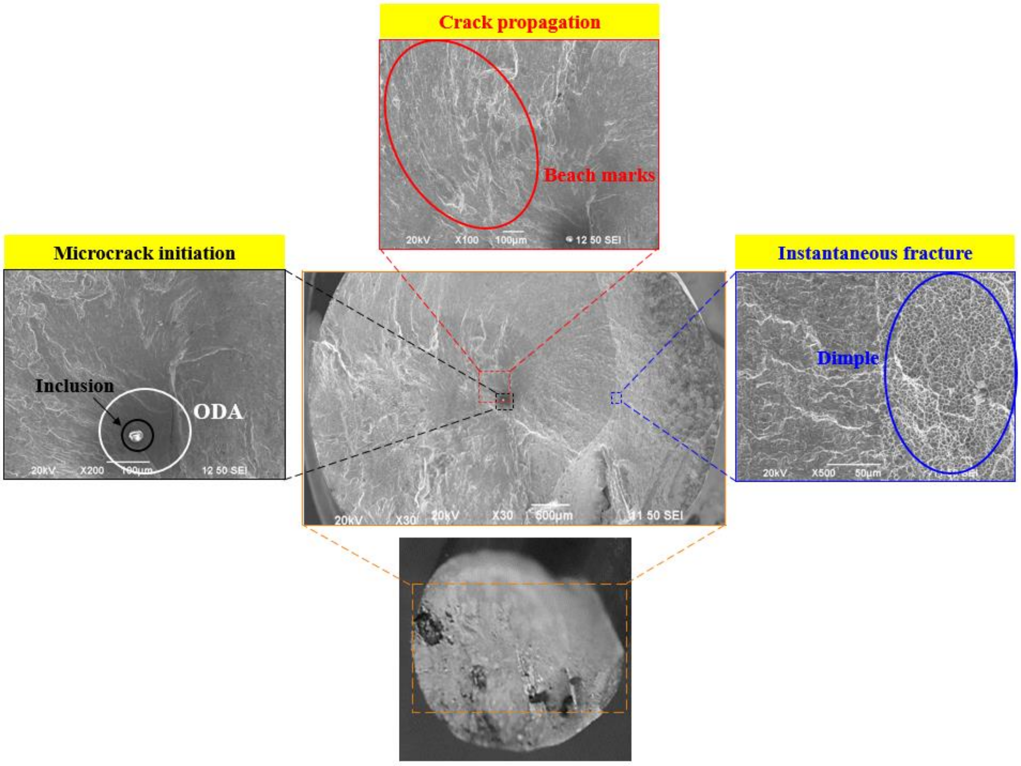

b) Coupon QT-150-W1

Figure 3.17 Microstructure analyses on cross-sectional surfaces of S690-QT welded sections after fracture

Figure 3.18a) and **Figure 3.18b)** illustrate the observed SEM images of the longitudinal surfaces of Coupons QT-200-W1 and QT-150-W1 after test. It is found that main cracks propagate transgranularly with a sharp and clear crack path across the microstructure of various grains (or lattices) while many secondary cracks propagate with intergranular paths along grain boundaries. It should be noted that grain boundaries are the regions where the crystallographic orientation of one grain (or a lattice) differs from that of its neighbours, while adjacent grains have same orientations and sizes. In addition, some small cracks propagate along the grain boundaries due to differential deformations between adjacent grains with different orientations and sizes. These secondary cracks may combine with the main cracks, and then, lead to a sudden fracture, when the cracked coupon is overloaded.

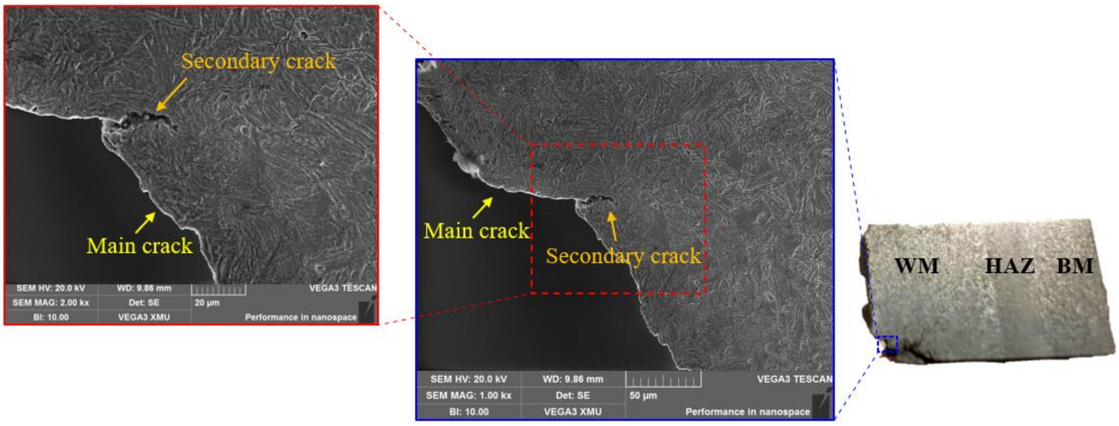

a) Coupon QT-200-W1

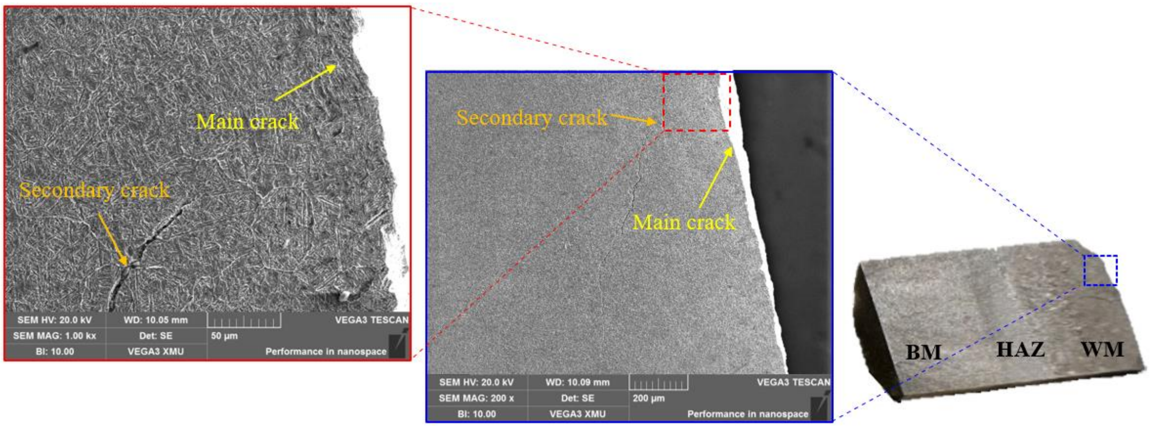

b) Coupon QT-150-W1

Figure 3.18 Microstructure analyses on longitudinal surfaces of S690-QT welded sections after fracture

3.4 S690-TM steel and their welded sections

The experimental investigation into the mechanical properties and the fatigue properties of the S690-TM steel and their welded sections are similar to those of S690-QT steel and their welded sections. Hence, some experimental details of both the monotonic tensile tests and the fatigue tests which are same as those mentioned in the previous part are not re-presented.

3.4.1 Monotonic tensile tests

- ***Test programme***

A total of 2 monotonic tensile tests were carried out to obtain full range stress-strain curves of the S690-TM and its welded sections, the diameters of the specimens were specified to be 10.0 mm, as shown in **Figure 3.19**.

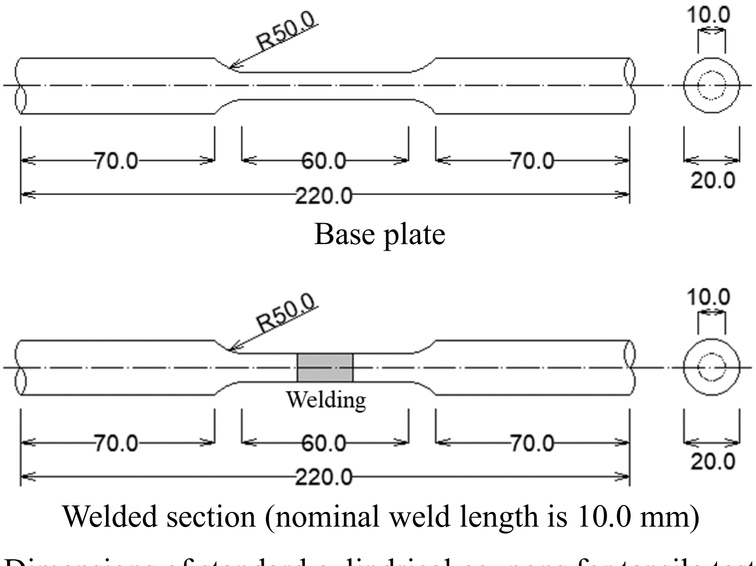

Figure 3.19 Dimensions of standard cylindrical coupons for tensile tests: S690-TM

- ***Test setup and instrumentation***

The details of test setup and instrumentation were the same as those of S690-QT. A high precision static extensometer with a gauge length of 50.0 mm and photographic analysis technique were adopted to measure changing of strain.

- ***Test results***

The engineering stress-strain curves of the S690-TM steel and its welded section are plotted in **Figure 3.20**. The fracture was found to take place always within the heat affected zones of S690-TM welded section, and both the yield and the tensile strengths were found to be reduced when compared with those of the base plate. Key mechanical properties of the S690-TM steel and its welded section are summarized in **Table 3.10**.

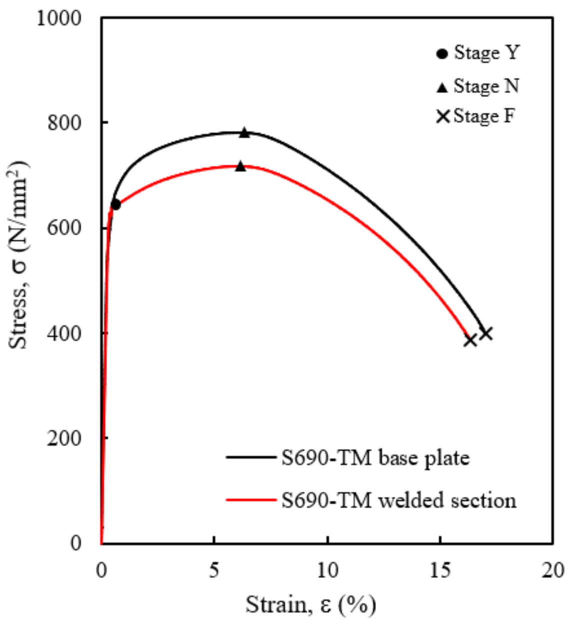

a) Engineering stress–strain curves

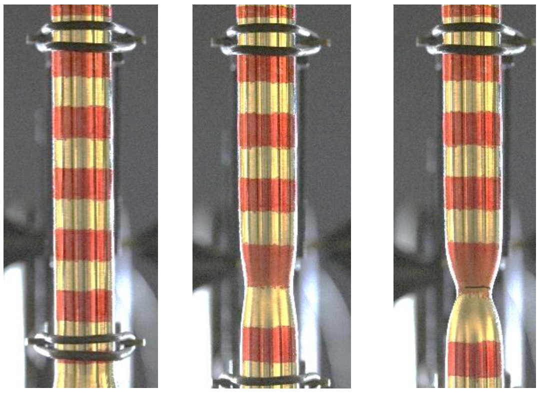

Stage Y Stage N Stage F

b) Base plate: ϕ = 10 mm

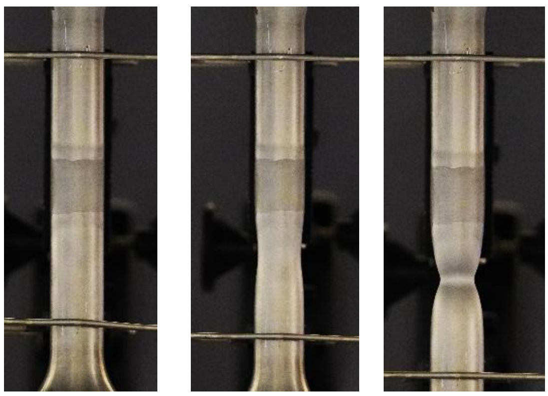

Stage Y Stage N Stage F

c) Welded section: ϕ = 10 mm

Figure 3.20 Mechanical properties of S690-TM steel and its welded section

Table 3.10 Mechanical properties of S690-TM steel and its welded sections

Specimens	Young's modulus E (kN/mm^2)	Yield strength f_y (N/mm^2)	Tensile strength f_u (N/mm^2)	Strain at tensile strength ε_u (%)	Elongation at fracture ε_L (%)
S690-TM	208.9	648	781	6.0	17.0
S690-TM-WS	206.8	628	716	6.1	16.3

The hardness measurements were also carried out on the S690-TM welded sections, a total of 90 points of hardness were measured on the specimens. The results are shown in **Figure 3.21**, it is found that the variation in hardness is minimal though minor hardening and softening phenomena are present within the heat affected zones. The maximum hardness in the coarse-grained regions of the heat affected zones is 280 HV while the minimum hardness in the fine-grained regions is 200 HV.

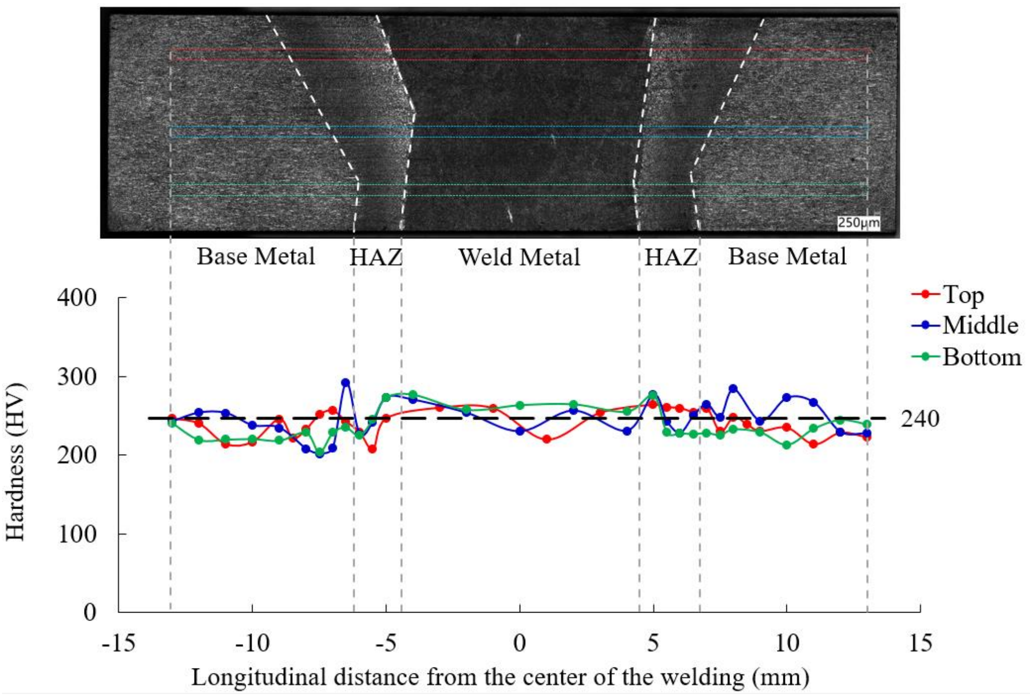

Figure 3.21 Variation in hardness of S690-TM welded sections

3.4.2 Fatigue tests

- ***Test programme***

A total of 24 *load-controlled* fatigue tests on cylindrical coupons of both the S690-TM steel and their welded sections were carried out, and **Table 3.11** summarises the test programme with various key parameters. It should be noted that the cyclic stress amplitudes $\Delta\sigma/2$ were determined according to the mechanical properties obtained in the monotonic tensile tests.

The dimensions and geometry of specially designed cylindrical coupons of the S690-TM steel and their welded sections for fatigue tests is shown in **Figure 3.22**. As the steel plates were 25 mm thick, the diameters of the coupons were specified to be 10.0 mm. The surfaces roughness of the coupons along their gauge lengths were also polished to be within 0.2μm.

- ***Test setup and instrumentation***

The test set-up of the *load-controlled* fatigue tests are the same as those adopted in the repeat tests of the load-controlled fatigue tests on S690-QT steel and their welded tests, as shown in **Figure 3.9**.

Similarly, the loading protocol was a sinusoidal waveform with a constant stress amplitude $\Delta\sigma/2$ with a loading frequency f at 10 Hz, and a loading frequency f of 100 Hz was adopted for the repeated tests whose fatigue life was expected to exceed 10^6 cycles. Due to limitation of load-controlled fatigue tests, only the data of stress amplitude and number of cycles completed were collecting during the tests.

Table 3.11 Test propramme of fatigue tests on S690-TM steel and their welded sections

Specimens	f (Hz)	Control mode	Δσ/2 (MPa)	Specimens	f (Hz)	Control mode	Δσ/2 (MPa)
TM-a-1	10	Load	0.70 f_y	TM-a-W1	10	Load	0.70 f_y
-2				-W2			
-3				-W3			
TM-b-1	10		0.65 f_y	TM-b-W1	10		0.60 f_y
-2				-W2			
-3				-W3			
TM-c-1	10		0.60 f_y	TM-c-W1	10		0.55 f_y
-2	100			-W2	100		
-3	100			-W3	100		
TM-d-1	10		0.575 f_y	TM-d-W1	10		0.50 f_y
-2	100			-W2	100		
-3	100			-W3	100		

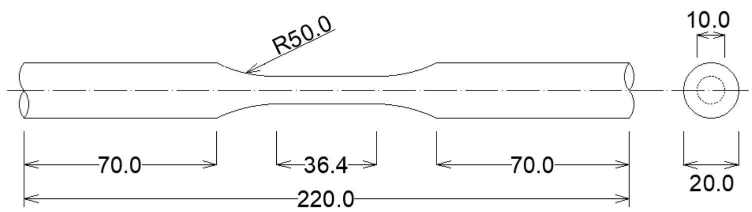

a) Base plate

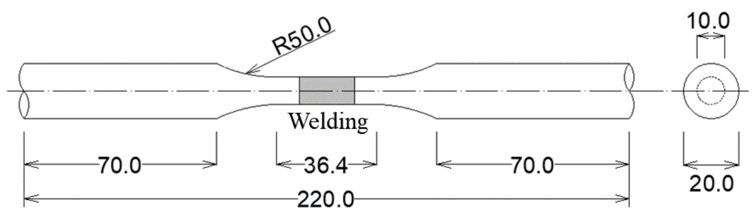

b) Welded section

Figure 3.22 Dimensions of cylindrical coupons for fatigue tests: S690-TM

- ***Test results***

Failure modes

As shown in **Figure 3.23**, all the fracture occurred along the parallel parts within the gauge lengths of all the coupons of the S690-TM steel. **Figure 3.23b)** illustrates the heat affected zones of the coupons of the S690-TM welded sections after etching with a 10% nitric acid solution. It is evident that clear boundaries of the weld metal, the heat affected zones, and the base metal are readily identified. It is shown that fracture occurred typically along the fusion lines between the weld metal and the coarse-grained regions of the heat affected zones.

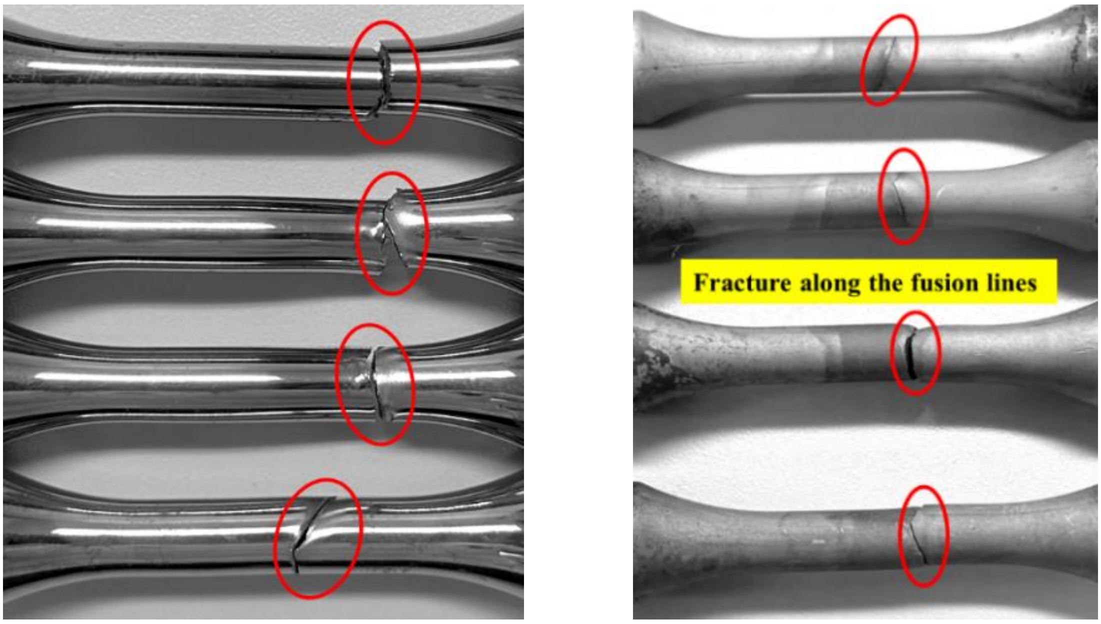

a) S690-TM base plate

b) S690-TM welded sections (after etching)

Figure 3.23 Typical fractured S690-TM coupons

S-N data

The S-N data of the fatigue tests of the S690-TM and their welded sections are summarized in **Table 3.12**, and they are also plotted in **Figure 3.24**. It is apparent that the fatigue resistances of the S690-TM steel are found to have deteriorated by only a small margin after welding, as illustrated in **Figure 3.24**. Similarly, the effect of welding onto the fatigue performance of these coupons of S690-TM steel is demonstrated to be less severe than those of S690-QT steel, and also as compared with those of S355 steel.

The fatigue life of these coupons tested with load-controlled cyclic actions at both 10 and 100 Hz are also found to vary *merely* within 10%, and this is well within the acceptable range of variability.

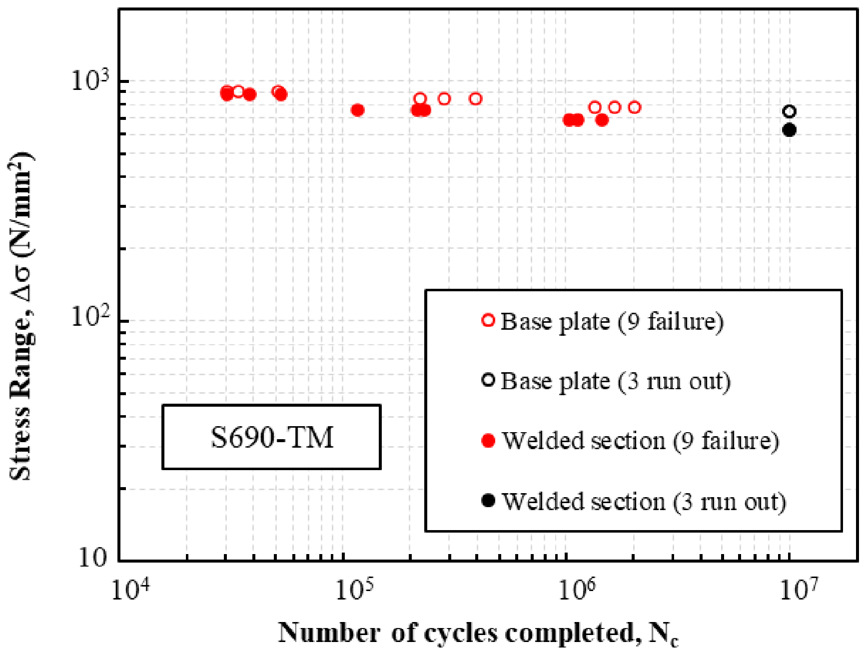

Figure 3.24 Test results of S690-TM steel and their welded sections

Table 3.12 Test results of fatigue tests on S690-TM steel and their welded sections

Specimens	f (Hz)	$\Delta\sigma$ (MPa)	Number of cycles completed N_c	Specimens	f (Hz)	$\Delta\sigma$ (MPa)	Number of cycles completed N_c
TM-a-1	10	907.3	34,103	TM-a-W1	10	879.3	38,367
-2			30,098	-W2			30,223
-3			51,432	-W3			52,568
TM-b-1	10	842.4	391,305	TM-b-W1	10	753.6	116,175
-2			222,397	-W2			230,602
-3			282,684	-W3			214,718
TM-c-1	10	777.6	1,640,672	TM-c-W1	10	690.8	1,119,963
-2	100		1,343,400	-W2	100		1,037,300
-3	100		2,006,800	-W3	100		1,448,200
TM-d-1	10	745.3	10,000,000	TM-d-W1	10	628.0	10,000,000
-2	100		10,000,000	-W2	100		10,000,000
-3	100		10,000,000	-W3	100		10,000,000

SEM observations on fractured coupons

SEM images of the fracture surfaces of two coupons of the S690-TM welded sections are shown in **Figure 3.25**. It is evident that optical dark areas (ODA) are identified within HAZ as a result of plastic deformations and micro-cracks under repeated cyclic actions. In addition, some obvious fatigue striations were identified at the fracture surfaces, which are also referred as ‘beach marks”, in the crack propagation regions. The unevenness of these surfaces indicates that some secondary cracks may propagate along other planes. Dimples are identified as the main microscopic features representing a fracture of the weld metal with significant deformations. It should be noted that the fatigue cracks were initiated and propagated along the fusion lines between WM and HAZ, probably due to different deformation characteristics of the microstructures of WM and HAZ under cyclic actions.

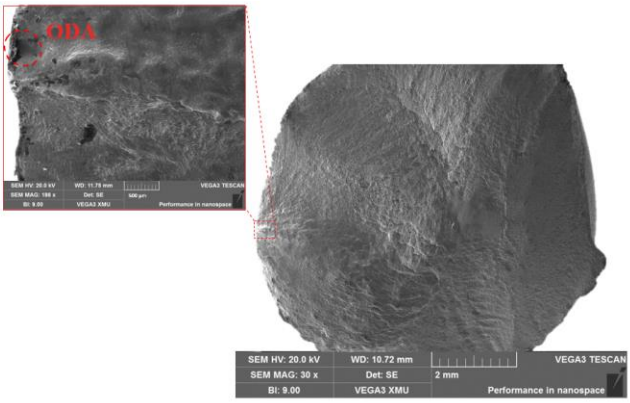

a) TM-b-W1

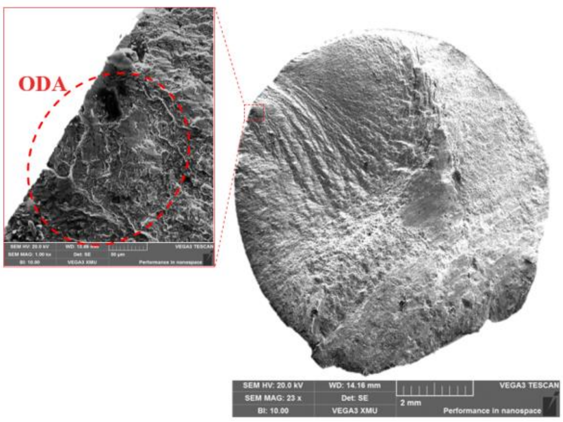

b) TM-c-W1

Figure 3.25 Fracture surfaces of S690-TM welded sections

3.5 S960-QT steel and their welded sections

The experimental investigation into the fatigue properties of the S960-QT steel and their welded sections are almost the same as those of S690-TM series. Hence, most of the details of test setup and instrumentation are not re-presented.

3.5.1 Monotonic tensile tests

- ***Test programme***

A total of 2 monotonic tensile tests were carried on the cylindrical coupons of S960-QT steel and its welded section, the diameters of the specimens were the same as those of S690-QT steel and its welded section, as shown in **Figure 3.2**.

- ***Test setup and instrumentation***

The details of test setup and instrumentation of the tensile tests on S960-QT are shown in **Figure 3.26**, a high precision static extensometer with a gauge length of 25.0 mm was adopted to measure changing of strain.

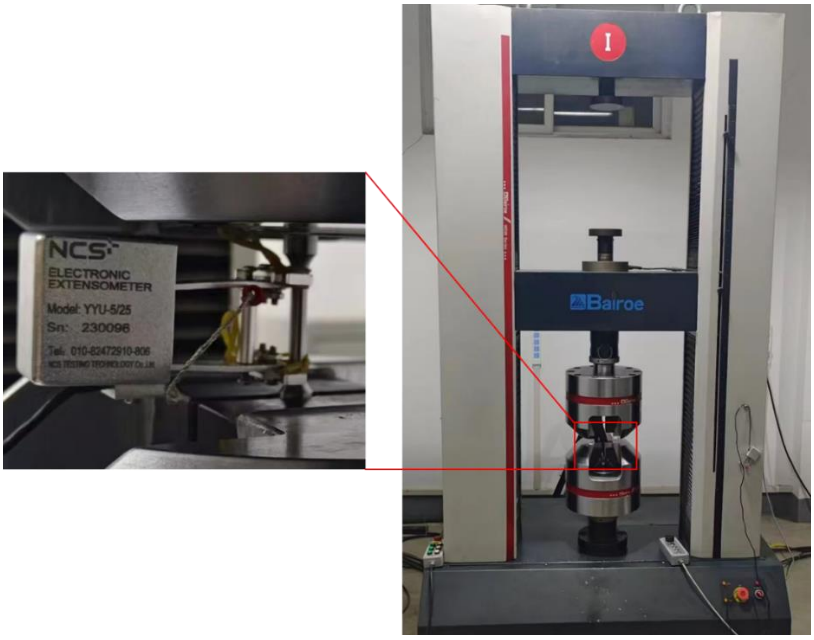

Figure 3.26 Test setup of monotonic tensile tests of S960-QT steel and its welded section

- ***Test results***

The engineering stress-strain curves of the S960-QT steel and its welded section are plotted in **Figure 3.27**. The fracture was found to take place at the weld metal of S960-QT welded section, and both the yield and the tensile strengths were found to be reduced when compared with those of the base plate. Key mechanical properties of the S960-QT steel and its welded section are summarized in **Table 3.13**.

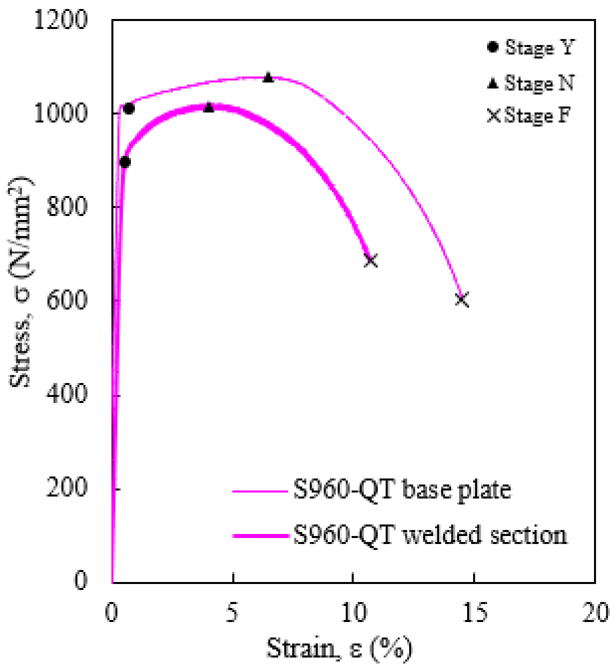

Figure 3.27 Engineering stress–strain curves of S960-QT steel and its welded section

Table 3.13 Mechanical properties of S960-QT steel and its welded sections

Specimens	Young's modulus E (kN/mm^2)	Yield strength f_y (N/mm^2)	Tensile strength f_u (N/mm^2)	Strain at tensile strength ε_u (%)	Elongation at fracture ε_L (%)
S960-QT	214.5	1031	1086	6.3	14.5
S960-QT-WS	206.1	888	1015	4.2	10.7

3.5.2 Fatigue tests

- ***Test programme***

A total of 30 *load-controlled* fatigue tests on cylindrical coupons of both the S960-QT steel and their welded sections were carried out, and **Table 3.14** summarises the test programme with various key parameters. It should be noted that the cyclic stress amplitudes $\Delta\sigma/2$ were determined according to the mechanical properties obtained in the monotonic tensile tests. The dimensions and geometry of cylindrical coupons of the S960-QT steel and their welded sections for fatigue tests is same as those of S690-QT steel and their welded sections, as shown in **Figure 3.6**. The surfaces roughness of the coupons along their gauge lengths were also polished to be within 0.2μm.

Table 3.14 Test propramme of fatigue tests on S960-QT steel and their welded sections

Specimens	f (Hz)	Control mode	$\Delta\sigma/2$ (MPa)	Specimens	f (Hz)	Control mode	$\Delta\sigma/2$ (MPa)
960-a-1	10	Load	0.70 f_y	960-a-W1	10	Load	0.60 f_y
-2				-W2			
-3				-W3			
960-b-1	10		0.60 f_y	960-b-W1	10		0.50 f_y
-2				-W2			
-3				-W3			
960-c-1	10		0.55 f_y	960-c-W1	10		0.45 f_y
-2	100			-W2	100		
-3	100			-W3	100		
960-d-1	10		0.50 f_y	960-d-W1	10		0.425 f_y
-2	100			-W2	100		
-3	100			-W3	100		
960-e-1	10		0.45 f_y	960-e-W1	10		0.40 f_y
-2	100			-W2	100		
-3	100			-W3	100		

- ***Test setup and instrumentation***

The test set-up of the *load-controlled* fatigue tests are the same as those adopted in the repeat tests of the load-controlled fatigue tests on S690-QT steel and their welded tests, as shown in **Figure 3.9**. Similarly, the loading protocol was a sinusoidal waveform with a constant stress amplitude $\Delta\sigma/2$ with a loading frequency f at 10 Hz, and a loading frequency f of 100 Hz was adopted for the repeated tests whose fatigue life was expected to exceed 10^6 cycles.

- ***Test results***

Failure modes

As shown in **Figure 3.28a)**, all the fracture occurred along the parallel parts within the gauge lengths of all the coupons of the S960-QT steel. **Figure 3.28b)** illustrates the tested coupons of S960-QT welded sections after etching, and clear boundaries of the weld metal, the heat affected zones, and the base metal are readily identified. It is shown that fracture occurred typically within the weld metal, and very close to the fusion lines between the weld metal and the coarse-grained regions of the heat affected zones.

a) S960-QT base plate

b) S960-QT welded sections (after etching)

Figure 3.28 Typical fractured S960-QT coupons

S-N data

The S-N data of the fatigue tests of the S960-QT and their welded sections are summarized in **Table 3.15**. In addition, the S-N data are plotted in logarithmic coordinates as shown in **Figure 3.29**, it is presented that the fatigue resistances of the S960-QT steel are found to be deteriorated after welding.

Table 3.15 Test results of fatigue tests on S960-QT steel and their welded sections

Specimens	f (Hz)	$\Delta\sigma$ (MPa)	Number of cycles completed N_c	Specimens	f (Hz)	$\Delta\sigma$ (MPa)	Number of cycles completed N_c
960-a-1			76,312	960-a-W1			21,496
-2	10	1443.4	74,858	-W2	10	1065.6	50,514
-3			46,213	-W3			72,278
960-b-1			512,553	960-b-W1			565,364
-2	10	1237.2	469,019	-W2	10	888.0	502,871
-3			374,891	-W3			309,107
960-c-1	10		1,771,696	960-c-W1	10		1,225,144
-2	100	1134.1	1,055,700	-W2	100	799.2	1,153,900
-3	100		2,273,400	-W3	100		1,952,900
960-d-1	10		3,343,215	960-d-W1	10		2,951,659
-2	100	1031.0	4,819,300	-W2	100	754.8	3,994,900
-3	100		4,018,400	-W3	100		5,333,900
960-e-1	10		10,000,000	960-e-W1	10		10,000,000
-2	100	927.9	10,000,000	-W2	100	710.4	10,000,000
-3	100		10,000,000	-W3	100		10,000,000

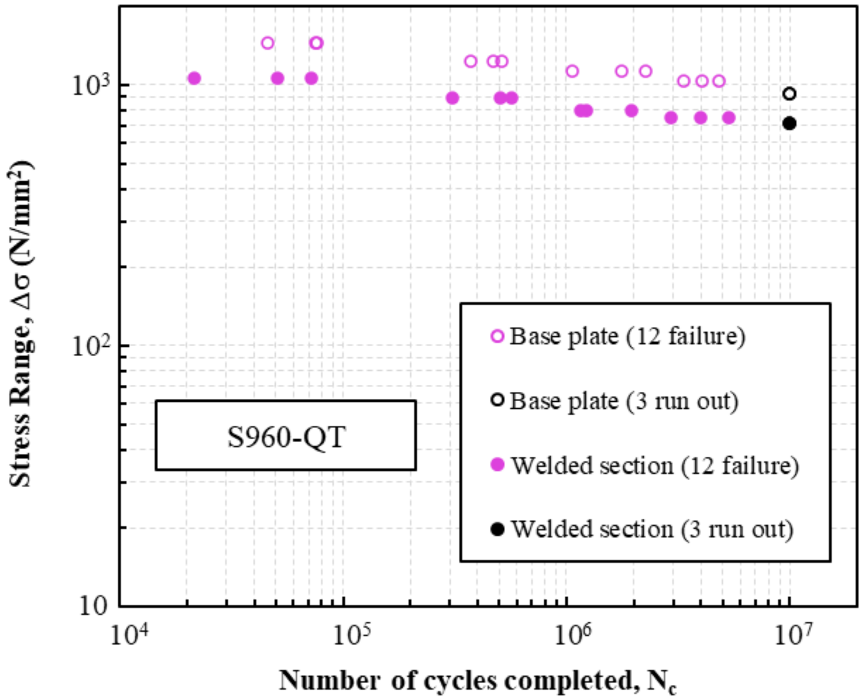

Figure 3.29 Test results of S960-QT steel and their welded sections

SEM observations on fractured coupons

Similar to the SEM images of the fracture surfaces of the S690-QT welded sections, some welding induced imperfections were found on the fracture surface of the S960-QT welded sections, as shown in **Figure 3.30**.

It is evident that a welding induced pore with a dimension at about 200 μm are found within HAZ on the fracture surface of Coupon 960-b-W1, and an inclusion with a dimension at around 30 μm are found within the weld metal on the fracture surface of Coupon 960-c-W1. It should be noted that fatigue cracks were initiated and propagated in the vicinity of an inclusion in the WM because of a significant difference in rigidity of the microstructures of the pore and the inclusion, when compared with those of WM under cyclic actions.

In addition, microscopic features of the fracture surfaces of the S960-QT welded sections, i.e.

ODA, beach marks and dimples, are very similar to those of the S690-QT and S690-TM welded sections. It is demonstrated that fatigue behaviour of these high strength S690 and S960 welded sections are similar, fatigue damages may take place within WM and HAZ under repeated cyclic actions. After a substantial development of fatigue damages, a sudden fracture on WM and HAZ take place with significant deformations.

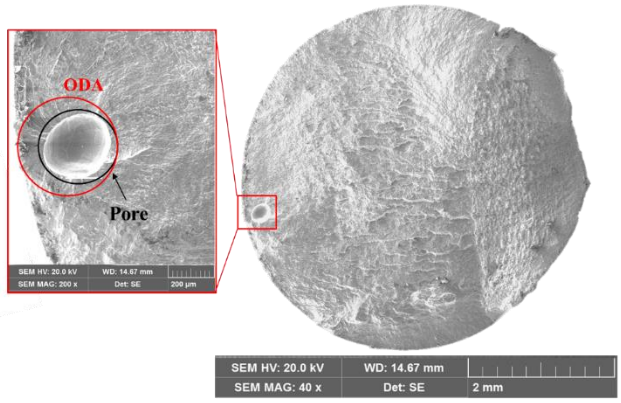

a) 960-b-W1

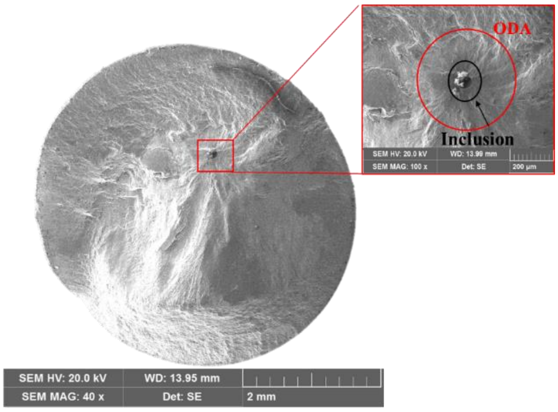

b) 960-c-W1

Figure 3.30 Fracture surfaces of S960-QT welded sections

3.6 Analyses on S-N data

It is important to perform analyses on the S-N data the high strength S690 and S960 steel and their welded sections under repeated cyclic actions obtained in Chapter 3.3, Chapter 3.4 and Chapter 3.5.

3.6.1 Formulation of S-N curves

The S-N curve approach relates a power-law relationship between the fatigue life N with the stress range of structures Δσ, as shown in the following:

$$N_c\,\Delta\sigma^m = C \tag{3-3}$$

where:

N_c	is the number of cycles completed before failure;
Δσ	is the cyclic stress range, and
m & C	are parameters to be determined by fatigue tests.

Taking the logarithm of this equation as follows:

$$\log N_c = A - m\log\Delta\sigma \tag{3-4}$$

where:

A	is a parameter to be determined by fatigue tests.

In general, the experimental data of fatigue tests is assumed to follow a normal distribution which probability density function $f(X)$ and cumulative density function $\Phi(X)$ are given by:

$$f(X) = \frac{1}{\sigma\sqrt{2\pi}}e^{-\frac{(X-\mu)^2}{2S^2}} \tag{3-5}$$

$$\Phi(X) = \frac{1+erf\frac{X-\mu}{S\sqrt{2}}}{2} \tag{3-6}$$

where:

$f(X)$ is the probability density function;

$\Phi(X)$ is the cumulative density function;

X is the logarithmic value of fatigue life $\log N_c$;

μ is the mean value of test data; and

S is the standard deviation of test data.

The standard error of $\log N_c$ is adopted to provide a conservative prediction by a proper survival probability, which is calculated as follows:

$$P_s = 1 - \Phi(X) \tag{3-7}$$

According to BS EN ISO 12017 (ISO, 2003), the design S-N curve is selected as the corresponding survival probability which is taken to be 97.7% in a fatigue assessment on steel bridges. The S-N curve with a survival probability of 97.7% is readily obtained by shifting the derived S-N curve with a survival probability of 50.0% with a reduction of twice of standard derivation of the S-N data.

Corresponding parameters of the derived S-N curves, i.e. A, m and $\Delta\sigma_{lim}$, are readily obtained, it should be noted that the fatigue stress limit $\Delta\sigma_{lim}$ is defined as the maximum value of the design cyclic stress range which does not cause any fatigue damage, and its value is commonly determined to be the corresponding stress range after a total of 10^7 cycles as allowed in the derived S-N curve. As $\Delta\sigma_{lim}$ is obtained with only a dozen of data, more data are generally expected to ensure its applicability. Nevertheless, it is argued that this value may be considered to be at least indicative, and it becomes a reference in the absence of test data.

- ***S690-QT steel and their welded sections***

Figure 3.31 plots the derived S-N curves with a 97.7% survival probability of S690-QT and their welded sections, while the corresponding parameters of these derived S-N curves are summarized in **Table 3.16**. It is apparent that the S-N curve of the S690-QT steel is shown to lie above that of the S690-QT welded sections.

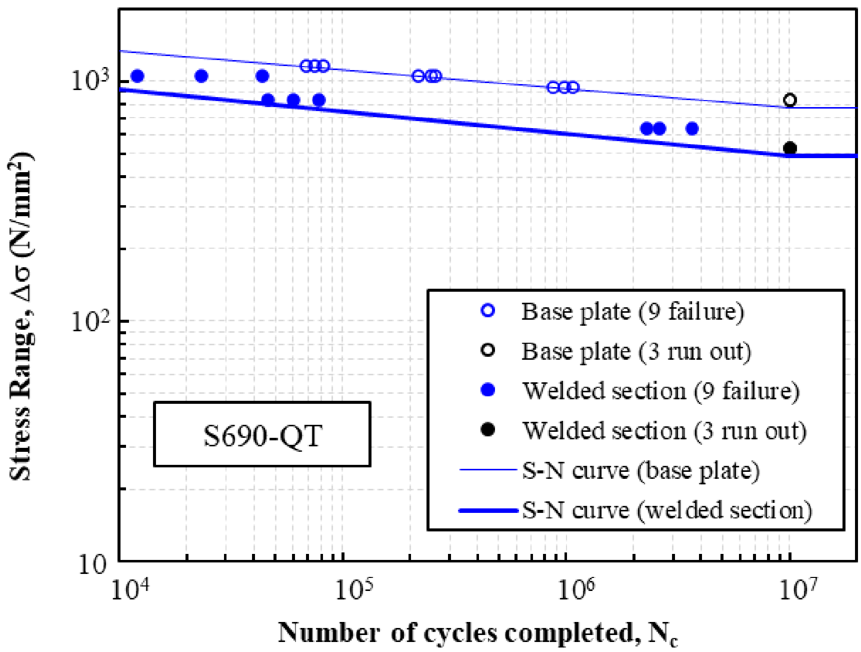

Figure 3.31 S-N curves of S690-QT steel and their welded sections

Table 3.16 Parameters of S-N curves of S690-QT steel and their welded sections

Test series	A	m	Fatigue stress limit $\Delta\sigma_{lim}$ (N/mm^2)
S690-QT	44.13	12.85	774.6
S690-QT-WS	36.13	10.56	485.4

- ***S690-TM steel and their welded sections***

Figure 3.32 plots the derived S-N curves with a 97.7% survival probability of S690-TM steel and their welded sections, while the corresponding parameters of these derived S-N curves are summarized in **Table 3.17**. The S-N curve of the S690-TM steel is also shown to lie marginally above that of the S690-TM welded sections.

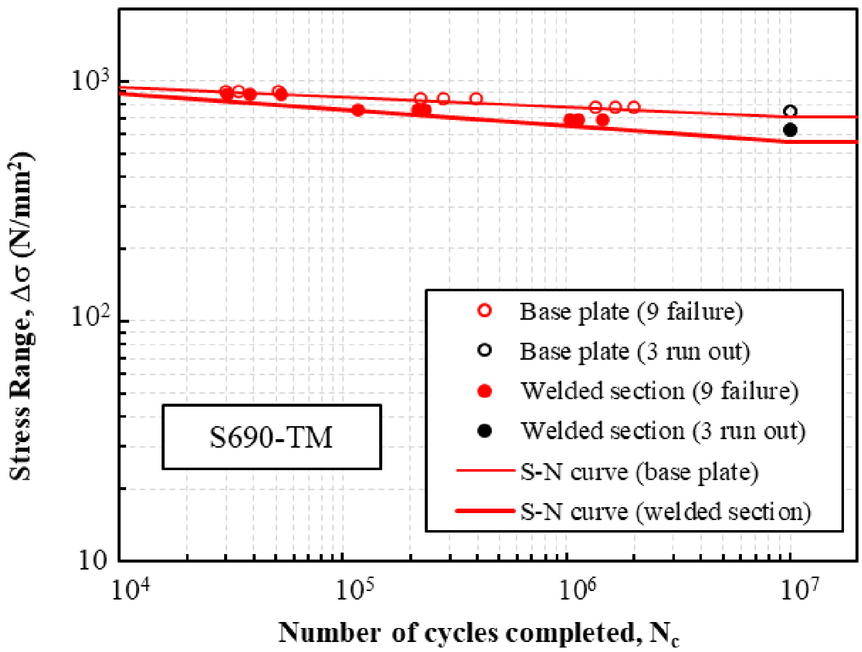

Figure 3.32 S-N curves of S690-TM steel and their welded sections

Table 3.17 Parameters of S-N curves of S690-TM steel and their welded sections

Test series	A	m	Fatigue stress limit $\Delta\sigma_{lim}$ (N/mm^2)
S690-TM	78.48	25.06	711.5
S690-TM-WS	47.49	14.75	556.2

- ***S960-QT steel and their welded sections***

Figure 3.33 plots the derived S-N curves with a 97.7% survival probability of S960-QT steel and their welded sections, and the corresponding parameters of these S-N curves are summarized in **Table 3.18**. Similarly, it is shown that the S-N curve of the S960-QT steel lies above that of the S960-QT welded sections.

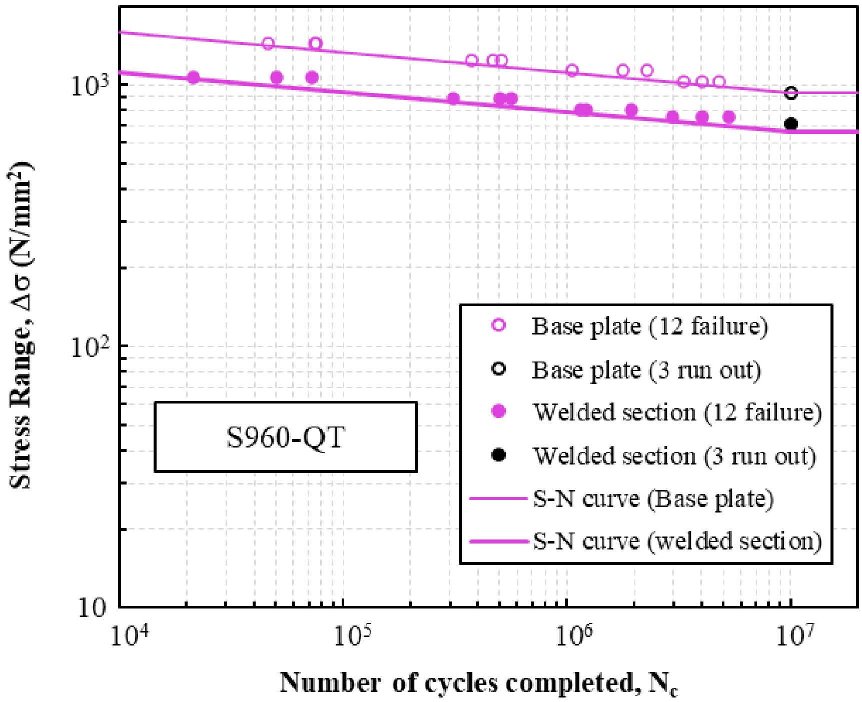

Figure 3.33 S-N curves of S960-QT steel and their welded sections

Table 3.18 Parameters of S-N curves of S960-QT steel and their welded sections

Test series	A	m	Fatigue stress limit $\Delta\sigma_{lim}$ (N/mm^2)
S960-QT	45.13	12.84	934.1
S960-QT-WS	44.67	13.35	662.8

- ***Comparisons on S-N curves of these high strength steel and their welded sections***

For ease of comparison and presentation, **Figure 3.34** plots the S-N curves of the S690-QT, S690-TM, S960-QT steel and their welded sections, while the corresponding parameters are summarized in **Table 3.19**. It is found that:

i) S690-QT vs S690-TM

- As shown in **Figure 3.34**, the S-N curve of the S690-QT steel is found to lie *above* that of the S690-TM steel, while both the S-N curves of the S690-QT welded sections and the S690-TM welded sections are found to *overlap* within the range of $N = 10^4$ to $N = 2\times10^5$ cycles, and then, the S-N curve of the S690-QT welded sections lie *marginally below* that of the S690-TM welded sections when $N \geq 2\times10^5$ cycles.

  It is demonstrated that reductions in fatigue resistances in the S690-QT steel after welding are found to be more pronounced, when compared with those in the S690-TM steel. Hence, the S690-TM steel possess a better fatigue performance when compared with the S690-QT steel after welding, provided that the mechanical properties of the welding electrodes selected are at least equal to those of the steel plates, i.e. a matching electrode. In general, the differences among the fatigue performance of both the S690-TM and the S690-QT steel, and also their welded sections, are considered to be primarily a direct result of their microstructures. It should be noted that the heat affected zones of the S690-TM steel after welding compose primarily of bainite while those in the S690-QT steel are tempered martensite in dual phase, i.e. martensite and ferrite with varying volumetric fractions.

- As shown in **Table 3.19**, it is found that the reduction in the fatigue performance under the effect of welding in the S690-QT steel may be allowed for with roughly a factor of ***0.8*** for the values of both A and m. Similarly, the reduction in the fatigue performance under the effect of welding in the S690-TM steel may be allowed for with roughly a factor of ***0.6***.

As shown in **Table 3.19**, the fatigue stress limits σ_{lim} of the S690-QT steel and their welded sections are 775 and 485 N/mm^2 respectively, i.e. a corresponding reduction of 0.63. Similarly, the fatigue stress limits σ_{lim} of the S690-TM steel and their welded sections are 712 and 556 N/mm^2 respectively, i.e. a reduction of 0.78 owing to the effect of welding. Hence, the fatigue stress limit σ_{lim} of the S690-TM welded sections is about 1.2 times that of the S690-QT welded sections.

ii) S960 vs S690

- As shown in **Figure 3.34**, the S-N curve of the S960-QT steel is found to lie *above* those of the S690-QT/TM steel, and the S-N curve of the S960-QT welded sections is also found to lie *above* those of the S690-QT/TM sections. More importantly, it is found that the slopes of both S-N curves of the S960-QT steel and their welded sections are *similar* to those of the S690-QT steel and their welded sections respectively. In addition, the reduction ratios of S-N curves of welded sections to those of base plates of both the S960-QT and the S690-QT steel are found to be *close*.

  It is demonstrated that reductions in fatigue resistances in the S960-QT steel after welding are found to be similar to those in the S690-QT steel, while more pronounced when compared with those in the S690-TM steel. The differences among the fatigue performance of these steel and their welding sections are also considered to be primarily a direct result of their microstructures.

- As shown in **Table 3.19**, the fatigue stress limits σ_{lim} of the S960-QT steel and their welded sections are 934 and 663 N/mm^2 respectively, i.e. a corresponding reduction of 0.71 owing to the effect of welding. The fatigue stress limit σ_{lim} of the S960-QT welded sections is about 1.2 times that of the S690-TM welded sections, and about 1.4 times that of the S690-QT welded sections.

Table 3.19 Parameters of S-N curves of S690 & S960 steel and their welded sections

Test series	A	*Ratio for* A	m	*Ratio for* m	Fatigue stress limit σ_{lim} (N/mm^2)	*Ratio for* σ_{lim}
S690-QT	44.13	1.0	12.85	1.00	774.6	1.00
S690-QT-WS	36.13	***0.82***	10.84	***0.84***	485.4	***0.63***
S690-TM	78.48	1.0	25.06	1.00	711.5	1.00
S690-TM-WS	47.49	***0.61***	14.75	***0.59***	556.2	***0.78***
S960-QT	45.13	1.0	12.84	1.00	934.1	1.00
S960-QT-WS	44.67	***0.99***	13.35	***1.04***	662.8	***0.71***

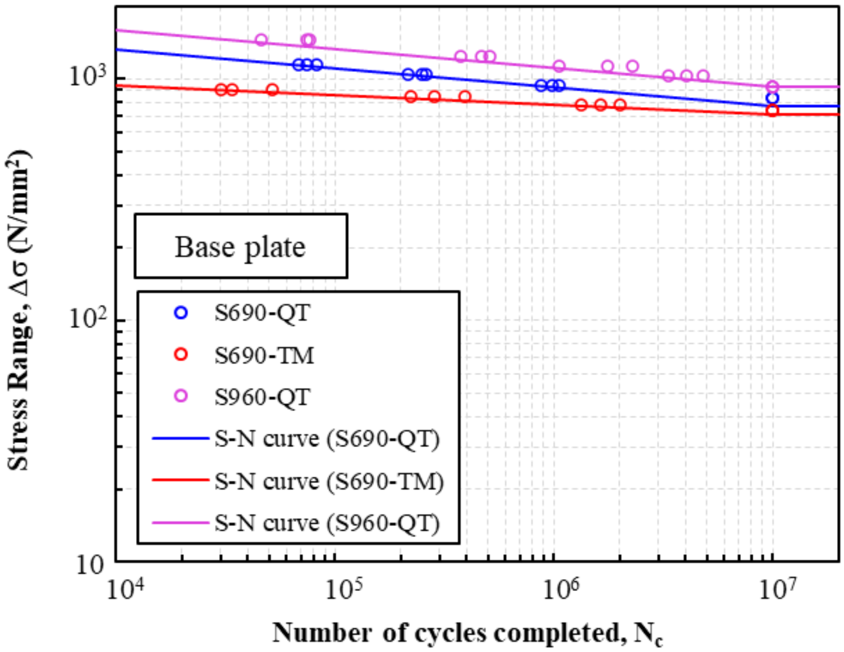

a) Base plates

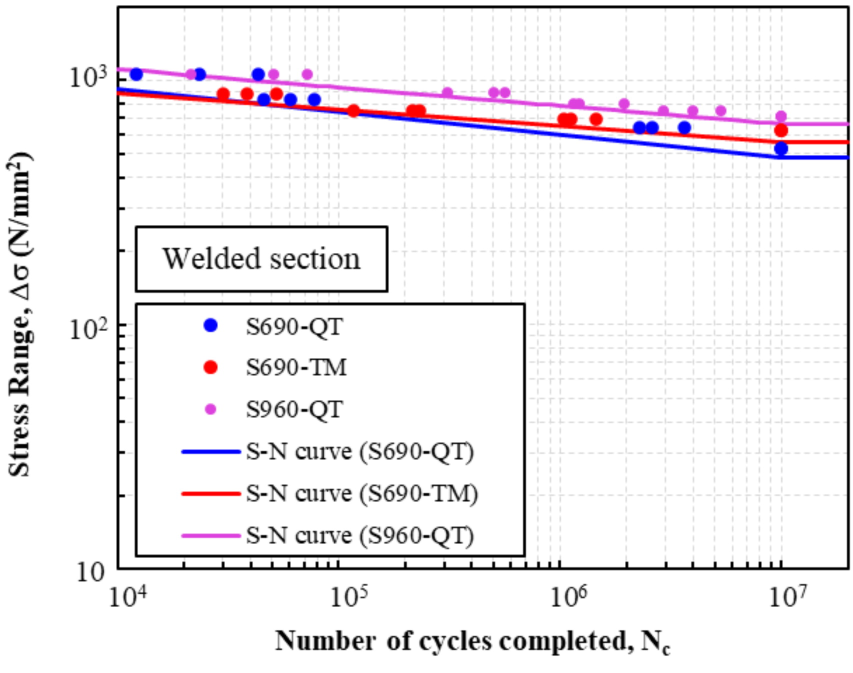

b) Welded sections

Figure 3.34 S-N curves of S690 & S960 steel and their welded sections

3.6.2 Design rules for fatigue assessment

- EN 1993-1-9 (CEN, 2005a)

This Code provides a total of 14 different S-N curves to determine fatigue life for various constructional details commonly found in steel structures under a wide range of cyclic stress ranges for up to S460 steel, as shown in **Figure 3.35**. These S-N curves were derived from test results of a large number of fatigue tests on various structural steel.

According to limit state design, fatigue cracks in steel members should be avoided during service in order to prevent structural failure. The design formula against fatigue failure under loads in the serviceability limit state is given as follows:

$$\Delta\sigma_R - \Delta\sigma_S = 0 \tag{3-8}$$

where:

$\Delta\sigma_R$ is the fatigue strength determined by a relevant S–N curve; and

$\Delta\sigma_S$ is the equivalent stress amplitude caused by a fatigue load.

It should be noted that the design method considers effects of geometric and structural imperfections, i.e. tolerances and residual stresses, during production and service.

These S-N curves are plotted with a logarithmic coordinate in both the y- and the x- axes, i.e. the abscissa is fatigue life N and the ordinate is stress range S. These S-N curves are all straight lines with a slope of 3.0 within a range of 10^4 to 5×10^6 cycles, and then another slope of 5.0 within a range of 5×10^6 to 10^8 cycles.

$$\Delta\sigma_R^m N = \Delta\sigma_C^m 2 \times 10^6 \quad \text{with } m = 3.0 \quad \text{for} \quad N \leq 5 \times 10^6 \tag{3-9}$$

$$\Delta\sigma_R^m N = \Delta\sigma_C^m 5 \times 10^6 \quad \text{with } m = 5.0 \quad \text{for} \quad 5 \times 10^6 < N \leq 10^8 \tag{3-10}$$

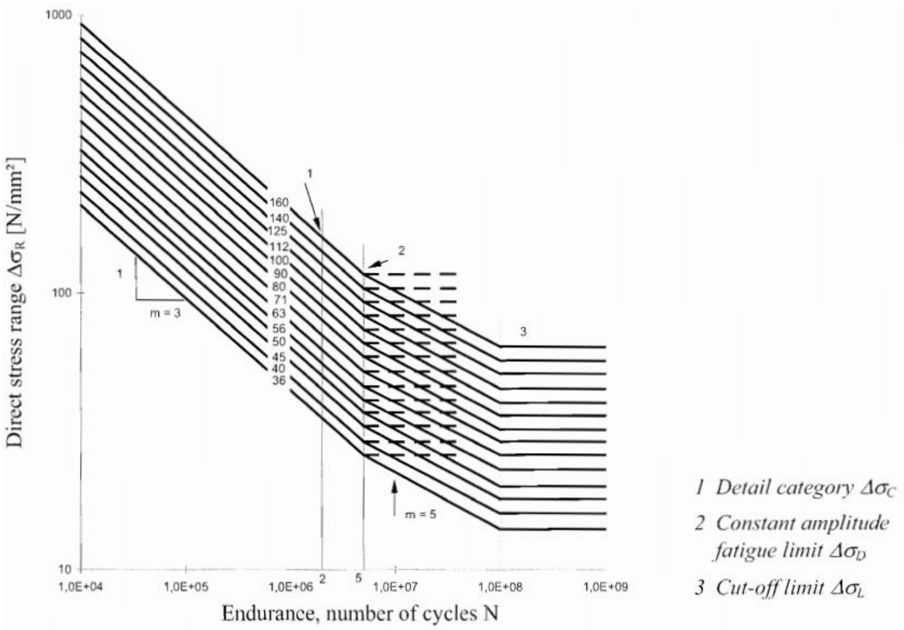

Figure 3.35 S-N curves given in EN 1993-1-9

- AISC 360-16 (AISC, 2010)

This Code adopts allowable stress design to conduct fatigue assessment, and the allowable stress ranges are provided based on specific stress states for different structural details. **Table 3.20** provides the various parameters for the fatigue design. A total of 8 stress categories for various steel and their welded joints are established, and the values of constants C_f are provided correspondingly. The design formula for allowable stress range is given as follows:

$$F_{SR} = 6900\left(\frac{C_f}{N_{SR}}\right)^{0.333} \geq F_{TH} \tag{3-11}$$

where:

C_f denotes constant according to fatigue category;

F_{SR} is the allowable stress range (N/mm²);

F_{TH} is the threshold allowable stress range; and

N_{SR} is the number of stress range fluctuations in design life.

Table 3.20 Parameters of fatigue design in AISC 360-16

Description	Stress Category	Constant C_f	Threshold F_{TH}, ksi (MPa)	Potential Crack Initiation Point
SECTION 1—PLAIN MATERIAL AWAY FROM ANY WELDING				
1.1 Base metal, except noncoated weathering steel, with as-rolled or cleaned surfaces; flame-cut edges with surface roughness value of 1,000 μin. (25 μm) or less, but without reentrant corners	A	25	24 (165)	Away from all welds or structural connections
1.2 Noncoated weathering steel base metal with as-rolled or cleaned surfaces; flame-cut edges with surface roughness value of 1,000 μin. (25 μm) or less, but without reentrant corners	B	12	16 (110)	Away from all welds or structural connections
1.3 Member with reentrant corners at copes, cuts, block-outs or other geometrical discontinuities, except weld access holes				At any external edge or at hole perimeter
$R \geq$ 1 in. (25 mm), with radius, R, formed by predrilling, subpunching and reaming or thermally cut and ground to a bright metal surface	C	4.4	10 (69)	
$R \geq$ $^3/_8$ in. (10 mm) and the radius, R, need not be ground to a bright metal surface	E′	0.39	2.6 (18)	
1.4 Rolled cross sections with weld access holes made to requirements of Section J1.6				At reentrant corner of weld access hole
Access hole $R \geq$ 1 in. (25 mm) with radius, R, formed by predrilling, subpunching and reaming or thermally cut and ground to a bright metal surface	C	4.4	10 (69)	
Access hole $R \geq$ $^3/_8$ in. (10 mm) and the radius, R, need not be ground to a bright metal surface	E′	0.39	2.6 (18)	
1.5 Members with drilled or reamed holes				In net section originating at side of the hole
Holes containing pretensioned bolts	C	4.4	10 (69)	
Open holes without bolts	D	2.2	7 (48)	

- GB/T 50017 (CNS, 2017)

This Code provides a total of 14 different S-N curves for fatigue assessment of steel structures, and the design formula against fatigue failure under loads in the serviceability limit state is given as follows:

$$\Delta_\sigma \leq [\Delta_\sigma] \tag{3-12}$$

These S-N curves for a cyclic stress range are expressed as the following equations:

$$[\Delta_\sigma] = (\frac{C_z}{n})^{\frac{1}{\beta_z}} \quad \text{when } n < 5 \times 10^6 \tag{3-13}$$

$$[\Delta_\sigma] = [([\Delta_\sigma]_{5\times10^6})\frac{C_z}{n}]^{\frac{1}{\beta_z+2}} \quad \text{when } 5.0\times 10^6 < n < 1 \times 10^8 \tag{3-14}$$

where:

Δσ is the nominal stress range;

[Δσ] is the allowable stress range;

n is the number of stress cycles; and

C_z and β_z are design parameters related to components and connection category.

The corresponding parameters of given S-N curves are summarized in **Table 3.21**.

Table 3.21 Parameters of fatigue design in GB50017

Categories	Correlation coefficient C_z	Correlation coefficient β_z	The allowable stress amplitude of 2×10^6 cycles (N/mm^2)	The allowable stress amplitude of 5×10^6 cycles (N/mm^2)	The fatigue limit of 1×10^8 cycles (N/mm^2)
Z1	1920×10^{12}	4	176	140	85
Z2	861×10^{12}	4	144	115	70
Z3	3.91×10^{12}	3	125	92	51
Z4	2.81×10^{12}	3	112	83	46
Z5	2.00×10^{12}	3	100	74	41
Z6	1.46×10^{12}	3	90	66	36
Z7	1.02×10^{12}	3	80	59	32
Z8	0.72×10^{12}	3	71	52	29
Z9	0.50×10^{12}	3	63	46	25
Z10	0.35×10^{12}	3	56	41	23
Z11	0.25×10^{12}	3	50	37	20
Z12	0.18×10^{12}	3	45	33	18
Z13	0.13×10^{12}	3	40	29	16
Z14	0.09×10^{12}	3	36	26	14

3.6.3 Comparison between test data and various design curves

All the design S-N curves given in EN 1993-1-9, AISC 360 and GB 50017 were derived from extensive test data of fatigue tests on steel up to S460 on a wide range of practical details under various loading protocols, as shown in Section 3.6.2. The selected FAT Classes of design S-N curves for the S690 steel and their welded section are:

i) *FAT 160* and *FAT 112* in EN 1993-1-9;

ii) *FAT 165* and *FAT 110* in AISC 360; and

iii) *FAT 176* and *FAT 144* in GB 50017.

It is essential to note that all the measured data conducted in the present study are subjected to a stress ratio at -1. In order to allow for effective comparisons with these specifications, a fatigue enhancement factor F(R) should be adopted by multiplying these design curves by F(R). According to Section 3.5 of the IIW document (Hobbacher, 1996), the F(R) are selected as *1.6* for the base plates and *1.3* for the welded sections, for comparisons with test data.

Hence, all the S-N data of the S690-QT, S690-TM and the S960-QT steel, and their welded sections presented are plotted in **Figure 3.36** together with the design S-N curves with F(R) of EN 1993-1-9, AISC 360 and GB 50017. All the S-N data are found to lie significantly above the design S-N curves, especially for those design fatigue life larger than 10^6 cycles.

Table 3.22 summarizes the fatigue stress limits σ_{lim} of both the S690-QT, S690-TM and S960-QT steel, and their welded sections. It is found that the fatigue stress limits σ_{lim} of all these high strength steel and their welded sections are found to be at least 3 times of the codified values, indicating superior performance against fatigue damage.

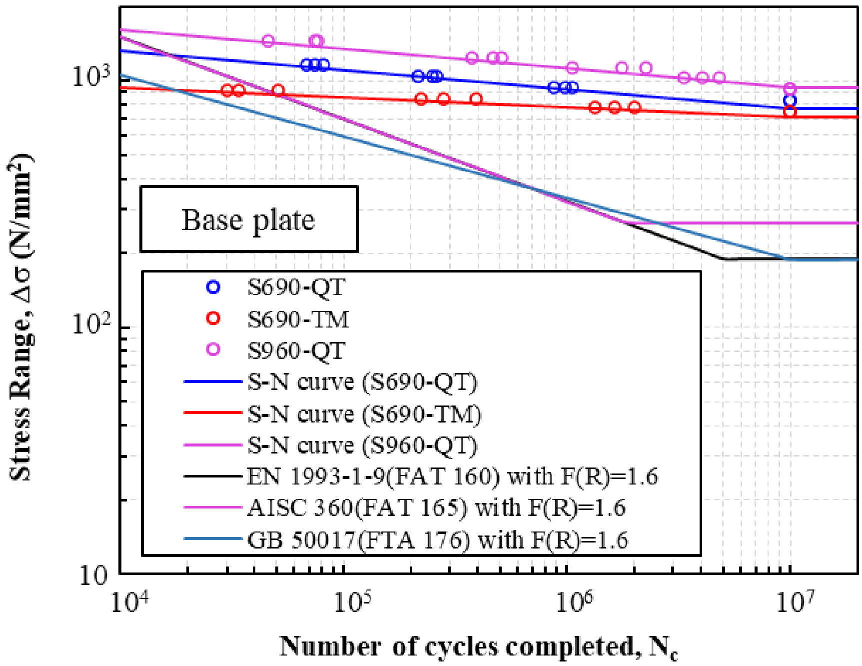

a) Base plates

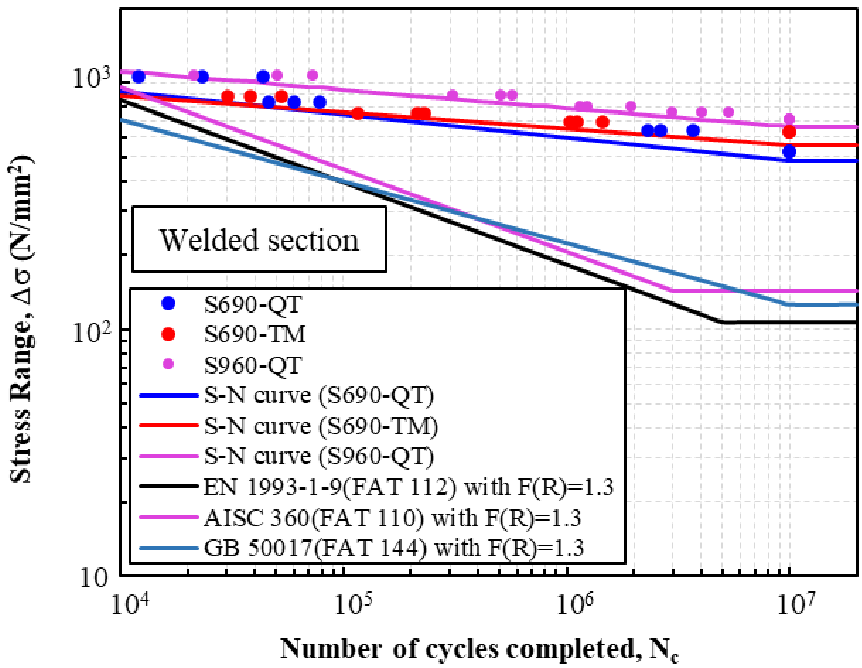

b) Welded sections

Figure 3.36 Comparison with design curves

Table 3.22 Comparison of fatigue stress limits

Steel plates	Fatigue stress limit σ_{lim} (N/mm^2)	Ratio	Welded sections	Fatigue stress limit σ_{lim} (N/mm^2)	Ratio
EN F(R)=1.6	188.8	*1.0*	EN-WS F(R)=1.3	107.3	*1.0*
S690-QT	774.6	*4.1*	S690-QT	485.4	*4.5*
S690-TM	711.5	*3.8*	S690-TM	556.2	*5.2*
S960-QT	934.1	*4.9*	S960-QT	662.8	*6.2*

3.6.4 Comparison with S355 S-N data

In addition, it is worthy to make a comparison on the fatigue performance of the S355, the S690 and S960 steel, and also with their welded sections. Hence, data collection and analysis were carried out on relevant technical papers (De Jesus *et al.*, 2012; Schubnell *et al.*, 2019; Wang *et al.*, 2023; Dantas *et al.*, 2021). It should be noted that selected S-N data of S355 steel and their welded sections were compiled from several fatigue tests with similar testing procedures, i.e. the stress ratio is -1, and the load application frequencies ranged from 10 Hz to 100 Hz.

All of these S355 S-N data were also plotted onto **Figure 3.37** for a direct comparison with those of S690 and S960 steel. It is shown that all the test data of the S690 and S960 steel lie above those of the S355 steel, especially for those design fatigue life larger than 10^6 cycles, and this is also applicable to their welded sections. Consequently, it is demonstrated that the high strength S690 and S960 steel and their welded sections covered in the present study behave superior to the S355 steel and their welded sections reported in the literature over a wide range of fatigue life.

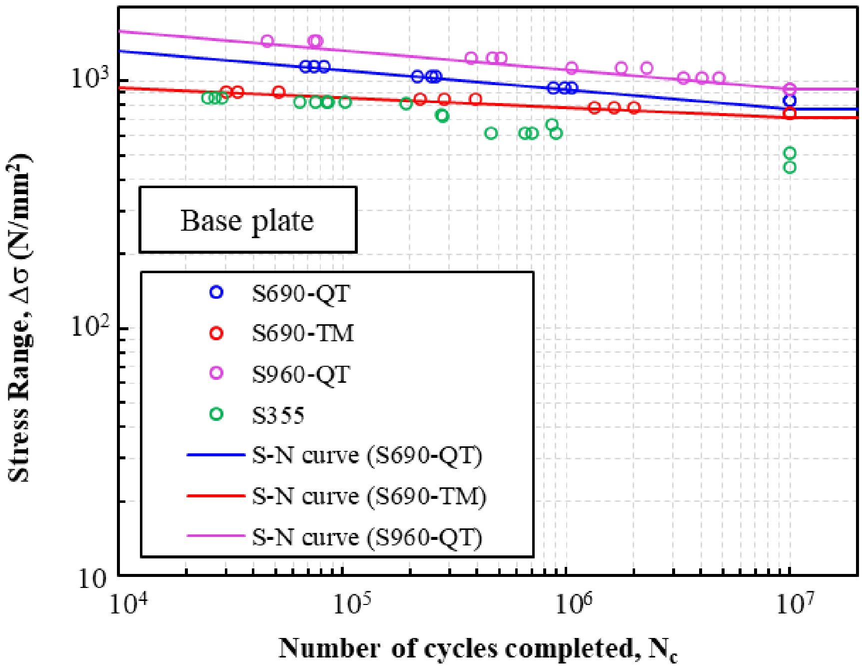

a) Base plates

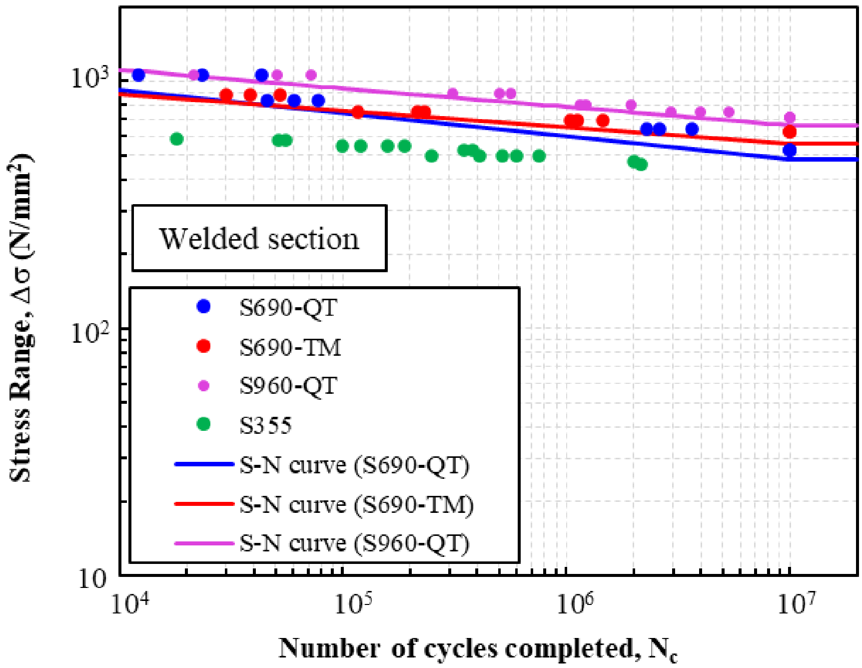

b) Welded sections

Figure 3.37 Comparison with references data of S355

Based on the analyses on the S-N Data, it is found that all the S690-QT, the S690-TM and the S960-QT steel, and their welded sections perform a good fatigue performance, when compared with the design curves, the S-N data of S355 steel and their welded sections, especially for those design fatigue life larger than 10^6 cycles.

It should be noted that these design S-N curves on welded joints include reductions in fatigue performance due to geometrical discontinuities, residual stresses and imperfections after welding. Many researchers have examined experimentally and numerically various effects of geometrical discontinuities induced by welding on the fatigue performance of specific welded joints (Ahola *et al.*, 2022; Baumgartner *et al.*, 2017; Schubnell *et al.*, 2024). Nevertheless, such a comparison with the design curves provides a preliminary reference on the fatigue performance of these S690 steel and their welded sections while effects of stress concentration and presence of residual stresses on their fatigue performance should be considered additionally for applications of these test results and data in engineering applications.

3.7 Conclusions

This Chapter presents an experimental investigation into fatigue behaviour of high strength S690 & S960 steel, and their welded sections. A total of 78 cyclic tests were carried out on cylindrical coupons of the high strength Grades S690 & S960 steel, and their welded sections. These cyclic tests were conducted as i) *load-controlled tests*, and ii) *strain-controlled tests* over a range of 10^4 to 10^7 cycles to provide test data to demonstrate their resistances against fatigue fracture under practical situations, such as bridge structures. Both scanning electron microscope observations and metallographic analyses were conducted on typical fractured coupons to examine micromechanics of fatigue fracture of these high strength steel and their welded sections. The key findings are as follows:

- Both the Grades 690 & 960 steel and also their welded sections exhibit excellent fatigue performance. Their fatigue resistances are superior to those of the S355 steel and their welded sections, when tested under a stress ratio R = -1 at frequencies ranging from 10 to 100 Hz over a fatigue life up to 10^7 cycles.

- In general, the fatigue strengths are found to be increased with an increase of the yield strengths, and the existing S-N curves are applicable conservatively for fatigue assessments of high strength steel and their welded sections. All the S-N data of these high strength steel and their welded sections are demonstrated to lie well above the design curves with F(R) given in EN 1993-1-9, AISC 360 and GB 50017. Hence, the use of existing design rules in these standards for fatigue assessment on the S690 steel is demonstrated to be applicable.

- In *the strain-controlled fatigue tests*, there are two stages of fatigue behaviour, namely, i) stable fatigue stage – a strength degradation within 5% due to micro-crack initiation and propagation, and ii) rapid fracture stage – a significant stiffness degradation due to macro-crack propagation. In the present study, the fatigue life ratios at 5% strength reduction $N_{5\%}$ are found to range from 0.959 to 0.989 for the S690-QT steel, and 0.914 to 0.987 for their welded sections.

- While both *the load*- and *the strain-controlled fatigue tests* provide engineering data for generation of design S-N curves commonly adopted in fatigue assessment, the strain-controlled tests provide additional information to quantify their fatigue behaviour, including *stiffness degradation, crack initiation and propagation*, and fracture. These tests are considered to be necessary in appraising the fatigue behaviour of the high strength steel as their application in construction is relatively new, and thus, detailed investigations are highly desirable to establish scientific understandings and engineering data on their fatigue performance.

Chapter 4 Fatigue behaviour of S690 T-joints under in-plane bending

4.1 Introduction

This Chapter presents a comprehensive experimental investigation into the fatigue behaviour of welded T-joints between high strength S690-QT circular hollow sections (CHS) under cyclic in-plane bending actions. The measured fatigue performance of these T-joints were then analysed in a rational manner to examine their deformation characteristic during the entire courses of fatigue tests. The following works were carried out:

Task 1 – Experimental investigation

A total of 10 welded T-joints between S690 circular hollow sections (CHS) under cyclic in-plane bending actions were carried out, and all the chords were 250 × 10 mm CHS while all the braces were 200 × 10 mm CHS. All these tests were conducted under *a displacement control* between the minimum and the maximum target displacements, δ_{min} and δ_{max} respectively, over 1×10^4 to 5×10^6 cycles, and the minimum and the maximum applied loads, F_{min} and F_{max} , were measured respectively to give the applied load ranges ΔF over the corresponding numbers of cycles N. The processes of crack initiation and propagation were closely monitored throughout the tests with a view to provide insights for improved understanding on the fatigue performance of these T-joints. Measured structural responses of these T-joints were examined in details to determine their strength and stiffness degradation during the entire course of the tests.

It should be noted that one of these S690 welded T-joints was selected to be tested under a monotonic action at small magnitudes, i.e. about 30% of the expected failure load, in order to establish the magnitudes of the controlled displacements in the cyclic tests.

Task 2 – Analyses on S-N data

i) Formulation of S-N curves

A comprehensive data analysis was performed on the measured S-N data of these S690 welded T-joints to derive S-N curves for a direct fatigue assessment on these T-joints according to various levels of strength reduction.

These curves were then compared with existing codified S-N curves, such as the classification method and the stress concentration factor method mentioned in Section 1.2 for similar T-joints of various steel grades. This aims to establish whether these existing codified S-N curves are able to predict fatigue life of these S690 welded T-joints effectively.

ii) Prediction on fatigue life

The S-N curve derived with coupons of the S690 welded sections, i.e. the $(S\text{-}N)_c$ curve shown in **Figure 3.31**, is adopted for a direct comparison with the S-N data of these S690 welded T-joints. Applicability of the use of the $(S\text{-}N)_c$ curve to assess fatigue performance of these S690 welded T-joints is examined in details.

4.2 Fabrication of cold-formed circular hollow sections and their T-joints

In order to fabricate welded T-joints between S690 cold-formed circular hollow sections (CHS), 10 mm thick S690 steel plates were cut to sizes first, and then, they were cold-rolled transversely, and welded longitudinally to form CHS.

Those CHS with a diameter of 200 mm were adopted as the braces while those sections with a diameter of 250 mm were adopted as the chords. **Table 4.1** presents the geometrical ratios of the CHS of the S690 welded T-joints, and the basic configuration of these T-joints is shown in **Figure 4.1**.

All the braces were profile-cut at one of their ends which were then carefully welded onto the chords by a qualified welder to form welded T-joints. The chemical compositions of these high strength steel plates given in EN 10025-6 are summarized in **Table 3.1**, and their welding electrodes are summarized in **Table 3.2**. Both pre-heating and post-weld heat treatment were adopted during and after welding to prevent cold cracks. Based on experiences from a number of experimental investigations (Liu *et al.*, 2018; Chung *et al.*, 2020; Jin *et al.*, 2024), the welding procedures were carefully controlled so that the heat input energy due to welding onto these sections was kept not to exceed 1.5 kJ/mm, as shown in **Figure 4.2**. Hence, there was little or even no reduction in the mechanical properties of these joints. **Table 4.2** summarizes the measured dimensions of both the chords and the braces of the T-joints.

Table 4.1 Test programme of S690 welded T-joints

Joints	Loading type	Loading frequency f (Hz)	Displacement range $\Delta\delta$ (mm)	Chord $d_0 \times t_0$ (mm)	Brace $d_1 \times t_1$ (mm)	α	β	γ	τ
C-T1a / b			0.5 ~ 7.0						
C-T2a / b			0.5 ~ 6.5						
C-T3a / b	Cyclic	3	0.5 ~ 4.0	250×10	200×10	9.6	0.8	12.5	1.0
C-T4a / b			0.5 ~ 3.5						
C-T5a / b			0.5 ~ 3.0						
M-T1	Monotonic	-	0.0 ~ 7.0	250×10	200×10	9.6	0.8	12.5	1.0

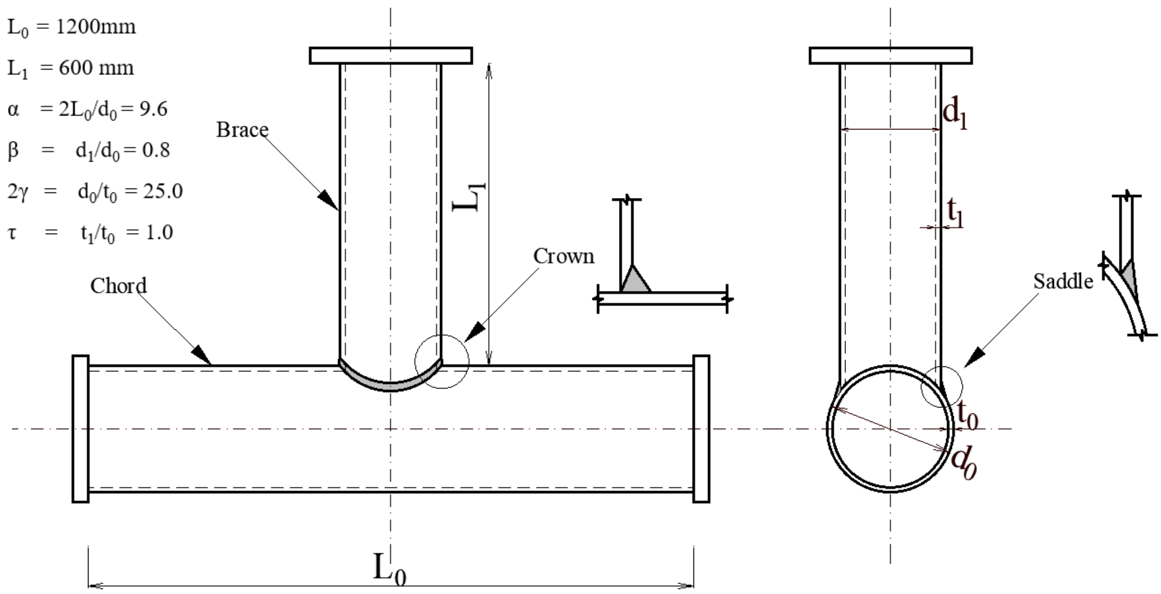

Figure 4.1 Configuration of S690 welded T-joint

a) Preparation works

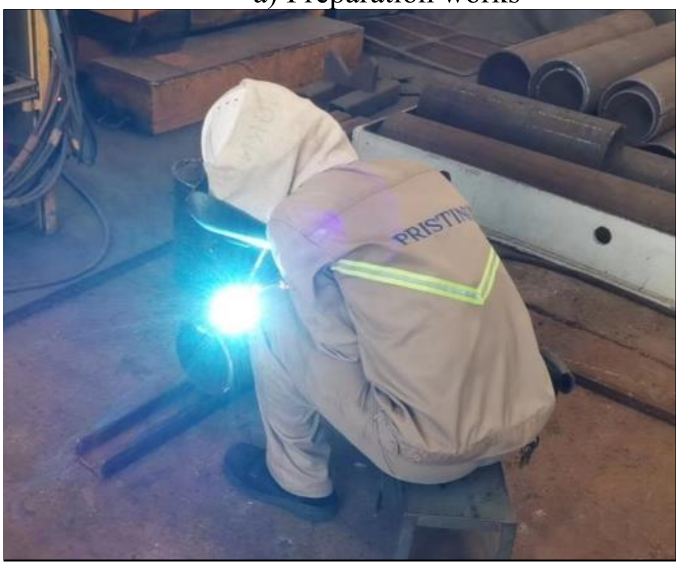

b) Gas metal arc welding

Figure 4.2 Welding procedures of S690 CHS

Table 4.2 Measured dimensions of S690 welded T-joints

Joints	Chord			Brace		
	Length L_0 (mm)	Diameter d_0 (mm)	Thickness t_0 (mm)	Length L_1 (mm)	Diameter d_1 (mm)	Thickness t_1 (mm)
M-T1	1199.2	250.6	10.2	599.5	150.7	10.2
C-T1a	1199.2	250.6	10.2	599.5	150.7	10.2
C-T1b	1200.3	250.3	9.9	599.2	150.6	10.2
C-T2a	1199.5	250.8	10.1	599.3	150.9	10.1
C-T2b	1199.9	205.8	9.9	599.2	151.1	10.2
C-T3a	1199.6	250.9	10.1	599.3	150.8	9.9
C-T3b	1200.0	250.6	9.9	599.6	151.2	10.0
C-T4a	1198.6	250.9	9.9	599.4	150.8	9.9
C-T4b	1200.5	250.4	10.1	599.2	150.6	10.2
C-T5a	1200.1	250.7	10.0	599.5	151.0	10.1
C-T5b	1199.8	250.5	10.2	599.3	150.6	9.9

As shown in **Figure 4.3**, curved coupons were extracted from these circular hollow sections, and standard tensile tests were conducted on the curved coupons to obtain their full range stress-strain curves to determine key mechanical properties, including both their yield and tensile strengths, and their elongations at fracture.

Figure 4.4 illustrates typical set-up of the standard tensile tests. It should be noted that a specially devised attachment was used to minimize load eccentricity during testing. The strain rates adopted in the tests are 0.05%/min form beginning to 1% strain, 0.2%/min for the strain range from 1% to the necking, and 0.5%/min from necking to fracture.

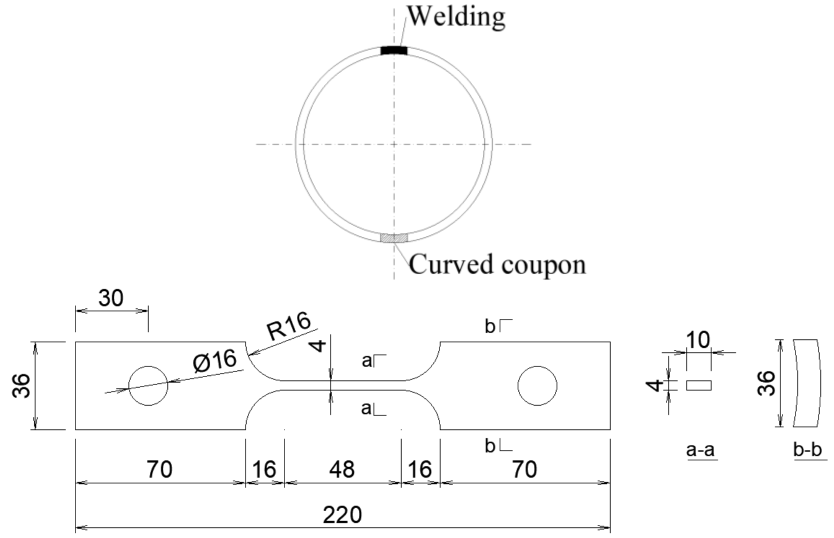

Figure 4.3 Dimensions of curved coupons

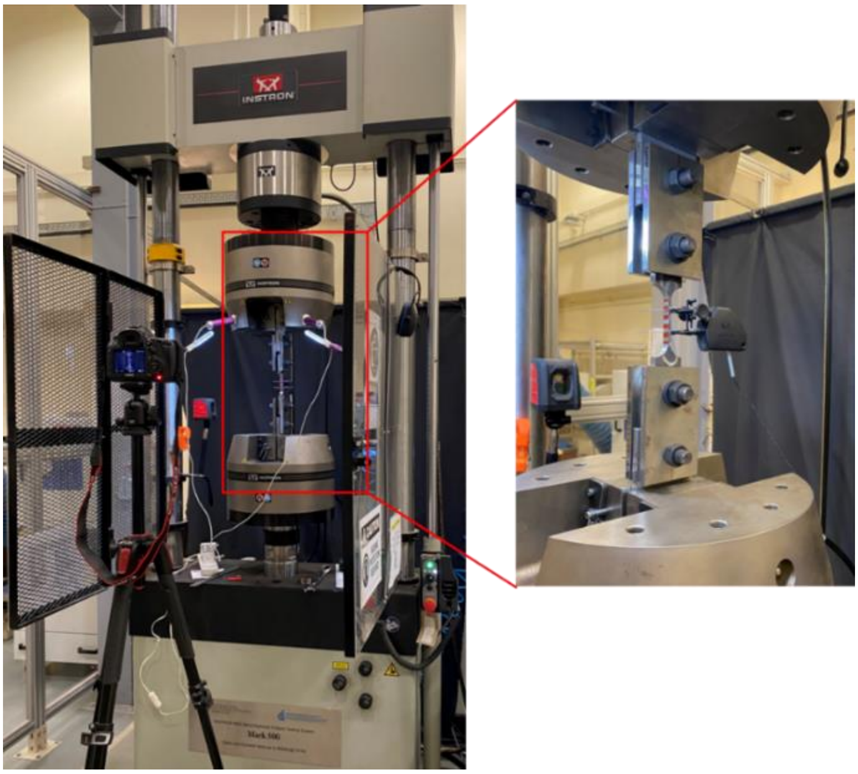

Figure 4.4 Test setup of monotonic tensile tests on curved coupons

The measured engineering stress-strain curves of the curved coupons are plotted in **Figure 4.5** while key mechanical properties of the coupons are summarized in **Table 4.3** for subsequent data analysis.

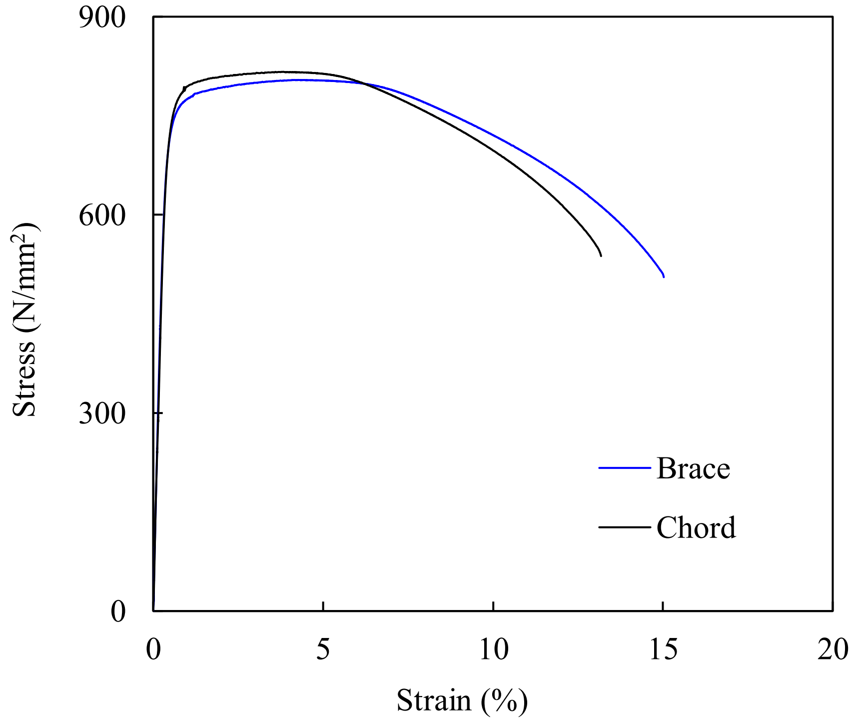

Figure 4.5 Stress-strain curves of curved coupons

Table 4.3 Mechanical properties of chord and brace

Steel Members	Thickness t (mm)	Young's modulus E (kN/mm^2)	Yield strength f_y (N/mm^2)	Tensile strength f_u (N/mm^2)	Strain at tensile strength ε_u (%)	Elongation at fracture ε_L (%)
Chord	9.98	212.7	744	817	3.77	13.2
Brace	10.10	216.1	731	804	4.08	15.0

4.3 Monotonic in-plane bending test

4.3.1 Test programme

Table 4.1 presents the test programme of the S690 welded T-joint under monotonic in-plane bending actions. In order to provide basic reference data on the deformation characteristic of these T-joints, one of them was first tested under monotonic action, and it was referred as Joint M-T1. This T-joint was then re-tested under cyclic actions, and it was referred as Joint C-T1a.

4.3.2 Test setup and instrumentation

Figure 4.6a) illustrates the set-up of the in-plane bending test of Joint M-T1. A hydraulic controlled actuator with a maximum loading capacity of 500 kN with a maximum travel range of 250 mm was employed. A total of 31 strain gauges were installed at specific positions of the T-joint accurately, as shown in **Figure 4.6a)**, to measure local strains, and these included i) a total of 5 strain gauges, namely, strain gauges SG1 to SG5, along the longitudinal direction of the chord, i.e. $\theta = 0^o$, to determine the longitudinal variation in strains in the vicinity of the welded collar of the T-joint, and hence, the hot spot stresses σ_{hs} at the weld toe, and ii) a total of 13 pairs of strain gauges installed radially along the circumference of the welded collar of the T-joint to determine the variations of hot spot stresses σ_{hs} at various θ along the perimeter of welded collar. As shown in **Figure 4.6b)**, a displacement transducer (LVDT) was installed at the brace end to measure the applied lateral displacement while 2 LVDT were installed at each of the chord ends to monitor any displacement, and hence, the overall displacement of the T-joint.

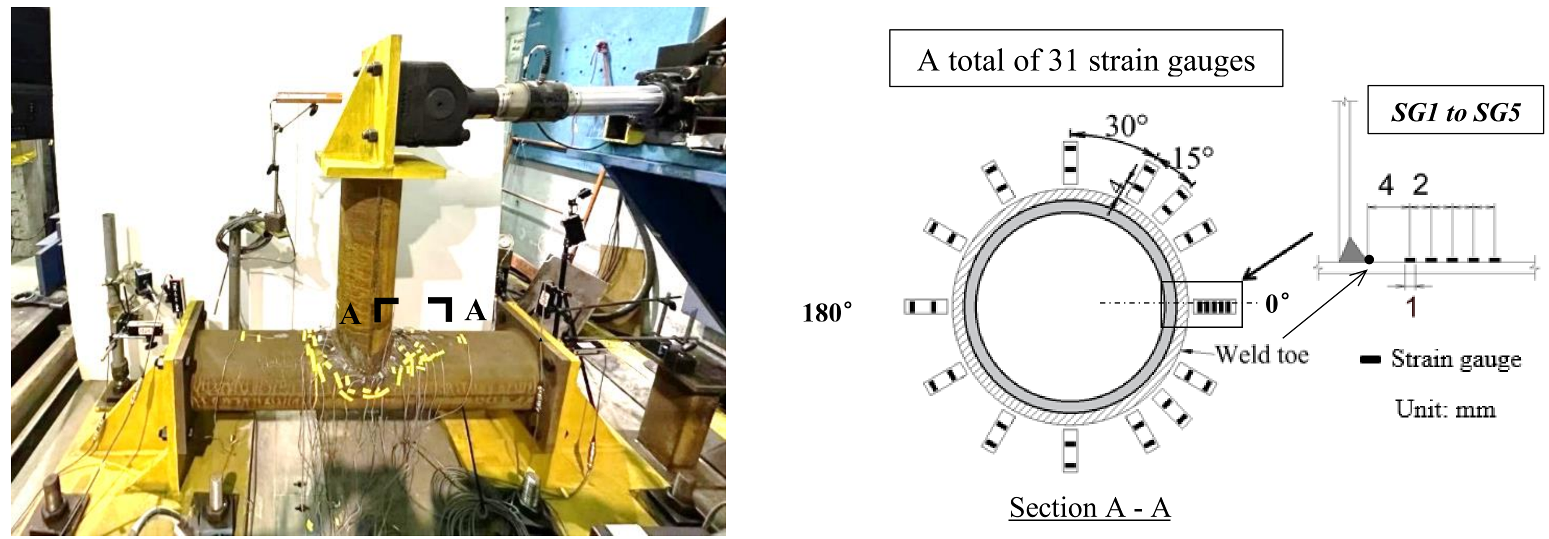

a) Test set-up

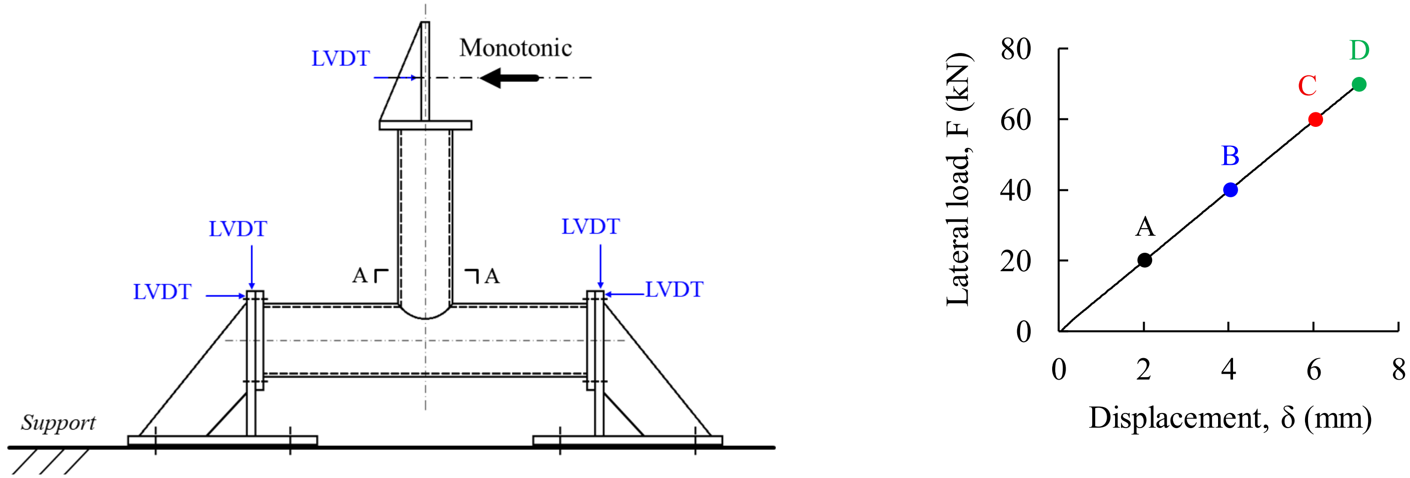

b) Locations of LVDT

Figure 4.6 Test setup and instrumentation

4.3.3 Experimental results

It should be noted that after Joint M-T1 was carefully installed and aligned, it was pre-loaded carefully in which a displacement was applied laterally to the brace end from 0.0 to 2.0 mm, and then back to 0.0 mm three times in order to eliminate any bedding effects. As the expected failure load, F_{Et} , of the joint was determined to be 250 kN according to CIDECT-1 (Wardenier *et al.*, 2008), the maximum applied load was limited to 0.3 N_{Et} , i.e. 70 kN, in order to ensure that the joint deformed well within the linear elastic stage. The corresponding displacement was found to be 7.0 mm.

Hence, the applied load F was applied with a displacement control at 0.5 mm / minute to four different deformation stages, i.e. δ = 2.0 mm at Stage A, 4.0 mm at Stage B, 6.0 mm at Stage C and 7.0 mm at Stage D. After reaching each of these stage, the lateral load was held for 1 minute, and the corresponding data of the 31 strain gauges were captured and recorded for subsequent analysis.

Figure 4.7a) illustrates the measured stresses along the longitudinal direction of the chord, i.e. $\theta = 0^{o}$. It was found that these stresses exhibited a nonlinear distribution in the vicinity of the welded collar, and the stresses increased significantly towards the weld toe. **Table 4.4** summarizes the derived values of the hot stress spots at the weld toe of the T-joint.

It should be noted that these hot spot stresses are derived from the measured data obtained from strain gauges SG1 to SG5 from Stages A to D. Based on the simple beam theory, the nominal stress σ_{nom} is given by:

$$\sigma_{nom} = \frac{M}{W} \tag{4-1}$$

where

M is the applied moment at the crown; and

W is the section modulus.

The stress concentration factor SCF is then given by:

$$SCF = \frac{\sigma_{hs}}{\sigma_{nom}} \tag{4-2}$$

where σ_{hs} is the hot spot stress derived from measured strain data in tests.

After an extensive data analysis on all the measured data obtained from the strain gauges at various deformation stages, **Figure 4.7b)** plots the variations of SCF along the perimeter of the welded collar of the T-joint. It is found that the SCF exhibits a fairly symmetrical distribution about the longitudinal direction of the chord at $\theta = 0^o$. The maximum SCF is found to be 2.84 at the crown, i.e. $\theta = 0^o$ while the minimum SCF is found to be 0.05 at the saddle, i.e. $\theta = 90^o$. It should be noted that the recommended value of SCF is 3.66 according to CIDECT-8, and hence, the measured value is merely 0.776 of the recommended one. Similar findings were also reported by other researchers on similar T-joints (Mashiri *et al.*, 2004a; 2004b; 2006).

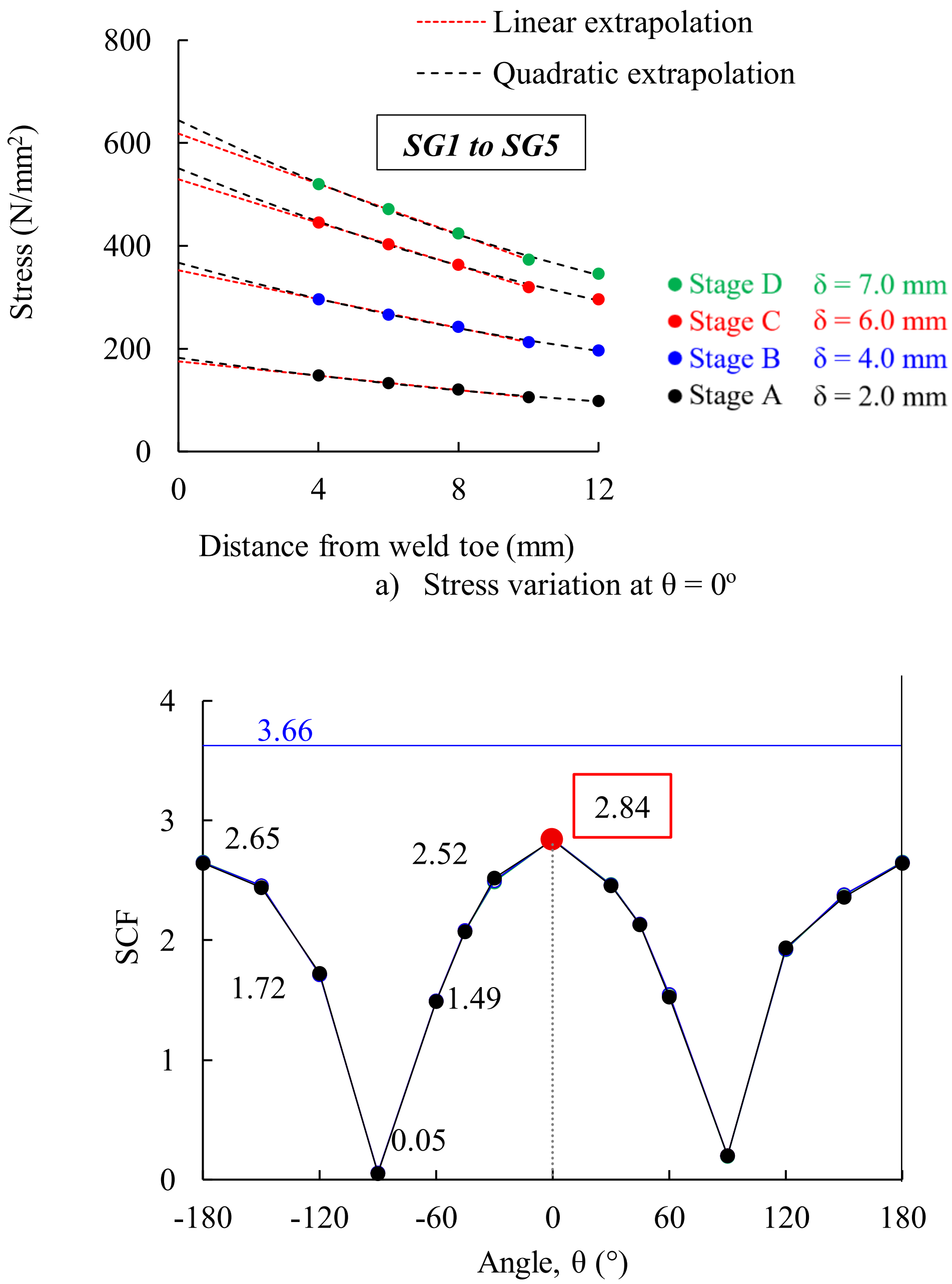

a) Stress variation at θ = 0º

b) Variations of SCF at various θ

Figure 4.7 Stress distributions along the perimeter of the welded collar of Joint M-T1

Table 4.4 Derived hot spot stresses σ_{hs} and SCF at the weld toe

Stages	Applied displacement δ (mm)	Measured stresses (N/mm^2)					Hot spot stresses σ_{hs} (N/mm^2)	Nominal stresses σ_{nom} (N/mm^2)	SCF $= \sigma_{hs} / \sigma_{nom}$
		SG1	SG2	SG3	SG4	SG5			
A	2.0	147	133	121	106	98	175	62	2.833
B	4.0	296	266	243	212	197	352	124	2.838
C	6.0	445	404	364	319	296	529	186	2.844
D	7.0	520	472	425	373	346	618	218	2.835
								Average	2.837 or **2.84**

4.4 Cyclic in-plane bending tests

4.4.1 Test programme

Table 4.1 presents the test programme of the S690 welded T-joints under cyclic in-plane bending actions together with various geometrical ratios of the circular hollow sections and key testing parameters. A total of five different target displacements were selected in the cyclic tests of the S690 welded T-joints, and they were considered to be able to provide a practical range of fatigue performance in these T-joints.

4.4.2 Test set-up and instrumentation

The same set-up shown in **Figure 4.6a)** was also adopted for the cyclic tests of the S690 welded T-joints, and the loading protocol is shown in **Figure 4.8**. The cyclic tests were performed under ***a displacement control***, and the loaded points of the braces of the T-joints were controlled to vary between the minimum and the maximum displacements, δ_{min} and δ_{max} , respectively, through a sinusoidal waveform at a loading frequency f of 3 Hz. While the minimum displacements δ_{min} were set to be 0.5 mm in all tests, the maximum displacements δ_{max} were set to range from 3.0 to 7.0 mm, as shown in **Table 4.5**. It should be noted that the values of the applied load F corresponding to both δ_{min} and δ_{max} were recorded at each cycle while a complete applied load-displacement (F - δ) curve at every 200 cycles was recorded.

A high-resolution video camera with 50 million pixels per frame was employed to record the deformations of the T-joints at close time intervals, in particular, the welded collars, in order to detect crack initiation and propagation in subsequent data analysis.

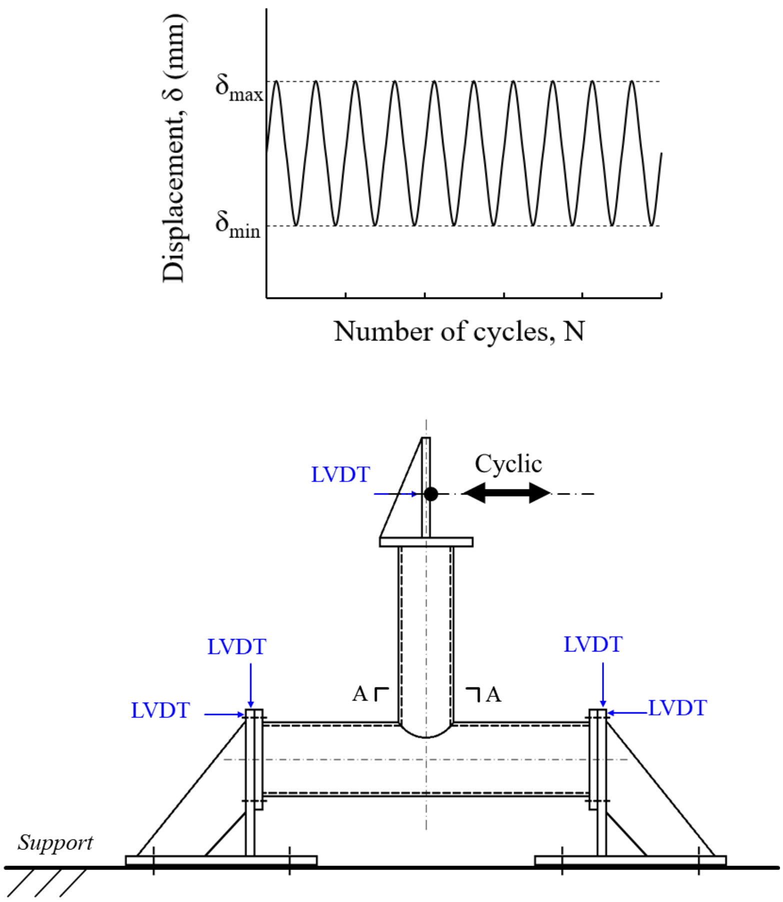

Figure 4.8 Test setup and loading protocol

4.4.3 Test results

All the cyclic in-plane bending tests were carried out successfully on these T-joints, and consistent deformation characteristics in these T-joints were evident. **Table 4.5** summarizes the numbers of cycles completed of these T-joints at various levels of strength reduction. It should be noted that only Joints C-T1a and C-T2a were terminated when fracture of the joints occurred. For all the other joints, the tests were terminated when the applied load ranges ΔF were found to have reduced to 80% of their initial values under the same displacement ranges $\Delta\delta$ as such reductions are considered to be very severe, and hence, these T-joints are regarded to have structurally failed.

Table 4.5 S-N data of S690 welded T-joints at various levels of strength reduction

T-joints	$\Delta\delta$ (mm)	ΔF (kN)	R	$\Delta\sigma_{nom}$ (N/mm^2)	Number of cycles completed N_c at various levels of strength reduction					
					$N_{2\%}$	$N_{5\%}$	$N_{10\%}$	$N_{20\%}$	$N_{30\%}$	N_f
C-T1a	0.5 ~ 7.0	68.2	0.068	202.3	38,707	55,909	71,700	89,927	97,868	108,806
					0.356	***0.514***	***0.656***	***0.826***	***0.899***	***1.0***
b		64.8	0.072	191.9	62,128	77,712	96,893	121,648	-	-
C-T2a	0.5 ~ 6.5	57.2	0.080	169.4	71,791	86,379	106,493	132,169	143,873	169,053
					0.425	***0.511***	***0.630***	***0.782***	***0.851***	***1.0***
b		57.0	0.080	168.8	70,914	93,342	111,684	137,931	-	-
C-T3a	0.5 ~ 4.0	35.2	0.124	104.3	385,246	539,366	655,074	827,822	-	-
b		35.6	0.123	105.4	365,647	429,963	530,432	669,415	-	-
C-T4a	0.5 ~ 3.5	28.7	0.148	85.0	1,335,361	1,604,178	2,004,154	2,449,123	-	-
b		30.2	0.142	89.4	1,126,210	1,360,895	1,675,873	2,086,411	-	-
C-T5a	0.5 ~ 3.0	25.2	0.166	74.6	2,385,749	2,742,918	3,188,915	3,691,315	-	-
b		25.6	0.163	75.8	3,215,131	3,772,247	4,165,435	4,784,651	-	-

- ***Degradation in strength and stiffness of Joint C-T1a***

One of the key areas of interest is the degradation in strength and stiffness of the S690 welded T-joints under cyclic actions. For ease of presentation, the test results of Joint C-T1a are selected as representatives to all these T-joints.

The measured load-displacement curves of Joint C-T1a are plotted in **Figure 4.9a)**, and both strength and stiffness reduction in the joint is evident as a result of progressive degradation. The initial values of the applied load F measured at the target displacements, i.e. δ_{min} = 0.5 mm and δ_{max} = 7.0 mm, are 6.0 and 74.2 kN respectively, and hence, the applied load range ΔF = 74.2 – 6.0 = 68.2 kN. As the cyclic test proceeds, there is an apparent decrease in the measured values of ΔF.

After a comprehensive data analysis on the measured deformation characteristics of the joint, 5 different levels of degradation, namely, 2%, 5%, 10%, 20% and 30% drop in the applied load ranges ΔF of the joint, are identified, as plotted in **Figure 4.9b)**. The corresponding load-displacement curves of the joint at these degradation levels are plotted in **Figure 4.9c)**. It is apparent that the stiffness of the joint, K, i.e. the slope of the load-displacement curve, decreases with a factor of about 0.8 when the corresponding strength degradation is smaller than or equal to 20% .

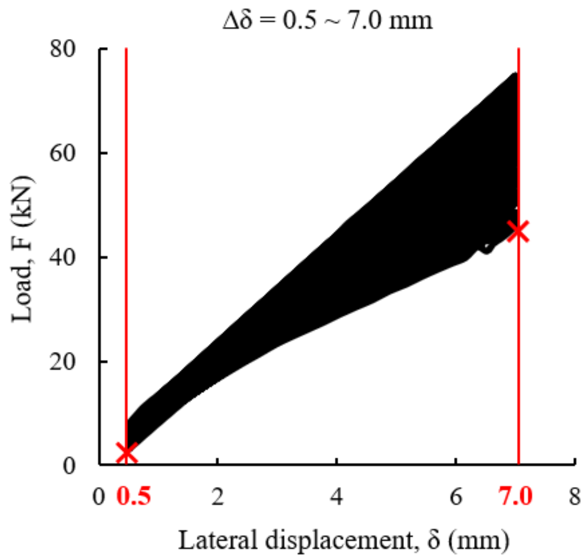

a) Load-displacement curves

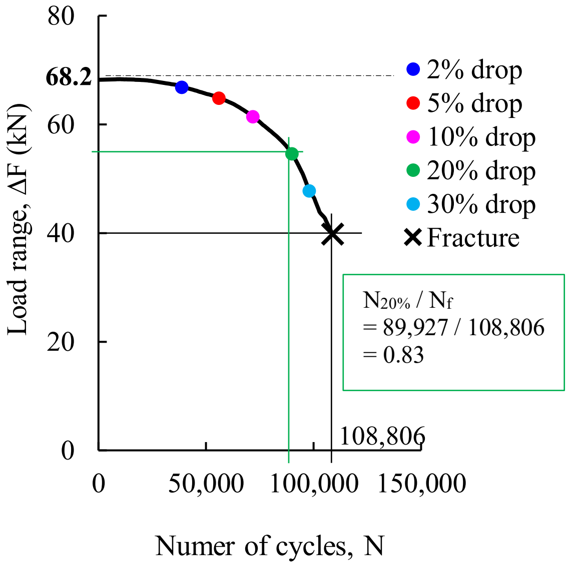

b) Strength degradation

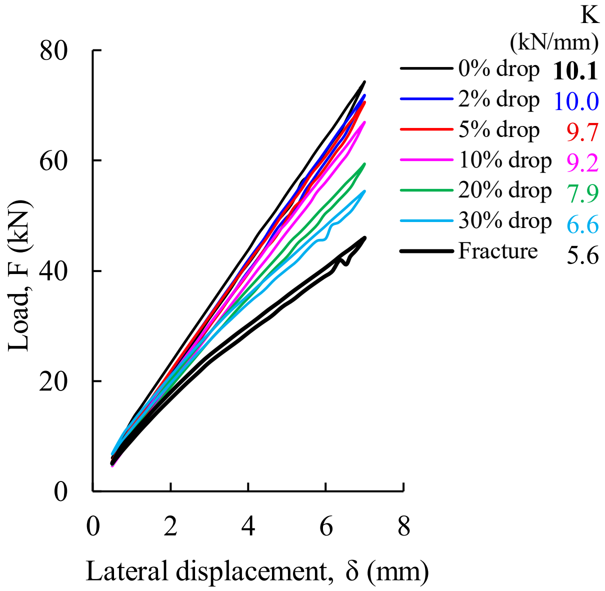

c) Stiffness degradation

Figure 4.9 Degradation in strength and stiffness during fatigue test - Joint C-T1a

Figure 4.10 illustrates the corresponding surface crack patterns at the welded collar of Joint C-T1a at various degradation levels, and it is shown that after crack initiation in the vicinity of the welded collar of the joint, crack propagation takes place in a gradual manner along the circumference of the brace/chord junction. It should be noted that:

- Crack initiation

  After 12,115 cycles, a small crack with a width about 0.1 mm is detected at the weld toe of the crown by imaging examination after 16 times magnification.

- 2% drop

  The measured applied load range ΔF is 66.8 kN, i.e. a 2% drop from its initial value, after 38,707 cycles. There is only *minimal reduction in the slope* of the corresponding load-displacement curve even though a crack is readily identified by a naked eye at the weld toe within a region of the welded collar from -21° to 20°.

- 5% drop

  The measured applied load range ΔF is 64.8 kN, i.e. a 5% drop from its initial value, after 55,909 cycles. A *small reduction in the slope* of the corresponding load-displacement curve is shown while a crack is visible to a naked eye at the weld toe within a region of the welded collar from -31° to 35°.

- 10% drop

  As the test continues, the measured applied load range ΔF is 61.4 kN, i.e. a 10% drop from its initial value, after 71,700 cycles. There is *an apparent reduction in the slope* of the corresponding load-displacement curve, and a crack is obviously visible to a naked eye at the weld toe within a region of the welded collar from -49° to 48°.

- 20% drop

  After 89,927 cycles, the measured applied load range ΔF is 54.6 kN, i.e. a 20% drop from its initial value. *A significant reduction in the slope* of the corresponding load-displacement curve is evident, and a crack is highly visible at the weld toe within a region of the welded collar from -66° to 63°.

- 30% drop

  After 97,868 cycles, the measured load range ΔF is 47.7 kN, i.e. a 30% drop from its initial value. *A severe reduction in the slope* of the corresponding load-displacement curve is present, and a crack is highly visible at the weld toe within a region of the welded collar from -71° to 70°.

- End of test

  The test was suddenly terminated after 108,806 cycles, and the last value of the applied load range ΔF is 39.9 kN, i.e. a 42% drop from its initial value. This deformation takes place in a rapid manner, and cracks propagate through the thickness of the chord, and also develop along parts of the welded collar.

According to the detailed analysis on the deformation characteristics of Joint C-T1a, and also its surface crack development throughout the entire course of testing, a termination criterion was proposed in which a fatigue test should be terminated when the load range ΔF was found to have reduced by 20%, and its cyclic deformation characteristics was found to exhibit a certain degree of non-linearity. It should also be noted that as shown in **Figure 4.9b)**, the corresponding number of cycles with a 20% drop in the load range, i.e. $N_{20\%}$, is found to be 83% of the number of cycles at fracture, i.e. N_f . Based on all these information, this termination criterion was adopted in all the subsequent fatigue tests.

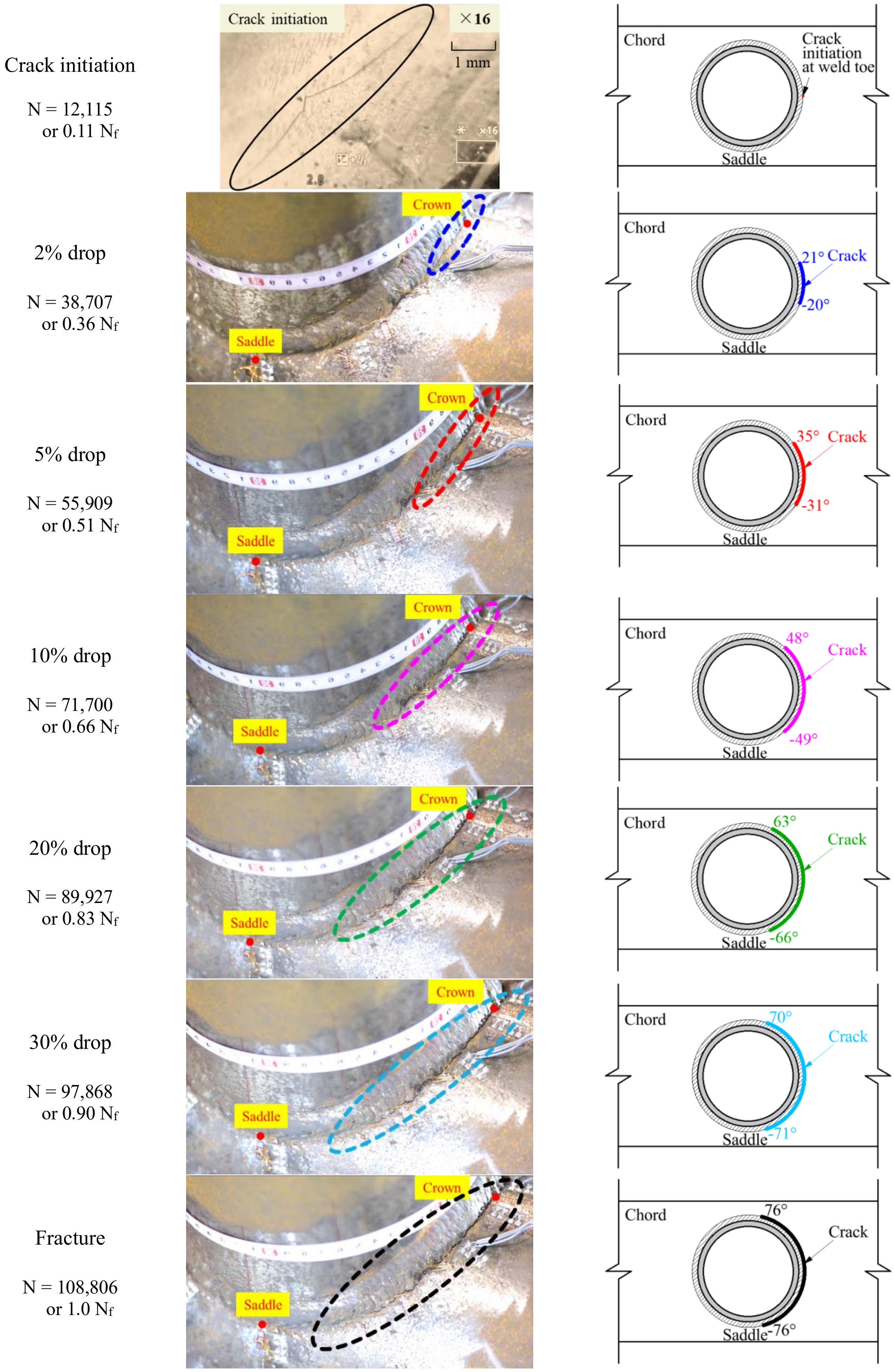

Figure 4.10 Surface crack propagation during fatigue test - Joint C-T1a

- ***Strength and stiffness degradation of all joints***

After a comprehensive data analysis, **Figure 4.11** illustrates the applied load ranges ΔF under constant cyclic displacement actions $\Delta\delta$ of all these fatigue tests, and also the corresponding levels of strength degradation, i.e. 2%, 5%, 10% and 20% reduction in the load ranges ΔF.

Owing to the use of displacement-controlled fatigue tests, additional data on both strength and stiffness degradation are readily obtained, when compared with conventional load-controlled fatigue tests. Hence, it is possible to co-relate the entire processes of strength and stiffness degradation with the number of cycles completed in these T-joints.

As plotted in **Figure 4.11**, it is evident that strength and stiffness degradation is a gradual process which take places incrementally, and their reductions at 2%, 5%, 10% and 20% drop may be well approximated as linear functions against the total number of cycles.

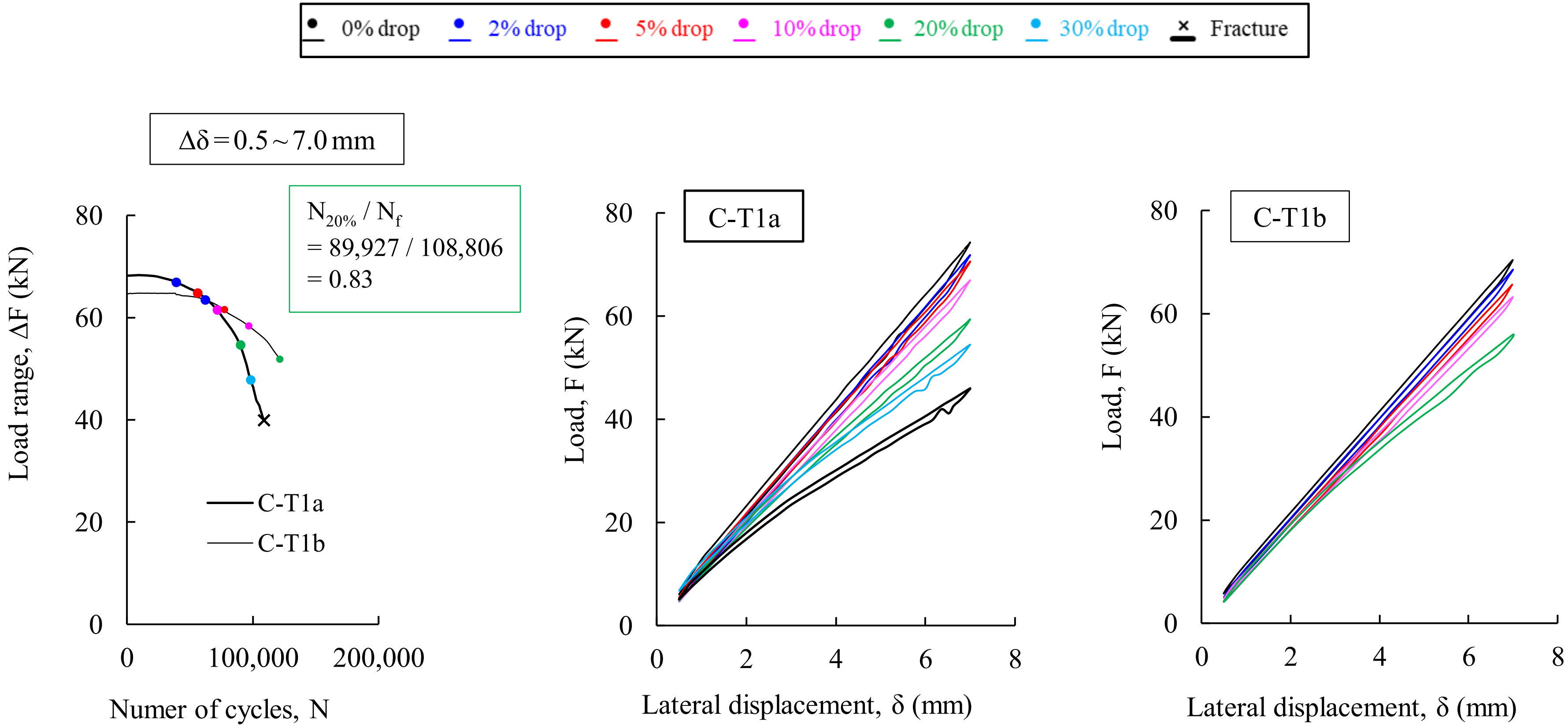
0% drop
2% drop
5% drop
10% drop
20% drop
30% drop
Fracture
Δδ = 0.5 ~ 7.0 mm
N20% / Nf
= 89,927 / 108,806
= 0.83
Load range, ΔF (kN)
Numer of cycles, N
C-T1a
C-T1b
0
100,000
200,000
80
60
40
20
0
Load, F (kN)
Lateral displacement, δ (mm)
C-T1a
0
2
4
6
8
Load, F (kN)
Lateral displacement, δ (mm)
C-T1b

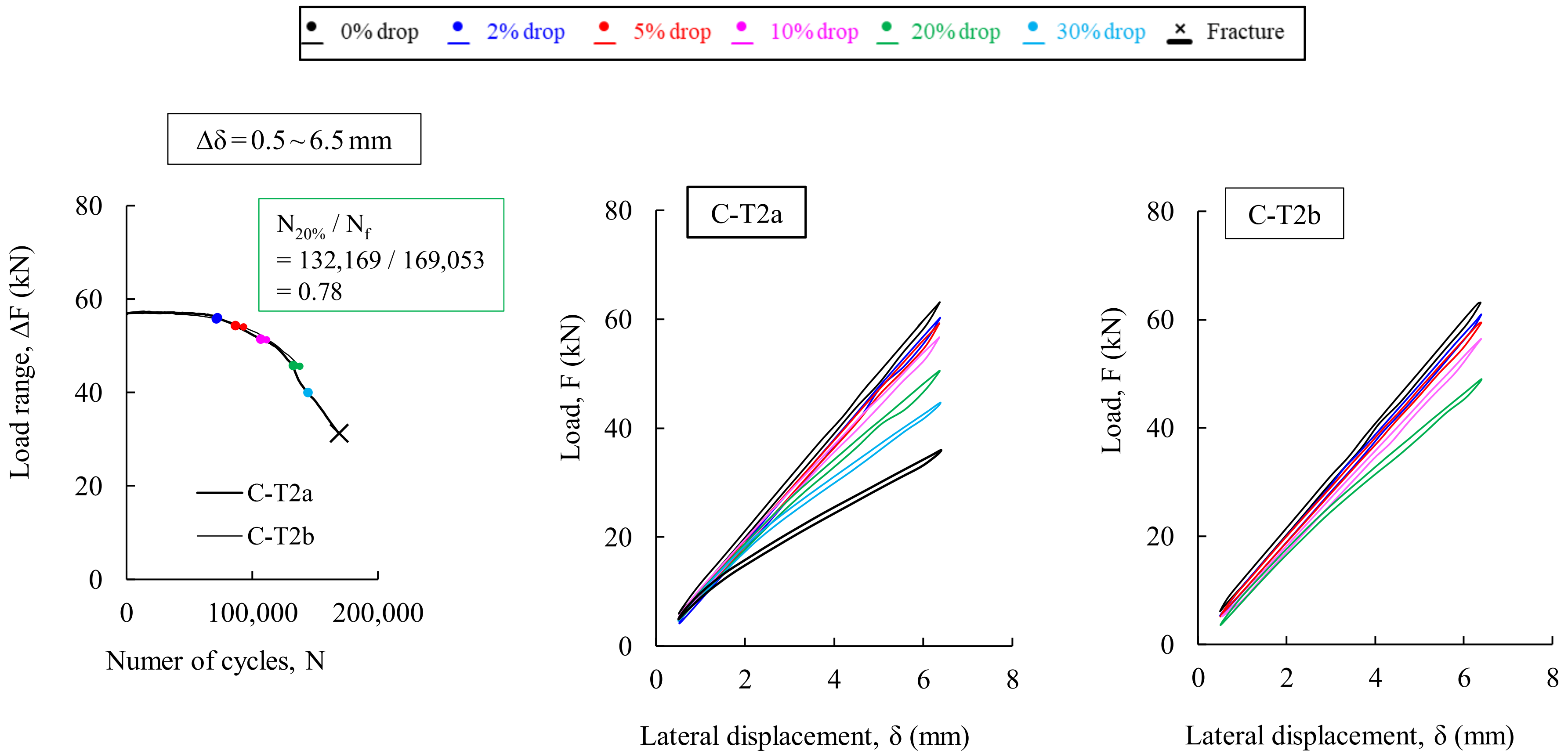
0% drop
2% drop
5% drop
10% drop
20% drop
30% drop
Fracture
Δδ = 0.5 ~ 6.5 mm
$N_{20\%}$ / N_f
= 132,169 / 169,053
= 0.78
Load range, ΔF (kN)
Numer of cycles, N
C-T2a
C-T2b
Load, F (kN)
Lateral displacement, δ (mm)
C-T2a
C-T2b

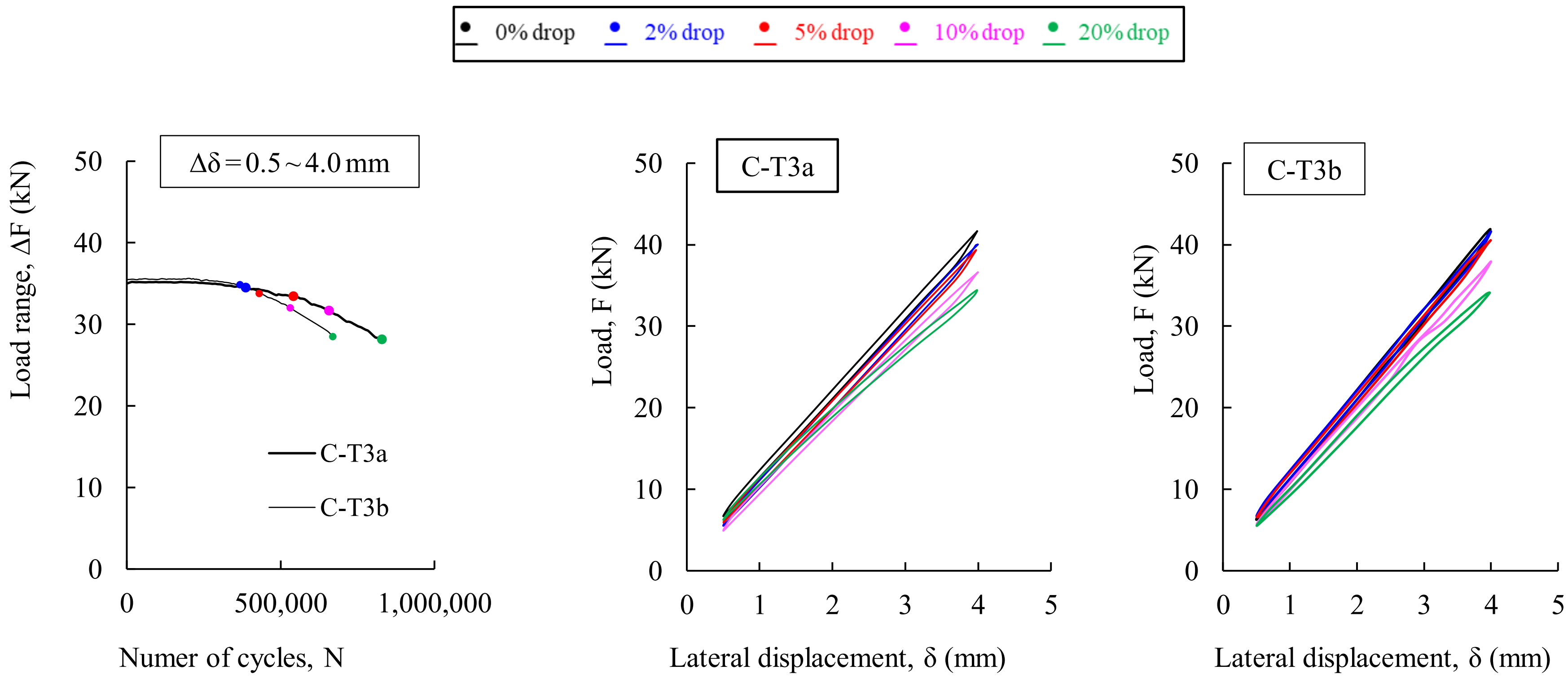
0% drop
2% drop
5% drop
10% drop
20% drop
Δδ = 0.5 ~ 4.0 mm
Load range, ΔF (kN)
50
40
30
20
10
0
C-T3a
C-T3b
0
500,000
1,000,000
Numer of cycles, N
C-T3a
Load, F (kN)
Lateral displacement, δ (mm)
C-T3b
Load, F (kN)
Lateral displacement, δ (mm)
0
1
2
3
4
5

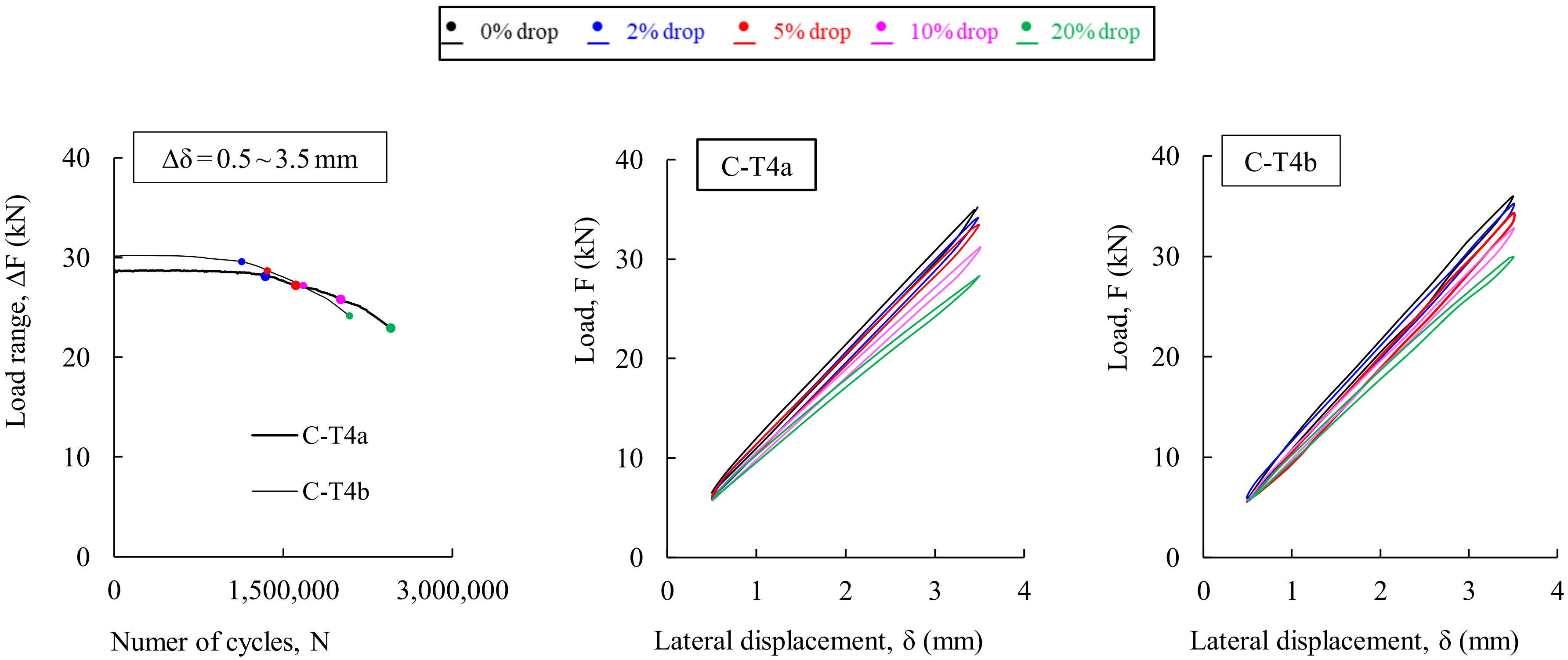

0% drop
2% drop
5% drop
10% drop
20% drop
Δδ = 0.5 ~ 3.5 mm
Load range, ΔF (kN)
C-T4a
C-T4b
Numer of cycles, N
0
1,500,000
3,000,000
C-T4a
Load, F (kN)
Lateral displacement, δ (mm)
C-T4b
Load, F (kN)
Lateral displacement, δ (mm)

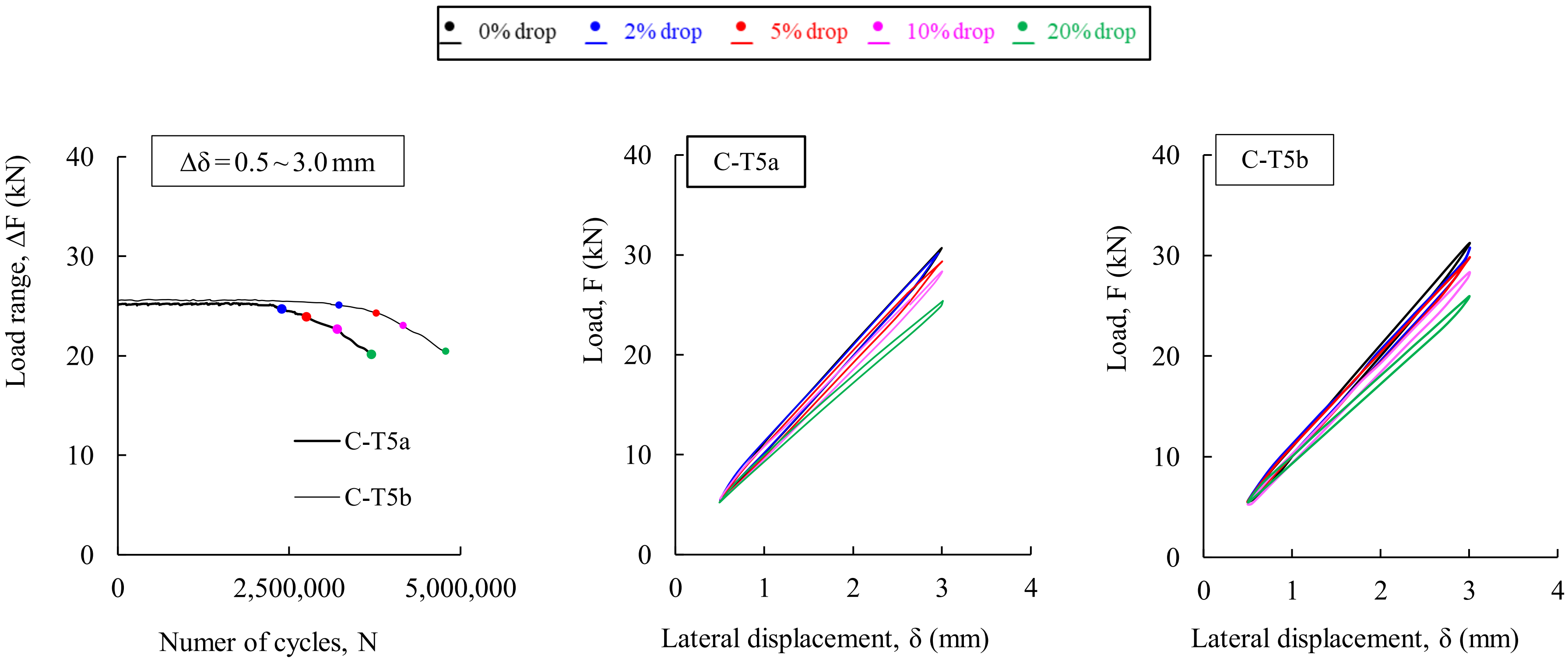

Figure 4.11 Strength and stiffness degradation of S690 welded T-joins

Key data of degradation in both strength and stiffness of the joints are summarized in **Table 4.5** and **Table 4.6**. It should be noted that:

- **Table 4.5** presents the number of cycles corresponding to various levels of strength reductions. It should be noted that only Joints C-T1a and C-T2a have been tested to fracture, and the ratios of the numbers of cycles completed corresponding to various strength reductions of these two joints are also given. It is shown that for a strength reduction at 5%, these two joints have completed at least 50 % of the total number of cycles to fracture, i.e. 0.50 N_f , while a 20% strength reduction corresponds to 0.75 N_f . Hence, the criterion of adopting a 20% strength reduction as the fatigue life of these T-joints is considered to be highly acceptable. In addition, for Joints C-T4a & b, and C-T5a & b, the total numbers of cycles corresponding to a 20% strength reduction have exceeded 2,000,000, and such a value is taken as the fatigue life of these joints by some researchers (Tong *et al.*, 2021a; Tong *et al.*, 2021b; Jiao *et al.*, 2013).

- Among all these T-joints, as shown in **Table 4.6**, the minimum levels of stiffness degradation at various levels of strength reductions, K, are found to be

  K = 0.972 when there is a 2% strength reduction;

  = 0.948 when there is a 5% strength reduction;

  = 0.886 when there is a 10 % strength reduction; and

  = 0.750 when there is a 20% strength reduction.

  Hence, for a degradation in strength at 20%, the corresponding residual stiffness is found to be at least 75% of their original values. For any further degradation in strength, the corresponding residual stiffness are considered to be very large.

Table 4.6 Stiffness degradation of S690 welded T-joints at various levels of strength reduction

T-joints	Levels of stiffness degradation at various levels of strength reduction					
	$K_{2\%}$	$K_{5\%}$	$K_{10\%}$	$K_{20\%}$	$K_{30\%}$	K_f
C-T1a	0.985	0.954	0.910	0.780	0.650	0.556
b	0.982	0.949	0.900	0.750	-	-
C-T2a	0.982	0.950	0.889	0.752	0.655	0.489
b	0.972	0.948	0.908	0.764	-	-
C-T3a	0.988	0.961	0.911	0.816	-	-
b	0.972	0.951	0.898	0.790	-	-
C-T4a	0.989	0.962	0.890	0.789	-	-
b	0.979	0.955	0.903	0.795	-	-
C-T5a	0.987	0.951	0.890	0.796	-	-
b	0.983	0.968	0.886	0.818	-	-
Minimum	*0.972*	*0.948*	*0.886*	*0.750*	*0.650*	*0.489*

Figure 4.12 plots the surface crack characteristics of the welded collars of all the T-joints at 5% strength reduction. The cracks were identified by the naked eye at the weld toe, and they developed along parts of the welded collar.

Once a 20% strength reduction is considered as the failure criterion in all these fatigue tests of the S690 welded T-joints, **Figure 4.13** plots the corresponding surface crack characteristics of the welded collars of all the T-joints for a direct comparison.

In addition, parts of the crowns were extracted from the T-joints which were subject to the maximum cyclic displacements during fatigue tests. After etching with a 10% nitric acid solution, details of the welded joints are readily identified, including the weld metal, the heat affected zones and the base metal, as shown in **Figure 4.14**.

It is evident that the surface fatigue cracks initiate from the weld toes of the chords within the heat affected zones of the welded sections, and then propagated into the thickness of the plate. For Joints C-T1a, C-T2a and C-T3a, fracture is found to propagate across the full thicknesses of the plates. However, for Joints C-T4a and C-T5a, only limited fracture is found to have propagated into the thicknesses of the plates.

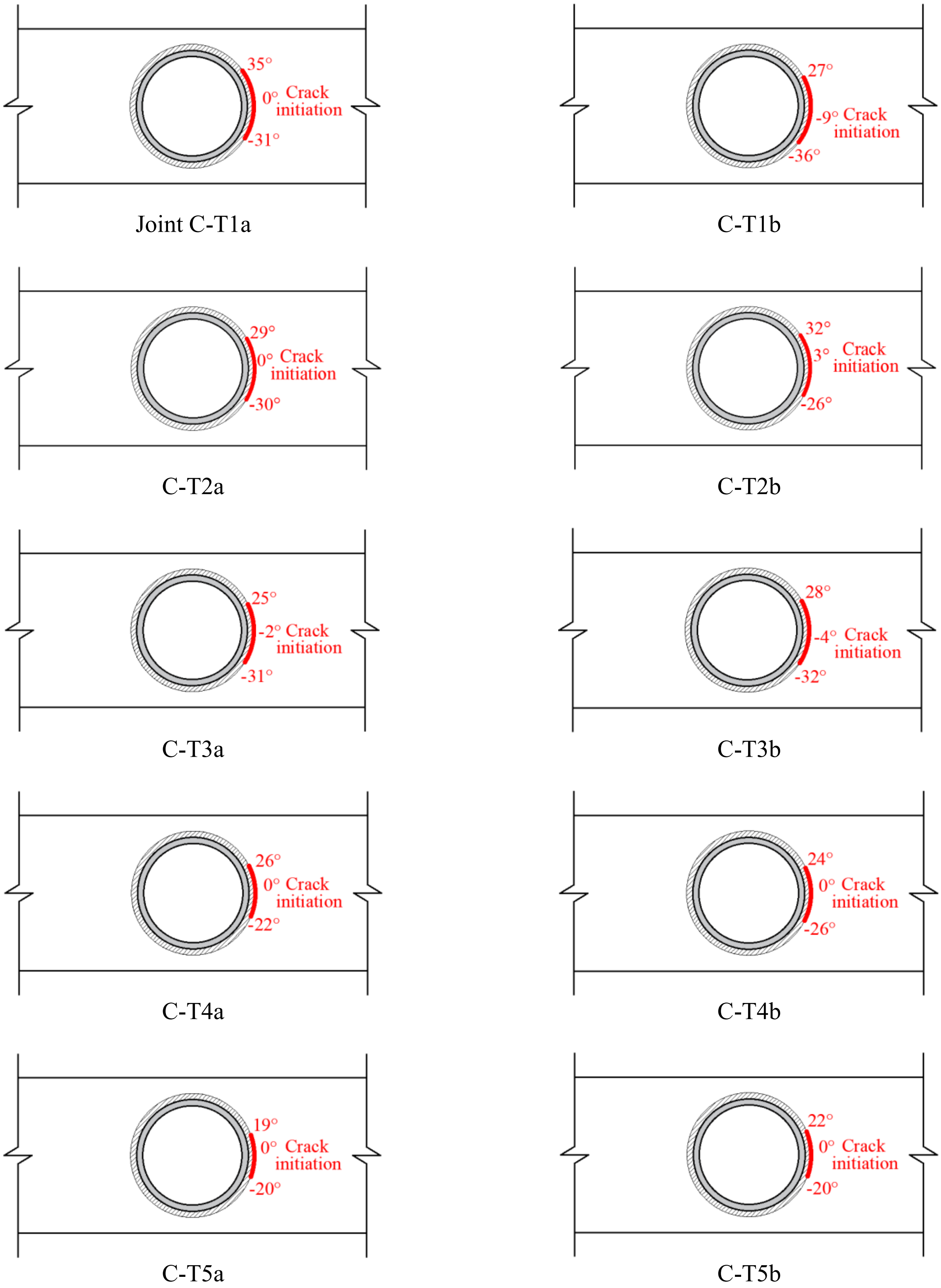

Figure 4.12 Surface crack characteristics along the weld collars of S690 welded T-joints at 5% strength reductions

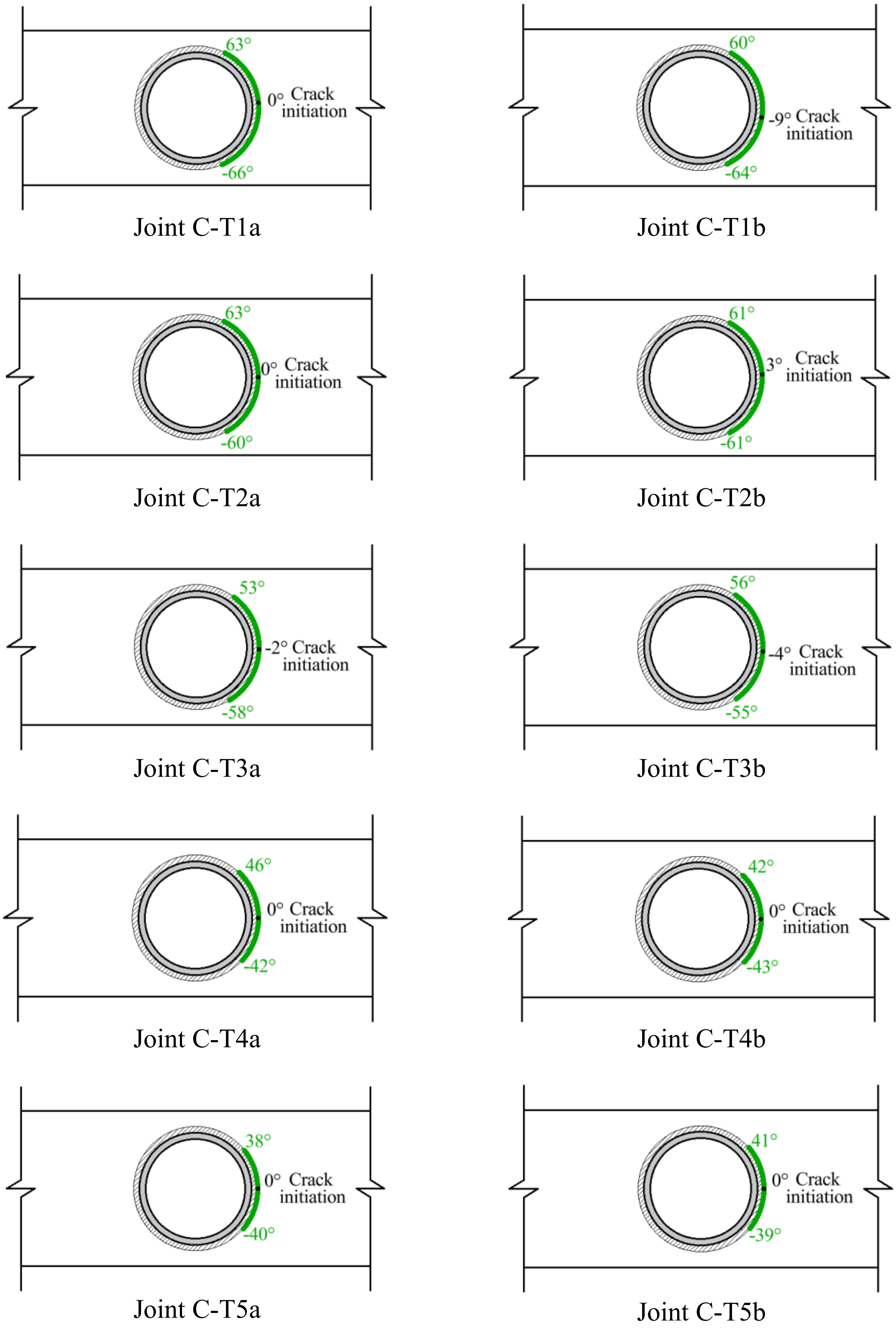

Figure 4.13 Surface crack characteristics along the weld collars of S690 welded T-joints at 20% strength reductions

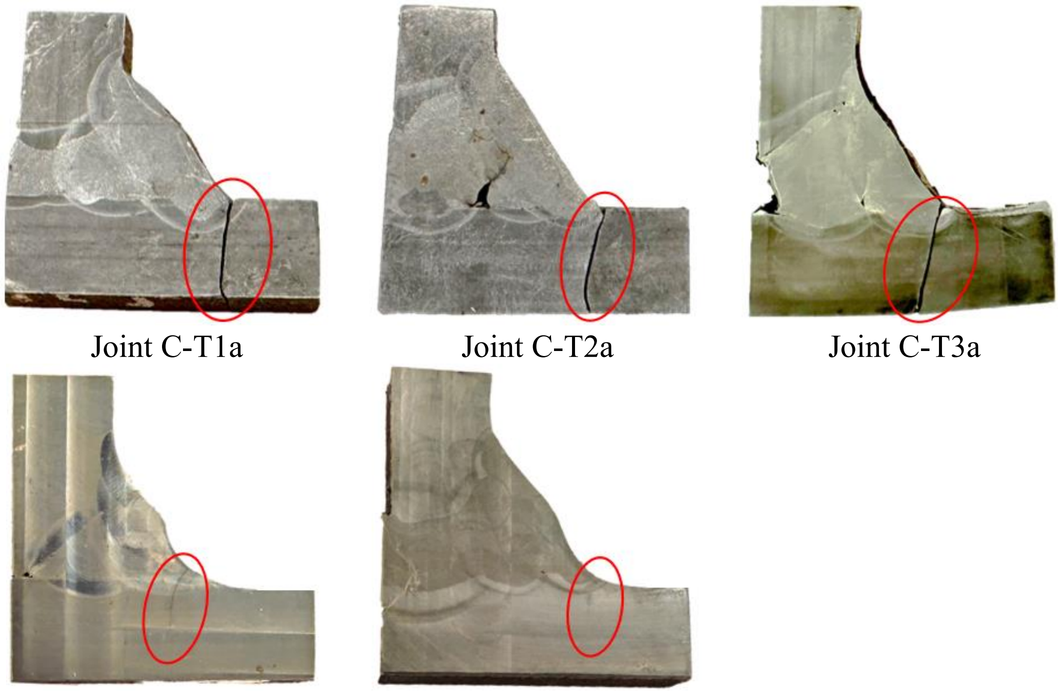

Joint C-T1a Joint C-T2a Joint C-T3a

Joint C-T4a Joint C-T5a

Figure 4.14 Crown parts of S690 welded T-joints after failure

Figure 4.15 plots the variations of the residual stiffness ratios against various levels of strength reductions of these S690 welded T-joints, and it is apparent that all of these data lie above a straight line between (0%, 1.0) and (20%, 0.75). Hence, there is a linear reduction in the residual stiffness ratios of the T-joints from 1.0 to 0.75 of their initial values when there is a steady increase in their strength reductions from 0% to 20%. Refer to **Table 4.6** for tabulated data of **Figure 4.15**.

More interestingly, by comparing the numbers of cycles at various levels of strength reductions of these T-joints with the number of cycles corresponding to a 20% drop in strength, $N_{20\%}$, the fatigue life ratios of all these T-joints are presented in **Table 4.7**, and they are plotted in **Figure 4.16**.

It is apparent that depending on the various load ranges adopted during fatigue tests in these T-joints, the fatigue life ratios vary from 0.43 to 0.67 with a 2% drop, from 0.62 to 0.79 with a 5% drop, and then, 0.79 to 0.87 with a 10% drop. Hence, these data provide an indication on the residual fatigue life of these T-joints based on the levels of strength reductions and also the stress ranges, and they are readily adopted to predict the residual life of these T-joints once their degradation in strength and stiffness is known.

Table 4.7 Fatigue life ratios of S690 welded T-joints at various levels of strength reduction

T-joints	Fatigue life ratios at various levels of strength reduction			
	$R_{2\%}$	$R_{5\%}$	$R_{10\%}$	$R_{20\%}$
C-T1a	*0.43*	*0.62*	*0.80*	*1.0**
b	*0.54*	*0.65*	*0.81*	
C-T2a	*0.46*	*0.65*	*0.79*	
b	*0.54*	*0.65*	*0.82*	
C-T3a	*0.65*	*0.74*	*0.86*	
b	*0.51*	*0.64*	*0.80*	
C-T4a	*0.51*	*0.68*	*0.81*	
b	*0.55*	*0.64*	*0.79*	
C-T5a	*0.54*	*0.65*	*0.80*	
b	*0.67*	*0.79*	*0.87*	

Note: * A 20% strength reduction is considered as the failure criterion in all these fatigue tests of the S690 welded T-joints, and hence, $R_{20\%}$ become 1.0 accordingly.

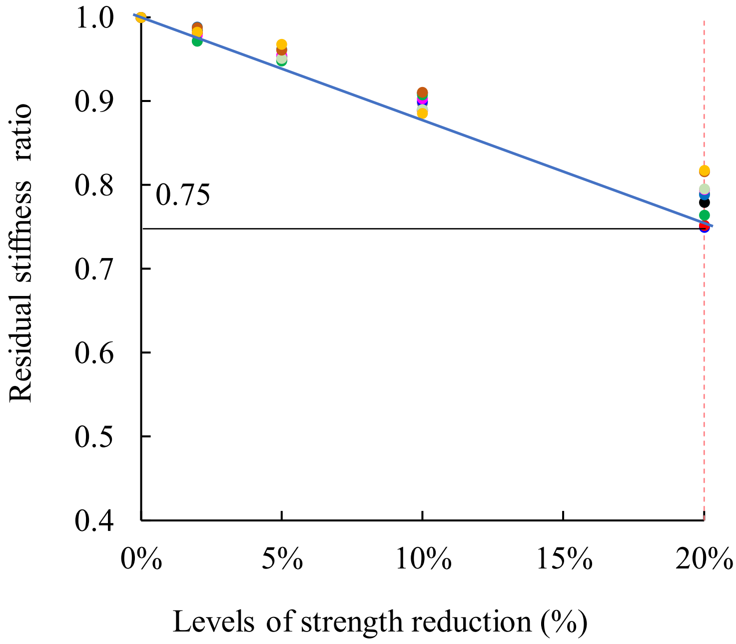

Figure 4.15 Ratios of residual stiffness at various levels of strength reduction

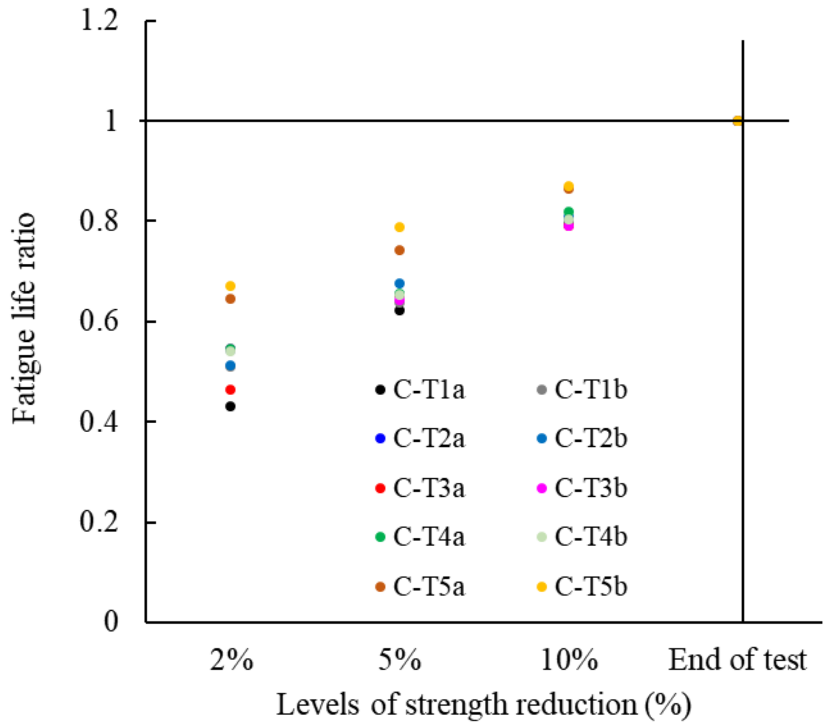

Figure 4.16 Ratios of fatigue life at various levels of strength reduction

4.5 Analysis on S-N data

A comprehensive data analysis is performed on the S-N data obtained from Chapter 4.4 above, and these data are adopted to compare with existing codified S-N curves to demonstrate whether these S-N curves are able to predict the fatigue performance of the S690 welded T-joints effectively.

4.5.1 Formulation of S-N curves

At present, two assessment approaches are widely used to predict the fatigue life of welded steel joint types under cyclic actions as follows:

- ***Classification approach***

  This approach relates the nominal cyclic stress ranges $\Delta\sigma_{nom}$ to the fatigue life N to give a stress-fatigue life curve, i.e. a S-N curve, for fatigue assessment on typical welded steel joint types with various steel grades. Through statistical analyses on test data of a large amount of fatigue tests, a series of S-N curves with different categories are derived for typical joint types commonly adopted in practice.

- ***Stress concentration factor approach***

  In order to provide assessment rules to cover welded steel joints with a wide range of joint types and sizes, the stress concentration factor approach is adopted to determine highly localized stresses in welded joints due to abrupt changes in geometry through both experimental and numerical investigations. The stress concentration factors are then applied to obtain the hot spot stresses, i.e. the revised stress ranges $\Delta\sigma_{hs}$, of the joints to determine their fatigue life through the use of the S-N curves mentioned above.

As presented in Section 3.6.1, the least squares method is adopted to perform a regression analysis on the S-N data of the fatigue tests obtained in Section 3. Both the classification and the stress concentration factor methods are adopted to determine the S-N curves of the S690 welded T-joints, i.e. $(S - N)_j$ curves, as shown in **Figure 4.17a)** and **b)** respectively.

It should be noted that these curves are derived according to various levels of strength reduction, i.e. 5%, 10% and 20% drop in the load ranges ΔF. The corresponding parameters of these derived $(S - N)_j$ curves, i.e. A, m and σ_{lim}, are summarized in **Table 4.8**. Hence, these $(S–N)_j$ curves are readily adopted to assess the fatigue performances of the S690 welded T-joints.

Table 4.8 Parameters of S-N curves of S690 welded T-joints at various levels of strength reduction

Cylic stress range	Strength reduction (%)	A	m	Fatigue stress limit σ_{lim} (N/mm^2)
Classification method with nominal stress $\Delta\sigma_{nom}$	5	13.93	4.12	48.2
	10	13.99	4.10	50.7
	20	13.85	3.98	52.5
Stress concentration method with hot spot stress $\Delta\sigma_{hs}$	5	15.80	4.12	137.8
	10	15.84	4.10	144.2
	20	15.66	3.98	149.3

Note: $\Delta\sigma_{hs}$ = SCF $\Delta\sigma_{nom}$ where SCF = 2.84

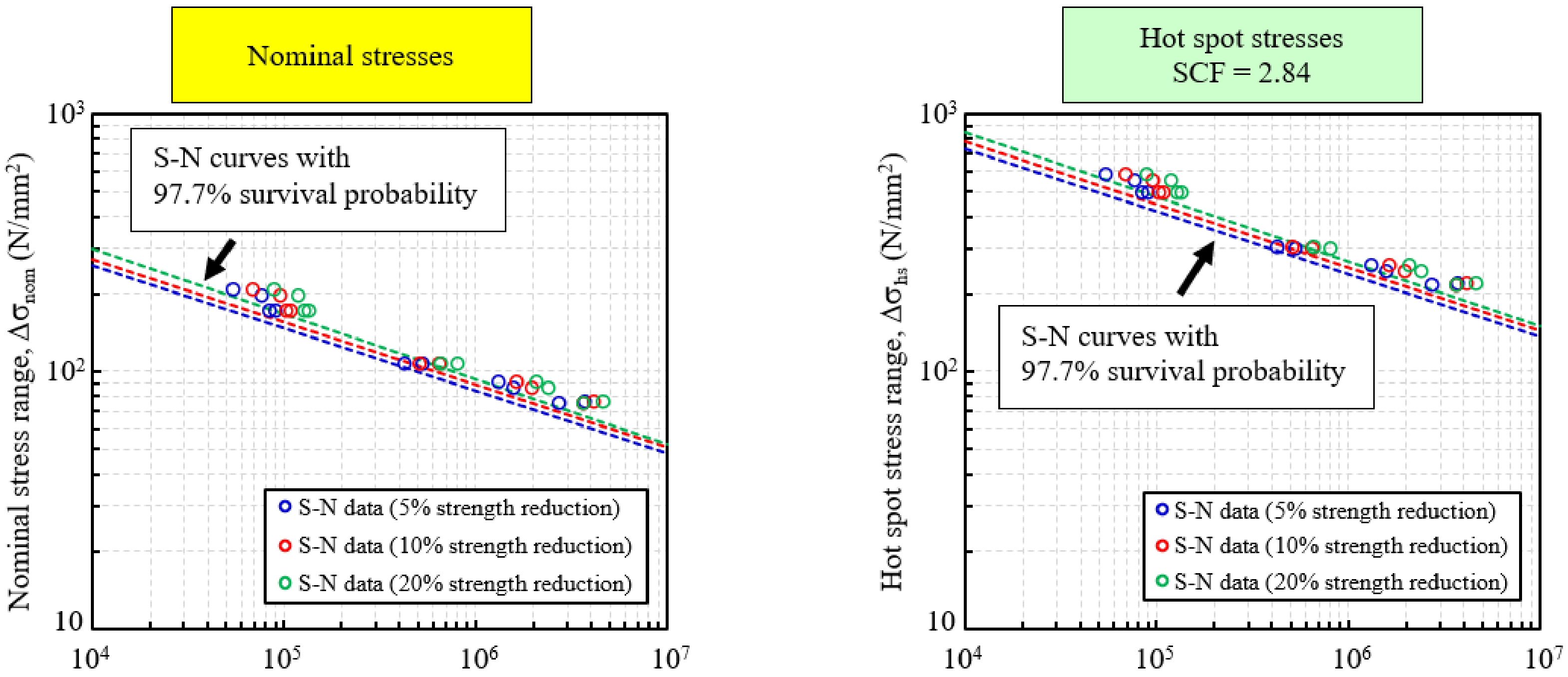

a) Classification method

b) Stress concentration method

Figure 4.17 $(S\text{-}N)_j$ curves of S690 welded T-joints

4.5.2 Design rules for fatigue assessment

Existing codified S-N curves given in different design rules for fatigue assessment on the welded joints are briefly described as follows.

- **EN 1993-1-9**

  This Code adopts the ***classification method*** to predict the fatigue life N of steel sections under cyclic nominal stress ranges $\Delta\sigma_{nom}$.

  Details of the design S-N curves given in this Code were presented in Chapter 3.6.2.

- **CIDECT-8**

  This Code adopts the ***stress concentration factor method*** to predict the fatigue life N of steel sections under cyclic hot spot stress ranges $\Delta\sigma_{hs}$.

  The stress concentration factors for steel sections with various joint details are correlated to their geometric parameters, and the S_{hs}-N curves are expressed as follows:

$$\log N = \frac{12.476 - 3\log S_{hs}}{1 - 0.18\log\frac{16}{t}} \qquad \text{for } 10^3 < N \leq 5\times10^6 \qquad (4\text{-}3)$$

$$\log N = 16.327 - 5\log S_{hs} + 2.01\log\frac{16}{t} \qquad \text{for } 5\times10^6 < N < 10^8 \qquad (4\text{-}4)$$

where

N	is the design fatigue life;
S_{hs}	is the design hot spot stress range; and
t	is the thickness of the steel section.

- **API RP 2A-WSD**

This Code also adopts the ***stress concentration factor method*** to predict the fatigue life N of steel sections, and the S_{hs}-N curves are expressed as the following equation:

$$\log N = \log k_1 - m \log S_{hs} \tag{4-5}$$

$$S_{hs} = S_{\mathrm{hs,0}} (\frac{t_{ref}}{t})^{0.25} \tag{4-6}$$

where

N	is the design fatigue life;
S_{hs}	is the design hot spot stress range;
k_1	is a constant which is taken to be 12.48 for welded joints;
m	is an inverse of the slope which is taken to be 3 for a design fatigue life less than 10^7 cycles;
$S_{hs,0}$	is the reference hot spot stress range; and
t	is the thickness of the steel section.

4.5.3 Comparison between test data and various design curves

Details of the derived S-N curves and the comparison with design curves are presented as follows.

a) Classification method – S_{nom}-N curves

Figure 4.18 illustrates the S_{nom}-N data of the S690 welded T-joints with 5%, 10% and 20% strength reduction, and also various design S_{nom}-N curves given in EN 1993-1-9. It should be noted that:

- All the S_{nom}-N data at various levels of strength reduction lie above the current design S_{nom}-

N curve for welded T-joints, i.e. **Class FAT 50**, especially for those design fatigue life larger than 10^6 cycles.

- Hence, a higher design S_{nom}-N curve is recommended to be adopted for the fatigue assessment on the S690 welded T-joints at various levels of strength reduction, i.e. **Class FAT 56** for both the T-joints at 5% and 10% strength reduction, and **Class FAT 63** for the T-joints at 20% strength reduction.

- The values of the corresponding fatigue stress limits $\sigma_{lim,nom}$ of the S690 welded T-joints with 5%, 10% and 20% strength reduction are found to be 1.3, 1.4 and 1.5 times of the codified values respectively, as shown in **Table 4.9**.

b) Stress concentration factor method – S_{hs}-N curves

Figure 4.19 illustrates the S_{hs}-N data of the S690 welded T-joints with 5%, 10% and 20% strength reduction, and also various design S_{hs}-N curves given in CIDECT-8 and API 2A-WS. It should be noted that:

- All the S_{hs}-N data at various levels of strength reduction lie above the current design S_{hs} - N curves for welded T-joints, especially for those design fatigue life larger than 10^6 cycles.

- Hence, the fatigue enhancement factors F(R) are recommended to be increased in assessing the fatigue performance of the S690 welded T-joints at various levels of strength reduction, i.e. F(R) = 1.2 for 5% strength reduction, and 1.3 for both 10% and 20% strength reduction.

- As shown in **Table 4.9**, the values of the corresponding fatigue stress limits $\sigma_{lim,hs}$ of the S690 welded T-joints are found to be at least 1.5 times of the codified values.

Hence, it is found that the existing codified S-N curves provide conservative predictions for the fatigue performance of the S690 welded T-joints under cyclic actions, especially for the design fatigue life larger than 10^6 cycles. It is also demonstrated that the current design curves given in EN 1993-1-9, CIDECT-8 and API RP 2A-WSD may be modified according to the results of the fatigue tests, and the limiting stress ranges should be increased by a factor of ***1.3, 1.5*** and ***1.8*** respectively, corresponding to a 5% strength reduction, as a minimum. Refer to **Table 4.9** for the other two cases of 10% and 20% strength reduction for further increases.

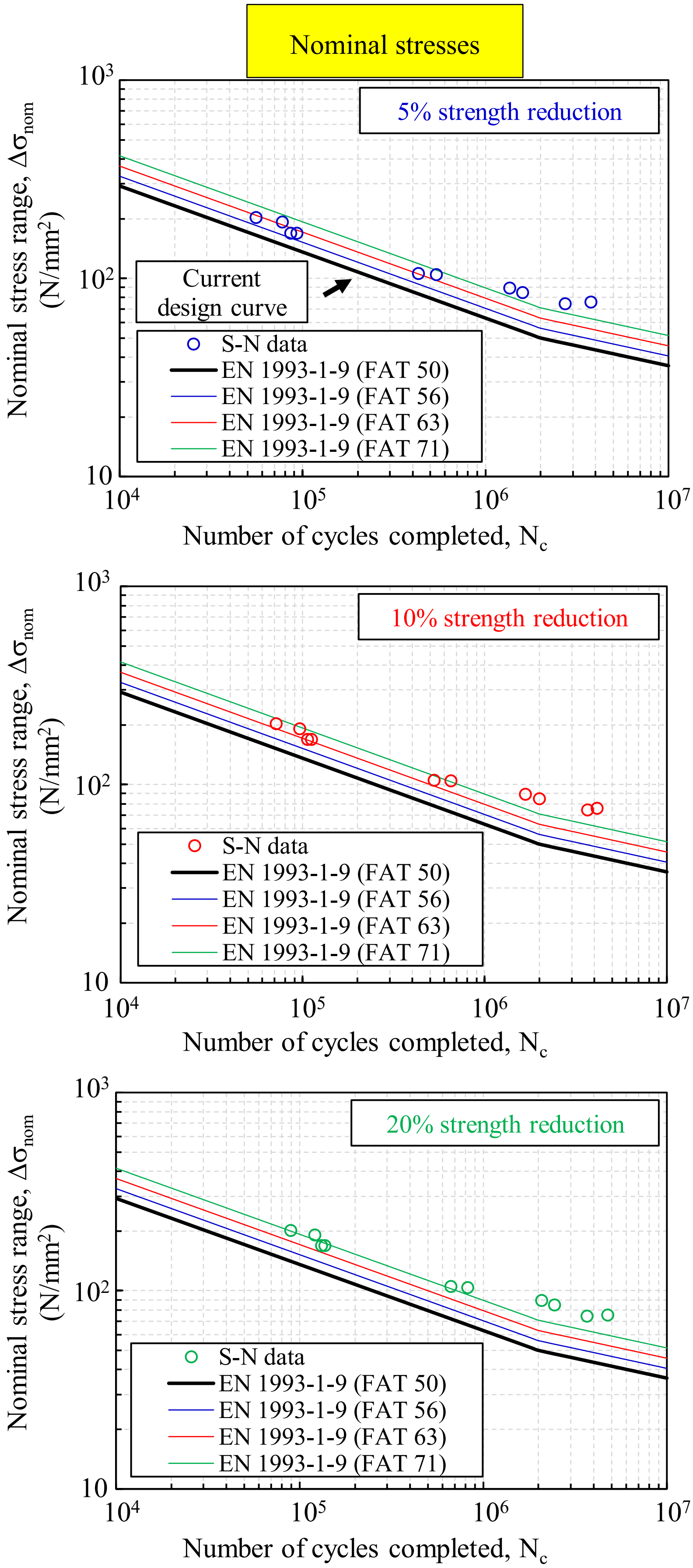

Figure 4.18 Comparison with EN

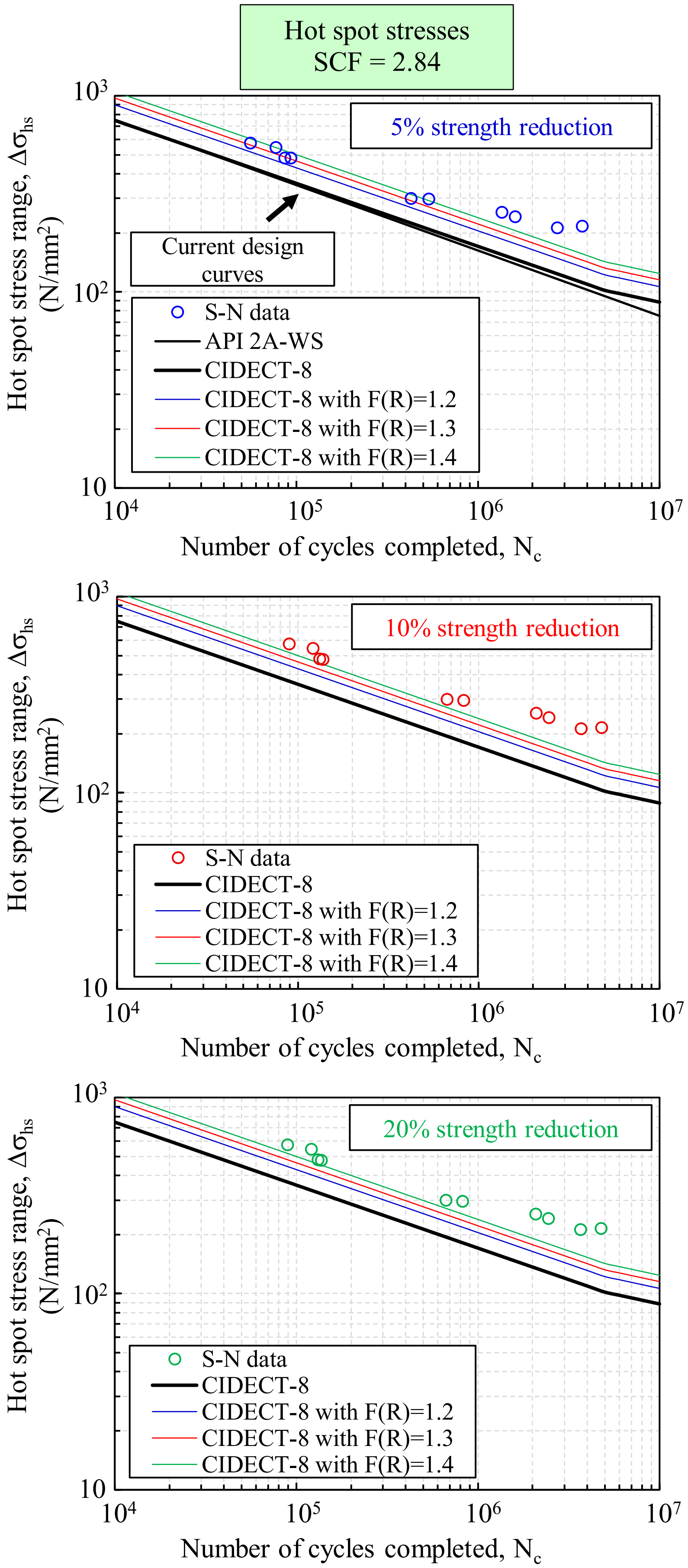

Figure 4.19 Comparison with CIDECT and API

Table 4.9 Comparison of fatigue stress limits given in various design codes

	Nominal stress of fatigue limit $\sigma_{lim,nom}$ (N/mm^2)		Ratio	Hot spot stress of fatigue limit $\sigma_{lim,hs}$ (N/mm^2)		Ratio to CIDECT	Ratio to API
Design codes	EN 1993-1-9	36.2	*1.0*	CIDECT-8	88.6	*1.0*	---
				API 2A-WSD	75.5	---	*1.0*
S690 welded T-joints at various levels of strength reductions	5% drop	48.2	*1.3*	5% drop	137.8	*1.5*	*1.8*
	10% drop	50.7	*1.4*	10% drop	144.2	*1.6*	*1.9*
	20% drop	52.5	*1.5*	20% drop	149.3	*1.7*	*2.0*

4.6 Fatigue life prediction using fatigue tests on coupons

It is interesting to find a rational way to co-relate the S-N data derived from typical fatigue tests on the coupons of the S690 welded sections, i.e. the $(S\text{-}N)_c$ curve shown in **Figure 3.31**, and those obtained from the S690 welded T-joints, i.e. the $(S\text{-}N)_j$ curve shown in **Figure 4.18**.

As presented in Chapter 3, it should be noted that the coupons of the S690 welded sections are specially designed and manufactured, i.e. they are cylindrical coupons with highly polished surfaces along their gauge lengths. Hence, the effects of stress concentration and residual stresses are assumed to have been fully eliminated in the coupons, i.e. a uniform stress always exists across the cross-section of the gauge length of each coupon, and there is no residual stress at all. As all these coupons have been tested under symmetric cyclic actions, and hence, the stress ratio R of these tests is -1.

On the contrary, the S690 welded T-joints are fabricated and tested differently, and various types of stresses in typical welded T-joints are shown in **Figure 4.20**.

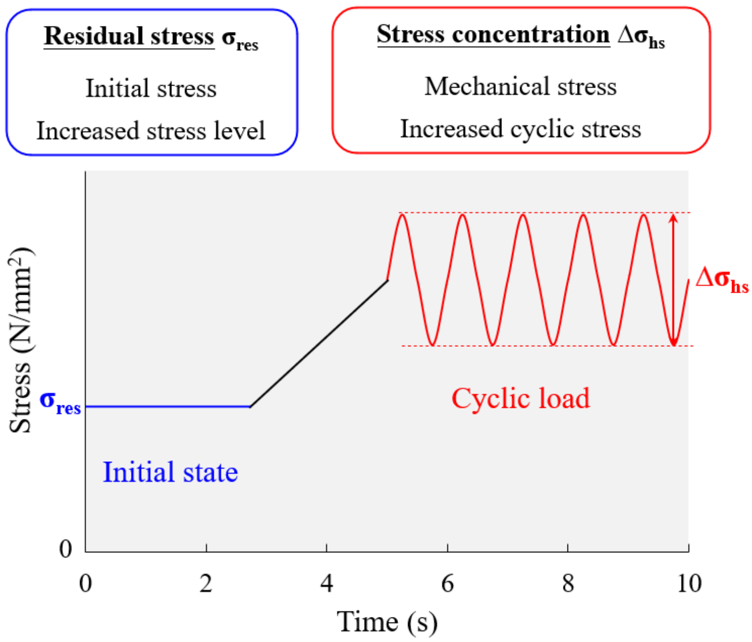

Figure 4.20 Various types of stresses in typical welded T-joints

Hence, it is important to consider the following;

- No surface polishing

  All of these welded T-joints are fabricated in accordance with common practice of steel fabrication that no polishing on the surfaces of the welded joints is carried out after welding.

- Presence of residual stresses

  The presence of welding-induced residual stresses is widely considered to have significant effects onto the fatigue life of welded joints though these stresses are often difficult to measure or predict accurately. Based on an advanced numerical welding simulation (Hu et al., 2020; 2022; 2023), the residual stress distributions along the welded collars of these S690 welded T-joints are readily obtained. It should be noted that details of the numerical models are presented in Chapter 5.4.2. As shown in **Figure 4.21**, the average value of von Mises residual stresses at the crown of Joint M-T1 across the chord thickness is found to be about 500 N/mm^2, and hence, this value is taken to be the initial stress σ_{res} at the crown of the S690 T-joints before tests.

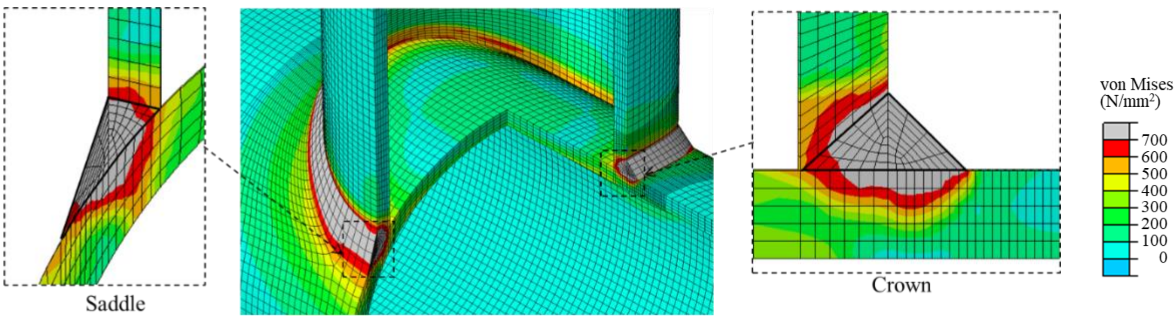

Figure 4.21 Advanced numerical welding simulation: Residual stress distribution of Joint M-T1

- Effects of stress concentration

In general, the mechanical stresses are readily evaluated according to Equation (4-1), and hence, the hot spot stresses σ_{hs} at the crown of these T-joints under monotonic action should be determined as follows:

$$\sigma_{hs} = SCF \times \sigma_{nom} \tag{4-7}$$

Under cyclic actions, both the minimum and the maximum hot spot stresses $\sigma_{hs,mim}$ and $\sigma_{hs,max}$ at the crown of these T-joints should be determined respectively as follows:

$$\sigma_{hs,min} = SCF \times \sigma_{nom,min} \tag{4-8}$$

$$\sigma_{hs,max} = SCF \times \sigma_{nom,max} \tag{4-9}$$

where

SCF is the stress concentration factor, and it is taken as 2.84 according to Chapter 4.3;

$\sigma_{nom,\ min}$ is the minimum applied stress under a cyclic action; and

$\sigma_{nom,\ max}$ is the maximum applied stress under a cyclic action.

It should also be noted that the stress ranges at the crown of these T-joints under cyclic actions are equal to the hot spot stress ranges, i.e. $\Delta\sigma_{hs} = \sigma_{hs,max} - \sigma_{hs,min}$.

- Effects of stress ratios during cyclic tests

Owing to different loading protocols during fatigue tests, it is necessary to modify the stress ranges in these S690 welded T-joints in order to compare their S-N data with R = 0.066 to 0.168 directly with those of coupons of the S690 welded sections with R = -1, i.e. the stress ranges under symmetric cyclic actions. This is readily achieved with the Smith-Watson-

Topper rule (Smith, 1970) as follows:

$$\Delta\sigma_{equ} = \Delta\sigma\sqrt{\frac{2}{1-R}} \tag{4-10}$$

where

$\Delta\sigma_{equ}$ is the equivalent stress range at a stress ratio R = -1;

$\Delta\sigma$ is the stress range adopted in a fatigue test with a stress ratio R; and

R is the stress ratio adopted in the fatigue test, $\frac{\sigma_{min}}{\sigma_{max}}$.

In the presence of welding-induced residual stresses σ_{res} , and the effects of stress concentration and stress ratios, the equivalent stress ranges $\Delta\sigma_{equ}$ of the S690 welded T-joints, after considering Equations (4-7) to (4-10), are given by:

$$\Delta\sigma_{equ} = \Delta\sigma_{hs}\sqrt{\frac{2}{1-\frac{\sigma_{res}+\sigma_{hs,min}}{\sigma_{res}+\sigma_{hs,max}}}} \tag{4-11}$$

After incorporating all these stresses discussed above, all the S-N data of the S690 welded T-joints have been modified with an increase in the stress values, and these modified S-N data are plotted in **Figure 4.22** together with the $(S\text{-}N)_c$ of the S690 welded sections.

It is found that the S_{equ}-N data of the S690 welded T-joints lie close to those of the S690 welded sections, and they all lie above the $(S\text{-}N)_c$ curve of the S690 welded sections. Consequently, it is demonstrated that the $(S\text{-}N)_c$ curve of the S690 welded sections may be adopted to assess the fatigue performance of these S690 welded T-joints.

It should be noted that the stress conditions and the welded details between the welded sections and the welded joints are different. While welding-induced residual stresses exist in all welded members and joints, and their magnitudes are large which may significantly increase their initial stresses without any applied loads. Hence, it is aimed to present the experimental investigation into fatigue behaviour of S690 welded joints, and to establish an assessment approach to relate the S-N data of large scale welded joints with those of the S-N data of small coupons of welded sections. Although there are some limitations of this approach for fatigue life prediction, and also only a limited number of fatigue tests conducted in the present research, the finding is considered to be very important as it highlights a possibility to adopt $(S\text{-}N)_c$ curves obtained in the fatigue tests on coupons of the welded sections to be used in assessing the fatigue performance of the welded T-joints after consideration of various stress effects.

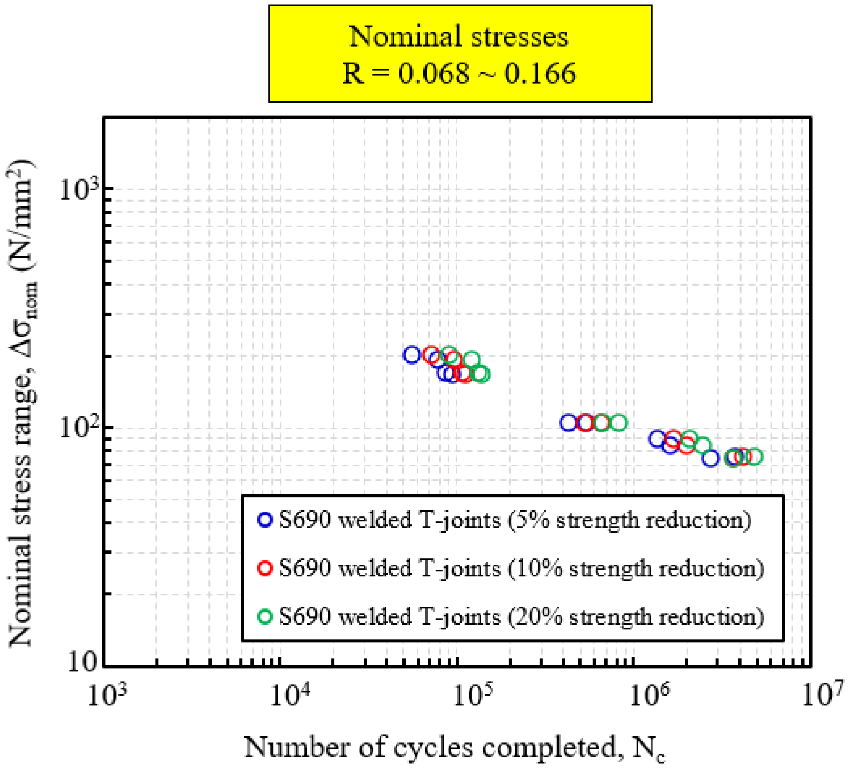

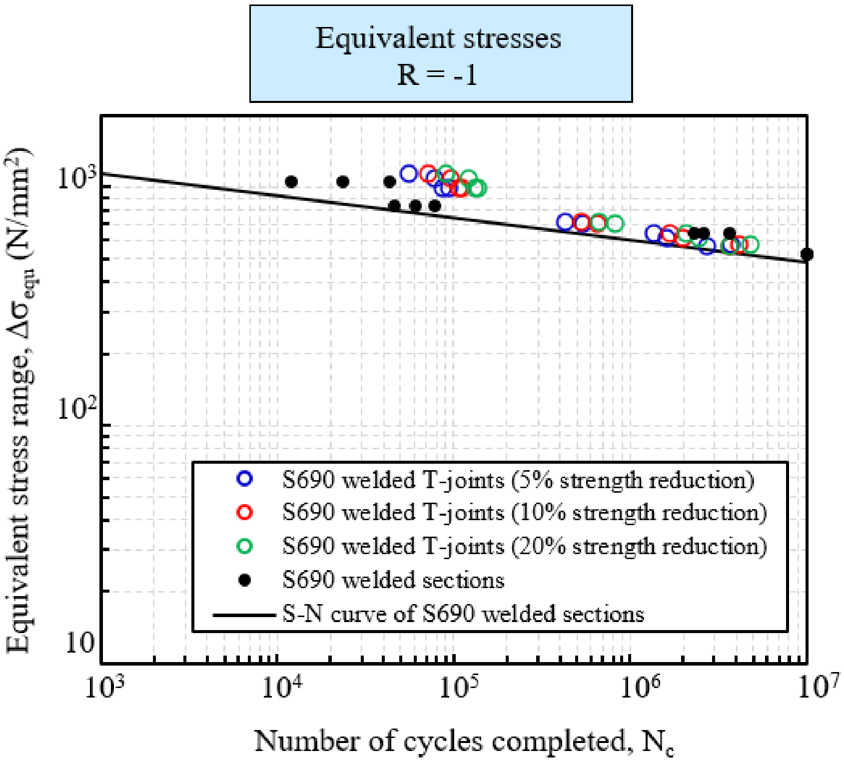

Figure 4.22 Comparison with (S-N)c and (S-N)j

4.7 Conclusions

This Chapter presents a comprehensive experimental investigation into the fatigue behaviour of welded T-joints between high strength S690 circular hollow sections under cyclic in-plane bending actions. A total of 10 fatigue tests were carried out on the S690 welded T-joints over a wide range from 1×10^4 to 5×10^6 cycles through ***displacement control***, and five different target displacements were selected. With proper instrumentation, the deformation characteristics of these welded T-joints in terms of reductions in strength and stiffness, and surface crack propagation were captured, and careful data analyses on their *strength and stiffness degradation* against the numbers of cycles were obtained. Through a comprehensive data analysis of the experimental results, key findings are:

- The deformation characteristics, i.e. degradation in strength and stiffness, and propagation of surface cracks, of the S690 welded T-joints under cyclic actions are carefully examined. These results provide important data for assessment on the residual fatigue life of these T-joints, once their degradation in strength and stiffness are known.

- Depending on the magnitudes of the target displacements, a 5% reduction in the resistances of these welded T-joints only happened after completion of 60 to 80 % of the number of the cycles to fatigue failure. There are always at least 10 to 20% more cycles to be completed with significant crack propagation before the end of the fatigue tests.

- The stress concentration factor SCF of these S690 welded T-joints is found to be 2.84 which is significantly smaller than the recommended value of 3.66 given in CIDECT-8.

- All the S_{nom}-N data of the S690 welded T-joints are found to lie above the design S_{nom}-N curve given in EN 1993-1-9. Hence, the design S_{nom}-N curve may be modified with an appropriate increase in the limiting stress range $\Delta\sigma_{lim}$ by a factor of 1.3 for fatigue assessment on these welded T-joints.

- Similarly, all the S_{hs}-N data of the S690 welded T-joints are also found to lie above both the design S_{hs}-N curves given in CIDECT-8 and API RP 2A-WSD. Hence, the design S_{hs}-N curves may be modified with an appropriate increase in the limiting stress range $\Delta\sigma_{lim}$ by a factor of 1.5 for CIDECT, and 1.8 for API for fatigue assessment on these welded T-joints.

- With the considerations on the presence of welding-induced residual stresses, effects of stress concentration due to geometry, and different stress ratios during fatigue tests, the $(S\text{-}N)_c$ curve of coupons of the S690 welded sections developed previously by the authors is demonstrated to be able to predict the fatigue life of these S690 welded T-joints over a practical range of cyclic actions.

In general, an important set of S-N data on the fatigue life of these S690 welded T-joints have been obtained through a comprehensive experimental investigation, and these data have been used to validate applicability of current codified design S-N curves in fatigue assessment of these welded T-joints.

Chapter 5 Local stresses of S690 welded T-joints under in-plane bending

5.1 Introduction

This Chapter presents a rational experimental and numerical investigation into critical local stresses present within the welded T-joints between high strength S690 circular hollow sections (CHS) under the effects of stress concentration. Improvement to existing design formula for determination of stress concentration factors was also presented.

Moreover, based on an advanced coupled thermomechanical modelling approach, the welding-induced residual stresses in the vicinity of the brace / chord junctions were predicted with a high level of accuracy. The 'stress and strain' conditions of the weld toes at the crowns of these T-joints were examined in details. The following works were carried out:

Task 1 – Experimental investigation

A total of 10 welded T-joint between S690 CHS under monotonic actions of in-plane bending were carried out. The loads were applied laterally onto the brace ends of these T-joints within their elastic linear stages, and the hot spot stresses σ_{hs} at the crowns were derived from measured strain gradients in the vicinity of the brace / chord junctions with suitable instrumentation. The corresponding stress concentration factors (SCF) of these T-joints were then obtained, and these data were adopted for subsequent calibration of the finite element models developed in Task 2.

Task 2 – Numerical investigation

In order to examine the effects of stress concentration, an advanced finite element model (FEM) using solid elements was established to predict local stresses in the vicinity of the welded toes of these 10 T-joints between S690 CHS with highly refined meshes.

After a careful calibration against test data, a comprehensive parametric study on a total of 96 welded T-joints was conducted to provide data for determination of the stress concentration factors (SCF). Modification to the SCF formula recommended in CIDECT-8 (Zhao *et al.*, 2001) was proposed for these T-joints of a wide range of cross-sectional dimensions under in-plane bending.

Task 3 – Examination on critical local stresses

An advanced coupled thermomechanical modelling approach was employed to predict critical local stresses in the vicinity of the brace / chord junctions of these T-joints under the effects of stress concentration and the presence of welding-induced residual stresses. Thus, the '*stress and strain*' conditions at the crowns of these T-joints were examined in details.

5.2 Experimental investigation

5.2.1 Test programme

Table 5.1 summarizes the test programme of the welded T-joints between S690 CHS under monotonic in-plane bending, and typical configuration of these T-joints is shown in **Figure 5.1**. A total of 10 S690 welded T-joints with braces and chords of different dimensions were designed with a wide range of geometric parameters, i.e. brace-to-chord diameter ratio, d_1 / d_o or β , and diameter to thickness ratio of chord, d_o / t_o or 2γ , in order to correlate the SCF with their geometric changes.

It should be noted that these T-joints were tested under monotonic actions of in-plane bending up to failure, but a proper instrumentation was provided to these T-joints to enable measurements of local strains in the vicinity of the crowns of the chords according to established methods given in CIDECT. Only the test results of these T-joints within the linear elastic deformation stages are detailly reported and analysed in this Chapter.

According to the designed dimensions of these S690 CHS, both 8 and 10 mm thick S690 steel plates were cut into pre-determined sizes for transverse cold-bending and then longitudinal welding to form both the braces and the chords of the T-joints. The heat input energy q during welding of all these S690 CHS and their welded T-joints was carefully controlled by a qualified welder to be not larger than 1.5 kJ/mm. **Table 5.2** summarizes the measured dimensions of both the braces and the chords, and also the measured weld sizes at both the crowns and the saddles of the brace / chord junctions.

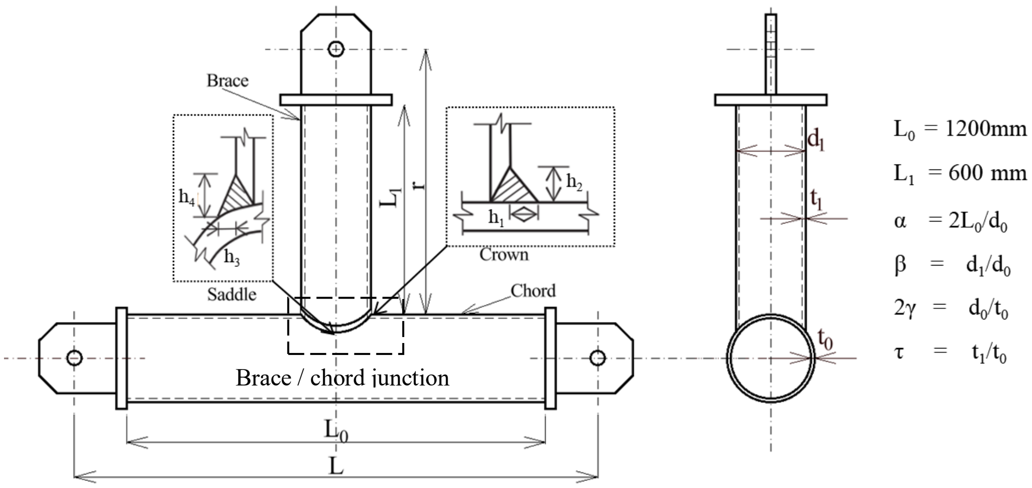

Figure 5.1 Configuration of typical welded T-joints between S690 CHS

Table 5.1 Test programme of S690 welded T-joints

In-plane bending tests and measurements for SCF

Joints	Chord $d_0 \times t_0$ (mm × mm)	Brace $d_1 \times t_1$ (mm × mm)	β	2γ	τ	l_r (mm)
T-1a		150×8	0.60			
T-1b	250×8	200×8	0.80	31.2	1.0	760
T-1c		225×8	0.90			
T-2a		150×10	0.60			
T-2b	250×10	200×10	0.80	25.0	1.0	760
T-2c		225×10	0.90			
T-3a		150×10	0.50			
T-3b	300×10	200×10	0.67	30.0	1.0	735
T-3c		250×10	0.83			
T-3d		275×10	0.92			

Table 5.2 Measured dimensions and properties of S690 welded T-joints

Joints	Chord				Brace				Crown		Saddle	
	L_0 (mm)	d_0 (mm)	t_0 (mm)	$W_{el,0}$ (10^3 mm^3)	L_1 (mm)	d_1 (mm)	t_1 (mm)	$W_{el,1}$ (10^3 mm^3)	h_1 (mm)	h_2 (mm)	h_3 (mm)	h_4 (mm)
T-1a	1,200	250.8	8.1	363.0	598	150.6	8.1	122.6	8.2	9.2	5.3	14.2
T-1b	1,202	249.9	8.0	356.3	600	200.5	8.1	226.4	10.3	11.5	5.2	16.0
T-1c	1,200	250.3	8.2	365.5	598	225.7	8.0	287.6	9.7	13.7	3.3	21.0
T-2a	1,200	251.4	9.8	432.5	598	151.8	9.9	147.1	8.5	11.0	4.5	13.7
T-2b	1,200	250.7	10.0	437.6	598	200.4	10.0	271.3	8.8	9.5	5.0	18.2
T-2c	1,200	250.2	10.0	435.8	600	225.0	9.8	341.6	9.7	10.3	2.3	20.2
T-3a	1,200	299.7	10.0	638.0	599	151.4	9.9	146.2	8.3	11.2	4.5	14.3
T-3b	1,201	300.5	10.0	641.5	599	200.1	10.0	270.4	10.0	12.8	3.5	16.8
T-3c	1,201	300.7	10.0	642.4	600	250.3	10.0	436.2	7.3	10.0	2.2	14.8
T-3d	1,201	300.9	9.9	637.5	600	274.8	9.9	526.7	8.3	10.0	1.5	18.5

As shown in **Figure 5.2**, a total of 9 curved coupons were extracted from these S690 CHS. Standard tensile tests were then conducted on these curved coupons to obtain their full range stress-strain curves. Typical test set-up is illustrated in **Figure 4.4** in Chapter 4.2, and both the extensometer and the digital photo analyses were adopted to measure elongations of these coupons during tests. The measured stress-strain curves of these curved coupons are plotted in **Figure 5.3**, and their key mechanical properties are summarized in **Table 5.3**.

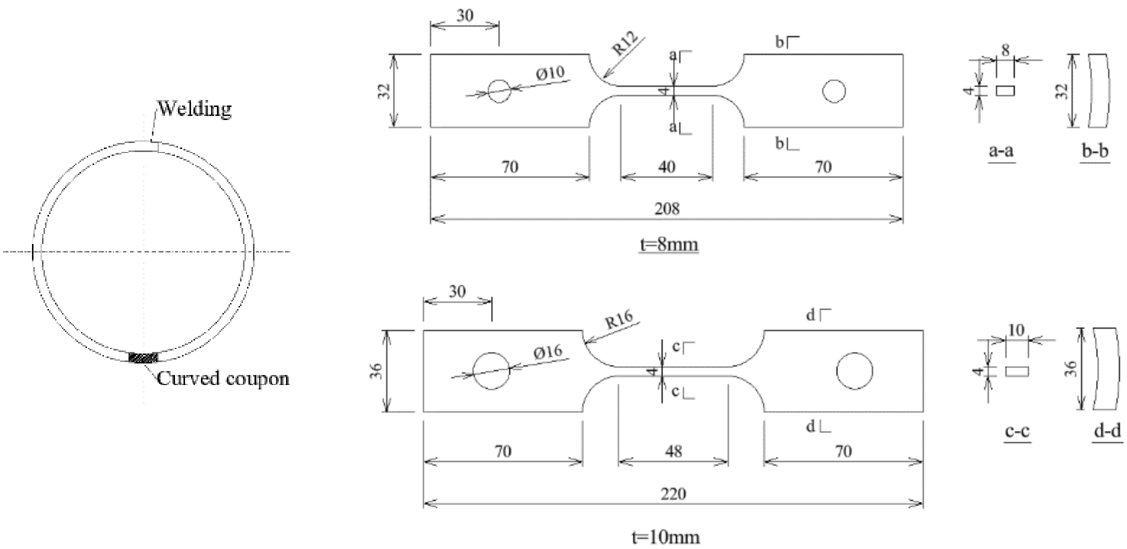

Figure 5.2 Dimension and geometry of curved coupons

Table 5.3 Key mechanical properties of curved coupons

Thickness (mm)	Measured thickness t (mm)	Young's modulus E (kN/mm^2)	Yield strength f_y (N/mm^2)	Tensile strength f_u (N/mm^2)	Elongation at fracture ε_L (%)
8	7.74	203	776	875	13.1
10	9.93	195	730	837	12.8

Note: All data are averaged values of 9 values.

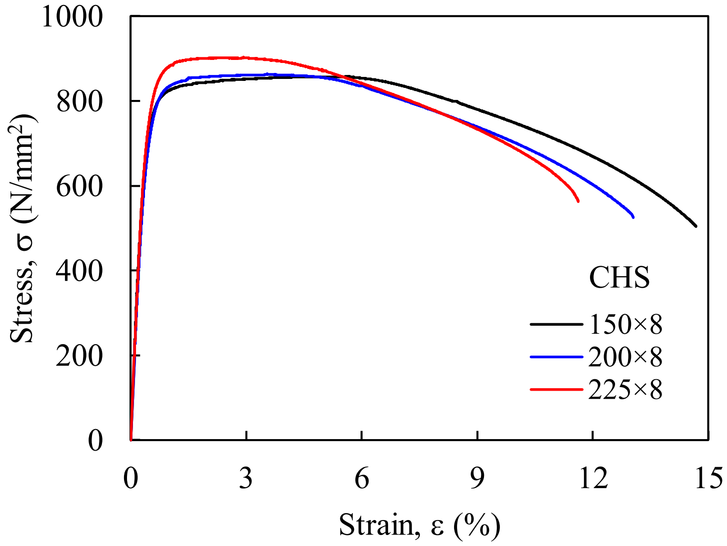

a) 8 mm thick curved coupons

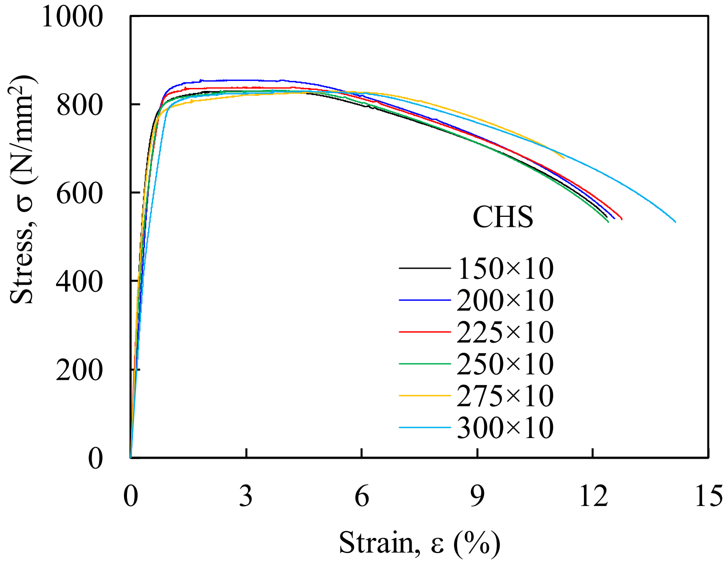

b) 10 mm thick curved coupons

Figure 5.3 Measured stress-strain curves of curved coupons extracted from S690 CHS

5.2.2 Test set-up and instrumentation

Figure 5.4 illustrates typical set-up of welded T-joints between S690 CHS under monotonic actions of in-plane bending. These T-joints were supported at both ends of the chords through pins while lateral loads were applied horizontally at the top ends of the braces with the use of a 500 kN hydraulic jack through a pinned connection. A total of 10 linear variation displacement transducers (LVDT) were employed to measure deformations of various parts of the T-joints throughout the tests.

In order to examine the effect of stress concentration in the vicinity of the brace / chord junctions of the T-joints, strain gauges were provided in the vicinity of the crown of the chord as shown in **Figure 5.4** according to CIDECT-8. The strain gauges should be located within an extrapolation region within a distance of 0.4 t_o to $0.4\sqrt[0.4]{r_0 t_0 r_1 t_1}$ from the weld toes in order to eliminate any local geometrical effect induced by the welds. Hence, two measurement stations, namely, S04 and S10, were set to be at 4 and 10 mm away the weld toes of the crowns of all these T-joints, and strain gauges SG1 & SG2 were installed carefully at these stations for strain measurements.

It should be noted that an advanced measurement method of digital image correlation was DIC adopted to determine local strain fields for Joints T-1c, T-2c and T-3d as shown in **Figure 5.5**.

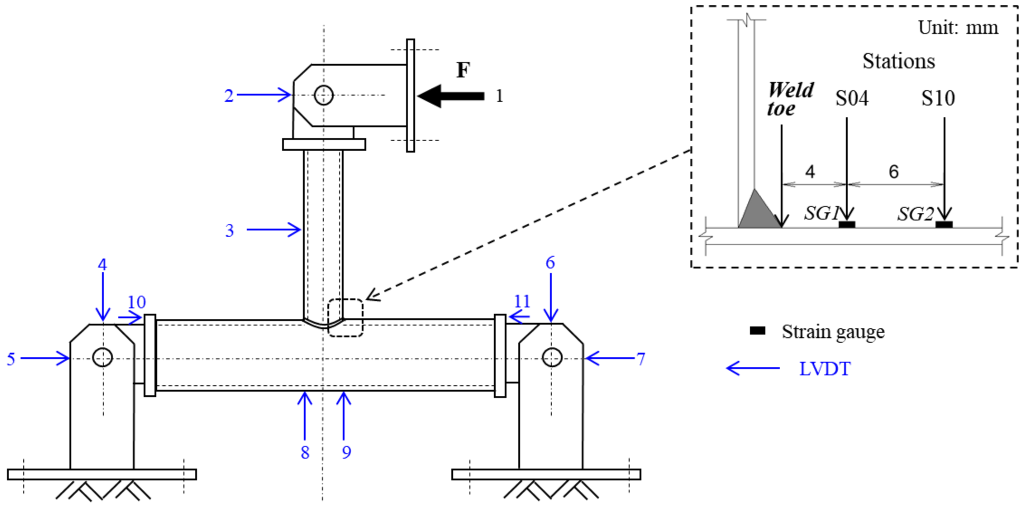

Figure 5.4 Typical set-up of welded T-joints between S690 CHS under monotonic actions of in-plane bending

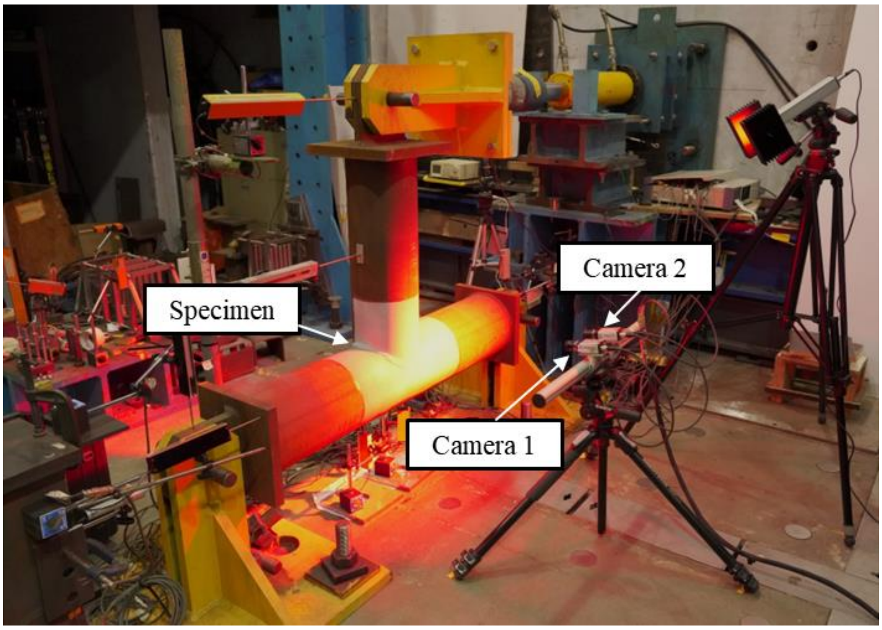

Figure 5.5 DIC system for strain measurement

For each T-joint, the following loading procedure was adopted:

a) The T-joint was carefully installed and aligned, and then a pre-loading procedure was performed at least 3 times to eliminate any initial bedding between the T-joint and the supports. The pre-loading procedure was conducted by applying a lateral load to the top end of the brace through displacement control so that the maximum displacement of the brace end was 2.0 mm.

b) During testing, a lateral load F was applied to the top end of the brace through displacement control at a rate of 0.2 mm / minute from the initial stage, i.e. Stage e0 , to four different deformation stages, i.e. Stages e_2, e_4, e_6 and e_8 with displacement δ = 2.0, 4.0, 6.0 and 8.0 mm respectively. After reaching each of these deformation stages, the lateral load F was held for at least 1 minute, and then, the applied load was measured through a load cell and data from LVDT and strain gauges were then acquired and stored electronically for subsequent analysis.

5.2.3 Test results

All the welded T-joints between S690 CHS were tested successfully. **Figure 5.6** illustrates typical failure mode of these T-joints under in-plane bending, gross deformations in both the brace section and the brace-chord junction of the T-joint were found to be apparent before failure. **Figure 5.7** present the deformed shape and the fractured parts of all these T-joints up to failure, and it is evident that all these S690 welded T-joints performed gross deformations under in-plane bending actions. The failure modes of these S690 welded T-joints are determined to be a punching shear fracture in the vicinity of the weld of chord sections after gross plastic deformations.

Figure 5.8 presents the deformation characteristics of these T-joints up to failure while **Figure 5.9** plots typical data of these T-joints within the linear elastic deformation stages, namely Stages e_o to e_8 . Key test data within the linear elastic deformation stages are presented in **Figure 5.9**.

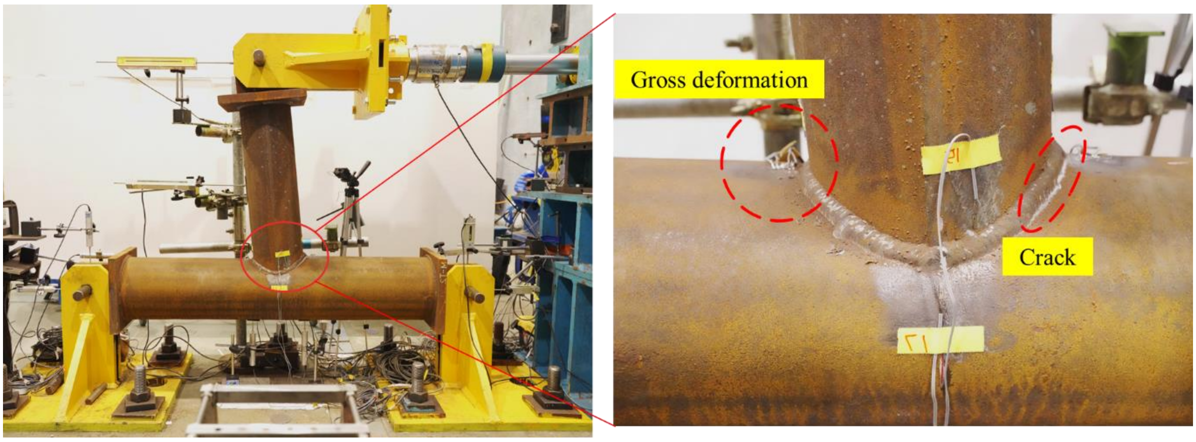

Figure 5.6 Typical failure mode of S690 welded T-joints under in-plane bending

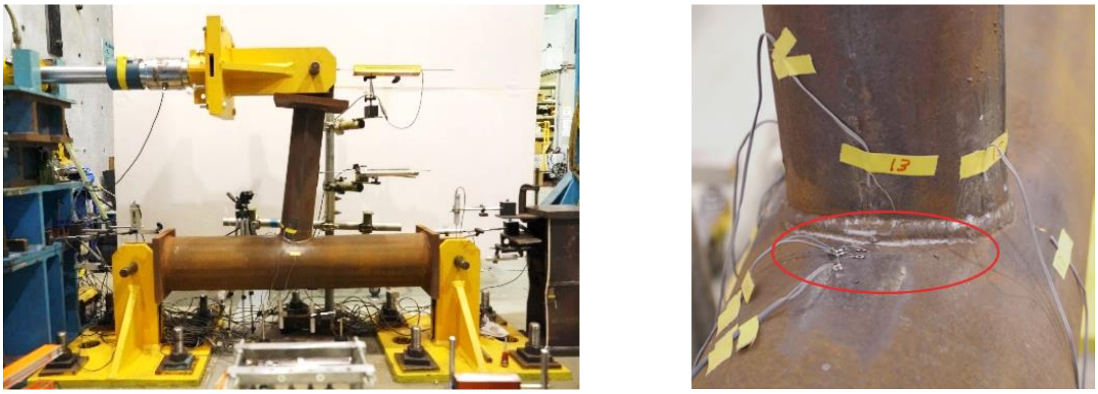

T-1a

T-1b

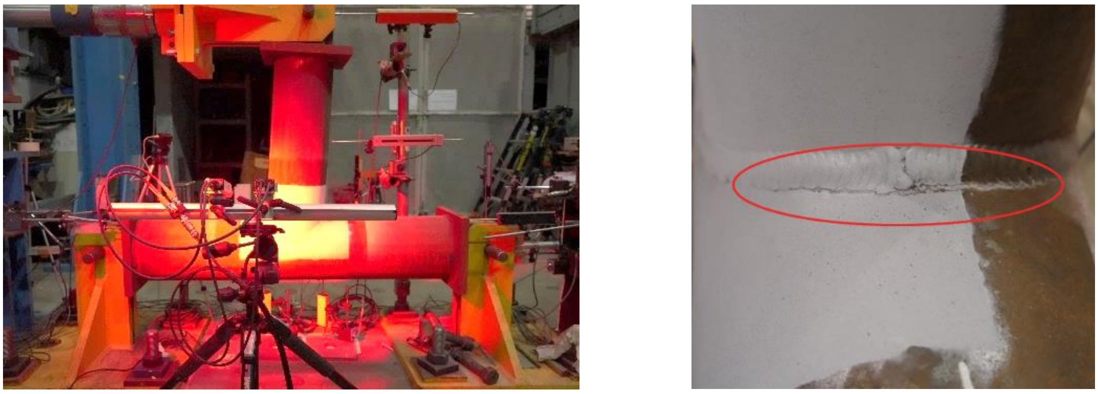

T-1c

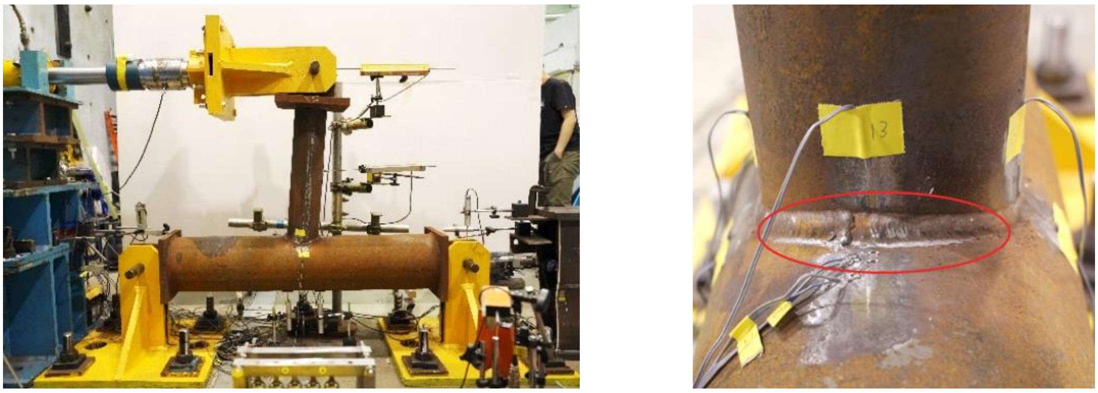

T-2a

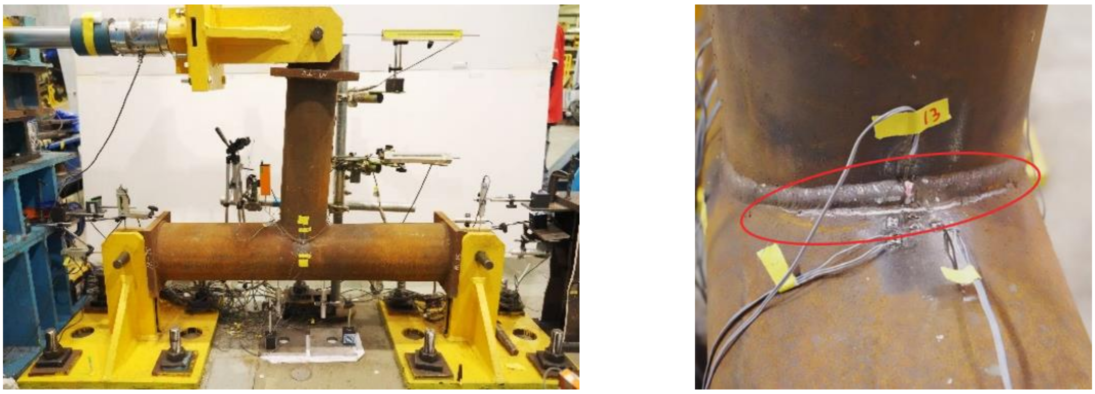

T-2b

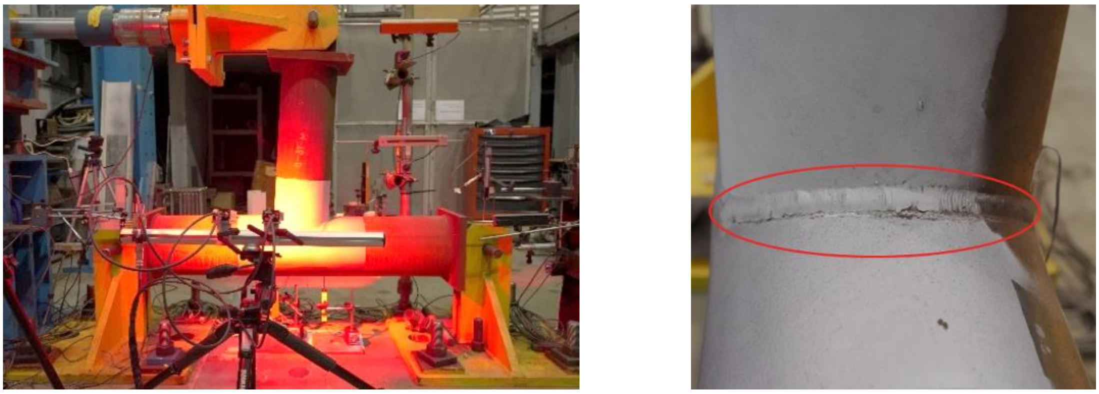

T-2c

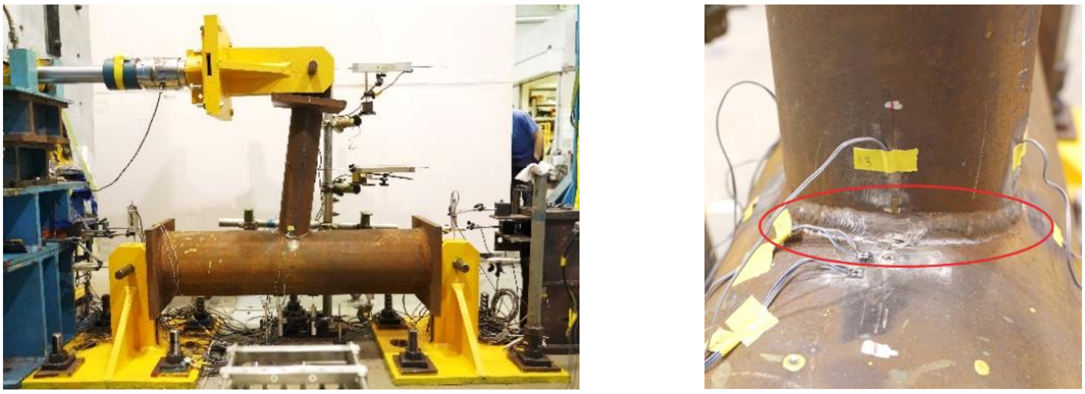

T-3a

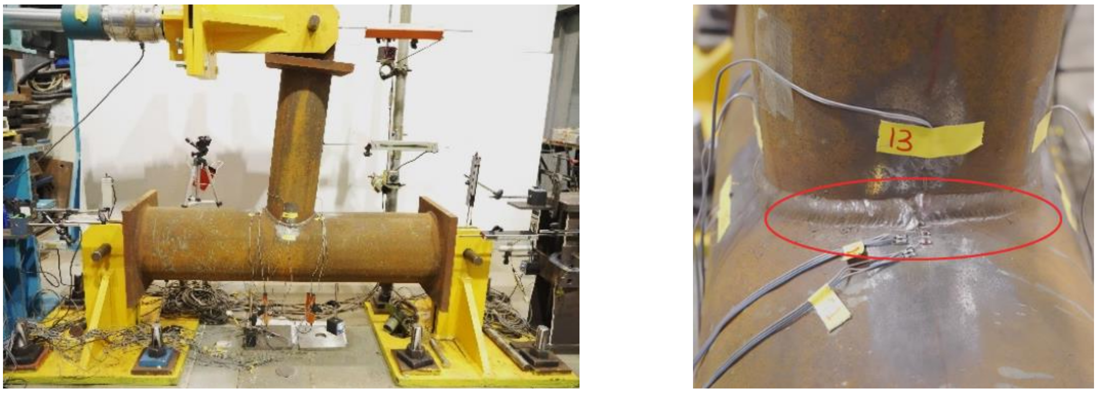

T-3b

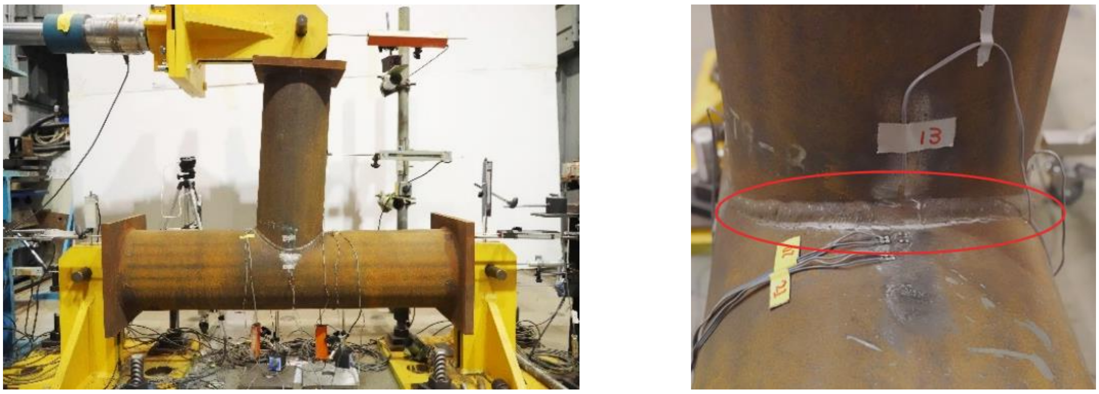

T-3c

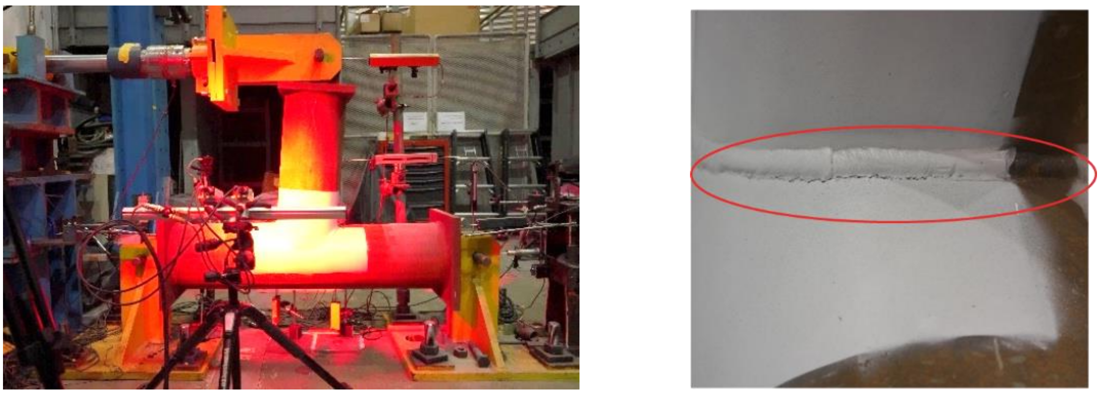

T-3d

Figure 5.7 Failure mode of T-joints between S690 CFCHS under in-plane bending

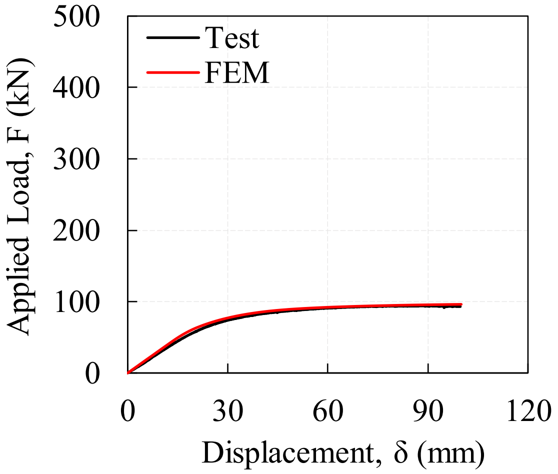

T-1a

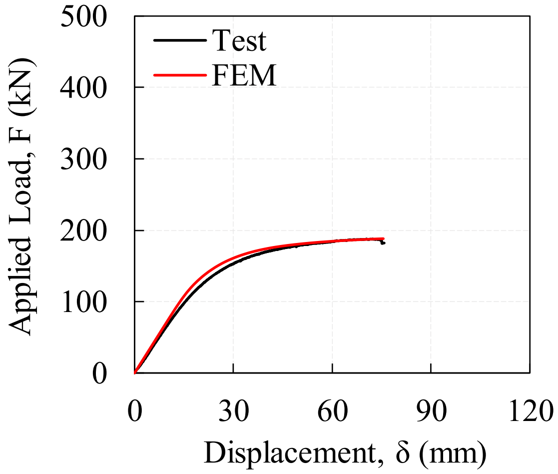

T-1b

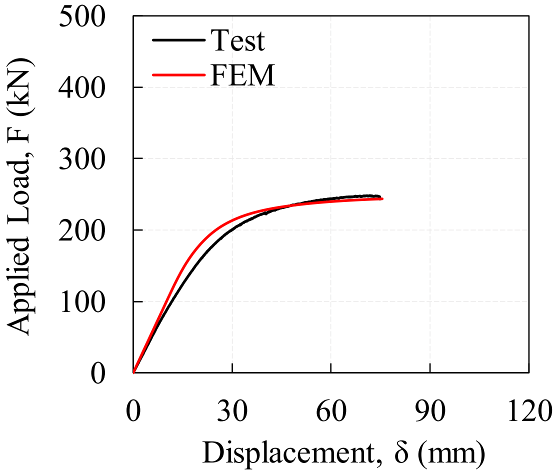

T-1c

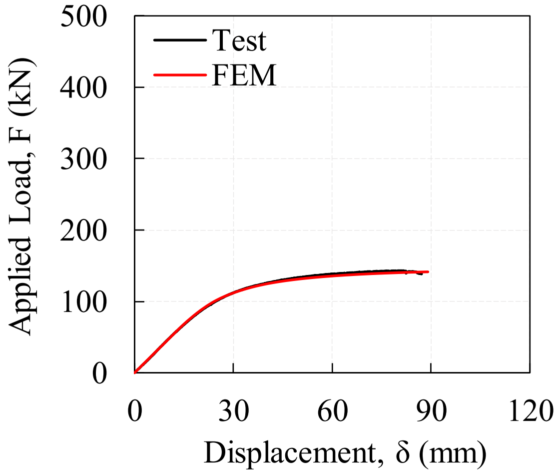

T-2a

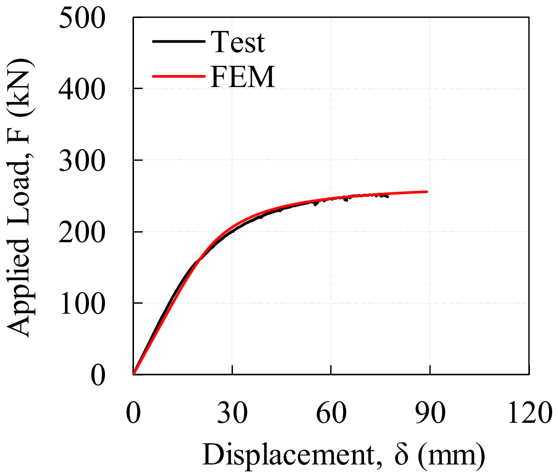

T-2b

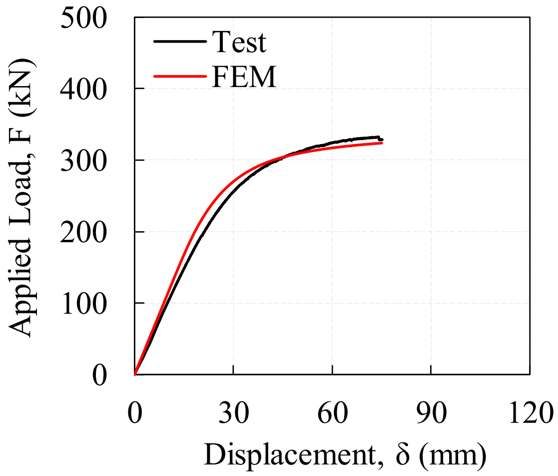

T-2c

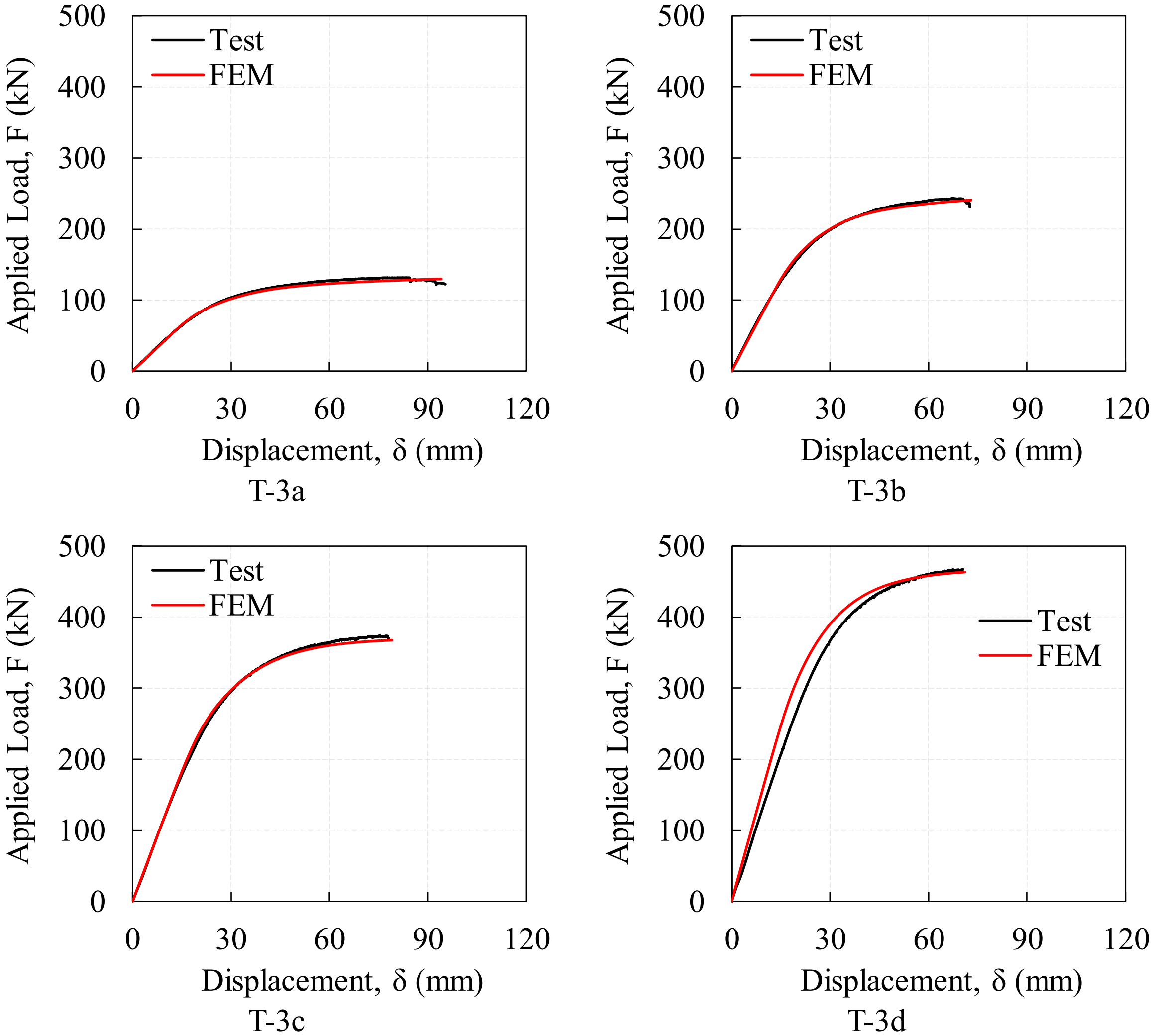

Figure 5.8 Load-displacement (F-δ) curves of various T-joints

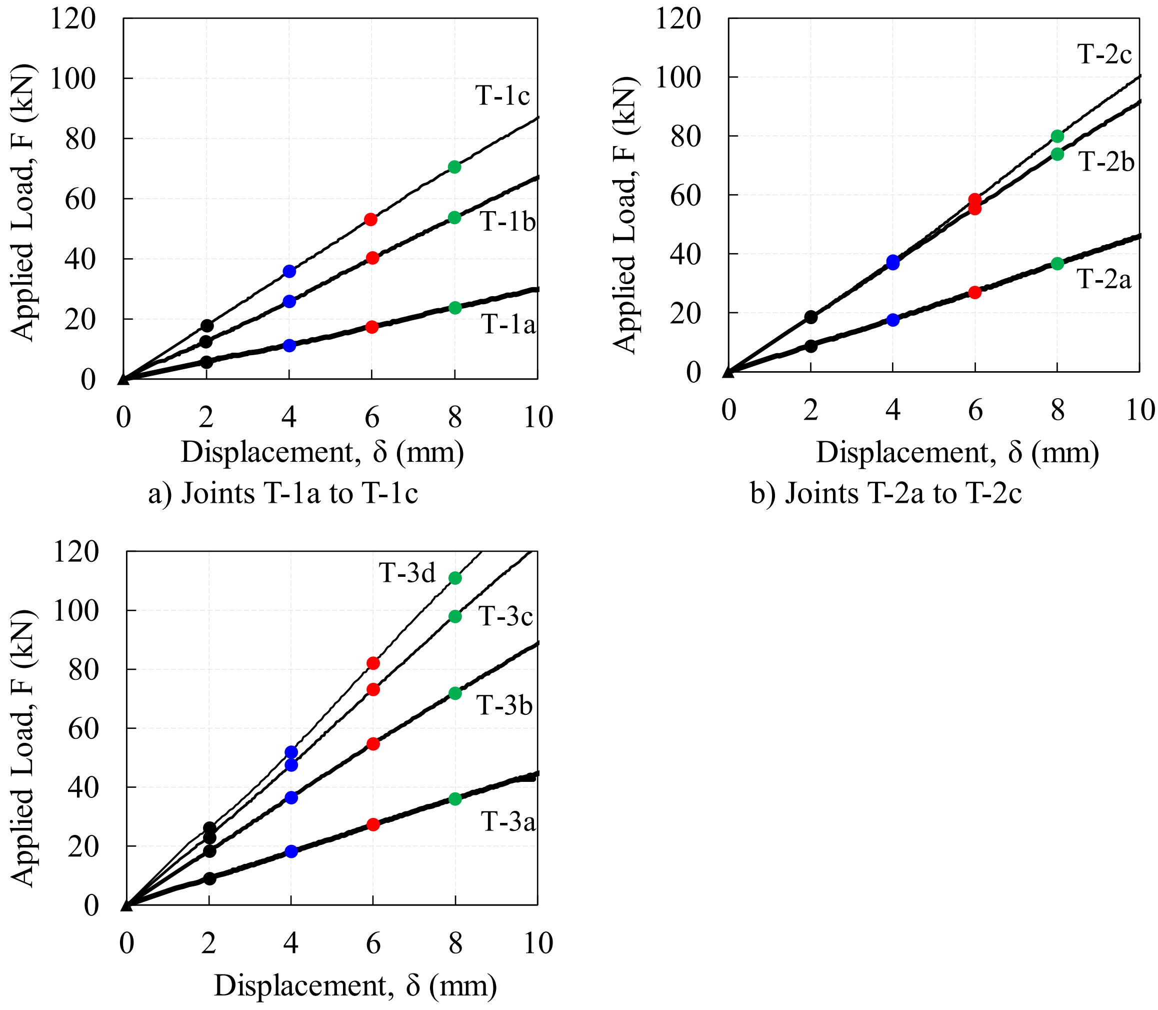

a) Joints T-1a to T-1c

b) Joints T-2a to T-2c

c) Joints T-3a to T-3c

Figure 5.9 Load-displacement (F-δ) curves of various T-joints within linear elastic range

- ***Determination of SCF***

According to CIDECT-8, the hot spot stress σ_{hs} at the crown of the chord for a T-joint between CHS is readily determined from those strains measured by strain gauges SG1 and SG2 installed at Stations S04 and S10 respectively through linear extrapolation, and hence, the hot spot stress σ_{hs} is given by:

$$\sigma_{hs} = 1.2\, E \times \left(\frac{5}{3} \varepsilon_{\mathrm{i}} - \frac{2}{3} \varepsilon_{ii} \right) \tag{5-1a}$$

where

E is the Young's modulus of the steel;

ε_i & ε_{ii} are the measured strains at Stations S04 and S10 respectively.

For ease of presentation, the test results of Joint T-2b are adopted for illustration as a representative to all the welded T-joints. While **Figure 5.10a)** plots the linear elastic deformations of Joint T-2b under in-plane bending, i.e. Stages e_0, e_2, e_4, e_6 and e_8 , **Figure 5.10b)** plots the corresponding hot spot stresses σ_{hs} derived from the measured strains ε_i and ε_{ii} at the four different deformation stages.

The hot spot stresses σ_{hs} corresponding to Stages e_6 and e_8 are found to be 447.7 and 600.9 N/mm^2, i.e. 65% and 87% of the nominal yield strength of the S690 steel, despite the applied loads are less than 30% of the expected failure load of the joint. As shown in **Table 5.4**, similar observations are also found in other T-joints of the present study.

Furthermore, based on the simple beam theory, the nominal stress σ_{nom} of the T-joint is given by:

$$\sigma_{nom} = \frac{M}{W_{el}} \tag{5-1b}$$

where

M is the applied moment at the brace / chord junction; and

W_{el} is the elastic section modulus of either the brace or the chord, whichever is smaller.

Through the use of Eq. 5-1a) and 5-1b), the stress concentration factor SCF_T obtained from the measured data ε_i and ε_{ii} is given by:

$$SCF_T = \frac{\sigma_{hs}}{\sigma_{nom}} \tag{5-1c}$$

The values of the hot spot stresses σ_{hs} , the nominal stresses σ_{nom} , and the corresponding SCF_T are also summarized in **Table 5.4** for various deformation stages. It is evident that the values of the SCF_T of each of the T-joints at various stages are very close to another, and hence, their average values are readily adopted for further analyses.

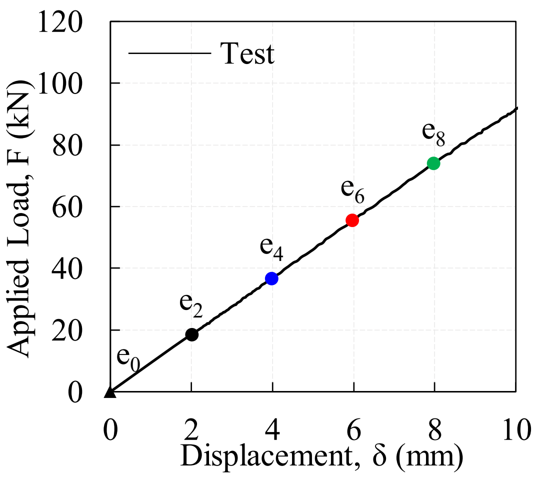

a) Load-displacement (F-δ) curve

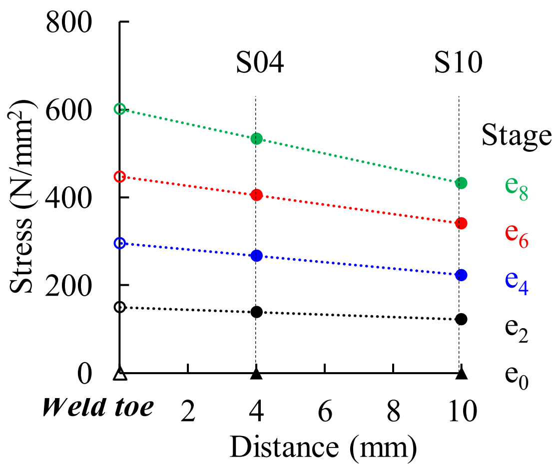

b) Hot spot stresses, σ_{hs}

Figure 5.10 Linear elastic deformations of typical joint under in-plane bending. Joint T-2b.

Table 5.4 Key test data of welded T-joints within linear elastic deformations

Joints	Deformation Stages	Applied load F (kN)	Measured strains ($\times 10^{-6}$) at Stations S04	S10	Nominal stress σ_{nom} (N/mm^2)	Hot spot stress σ_{hs} (N/mm^2)	$SCF_T = \frac{\sigma_{hs}}{\sigma_{nom}}$	Average SCF_T
T-1a	e_2	5.76	401	301	35.7	113.8	3.19	***3.17***
	e_4	11.21	772	578	69.5	219.7	3.16	
	e_6	17.27	1,189	889	107.0	338.4	3.16	
	e_8	23.63	1,631	1,212	146.4	465.6	3.18	
T-1b	e_2	12.73	407	196	42.7	133.5	3.12	***3.14***
	e_4	25.76	818	372	86.5	271.8	3.14	
	e_6	40.30	1,273	566	135.3	425.1	3.14	
	e_8	53.63	1,685	732	180.0	565.2	3.14	
T-1c	e_2	17.88	514	389	47.2	145.6	3.08	***3.07***
	e_4	35.75	1,028	776	94.5	291.3	3.08	
	e_6	53.63	1,531	1,153	141.7	434.2	3.06	
	e_8	70.60	2,009	1,510	186.6	570.5	3.06	
T-2a	e_2	8.79	422	132	45.4	143.9	3.17	***3.15***
	e_4	17.88	841	236	92.4	291.2	3.15	
	e_6	27.27	1,272	337	140.9	443.4	3.15	
	e_8	36.97	1,715	434	191.1	601.2	3.15	
T-2b	e_2	18.48	593	522	51.8	149.7	2.88	***2.88***
	e_4	36.66	1,141	956	102.7	295.8	2.87	
	e_6	55.45	1,730	1,456	155.4	447.7	2.87	
	e_8	73.93	2,280	1,849	207.1	600.9	2.89	
T-2c	e_2	27.88	656	526	62.0	173.8	2.80	***2.80***
	e_4	37.57	885	714	83.6	233.9	2.80	
	e_6	47.57	1,120	907	105.8	295.5	2.79	
	e_8	58.48	1,388	1,139	130.1	363.7	2.80	

T-3a	e_2	9.09	504	277	47.2	153.1	3.24	***3.23***
	e_4	18.18	1,005	552	94.5	305.6	3.23	
	e_6	27.27	1,506	828	141.7	458.3	3.23	
	e_8	36.36	1,980	1,037	189.0	610.5	3.23	
T-3b	e_2	18.48	604	458	51.9	164.0	3.16	***3.16***
	e_4	36.36	1,188	903	102.2	322.3	3.15	
	e_6	54.54	1,781	1,354	153.3	483.5	3.15	
	e_8	71.81	2,342	1,777	201.8	636.2	3.15	
T-3c	e_2	23.03	491	436	40.1	123.5	3.08	***3.10***
	e_4	47.57	1,020	903	82.9	256.9	3.10	
	e_6	73.02	1,584	1,407	127.2	398.5	3.13	
	e_8	97.87	2,121	1,879	170.5	534.1	3.13	
T-3d	e_2	26.36	393	253	38.0	113.7	2.99	***3.01***
	e_4	51.81	776	502	74.8	224.4	3.00	
	e_6	82.11	1,230	794	118.5	355.9	3.00	
	e_8	110.90	1,664	1,078	160.0	481.0	3.01	

Note: $\sigma_{nom} = M / W_{el,1}$ where $M = F \times$ level arm, l_r

5.3 Numerical investigation

In order to predict critical local stresses in the vicinity of the brace / chord junctions of the welded T-joints between S690 CHS under in-plane bending, finite element technique was adopted, and full details of finite element modelling of these T-joints are presented as follows:

5.3.1 Finite element modelling

A total of 10 finite element models of the welded T-joints between S690 CHS with solid elements **C3D8R** were established using the general finite element package ABAQUS (ABAQUS, 2020). **Figure 5.11** illustrates typical support and loading conditions, and typical mesh of a finite element model. It should be noted that:

- Material properties

  According to the measured mechanical properties of these S690 CHS, as shown in **Table 5.3**. Young's modulus of the 8 and 10 mm thick S690 CHS are taken to be 203 kN/mm^2 and 195 kN/mm^2 respectively, and the Poisson's ratio of all the CHS is taken to be 0.3. The yield strengths of the 8 and 10 mm thick S690 CHS are taken to be 776 and 730 N/mm^2.

- Boundary conditions

  As shown in **Figure 5.11**, both the support and the loading conditions of the model are consistent with those of the tests, i.e. pinned connections at both ends of the chord while an in-plane lateral load at top end of the brace. Two reference points are set up to couple with the surfaces of the chord ends, and the corresponding boundary conditions are applied at the reference points. Another one reference was set up to couple with the surface of the brace end for applying lateral loads.

- Mesh configurations and sizes

According to relevant numerical investigations conducted by other researcher (Matti and Mashiri, 2020), solid element C3D8R was adopted to establish the models. A number of trial analyses and convergence study were conducted to determine the mesh configuration of these T-joints. The numerical results of Model T-2b are adopted for ease of presentation, a total of 4 different mesh configurations in the brace / chord junctions are adopted: i) 2.0 × 5.0 mm, ii) 1.0 × 5.0 mm, iii) 0.5 × 5.0 mm, and iv) 0.5 × 2.0 mm. The corresponding computational time are 1 hours, 4 hours, 20 hours and 50 hours respectively, and the predicted SCF are 2.89, 2.88, 2.88 and 2.88 respectively. As shown in **Figure 5.11**, the mesh configuration was established as follows after a number of trial analyses and convergence study:

i) typical mesh size in both the braces and the chords ae 5.0 × 5.0 mm;

ii) typical mesh size in the brace / chord junctions is 1.0 × 5.0 mm; and

iii) a total of five layers of solid elements across the thicknesses of both the braces and the chords.

It should be noted that similar to many numerical models reported in the literature, no residual stress is incorporated in the models.

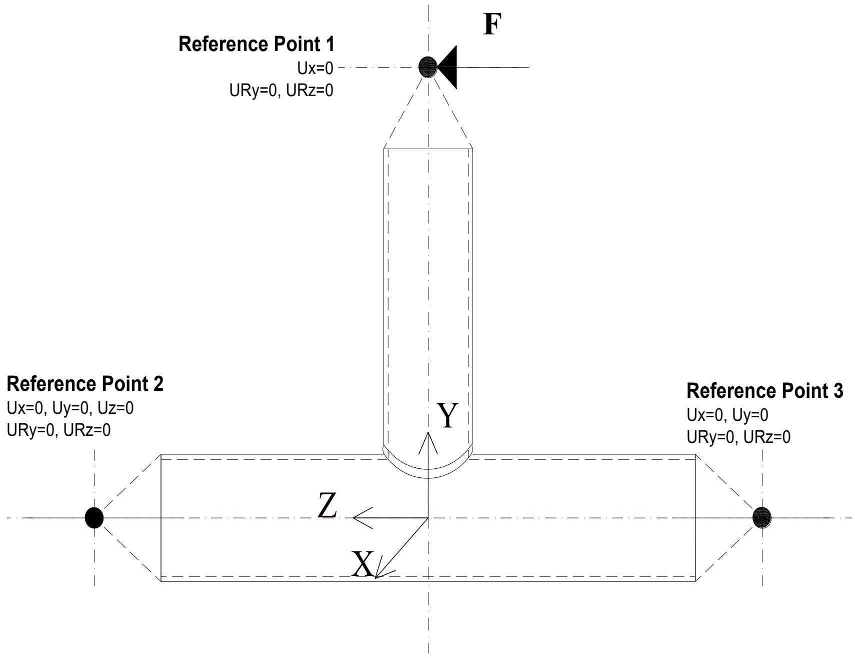

a) Support and loading conditions

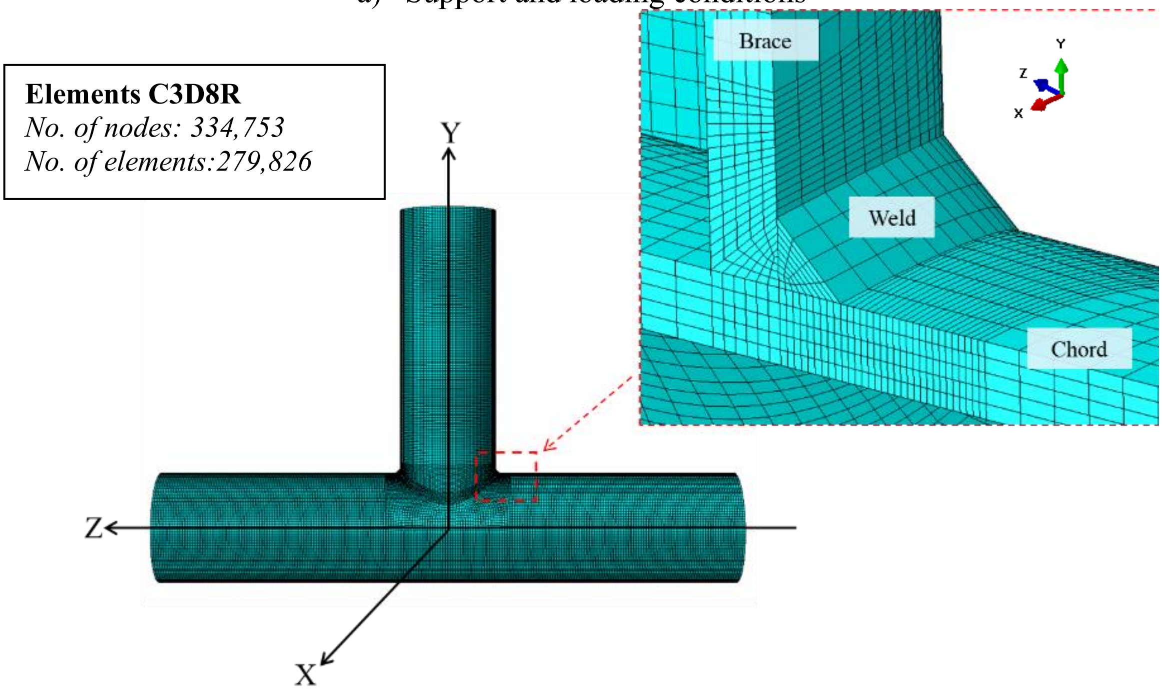

b) Finite element mesh

Figure 5.11 Finite element model of a welded T-joint

5.3.2 Finite element results

Elastic non-linear analyses for these 10 finite element models have been successfully completed, and average time for a non-linear analysis for each model is about 4 hours.

- ***Local stresses***

For ease of discussion, the numerical results of Model T-2b are plotted in **Figure 5.12**. It is shown that the predicted displacements δ follow closely to those measured values at various stages, i.e. Stages e_2 to e_8 . Moreover, the predicted longitudinal stresses at Stations S04 and S10 of the chord are found to be in a good agreement with the corresponding measured values at various stages, as shown in **Figure 5.12b)**. However, the predicted critical local stresses σ_{wt} at the weld toe are significantly larger than those hot spot stress σ_{hs} obtained from Eq. 5-1a) to 5-1c). A comparison on these stresses is summarized in **Table 5.5**, and the ratios σ_{wt} / σ_{hs} are found to range from 1.17 to 1.30 with an average value of 1.22.

Various stress distributions of Model T-2b at Stage e_8 under applied load F, i.e. mechanical stresses, are plotted in **Figure 5.13**, and these are a) von Mises stresses, b) Principal stress S11, c) Principal stress S22, and d) Principal stress S33. It is evident that in the absence of any residual stress in the model, large longitudinal stresses along the chord, i.e. S33, at a value of 725.8 N/mm^2, are induced in the vicinity of the weld toe of the brace / chord junction of the welded T-joint under in-plane bending. These stress distributions are considered as reference data for subsequent comparison described in Chapter 5.4.

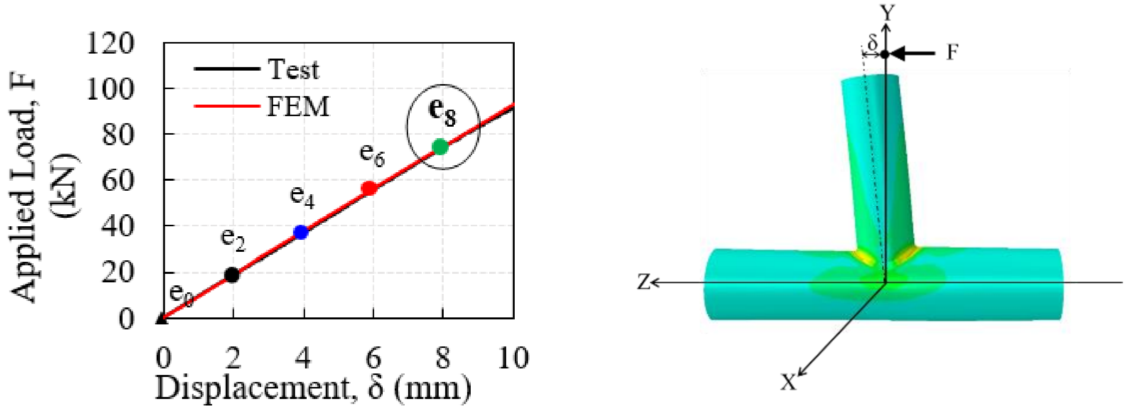

a) Load-displacement (F-δ) curve

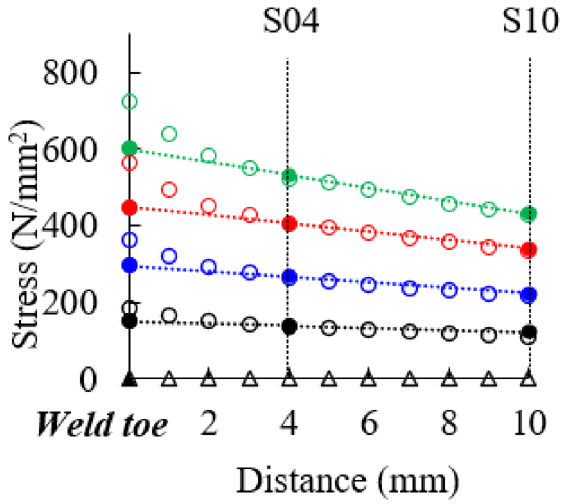

b) Longitudinal stresses of the chord due to applied loads only.

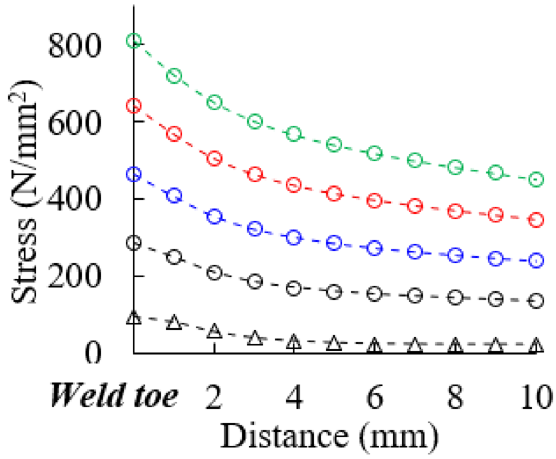

c) Longitudinal stresses of the chord due to applied loads and welding-induced residual stresses.

Principal stresses S33

Principal stresses S33

Figure 5.12 Predicted local stresses at Stations S04 and S10 near the weld toe of Joint T-2b

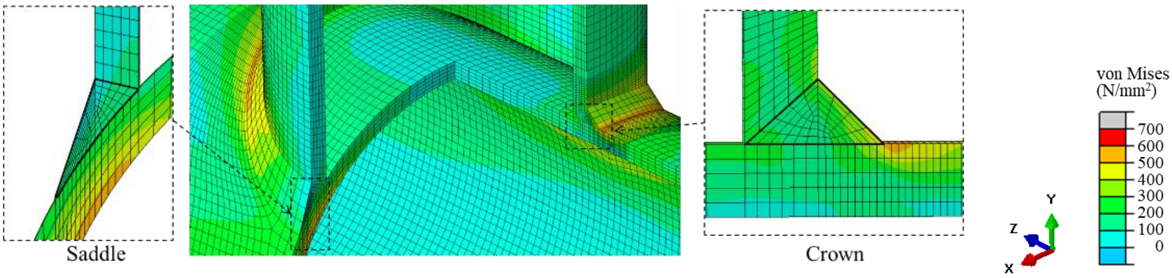

a) von Mises stresses – mechanical stress

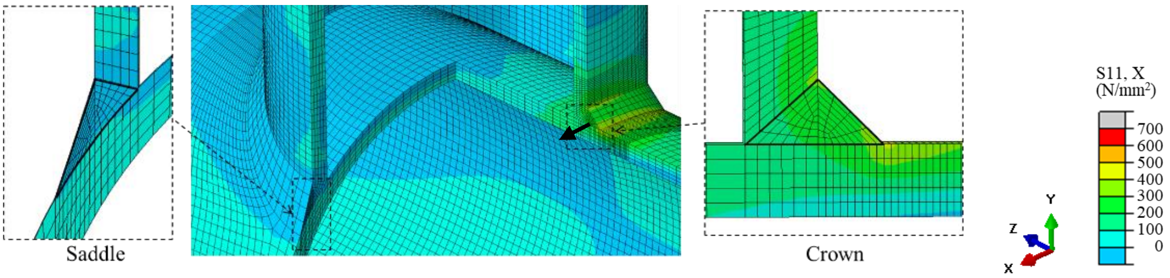

b) Principal stresses S11 – mechanical stress

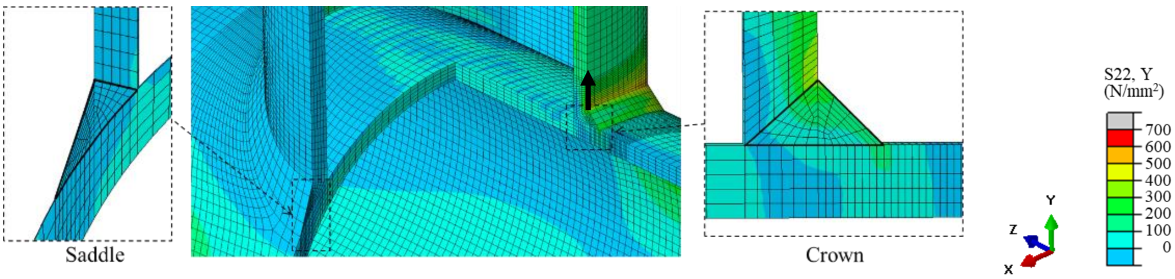

c) Principal stresses S22 – mechanical stress

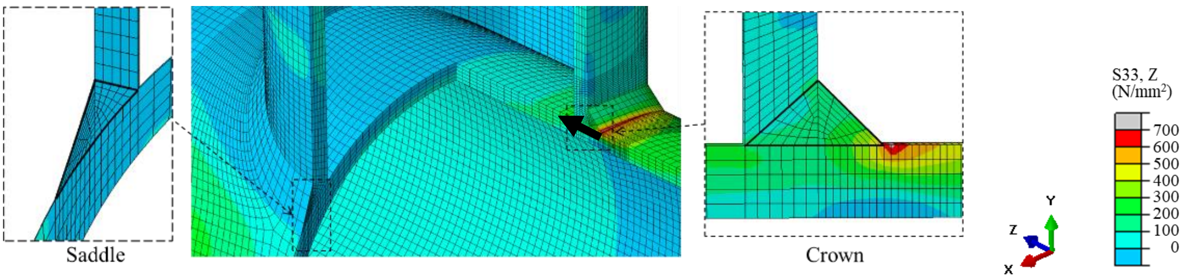

d) Principal stresses S33 – mechanical stress

Figure 5.13 Stress distributions of Joint T-2b at Stage e_8 . Mechanical stresses with stress concentration effects.

Table 5.5 Comparisons on local stresses σ_{wt} at Stage e_8

Joints	σ_{hs} test	σ_{wt} FEM	$\frac{\sigma_{wt}}{\sigma_{hs}}$
T-1a	465.6	603.8	1.30
T-1b	565.2	684.5	1.21
T-1c	570.5	687.0	1.20
T-2a	601.2	748.0	1.24
T-2b	600.9	725.8	1.21
T-2c	363.7	433.0	1.19
T-3a	610.5	753.9	1.23
T-3b	636.2	742.4	1.17
T-3c	534.1	643.7	1.21
T-3d	481.0	569.5	1.18
		Max ~ Min	***1.17 ~ 1.30***
		Mean	***1.22***
		COV	***0.030***

- ***Stresses concentration factors SCF***

It is important to compare the SCF obtained from the finite element models, i.e. SCF_{FEM} , with those obtained from the tests according to Eq. 5-1a) to c) given above, i.e. SCF_{T} , and these data are summarized in **Table 5.6**. The ratios of SCF_{T} / SCF_{FEM} are found to range from 0.96 to1.03 with an average value of 0.99 and a coefficient of variation at 0.025. Hence, the finite element models are demonstrated to be able to simulate the effects of stress concentration, and also to predict local stresses of the welded T-joints with a high level of accuracy.

In addition, the experimental investigations on the welded T-joints between S355 CHS with similar configurations were adopted for further calibration and verification of the proposed

FEM (Mashiri *et al.*, 2004a). **Table 5.7** summarizes the details of the S355 welded T-joints. As details of the weld sizes were not reported in the literature, the weld sizes at crown, i.e. h_1 and h_2, were set to be 1/7 of the brace diameters according to the imaging analyses on the figures of test specimens provided in the literature. **Figure 5.14** presented the predicted SCF_{FEM} obtained from the proposed FEM, the reported SCF_T obtained from the tests, and also the recommended SCF_{CID} given by CIDECT-8, and they are also summarized in **Table 5.7**. It is demonstrated that the predicted SCF_{FEM} are almost the same as the SCF_T, while they are much lower than the SCF_{CID}.

Table 5.6 Comparisons on SCF

Joints	SCF_T	SCF_{FEM}	SCF_{CID}	$\frac{SCF_T}{SCF_{FEM}}$	$\frac{SCF_T}{SCF_{CID}}$
T-1a	3.17	3.29	4.42	*0.96*	*0.72*
T-1b	3.14	3.05	4.06	*1.03*	*0.77*
T-1c	3.07	2.99	3.79	*1.03*	*0.81*
T-2a	3.15	3.25	3.88	*0.97*	*0.81*
T-2b	2.88	2.84	3.67	*1.01*	*0.78*
T-2c	2.80	2.81	3.48	*1.00*	*0.80*
T-3a	3.23	3.30	4.33	*0.98*	*0.75*
T-3b	3.16	3.07	4.24	*1.03*	*0.75*
T-3c	3.10	3.04	3.99	*1.02*	*0.78*
T-3d	3.01	3.00	3.68	*1.00*	*0.82*
			Max ~ Min	***1.03 ~ 0.96***	***0.82 ~ 0.72***
			Mean	***0.99***	***0.78***
			COV	***0.025***	***0.044***

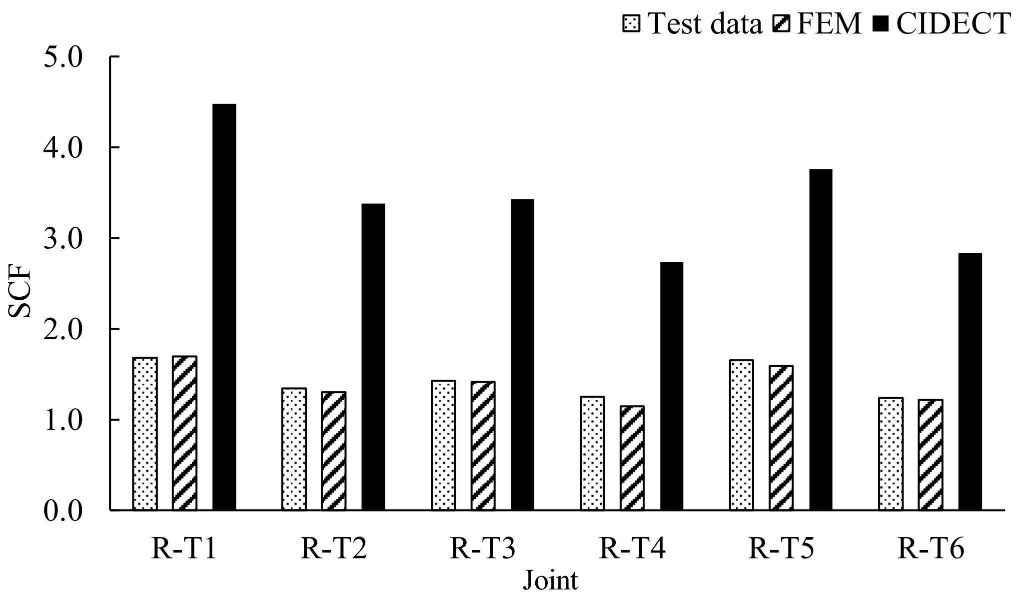

Figure 5.14 Comparison on SCF obtained from Reference (Mashiri *et al.*, 2004a), FEM and CIDECT

Table 5.7 Comparisons on SCF from Reference (Mashiri *et al.*, 2004a)

Joints	β	2γ	τ	SCF_{Ref}	SCF_{FEM}	SCF_{CID}	$\frac{SCF_{Ref}}{SCF_{FEM}}$	$\frac{SCF_{Ref}}{SCF_{CID}}$
R-T1	0.48	32	1.00	1.68	1.694	4.48	*0.99*	*0.38*
R-T2	0.48	32	0.72	1.34	1.298	3.38	*1.03*	*0.40*
R-T3	0.33	32	0.81	1.43	1.416	3.43	*1.01*	*0.42*
R-T4	0.33	32	0.63	1.25	1.147	2.74	*1.09*	*0.46*
R-T5	0.63	24	1.00	1.65	1.593	3.76	*1.04*	*0.44*
R-T6	0.63	24	0.72	1.24	1.216	2.84	*1.02*	*0.44*
							1.09 ~ 0.99	***0.46 ~ 0.38***
						Mean	***1.03***	***0.42***
						COV	***0.032***	***0.072***

5.3.3 Parametric study and design development

After verification of the finite element models, a comprehensive parametric study was conducted to cover a total of 96 welded T-joints between S690 CHS with various cross-sectional dimensions. The study provides a large amount of numerical data to compare with design values of SCF obtained from the formula given in CIDECT.

- ***Basic data***

Similar with the geometry and dimensions of those welded T-joints between S690 CHS presented in Section 2, the diameter of the chord d_0 was set to be 250 mm, and the length of the chord, L_o , and that of the brace, L_1 , were set to be 1,200 and 600 mm respectively. It should be noted that

- Material properties

  The Young's modulus of all the S690 CHS are taken to be 205 kN/mm^2, and the yield strength of all the S690 CHS was taken to be 690 N/mm^2. The Poisson's ratio was taken to be 0.3.

- Mesh size

  Solid element C3D8R was adopted to establish the models, and the mesh details were the same as those presented in Chapter 5.3.1.

- Weld sizes

  According to the welding design guidance AWS D1.1 (ANSI, 2004) and the relevant numerical investigations conducted by other researchers (Tong *et al.*, 2015; Lan *et al.*, 2021), the weld sizes at the crowns of the chords of these T-joints were taken to be equal to the brace thickness, i.e. $h_1 = h_2 = t_1$.

Details of the boundary conditions are the same as those presented in Chapter 5.3.1, and shown on **Figure 5.11**.

It should be noted that thicknesses of the chord t_0 and the brace t_1 were set to range from 2.0 to 16.0 mm, in order to cover a wide range of geometric parameters, i.e. diameter ratio $\beta = 0.2$, 0.4, 0.6, 0.8, diameter to thickness ratio of chord $2\gamma = 15$, 20, 25, 30, 40, 50, and thickness ratio of brace to chord $\tau = 0.25$, 0.50, 0.75, 1.00. The numerical programme for parametric study is summarized in **Table 5.8**.

Table 5.8 Numerical programme for parametric study

Joints	τ	2γ	β
P-T1 to P-T96	0.25 0.50 0.75 1.00	15 20 25 30 40 50	0.2 0.4 0.6 0.8
No. of parameters	4	6	4
No. of analysis		96	

- ***Predicted SCF_{FEM}***

All the geometric parameters of these T-joints and the predicted values of SCF_{FEM} of the parametric study are plot in **Figure 5.15**, and they are also summarized in **Table 5.9**. The values of SCF_{FEM} of these T-joints are found to decrease with a decrease of γ and τ, but increase and then decrease with an increase of β for most of the cases. These observations are found to be generally in-line with those reported in the literature (Tong *et al.*, 2014; Mashiri *et al.*, 2004a; Mashiri *et al.*, 2004b), and also with the recommendations given in CIDECT-8.

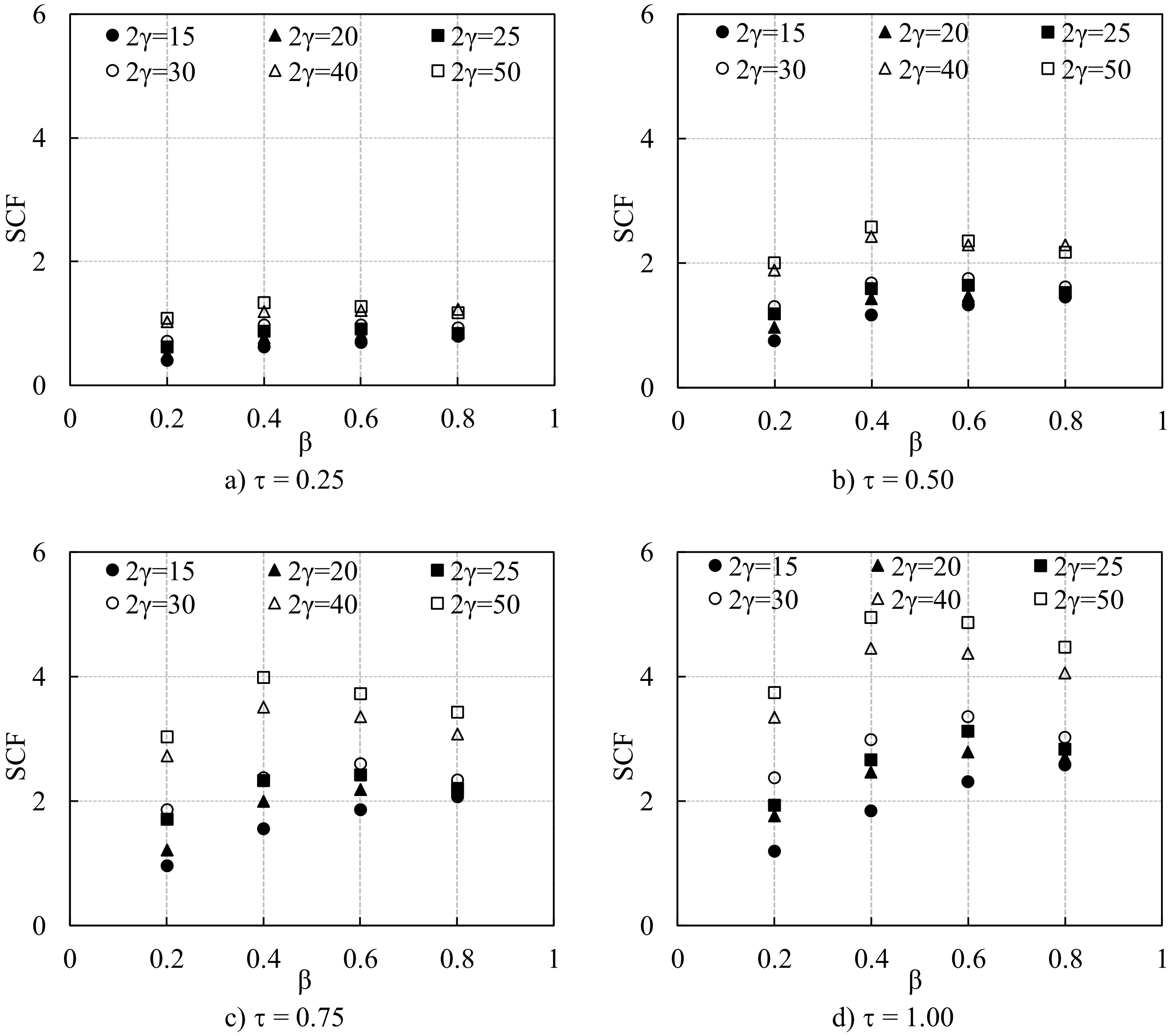

Figure 5.15 SCF of various S690 welded T-joints obtained from parametric studies

Table 5.9 Comparisons on SCF. Numerical and design results

Joints	τ	2γ	β	SCF_{FEM}	SCF_{PDF}	$\frac{SCF_{FEM}}{SCF_{PDF}}$
P-T1	0.25	15	0.2	0.405	0.392	1.047
P-T2			0.4	0.623	0.587	1.057
P-T3			0.6	0.692	0.659	1.047
P-T4			0.8	0.794	0.658	1.201
P-T5		20	0.2	0.505	0.501	0.997
P-T6			0.4	0.764	0.728	1.044
P-T7			0.6	0.825	0.793	1.034
P-T8			0.8	0.846	0.768	1.107
P-T9		25	0.2	0.620	0.607	1.021
P-T10			0.4	0.872	0.861	1.010
P-T11			0.6	0.914	0.916	0.994
P-T12			0.8	0.837	0.866	0.970
P-T13		30	0.2	0.715	0.710	1.014
P-T14			0.4	0.973	0.987	0.982
P-T15			0.6	0.973	1.030	0.942
P-T16			0.8	0.927	0.955	0.974
P-T17		40	0.2	1.027	0.909	1.133
P-T18			0.4	1.193	1.226	0.971
P-T19			0.6	1.212	1.240	0.976
P-T20			0.8	1.228	1.115	1.103
P-T21		50	0.2	1.083	1.101	0.981
P-T22			0.4	1.341	1.450	0.924
P-T23			0.6	1.274	1.432	0.887
P-T24			0.8	1.172	1.257	0.931

Joints	τ	2γ	β	SCF_{FEM}	SCF_{PDF}	$\frac{SCF_{FEM}}{SCF_{PDF}}$
P-T25	0.50	15	0.2	0.753	0.727	1.031
P-T26			0.4	1.165	1.089	1.065
P-T27			0.6	1.331	1.224	1.087
P-T28			0.8	1.461	1.222	1.195
P-T29		20	0.2	0.975	0.931	1.042
P-T30			0.4	1.433	1.352	1.058
P-T31			0.6	1.472	1.473	0.998
P-T32			0.8	1.530	1.426	1.073
P-T33		25	0.2	1.186	1.128	1.055
P-T34			0.4	1.591	1.599	0.994
P-T35			0.6	1.643	1.701	0.964
P-T36			0.8	1.528	1.608	0.951
P-T37		30	0.2	1.302	1.318	0.986
P-T38			0.4	1.685	1.834	0.916
P-T39			0.6	1.755	1.913	0.915
P-T40			0.8	1.618	1.774	0.913
P-T41		40	0.2	1.889	1.688	1.120
P-T42			0.4	2.427	2.276	1.068
P-T43			0.6	2.295	2.303	0.999
P-T44			0.8	2.297	2.070	1.111
P-T45		50	0.2	2.009	2.044	0.983
P-T46			0.4	2.584	2.692	0.958
P-T47			0.6	2.359	2.659	0.888
P-T48			0.8	2.182	2.334	0.934

Joints	τ	2γ	β	SCF_{FEM}	SCF_{PDF}	$\frac{SCF_{FEM}}{SCF_{PDF}}$
P-T49	0.75	15	0.2	0.962	1.045	0.919
P-T50			0.4	1.551	1.565	0.991
P-T51			0.6	1.856	1.757	1.058
P-T52			0.8	2.070	1.755	1.180
P-T53		20	0.2	1.216	1.337	0.912
P-T54			0.4	1.998	1.942	1.030
P-T55			0.6	2.183	2.116	1.030
P-T56			0.8	2.193	2.048	1.069
P-T57		25	0.2	1.706	1.619	1.056
P-T58			0.4	2.332	2.297	1.015
P-T59			0.6	2.418	2.443	0.991
P-T60			0.8	2.200	2.310	0.953
P-T61		30	0.2	1.864	1.894	0.982
P-T62			0.4	2.375	2.634	0.904
P-T63			0.6	2.594	2.747	0.943
P-T64			0.8	2.335	2.548	0.915
P-T65		40	0.2	2.724	2.424	1.122
P-T66			0.4	3.503	3.269	1.071
P-T67			0.6	3.358	3.307	1.016
P-T68			0.8	3.071	2.974	1.032
P-T69		50	0.2	3.031	2.936	1.032
P-T70			0.4	3.982	3.866	1.029
P-T71			0.6	3.724	3.819	0.974
P-T72			0.8	3.424	3.353	1.020

Joints	τ	2γ	β	SCF_{FEM}	SCF_{PDF}	$\frac{SCF_{FEM}}{SCF_{PDF}}$
P-T73			0.2	1.196	1.351	0.888
P-T74		15	0.4	1.843	2.023	0.910
P-T75			0.6	2.306	2.272	1.017
P-T76			0.8	2.579	2.269	1.137
P-T77			0.2	1.757	1.729	1.018
P-T78		20	0.4	2.464	2.511	0.980
P-T79			0.6	2.788	2.735	1.020
P-T80			0.8	2.695	2.648	1.019
P-T81			0.2	1.932	2.094	0.922
P-T82		25	0.4	2.662	2.969	0.896
P-T83			0.6	3.123	3.158	0.988
P-T84	1.00		0.8	2.829	2.986	0.948
P-T85			0.2	2.376	2.448	0.972
P-T86		30	0.4	2.986	3.405	0.878
P-T87			0.6	3.358	3.552	0.946
P-T88			0.8	3.021	3.294	0.917
P-T89			0.2	3.348	3.134	1.069
P-T90		40	0.4	4.450	4.227	1.053
P-T91			0.6	4.369	4.276	1.022
P-T92			0.8	4.055	3.845	1.056
P-T93			0.2	3.744	3.796	0.985
P-T94		50	0.4	4.946	4.999	0.990
P-T95			0.6	4.862	4.938	0.984
P-T96			0.8	4.471	4.335	1.031
				Max ~ Min		1.201 ~ 0.878
				Mean		***1.006***
				COV		***0.070***

- ***Comparison with SCF_{CID}***

Existing design formula given in CIDECT for determination of SCF_{CID} of the welded T-joints between CHS under in-plane bending is as follows:

$$SCF_{CID} = 1.45\beta\tau^{0.85}\gamma^{1-0.68\beta}\sin^{0.7}\theta \qquad (5\text{-}2)$$

Figure 5.16 illustrates a comparison between the measured SCF_T obtained in the tests, the corresponding predicted SCF_{FEM} obtained from the finite element models, and the SCF_{CID} obtained in accordance with CIDECT-8. It is evident that all SCF_T and SCF_{FEM} are found to lie well below the curves of CIDECT, and hence, it is demonstrated that CIDECT tends to overestimate the effects of stress concentration in these welded T-joints. The ratios of SCF_T / SCF_{CID} are also summarized in **Table 5.6**, and it is shown that these ratios range from 0.72 to 0.82 with an average value of 0.78 and a coefficient of variation at 0.044.

Further comparison with the predicted SCF_{FEM} obtained from the parametric study with those SCF_{CID} is made, and these data are plotted in **Figure 5.17a)** illustrates the ratios of SCF_{FEM} / SCF_{CID} . It is evident that the values of all these ratios are smaller than 1.0 with an average value at 0.801. Hence, it is demonstrated that SCF_{CID} are typically 20% large than those of SCF_{FEM}.

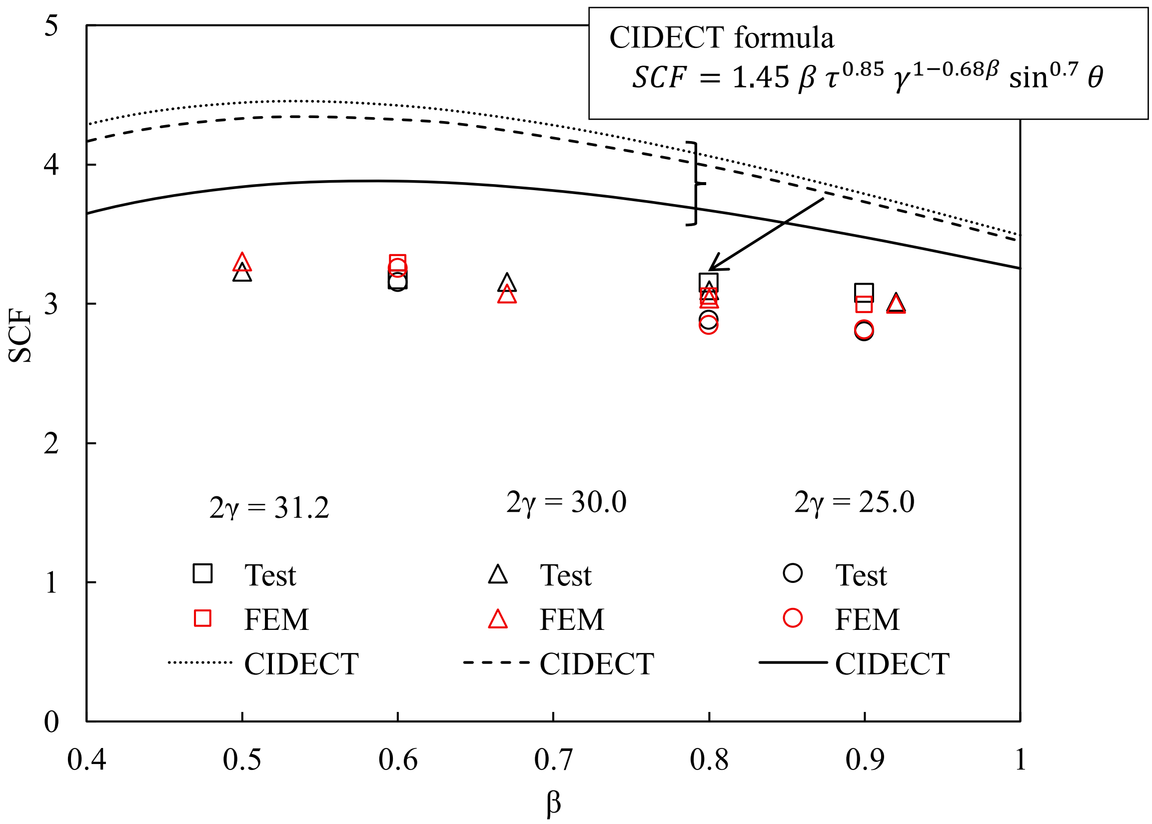

Figure 5.16 SCF of various S690 welded T-joints

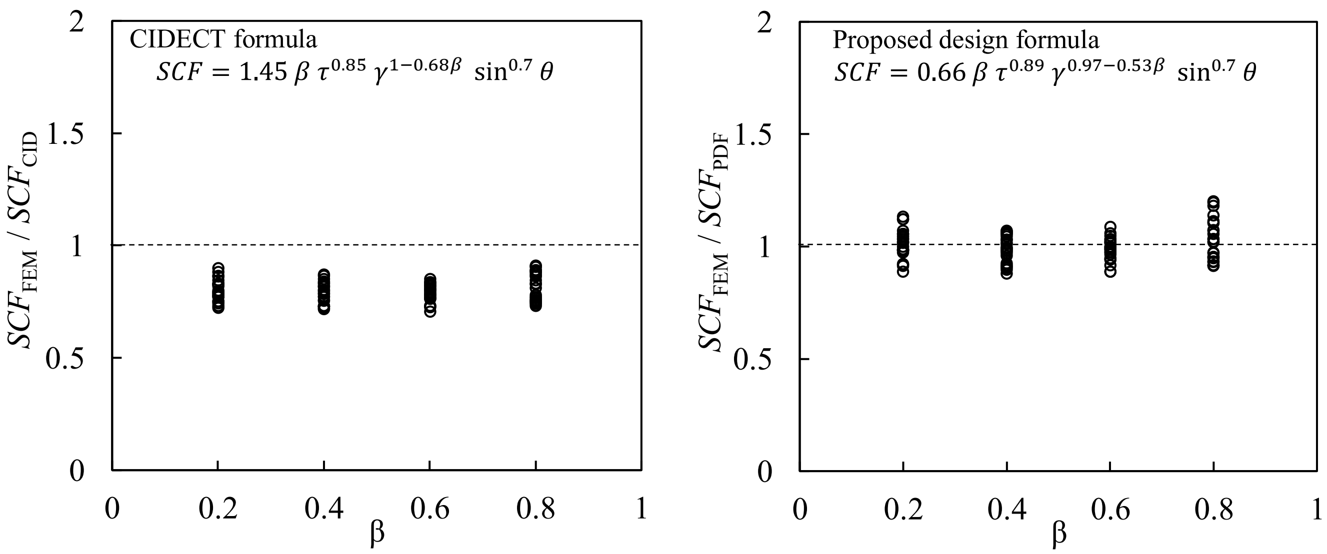

Figure 5.17 SCF obtained from CIDECT and proposed design formula

- ***Proposed design formula***

Based on the results of both the experimental and the numerical investigations in the present study, it is considered beneficial to improve accuracy of the existing design formula given in CIDECT. It is decided to adopt the general format of the formulae as follows:

$$SCF = a\,\beta\,\tau^{b}\,\gamma^{c+d\beta}\,\sin^{0.7}\theta \qquad (5\text{-}3)$$

where a, b, c and d are constants to be determined through regression analyses.

After a careful multiple regression analysis against the SCF_{FEM} obtained from the parametric study described in Chapter 5.3.3, the proposed design formula for SCF_{PDR} of the welded T-joints between S690 CHS under in-plane bending is given by:

$$SCF_{PDF} = 0.66\,\beta\,\tau^{0.89}\,\gamma^{0.97-0.53\beta}\,\sin^{0.7}\theta \qquad (5\text{-}4)$$

All the SCF_{PDF} are also summarized in **Table 5.9**, and the ratios of SCF_{FEM} / SCF_{PDR} are found to range from 0.878 to 1.201 with an average value of 1.006 and a coefficient of variation at 0.069. It is shown that the proposed design formula is able to predict the effects of stress concentration on the welded T-joints between S690 CHS under in-plane bending satisfactorily. The ratios SCF_{FEM} / SCF_{PDF} are also plotted in **Figure 5.17b)** for a direct comparison with those ratios of SCF_{FEM} / SCF_{CID} plotted in **Figure 5.17a)**.

5.4 Coupled thermomechanical modelling for welding simulation

It should be noted that all the numerical results presented in Chapter 5.3 above are obtained from finite element models without considering the effects of welding onto these welded T-joints between S690 CHS, i.e. no residual stresses. However, such an assumption is rather unrealistic as there are significant residual stresses in the vicinity of the brace / chord junctions of the welded T-joints. Thus, an examination into the “stress and strain” conditions in the vicinity of the brace / chord junctions in the presence of residual stresses is considered to be essential to provide a good understanding on the critical stresses of these welded T-joints.

It should be noted that an advanced coupled thermomechanical modelling approach has been successfully developed and thoroughly calibrated, and **Figure 5.18** presents an overall view of the modelling approach. It should be noted that:

- a heat transfer analysis is first conducted to determine transient temperature distributions of the T-joint during welding, and 3D solid elements ***DC3D8*** are adopted for determination of temperature changes;
- a thermomechanical analysis based on the transient temperature distributions obtained above is then conducted to determine welding-induced residual stresses of the T-joint after welding, and 3D solid elements ***C3D8R*** are adopted for determination of “locked-up” stresses; and
- a structural analysis of the T-joint incorporating the “locked-up” stresses obtained above as initial stresses is then conducted according to specific loading and support conditions, and 3D solid elements ***C3D8R*** are also adopted for determination of mechanical stresses.

Based on these coupled thermomechanical analyses, welding-induced residual stresses in the vicinity of the brace / chord junctions of these welded T-joints are readily predicted with a high level of accuracy. For a detailed description of the modelling approach and applications in various types of high strength S690 tubular sections and joints, refer to References (Hu et al., 2020; 2022; 2023)

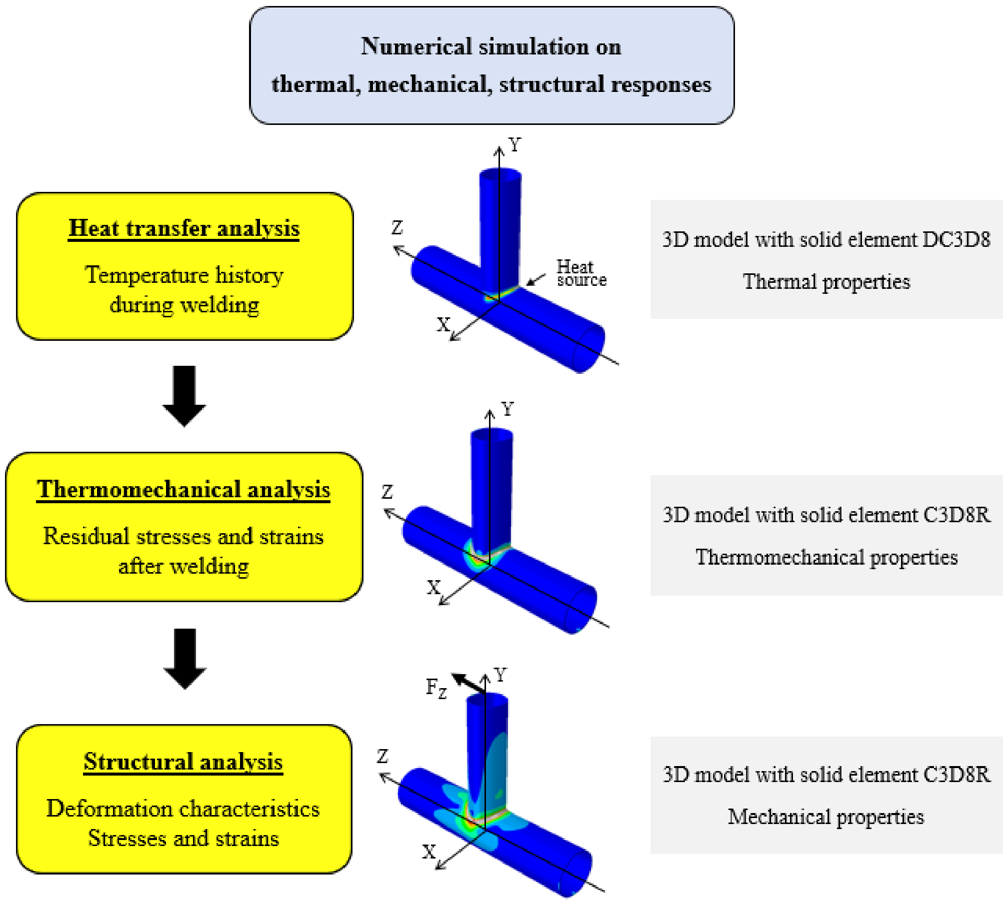

Figure 5.18 Coupled thermomechanical modelling approach

5.4.2 Welding-induced residual stresses

In general, the welding-induced residual stresses are found to have significantly changed the initial stress distributions within the welded T-joints, particularly in the vicinity of the brace / chord junction. Numerical results of Joint T-2b are selected to illustrate the effects of welding-induced residual stresses of the S690 welded T-joints under linear elastic deformations, and a detailed examination on various stresses at both the crown and the saddle of the welded T-joints is essential. **Figure 5.19** illustrates various stress distributions of Joint T-2b at the initial condition, i.e. Stage e_0 , while various stress distributions at Stage e_8 are illustrated in **Figure 5.20.** It should be noted that:

- At Stage e_0, based on the von Mises stress distribution of the brace / chord junction of the joint shown in **Figure 5.19a)**, most parts of the welded collar are found to have been yielded after welding. It is also evident that the principal stresses at the crown along the *transverse* direction of the chord, i.e. S11, are most critical, as shown in **Figure 5.19b)**. Similarly, the principal stresses at the saddle along the *longitudinal* direction of the chord, i.e. S33, are most critical, as shown in **Figure 5.19d)**.
- At Stage e_8, the mechanical stresses induced by the applied force are found to have significantly changed the stress state in the brace / chord junction of the joint, as shown in the von Mises stress distribution in **Figure 5.20a)**. The entire welded collar together with parts of the brace and the chord of the junction, i.e. heat affected zones, have been yielded. Similarly, as shown in **Figure 5.20b)** and **Figure 5.20d)**, principal stresses S11 and S33 are found to be critical at the crown and the saddle of the junction respectively. In addition, there are significant increases in principal stresses at the crown, i.e. S22 in the vicinity of the weld toe of the brace, as shown in **Figure 5.20c)**, and also S33 in the vicinity of the weld toe of the chord, as shown in **Figure 5.20d)**.

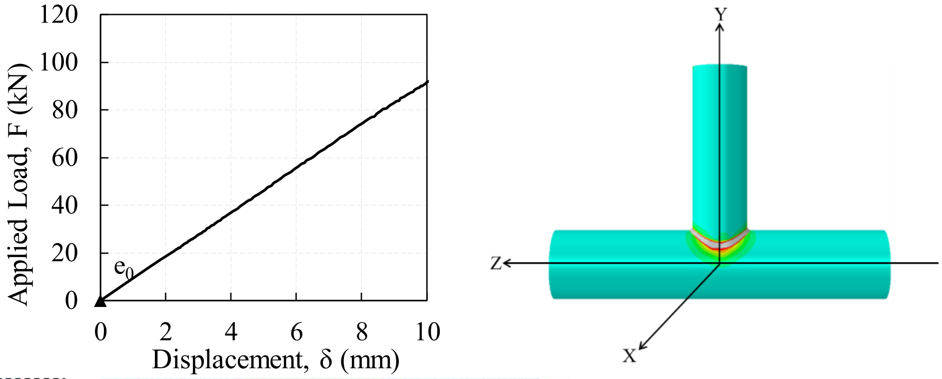

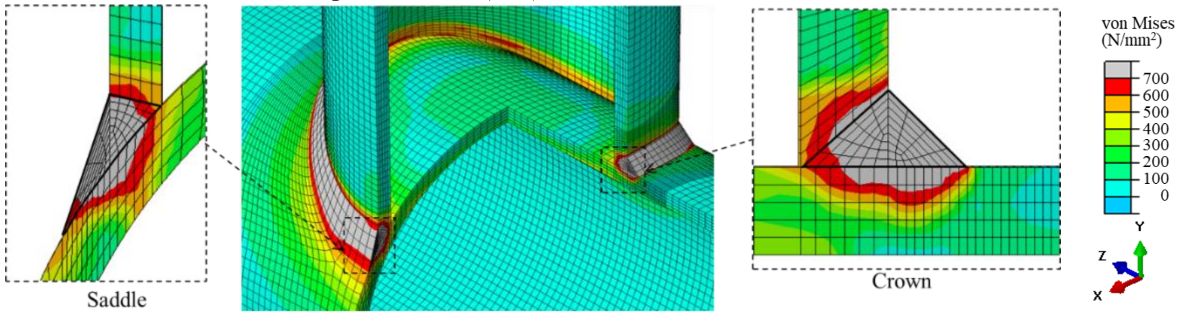

a) von Mises stresses - residual stress

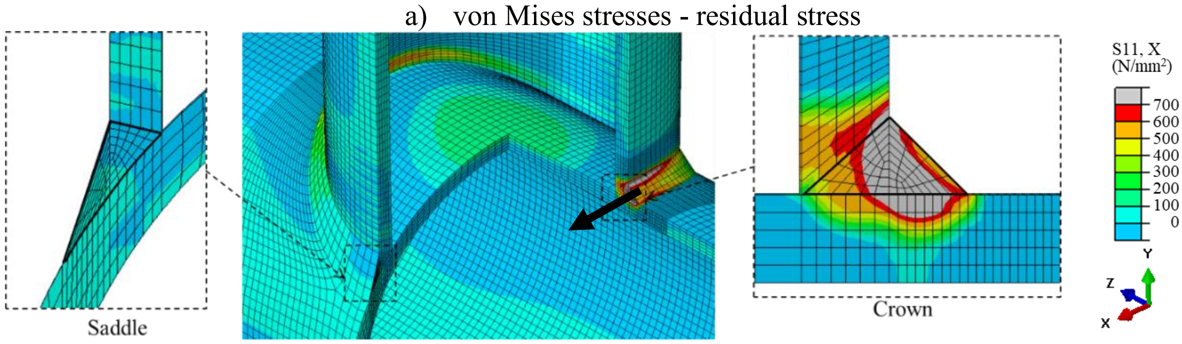

b) Principal stresses S11 – residual stress

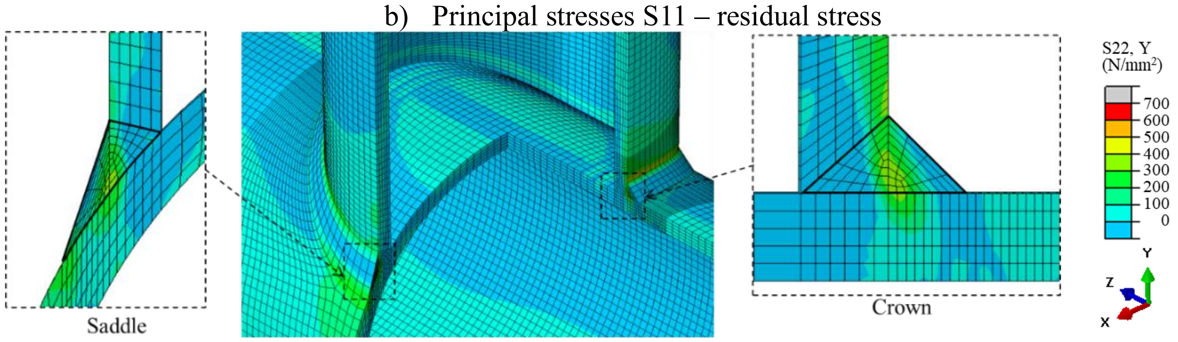

c) Principal stresses S22 – residual stress

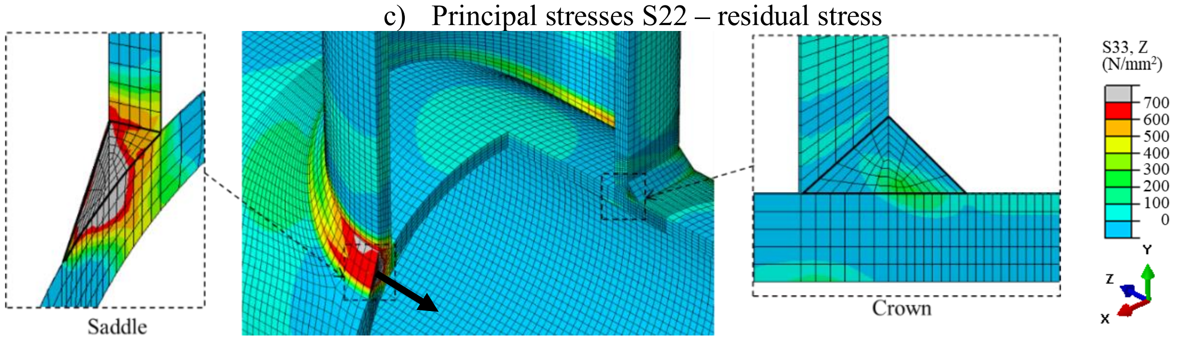

d) Principal stresses S33 – residual stress

Figure 5.19 Residual stress distributions of Joint T-2b at Stage e_0. Initial condition.

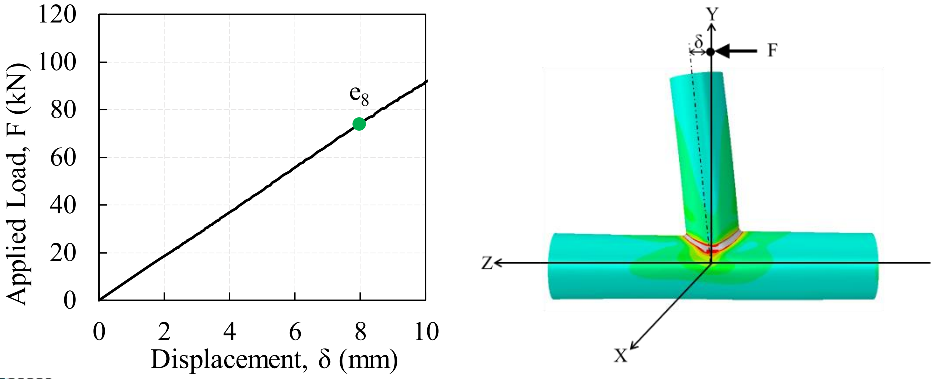

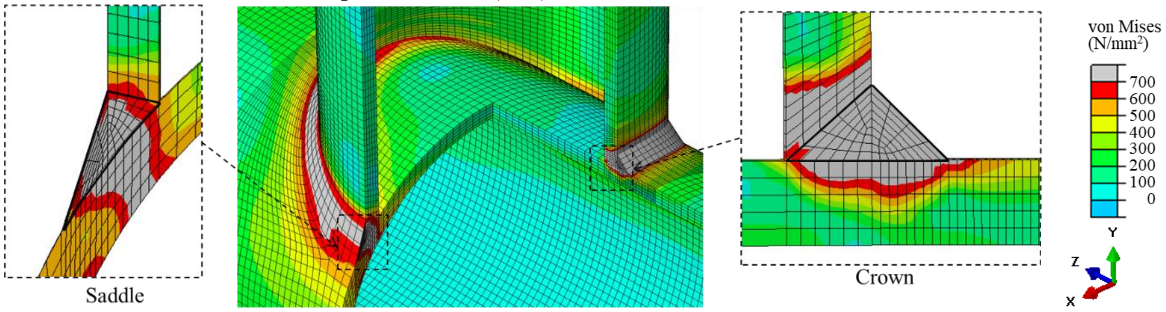

a) von Mises stresses – total stress

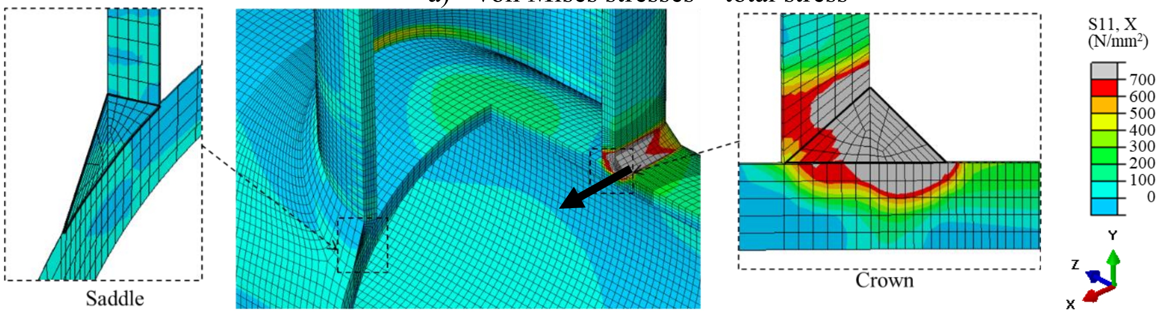

b) Principal stresses S11 – total stress

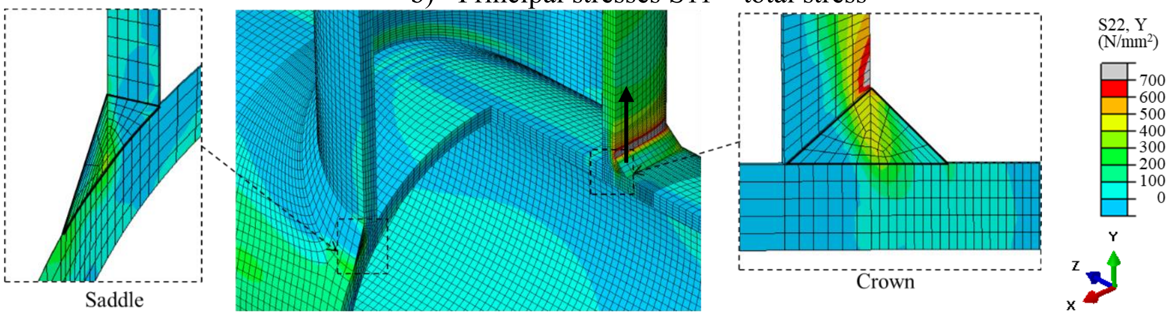

c) Principal stresses S22 – total stress

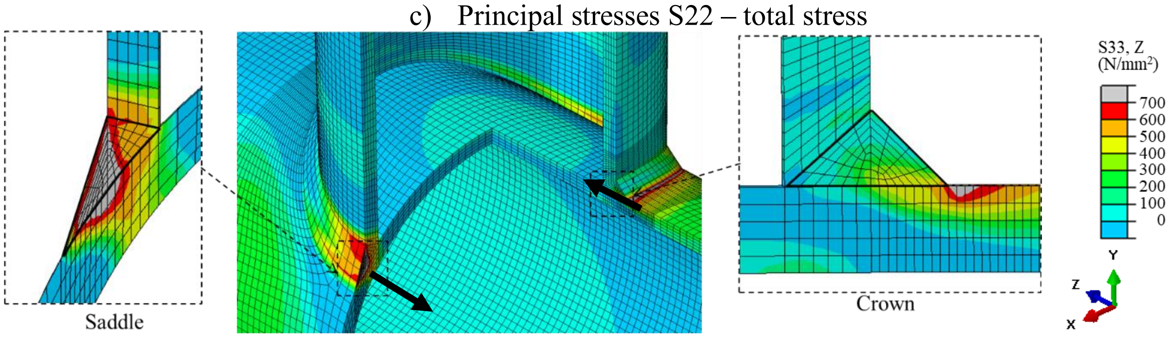

d) Principal stresses S33 – total stress

Figure 5.20 Stress distributions of Joint T-2b at Stage e_8 . Total stresses

5.4.3 Critical local stresses at the crown of T-joints

A comparison between these critical local stresses at the crown of Joint T-2b at both Stages e_0 and e_8 is shown in **Figure 5.21a)**. It is apparent that owing to the presence of large welding-induced residual stresses, the weld toe of the crown of the welded T-joint has already been yielded after welding, and its von Mises stresses well exceed the yield strength of the steel. Application of an applied load will impose large local mechanical stresses, under the effect of stress concentration, at the weld toe to undergo further yielding.

Table 5.10 summarizes various critical local stresses obtained from the test described in Chapter 5.2, and also from the finite element models with and without incorporation of the effects of welding described in Chapter 5.3, and Section Chapter 5.4 above. It is evident that the presence of welding-induced residual stresses has a significant effect on the stress levels of both the principal stresses S11 and S33.

Furthermore, it is interesting to compare directly with typical fatigue crack, as shown in **Figure 5.21b)**, obtained in a complementary experimental investigation into fatigue behaviour of these T-joints as presented in Chapter 4. It is apparent that the fatigue crack is originated at the critical location of the weld toe with large residual stresses and strains.

Consequently, it is demonstrated that despite the mechanical, or fatigue, stresses due to applied loads are typically small, when compared with the yield strength of the steel, fatigue behaviour of these welded T-joints is essentially a matter of plastic responses, and the plastic 'stress and strain' conditions of the weld toes of the crowns of these T-joints should be considered.

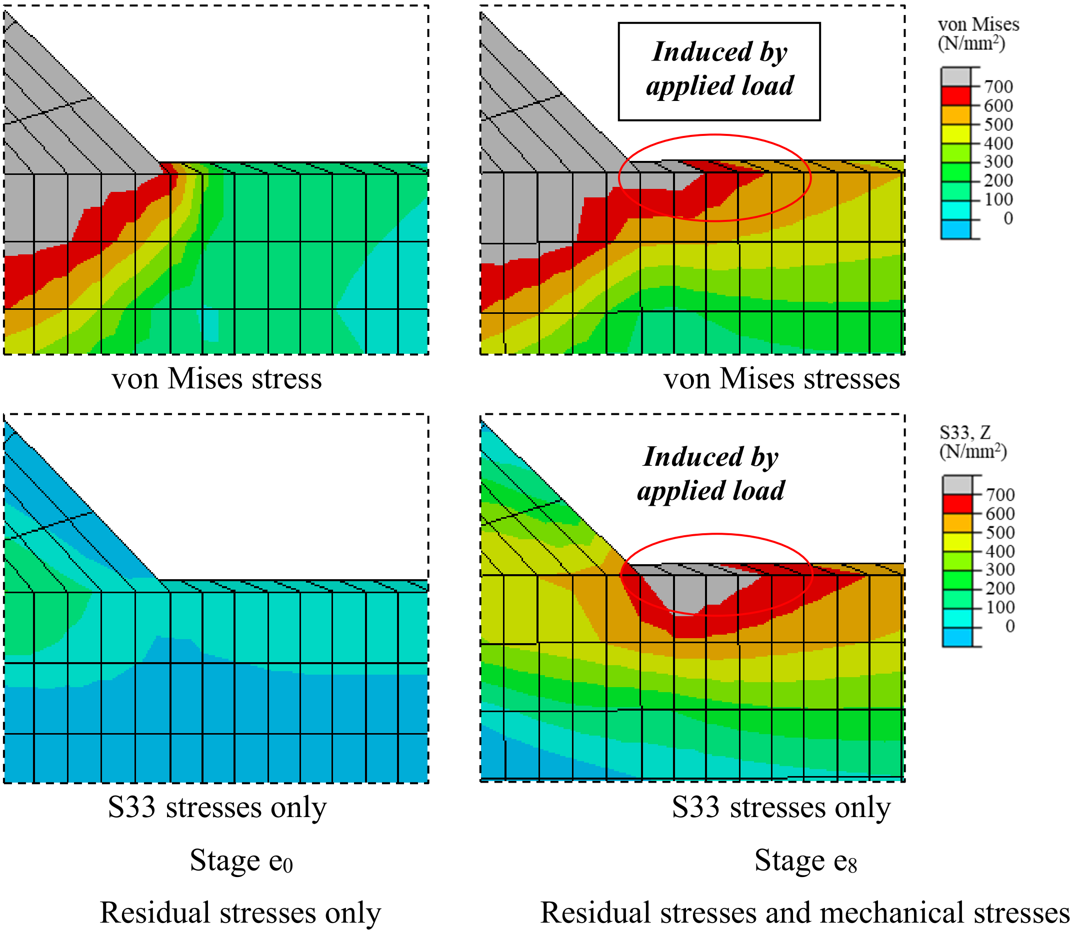

a) Typical stress plots
– welding-induced residual stresses and mechanical stresses

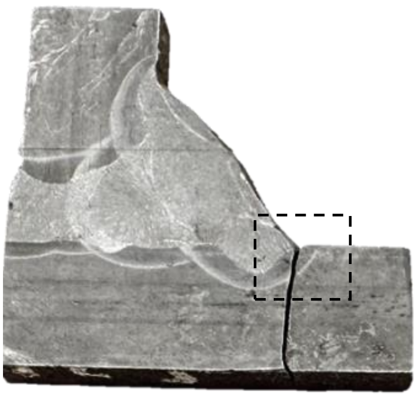

b) Typical fatigue crack

Figure 5.21 Critical local stresses at the weld toe of the crown of the welded T-joint

Table 5.10 Comparison on critical local stresses σ_{wt} with residual stresses. Joint T-2b.

	Test data	Numerical models					
Stages	Hot spot stress σ_{hs} without measuring residual stress S33	Local stress σ_{wt} without considering residual stress S33	Local stress σ_{wt} considering residual stress S33_R	*Ratio*	Local stress σ_{wt} without considering residual stress S11	Local stress σ_{wt} considering residual stress S11_R	*Ratio*
e_8	600.9	725.8	810.5	*1.12*	482.5	882.6	*1.83*
e_6	447.7	562.6	642.2	*1.14*	374.3	854.2	*2.28*
e_4	295.8	363.1	464.9	*1.28*	241.7	794.9	*3.29*
e_2	149.7	186.5	284.0	*1.52*	121.0	716.2	*5.92*
e_o	0.0	0.0	96.4	---	0.0	610.3	---

5.5 Conclusions

This paper presents a systemic experimental and numerical investigation into critical local stresses within the welded T-joints between high strength S690 circular hollow sections (CHS) under in-plane bending. A total of 10 welded T-joints between S690 CHS with different cross-sectional dimensions were tested under monotonic actions of in-plane bending to failure. In additional to a conventional investigation into effects of stress concentration to give highly localized stresses in the vicinity of the brace / chord junctions, the effects of welding-induced residual stresses in the heat affected zones of the welded joints were also examined. Key findings of the research are:

a) The hot spot stresses σ_{hs} at the weld toes of the crowns of the brace / chord junctions of these 10 welded T-joints under in-plane bending have been successfully obtained from tests. Finite element models with linear elastic analyses have been established, and the corresponding numerical stresses σ_{hs} have also been successfully predicted in the absence of residual stresses.

b) The stress concentration factors SCF_{T} and SCF_{FEM} obtained from both the experimental and the numerical investigations are found to be in a good agreement. However, the existing design formula given in CIDEC is demonstrated to give rather conservative SCF_{CID} .

c) After calibration against the test data, a parametric study using the finite element models on a total of 96 welded T-joints with a wide range of geometrical ratios was also conducted. Through a multiple regression analysis on the predicted values of SCF, an improved design formula for SCF is proposed.

d) Various stress distributions of the brace / chord junctions of the welded T-joints due to the effects of welding have been successfully predicted by the coupled thermomechanical modelling approach developed by the authors.

e) Owing to the presence of large welding-induced residual stresses and strains, the weld toes at the crowns of the brace / chord junctions of these welded T-joints were found to have been yielded after welding. Under the effects of stress concentration, significantly increased mechanical stresses due to applied loads are also found at the weld toes of these welded T-joints, making these locations highly vulnerable to fatigue failure.

Chapter 6 Fatigue behaviour of S690 U-rib stiffened steel decks under axial compression

6.1 Introduction

This Chapter presents a comprehensive experimental investigation into the fatigue behaviour of S690 U-rib stiffened steel decks under transverse cyclic actions. A total of 14 stiffened steel decks were successfully tested under a wide range of stress levels. The processes of crack initiation and propagation in these stiffened steel decks were closely monitored throughout the tests, and the hot spot stresses in the vicinity of weld toes of these U-rib stiffened steel decks were measured. Hence, a total of 14 S-N data were obtained to establish the fatigue behaviour of these U-rib stiffened steel decks according to IIW format.

The following works were carried out:

Task 1 – Experimental investigation

A total of 14 fatigue tests on S690 U-rib stiffened steel decks under transverse cyclic actions were conducted. All these tests were conducted under cyclic loads of a practical load range, i.e. $\Delta F = F_{max} - F_{min}$, with a stress ratio at $R = F_{min} / F_{max} = 0.1$. Hot spot stresses σ_{hs} at the weld toes of the steel decks were derived from measured strain gradients in the vicinity of the weld toes with suitable instrumentation. Key results were the number of cycles completed before fracture N, and the corresponding hot spot stress ranges $\Delta\sigma_{hs}$. The fatigue behaviour of crack initiation and propagation of these U-rib stiffened steel decks were monitored carefully, and the corresponding stress variations in the vicinity of weld toes were also examined to determine any deterioration in stiffness and strength.

It should be noted that one of the U-rib stiffened steel decks was selected to be tested under a monotonic transverse load up to 20% of the expected failure load in order to determine the corresponding values of the cyclic applied load ranges ΔF in all subsequent fatigue tests.

Task 2 – Analyses on S-N data

i) Formulation of S-N curves

After a comprehensive data analysis, the S-N data obtained from the fatigue tests were used to derive the S-N curve for fatigue assessment on these S690 U-rib stiffened steel decks. The S-N data were then compared with the design S-N curve given in IIW.

ii) Comparison with various S-N data of welded sections and joints

A comparison between the S-N data of the S690 U-rib stiffened steel decks and those of the S690 welded T-joints presented in Chapter 4 was then conducted. It should also be noted that the S-N data of the coupons of the S690 welded sections presented in Chapter 3 are also adopted for comparison.

This Chapter aims to demonstrate whether the S-N data of the S690 U-rib stiffened steel decks are directly comparable with those of the S690 welded T-joints and also of the S690 welded sections. Hence, the assessment methods developed in Chapter 4 for the S690 welded T-joints are equally applicable to the S690 U-rib stiffened steel decks.

6.2 Fabrication of S690 U-rib stiffened steel decks

According to the designed dimensions of the S690 U-shape stiffeners as shown in **Figure 6.1**, the 8 mm thick S690 steel plates were cut into pre-determined sizes for transverse cold-bending. And the 16 mm thick steel plates were also cut into pre-determined sizes according to the designed dimensions of the steel decks.

Figure 6.2 presents typical welding process of the S690 U-rib stiffened steel decks. Two 50mm-long run-on and run-off plates were set at both ends of the rib-to-deck joints for welding. The welding consumable of CHW-80C with a diameter of 1.2 mm was employed for the welding. Both pre-heating and post-weld heat treatment were employed, and the S690 U-rib stiffened steel deck was rotated 45° for weld pass 1. It should be noted that the heat input energy q during welding of all these rib-to-deck joints was carefully controlled by a qualified welder to be about 1.0 kJ/mm. A non-destructive inspection was then conducted on these S690 rib-to-deck welded joints 24 hours after welding. It should be noted that no welding defect was identified along the welds.

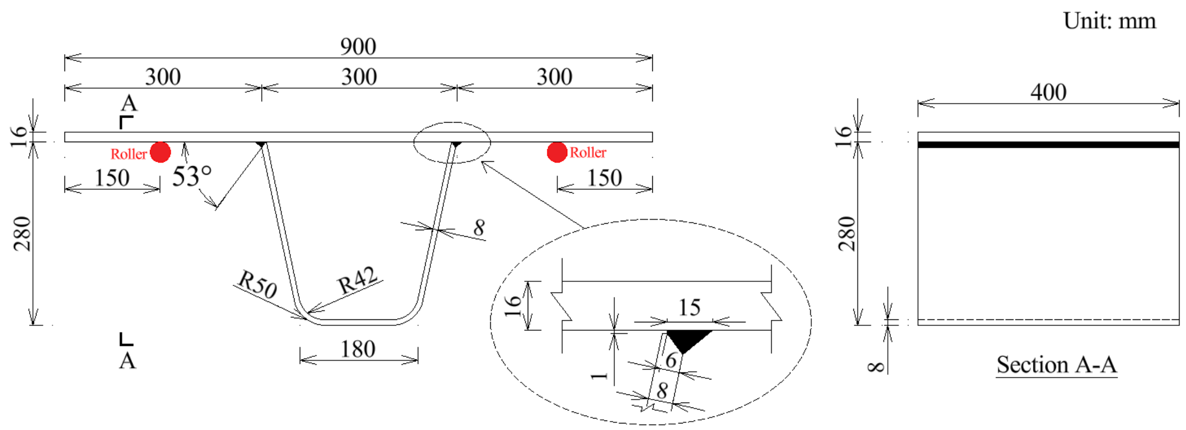

Figure 6.1 Configuration of S690 U-rib stiffened steel deck

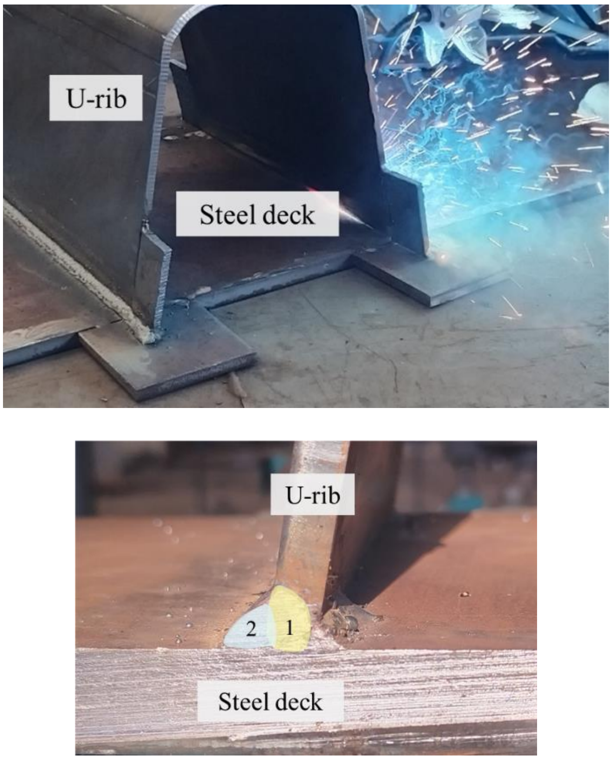

Figure 6.2 Welding of S690 U-stiffened steel deck

It should be noted that the welding consumable used in the welding of the S690 U-stiffened steel deck was different from those of the S690 welded sections and the S690 welded T-joints presented in Chapters 4 and 5 respectively. Standard tensile tests were conducted on the rectangular coupons of the base plate, the welded sections and the weld metal to examine their mechanical properties. The arrangement of test coupons in a welded section, and also the dimensions of these test coupons are shown in **Figure 6.3**.

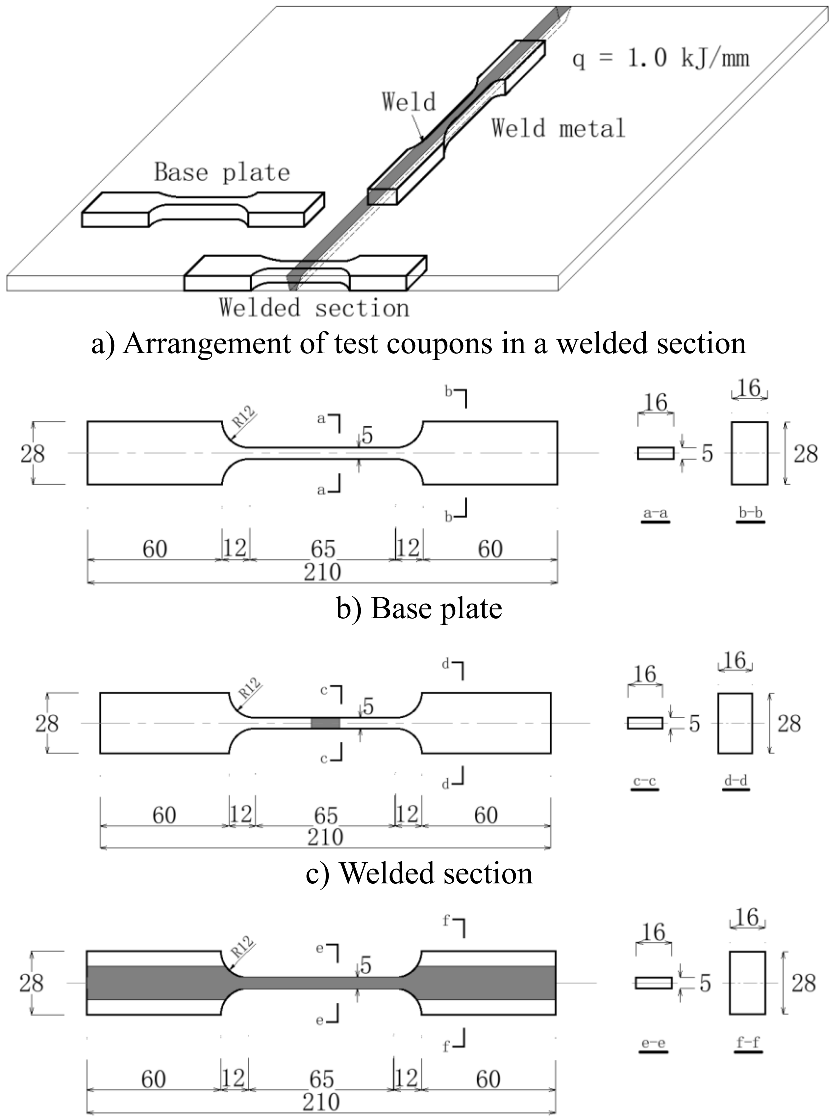

a) Arrangement of test coupons in a welded section

b) Base plate

c) Welded section

d) Weld metal

Figure 6.3 Dimension of standard rectangular coupons for tensile tests

Details of the test setup and instrumentation were the same as those presented in Chapter 3.3.1. The engineering stress-strain curves of these coupons are plotted in **Figure 6.4**. Fracture was found to always take place within the heat affected zones of the welded section, and the yield strengths of both the welded section and the weld metal were found to be reduced when compared with those of the base plate while the tensile strengths of these coupons were found to be almost the same. Key mechanical properties of these coupons are summarized in **Table 6.1**.

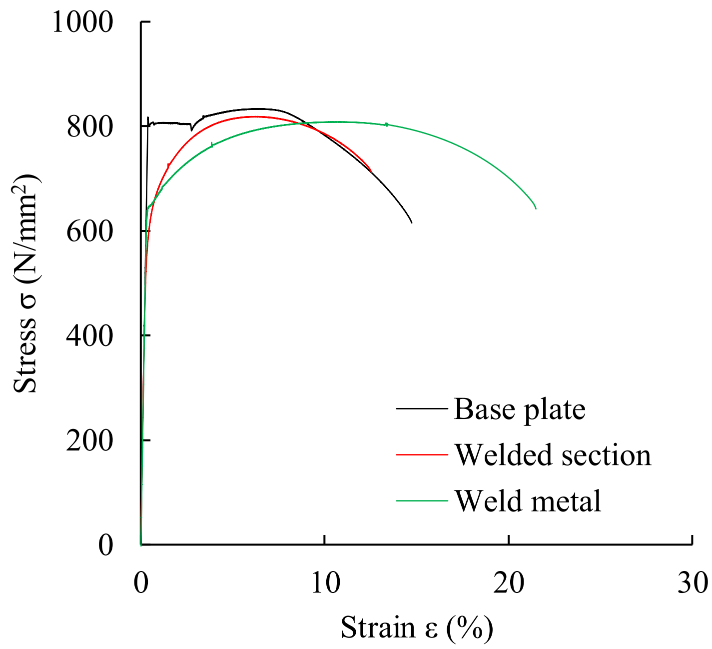

Figure 6.4 Measured engineering stress-strain curves

Table 6.1 Measured mechanical properties

Coupons	Young's modulus E (kN/mm^2)	Yield strength f_y (N/mm^2)	Tensile strength f_u (N/mm^2)	Elongation at fracture ε_L (%)
Base plate	211.2	791	833	14.8
Welded section	216.8	613	819	21.5
Weld metal	213.6	648	808	12.9

6.3 Monotonic test on S690 U-rib stiffened steel decks

6.3.1 Test programme

As shown in **Table 6.2**, one of the S690 U-rib stiffened steel decks was selected to be tested under transverse monotonic load, and it was referred to as Specimen SD-M. This specimen was then re-tested under transverse cyclic action, and it was referred to as Specimen SD-6a.

Table 6.2 Test programme of S690 U-stiffened steel deck

Specimens	Loading type	Loading frequency f (Hz)	Applied load range ΔF (kN)	R
SD-1a / b	Cyclic	1.5	12.8 ~ 128.0	0.1
SD-2a / b		2.0	10.2 ~ 102.0	
SD-3a / b		2.0	7.7 ~ 77.0	
SD-4a / b		2.5	6.7 ~ 67.0	
SD-5a / b		2.5	6.4 ~ 64.0	
SD-6a / b		2.5	5.9 ~ 59.0	
SD-7a / b		3.0	4.3 ~ 43.0	
SD-M	Monotonic	---	0.0 ~ 100.0	---

6.3.2 Test setup and instrumentation

Figure 6.5 illustrates the setup of the monotonic test of Specimen SD-M. It should be noted that a specially designed attachment was employed to limit both the lateral and the horizontal slippages of the specimen under transverse action, and both sides of the steel deck were installed to be within the rollers. A hydraulic controlled actuator with a maximum loading capacity of 500 kN with a maximum travel range of 250 mm was employed, and the load was directly applied to the central position of the top surface of the steel deck. A 200 × 200 × 35 mm rubber pad was placed between the actuator and the specimen in order to simulate the vehicle wheel loadings acting onto the U-rib stiffened steel deck in a bridge.

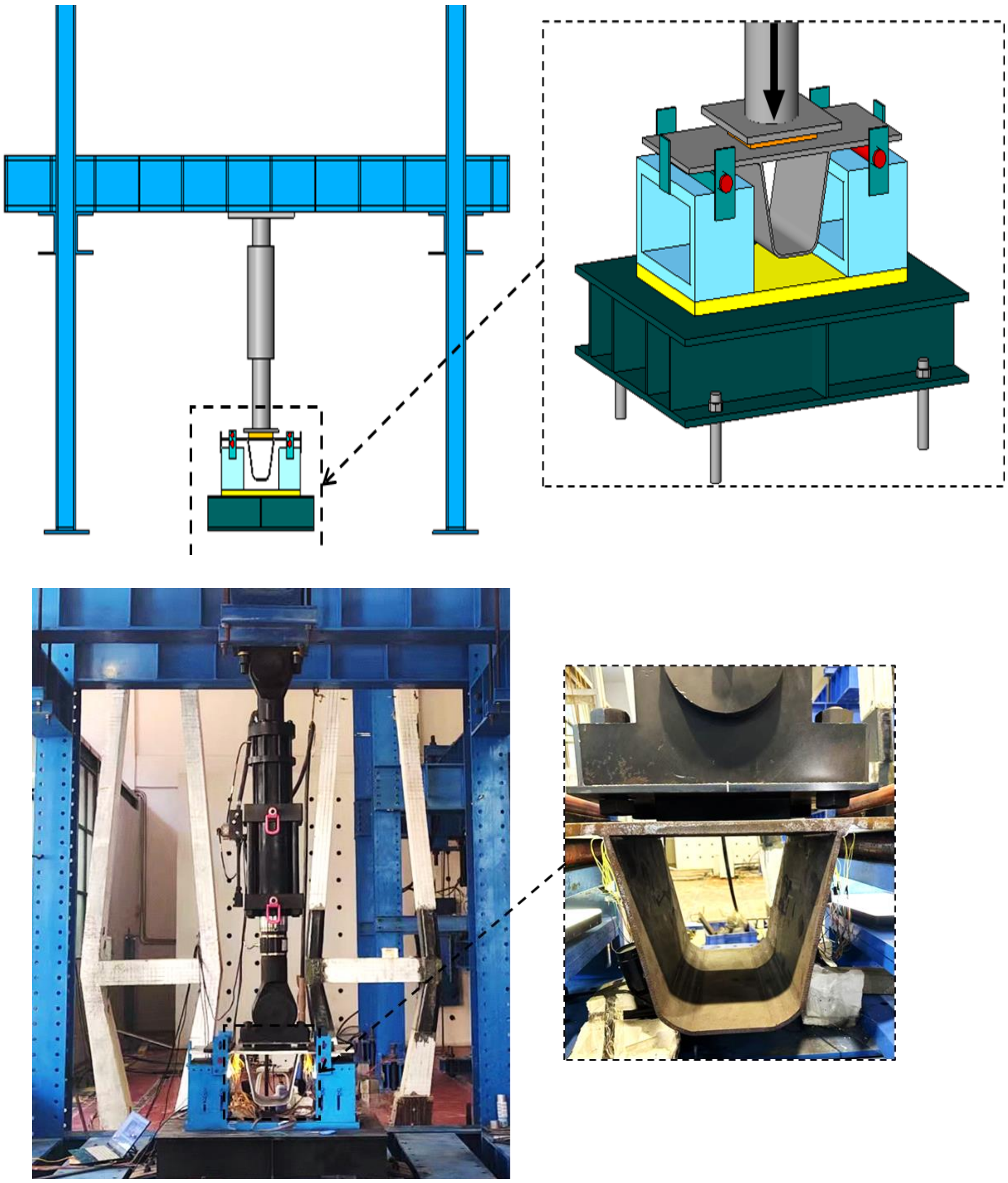

Figure 6.5 Test setup and instrumentation

According to IIW (Hobbacher, 1996), hot spot stresses at the weld toes of the steel deck are readily obtained from measured strains. As shown in **Figure 6.6**, a total of 20 strain gauges were installed at specific positions at the bottom surface of the steel deck to measure the strains in the vicinity of the weld toe, and they should be located within an extrapolation region within a distance of 0.4 t to 1.0 t. Hence, all of these 20 strain gauges, namely, Strains S1-1 to S4-5, were set to be at 6.4 and 16.0 mm away the weld toes of the steel deck.

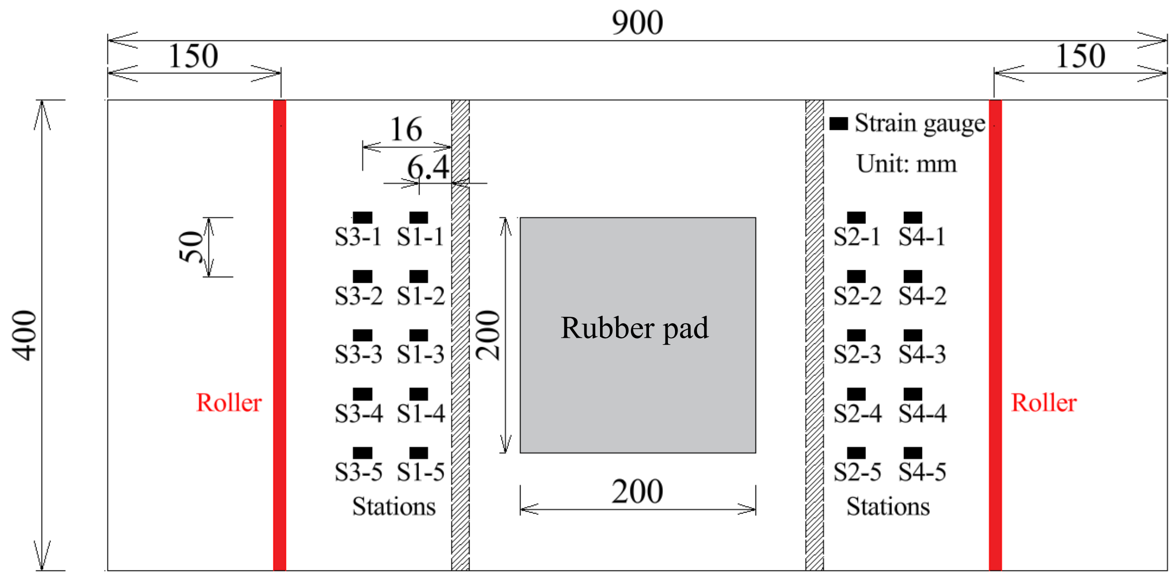

Figure 6.6 Locations of strain gauges

6.3.3 Experimental results

Specimen SD-M was carefully installed and aligned, and then a pre-loading procedure was performed at least 3 times to eliminate any initial bedding between the specimen and the support. The pre-loading procedure was conducted by applying a transverse load F on the top surface of the steel deck at a loading rate at 5 kN / minute, and the maximum applied load was set to be 20 kN for pre-loading.

During testing, a transverse load F was applied to the top surface of the steel deck at a loading rate of 5 kN / minute, to five different loading stages, i.e. Stages F_2, F_4, F_6, F_8 and F_{10} with applied load F at 20.0, 40.0, 60.0, 80.0 and 100.0 kN respectively. After reaching each of these loading stages, the transverse load F was held for at least 1 minute, and then, the applied load was measured through a load cell, and data from strain gauges were then acquired and stored electronically for subsequent analyses.

Figure 6.7 illustrates typical data of measured stresses at various measurement stations in the vicinity of the weld toes of the steel deck. The values of measured stresses at Stations S1-5, i.e. the corner of the rubber pad, are found to be larger than those at other Stations. Hence, the hot spot stress σ_{hs} of Specimen SD-M is given by:

$$\sigma_{hs} = 1.1\, E \times \left(\tfrac{5}{3} \varepsilon_{1-5} - \tfrac{2}{3} \varepsilon_{3-5} \right) \tag{6-1}$$

where

E	is the Young's modulus of the steel;
ε_{1-5} & ε_{3-5}	are the measured strains at Stations S1-5 and S3-5 respectively.

After an extensive data analysis on all the measured data obtained from the strain gauges at various loading stages, **Table 6.3** summarizes the derived values of the hot stress spots σ_{hs} at the weld toes of the U-rib stiffened steel decks. The maximum value of the derived hot spot stress σ_{hs} of Specimen SD-M is found to be 393.6 N/mm^2 at Stage F_{10}.

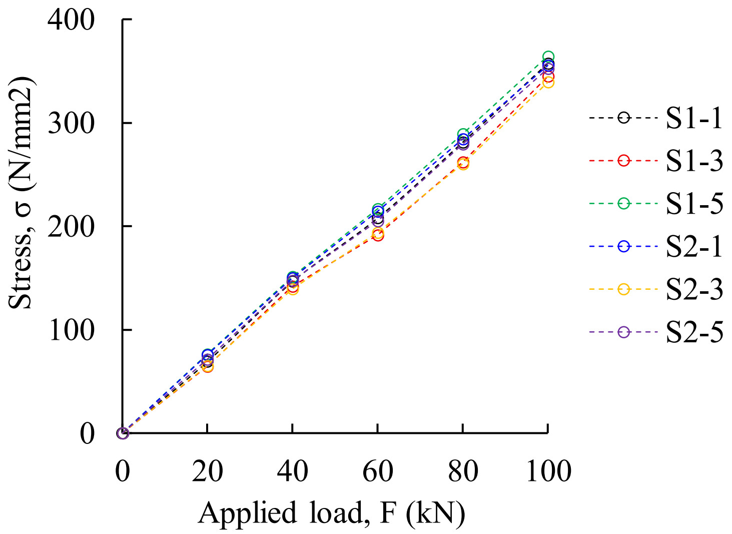

Figure 6.7 Measured stresses at different loading stages

Table 6.3 Derived hot spot stresses σ_{hs} of Specimen SD-M

Stages	Applied load F (kN)	Measured stresses (N/mm^2)		Hot spot stresses σ_{hs} (N/mm^2)
		S3-5	S1-5	
F_2	20.0	67.0	76.1	82.2
F_4	40.0	133.1	151.3	163.4
F_6	60.0	190.6	216.6	233.9
F_8	80.0	254.8	289.5	312.7
F_{10}	100.0	320.7	364.4	393.6

6.4 Cyclic in-plane bending tests

6.4.1 Test programme

Table 6.2 summarizes the test programme of the S690 U-rib stiffened steel decks under transverse cyclic actions together with key testing parameters. A total of seven different applied load ranges were selected, and they were considered to be able to provide a practical range of S-N data to derive fatigue performance of these U-rib stiffened steel decks.

6.4.2 Test set-up and instrumentation

The same set-up was also adopted for the cyclic tests of the S690 U-rib stiffened steel decks, as shown in **Figure 6.8**. The cyclic tests were performed under a load control through a sinusoidal waveform at a loading frequency *f* of 1.5 ~ 3.0 Hz. The stress ratio R was set to be 0.1 in all these tests, and the applied load ranges ΔF were determined in accordance with the test results obtained from the monotonic test on Specimen SD-M.

A total of 20 strain gauges were also installed at specific positions at the bottom surface of the steel decks to measure the strains in the vicinity the weld toes, as shown in **Figure 6.6**. A total of 20 strain gauges, namely, S1-1 to S4-5, were installed at 6.4 and 16.0 mm away the weld toes of the steel deck for strain measurements. The data obtained from strain gauges were acquired and stored electronically for subsequent analyses.

As shown in **Figure 6.9**, two high-resolution industrial cameras were employed to detect crack initiation and propagation on both sides of the U-rib stiffeners for subsequent data analyses..

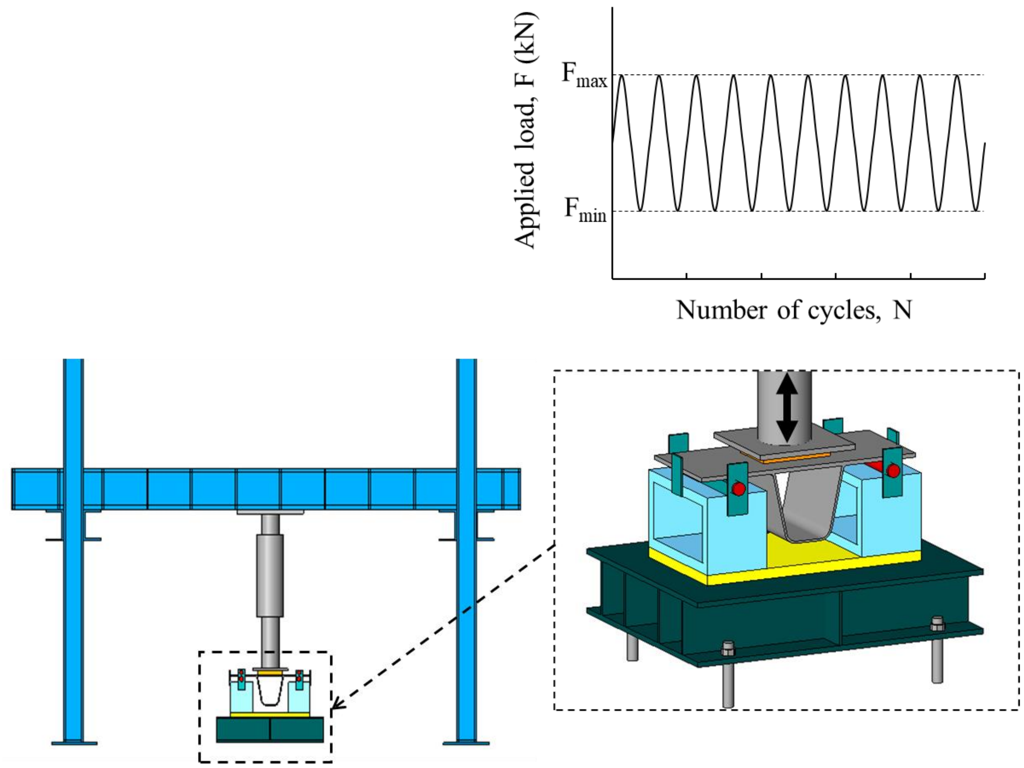

Figure 6.8 Test setup and instrumentation

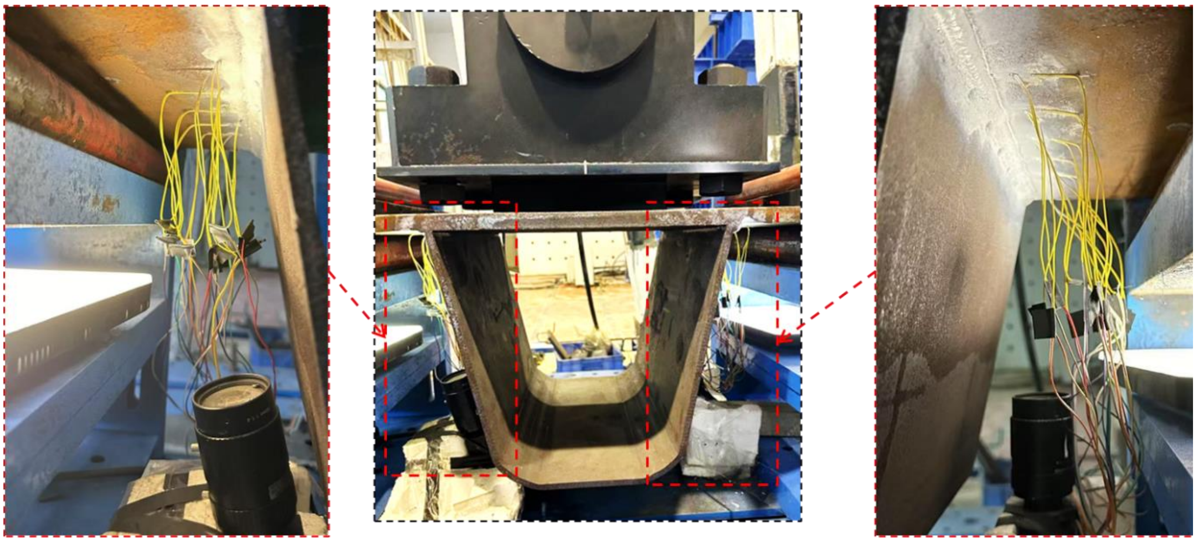

Figure 6.9 Measured stresses at different loading stages

6.4.3 Test results

All the cyclic tests were carried out successfully on these S690 U-rib stiffened steel decks, and these tests were terminated straightaway after a sudden fracture occurred. **Table 6.4** summarizes the numbers of cycles completed N of these U-rib stiffened steel decks at fatigue failure, and also the hot spot stresses σ_{hs} at the weld toe.

Table 6.4 S-N data of S690 U-rib stiffened steel decks

Specimens	Applied load range ΔF (kN)	Hot spot stresses σ_{hs} (N/mm^2)	Number of cycles completed N	Crack type
SD - 1a	12.8 ~ 128.0	429.1	136,194	WTD
- 1b		423.1	113,195	WTD & *WTR*
SD - 2a	10.2 ~ 102.0	348.8	278,612	WTD
- 2b		352.1	206,755	WTD
SD - 3a	7.7 ~ 77.0	278.0	506,118	*WTR*
- 3b		281.1	570,758	WTD
SD - 4a	6.7 ~ 67.0	238.5	758,535	WTD
- 4b		235.7	649,135	WTD
SD - 5a	6.4 ~ 64.0	240.0	860,023	*WTR*
- 5b		244.7	719,956	*WTR*
SD - 6a	5.9 ~ 59.0	224.4	1,506,025	WTD
- 6b		223.6	1,162,459	WTD
SD - 7a	4.3 ~ 43.0	175.1	4,214,898	WTD
- 7b		172.0	3,555,135	WTD

- ***Failure mode***

The following failure modes of these S690 U-rib stiffened steel decks are readily identified:

i) Type WTD: Crack initiation was found at the weld toes of the steel deck, and the crack was then propagated into the thickness of the steel deck, as shown in **Figure 6.10a)**; and

ii) Type WTR: Crack initiation was found at the weld toes of the rib plate, and the crack was then propagated into the thickness of the rib plate, as shown in **Figure 6.10b)**.

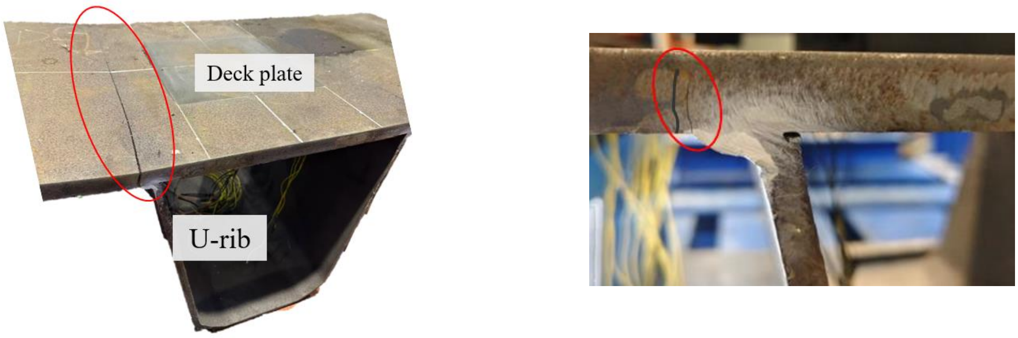

a) Typical fatigue crack of WTD

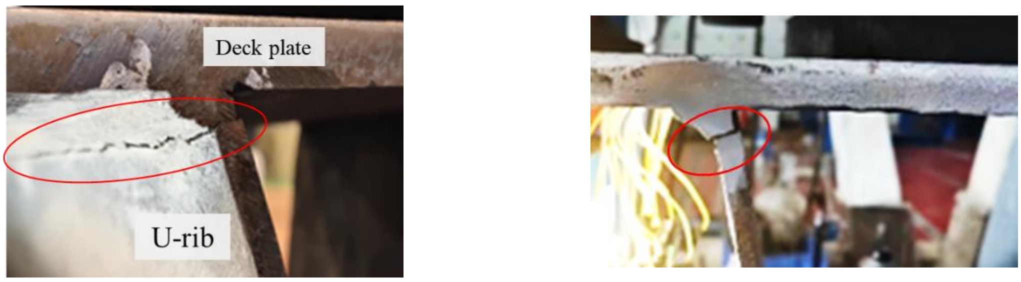

b) Typical fatigue crack of WTR

Figure 6.10 Typical fatigue cracks

- ***Local stress variations and crack characteristics***

In order to examine the fatigue behaviour of stiffness and strength degradation of the S690 U-rib stiffened steel decks, stress variations in the vicinity of the weld toes of the steel decks were measured during the entire course of fatigue tests. As shown in **Figure 6.11**, the measured stresses at both Stations S1-5 and S2-1 for all these S690 U-rib stiffened steel decks were found to be the most critical due to the effects of stress concentration, and hence, the corresponding values of the measured stresses were selected for a detailed analysis. All the strain gauges are arranged in the vicinity of the weld toes of the deck plates according to numerical analyses on these steel decks. It should be noted that strain gauges should also be provided in the vicinity of the weld toes of the U-ribs in any subsequent fatigue tests. The hot spot stresses of the fatigue crack WTD were also determined as the maximum stresses measured in the vicinity of the weld toe of the steel decks.

Moreover, the fatigue behaviour of crack characteristics including initiation and propagation of these U-rib stiffened steel decks were also examined during the tests. All the fatigue cracks of these U-rib stiffened steel decks were found to be initiated in the vicinity of weld toes of the rib-to-deck welded joints in the vicinity of the critical positions, and two different types of fatigue cracks, i.e. Types WTD and WTR, were identified.

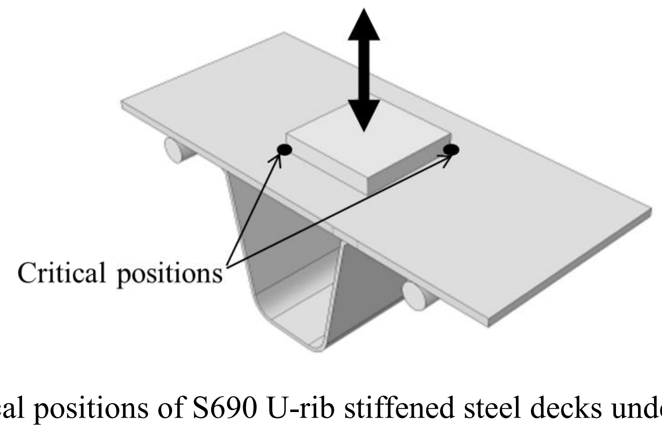

Figure 6.11 Critical positions of S690 U-rib stiffened steel decks under cyclic actions

It should be noted that these data of both the stress variations and the crack characteristics provide an indication on accumulative degradation in strength and stiffness of these S690 U-rib stiffened steel decks under cyclic actions. For ease of presentation, typical test results of Specimens SD-3a and SD-3b are selected as representatives of these S690 U-rib stiffened steel decks. The measured stresses of Specimens SD-3a and SD-3b are plotted in **Figure 6.12a)**, and the corresponding crack characteristics are also plotted in **Figure 6.12b)**. It should be noted that:

- For Specimen SD-3a

  Under an applied load range $\Delta F = 77.0 - 7.7 = 69.3$ kN, the initial value of the stress measured at Station S1-5 was 257.4 N/mm^2, which was found to be the most critical stress measured at all these Stations, as shown in **Figure 6.12a).**

  After about 330,000 cycles, a small crack with a width about 0.1 mm was detected to take place at Station S1-5, as shown in **Figure 6.12b)**.

  After 362,858 cycles, a visible crack with a length of 8.0 mm was identified along the weld toe of the U-rib.

  As the test continued, a highly visible crack with a length of 42.5 mm was identified along the weld toe of the U-rib after 431,650 cycles.

  At 506,118 cycles, the test was terminated when a sudden fracture occurred, and the crack was found to have propagated across both the full thickness and the full length of the weld toe of the U-rib.

  While only a small reduction in the measured stresses was found at the last 50,000 cycles as the fatigue cracks were found to initiate and propagate along the weld toe of the rib plate, i.e. Type WTR. Hence, an accumulative fatigue damage in terms of both stiffness and strength in the U-rib plate was identified.

- For Specimen SD-3b

Under an applied load range ΔF 77.0 – 7.7 = 69.3 kN, the initial value of the stress measured at Station S2-1 was 260.3 N/mm^2, which was found to be the most critical stress measured among all these Stations, as shown in **Figure 6.12a)**.

After about 400,000 cycles, a small crack with a width about 0.1 mm was detected near Station S2-1 at the weld toe of the steel deck, as shown in **Figure 6.12b)**. It should be noted that there was a slight increase in the measured stress at Station S2-1, i.e. 261.6 N/mm^2, as local stiffness degradation in the steel deck was found due to a small crack initiation.

After 425,326 cycles, a visible crack with a length of 5.7 mm was identified to have propagated along the weld toe of the steel deck, almost up to Station S2-1. A small increase in the measured stress, i.e. 264.0 N/mm^2, was identified as accumulative degradation in stiffness and strength of the steel deck due to propagation of the crack.

As the test continued, a highly visible crack with a length of 24.5 mm was identified to have propagated to Station S2-1 along the weld toe of the U-rib after 483,930 cycles. A small reduction in the measured stress at Station S2-1, i.e. 258.5 N/mm^2, was identified as a reduction in stiffness and strength at this Station.

At 570,758 cycles, the test was terminated when a sudden fracture occurred, and the crack was identified to have propagated across both the full thickness and the full length of the weld toe of the steel deck. There was a significant reduction in the measured stress at Station S2-1, i.e. 162.2 N/mm^2 , just before fracture.

The fatigue cracks were initiated and propagated at the weld toe of the steel deck, i.e. Type WTD. Hence, an accumulative fatigue damage in terms of both stiffness and strength degradation in the steel deck was identified.

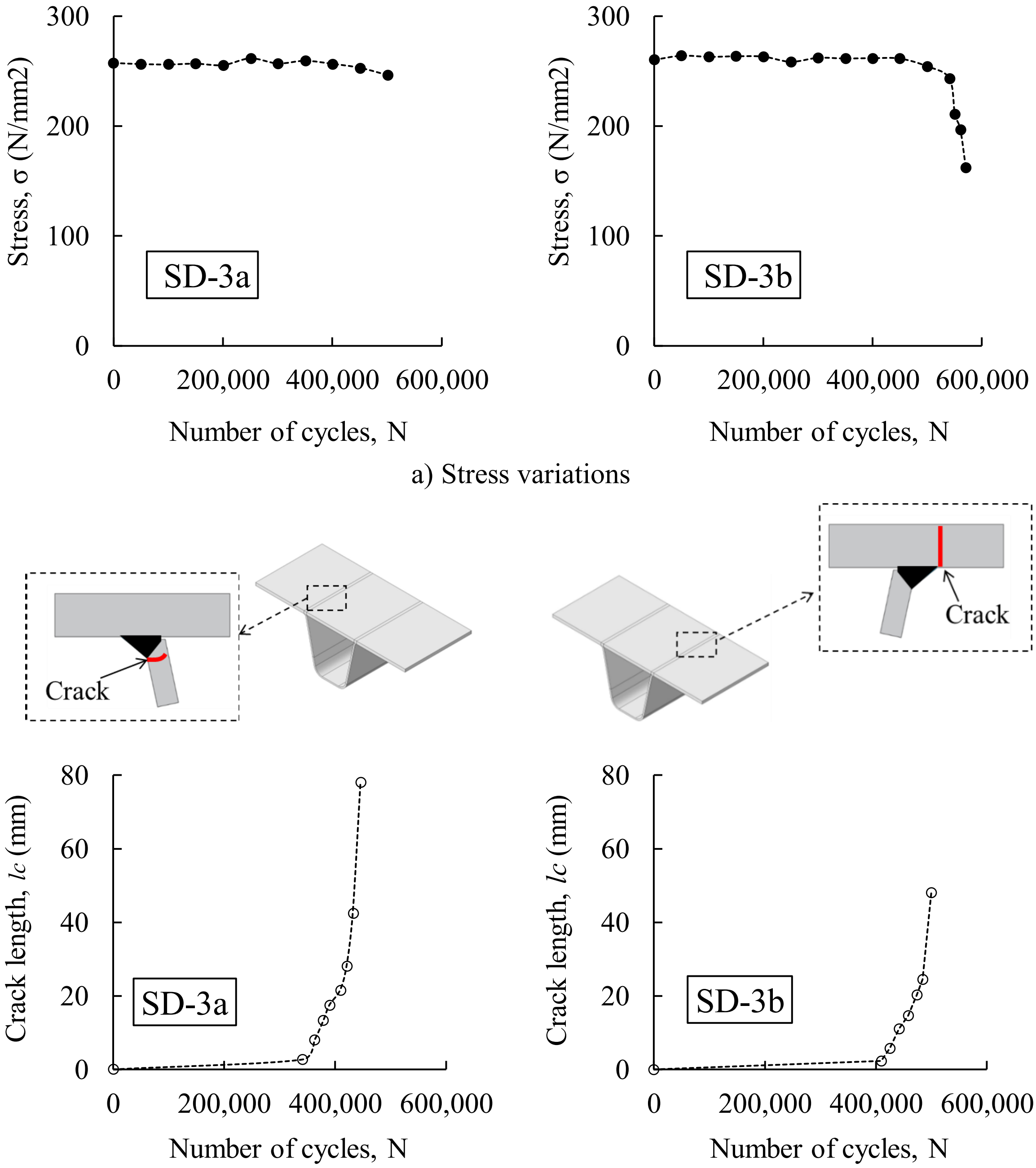

b) Crack propagation

Figure 6.12 Typical test data of Specimen SD-3a & -3b

After a comprehensive data analysis, the local stress variations in the vicinity of the weld toes of the deck plates of all these S690 U-rib stiffened steel decks measured during the tests were presented in **Figure 6.13a)**. The corresponding crack characteristics of these U-rib stiffened steel decks were presented in **Figure 6.13b)**, and it is evident that the fatigue behaviour of crack initiation and propagation in all these U-rib stiffened steel decks are similar.

Hence, two typical stages of fatigue behaviour of these U-rib stiffened steel decks were identified, i.e. stable fatigue stage – local stiffness and strength degradation due to crack initiation and propagation (crack length l_c < 3 mm), and rapid fracture stage – global stiffness and strength degradation due to crack propagation (crack length 3 mm < l_c). It should be noted that:

- For Specimens SD-3a and SD-5a & -5b

  Only small reductions in the measured local stresses in the vicinity of the weld toe of the deck plates were found as fatigue cracks were identified to initiate and propagate from the weld toe of the U-rib for these Specimens, i.e. Type WTR.

  At the rapid fracture stage, fatigue cracks propagated quickly through the thickness of the rib plates, and also propagated along the weld toes of the rib plates. The U-rib stiffened steel decks were fractured suddenly due to an accumulative fatigue damage in terms of stiffness and strength degradation in the rib plate.

- For Specimens SD-1b

  Both the crack types of WTR and WTD were identified in this Specimen. At the rapid fracture stage, fatigue cracks propagated quickly along the weld toes of both the deck plates and the U-rib plate, together with a significant reduction in measured local stresses due to global degradation in stiffness and strength.

- For other Specimens

Fatigue cracks were identified to initiate from the weld toes of the steel decks, and then propagated along the weld toes of these S690 U-rib stiffened steel decks, i.e. fatigue crack type of Type WTD.

At the stable fatigue stages, the measured local stresses in the vicinity of the weld toes of the steel decks were almost the same although small cracks, i.e. $l_c < 3$ mm, were identified at the weld toes of the steel decks.

At the rapid fracture stages, significant reductions in the measured local stresses in the vicinity of the weld toes of the steel decks were found due to global degradation in stiffness and strength in the steel decks caused by highly visible fatigue cracks at the weld toes of the steel decks. And then, these U-rib stiffened steel decks were fractured suddenly due to an accumulative fatigue damage in terms of stiffness and strength in the steel decks..

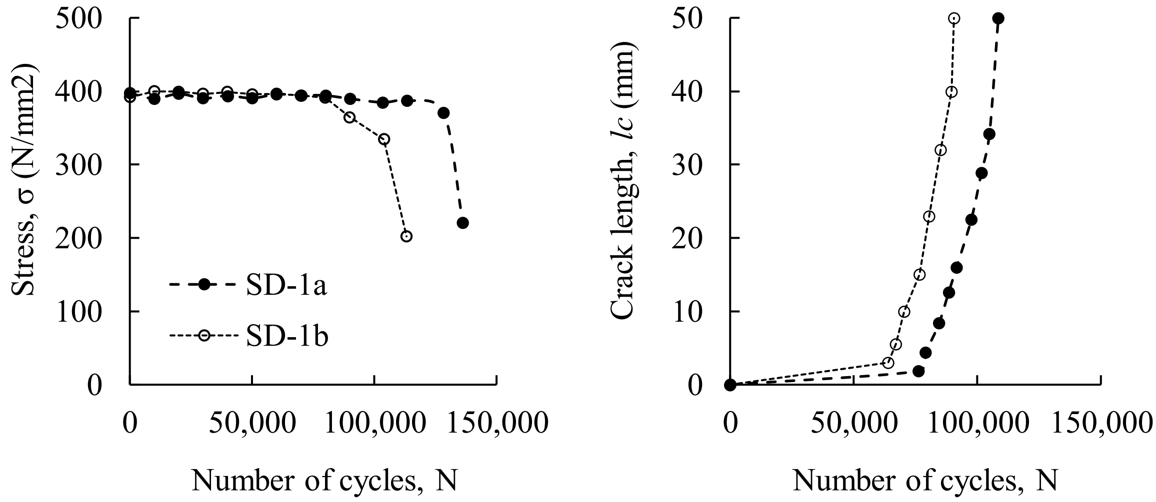

SD-1a / b

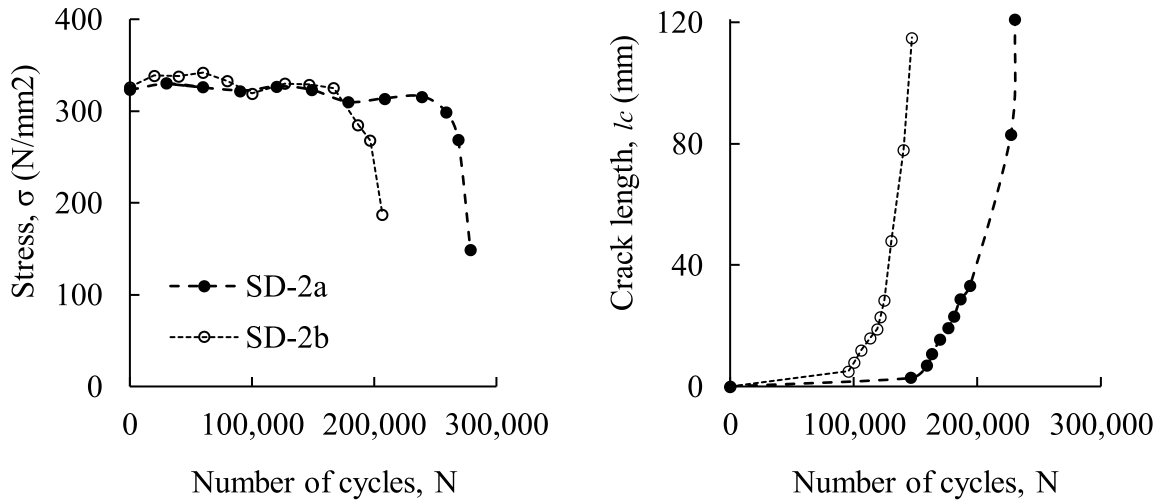

SD-2a / b

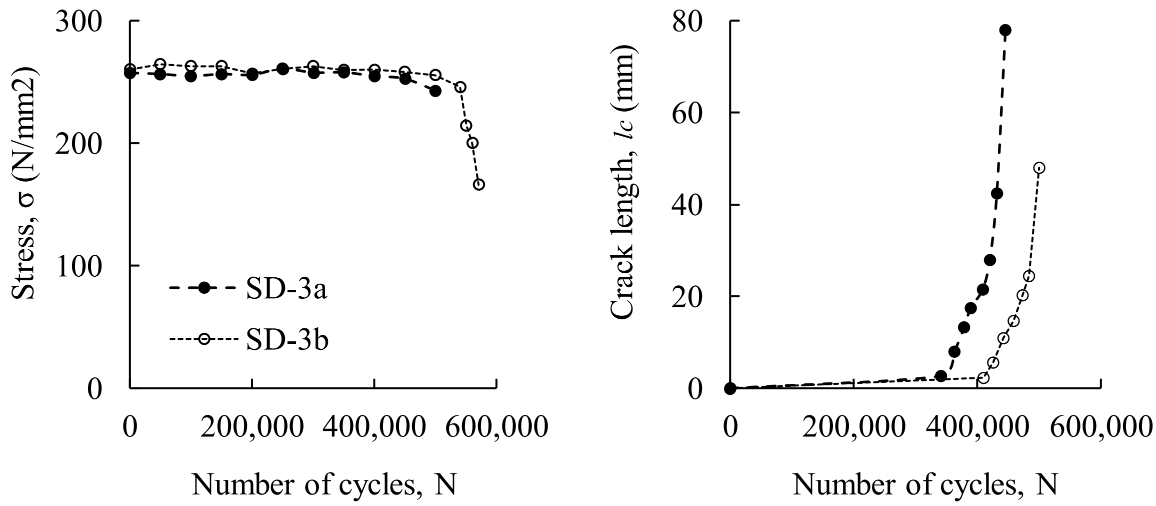

SD-3a / b

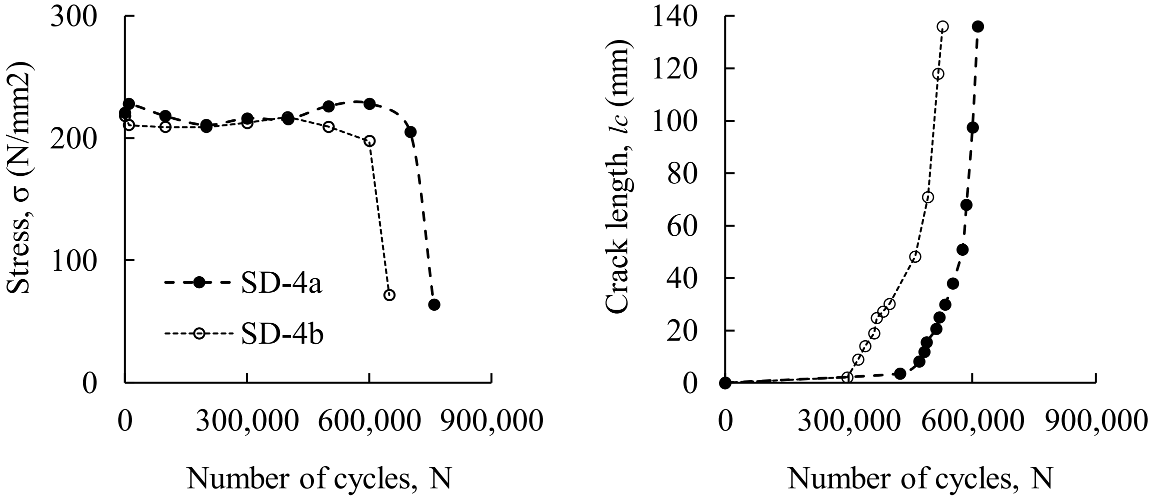

SD-4a / b

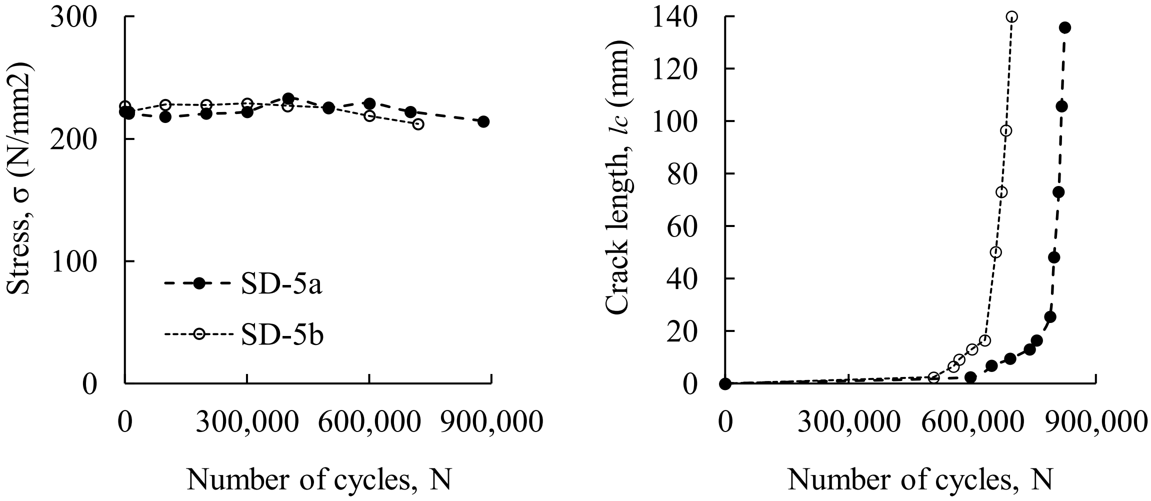

SD-5a / b

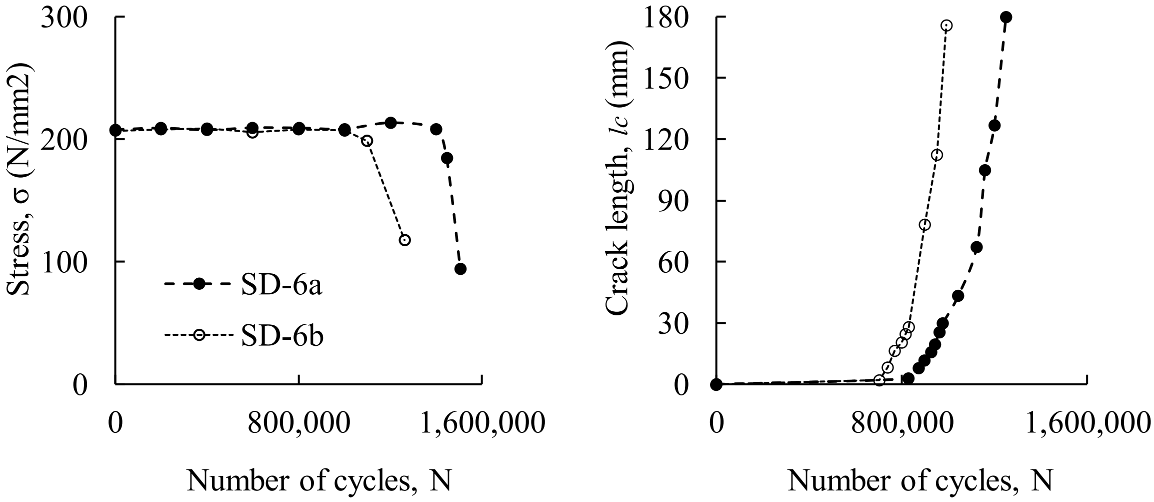

SD-6a / b

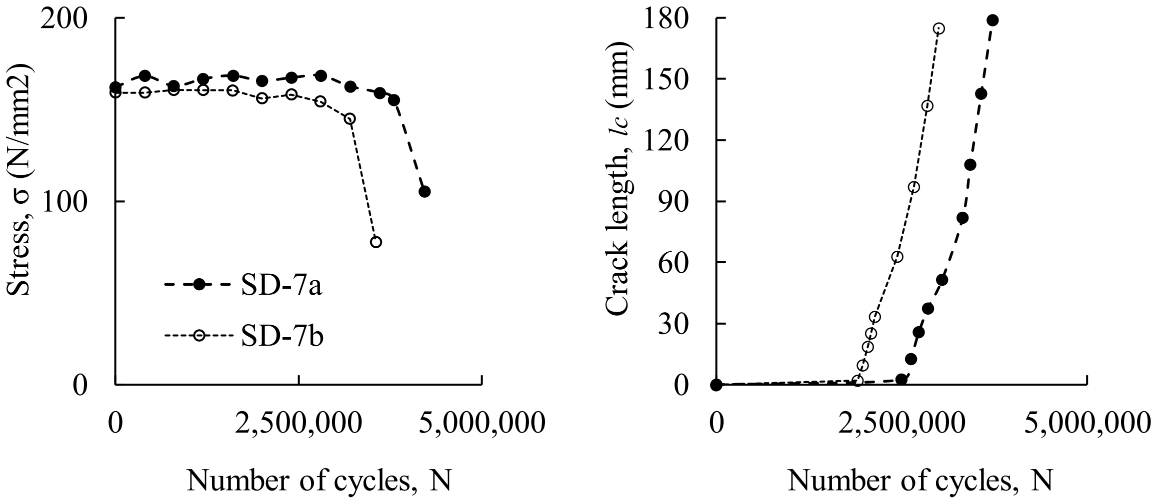

SD-7a / b

a) Stress variations b) Crack characteristics

Figure 6.13 Local stress variations and crack characteristics of S690 U-rib stiffened steel decks under cyclic actions

6.5 Analysis on S-N data

6.5.1 Formulation of S-N curve

It should be noted that the hot spot stresses σ_{hs} was generally employed for assessing the fatigue stresses of the U-rib stiffened steel deck under cyclic actions. Hence, the stress concentration factor approach is adopted to determine the S-N curve of these S690 U-rib stiffened steel decks under transverse cyclic actions. Refer to Chapter 4.5.1 for details of the stress concentration factor approach.

The derived S-N curve with a 97.9% survival probability of the S690 U-rib stiffened steel decks is plotted in **Figure 6.14**, and the corresponding parameters of the S-N curve are also summarized in **Table 6.5**.

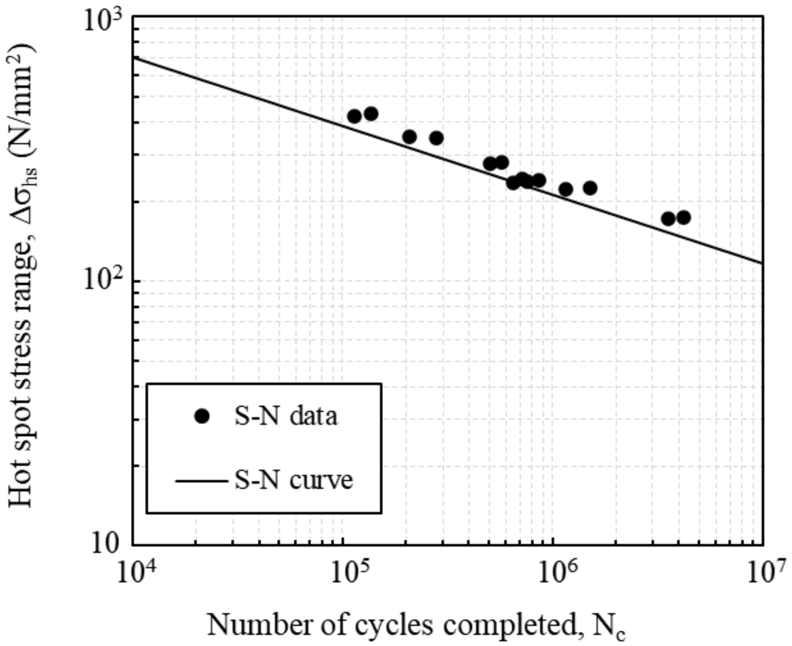

Figure 6.14 S-N curve of S690 U-rib stiffened steel decks

Table 6.5 Parameters of S-N curve of S690 U-rib stiffened steel decks

A	m	Fatigue stress limit σ_{lim} (N/mm^2)
14.92	3.83	116.3

6.5.2 Design rules for fatigue assessment

Existing design S-N curves given in IIW are widely adopted for the fatigue assessments on the U-rib stiffened steel deck. This Code provides different S-N curves for various structural details, and the hot spot stresses σ_{hs} in these joints were adopted in assessing their fatigue life. The S_{hs}-N curves are given by:

$$N = \frac{C}{\Delta\sigma^m} \qquad 10^4 \leq N \leq 10^7 \qquad (6\text{-}2)$$

The slope m of the S-N curves for welded connections is 3. And these design S-N curves are identified by the characteristic hot spot stress range $\Delta\sigma_{hs}$ at corresponding fatigue life $N = 2\times10^6$ cycles for various structural details, i.e. FAT.

6.5.3 Comparison with design curves

Figure 6.15 illustrates the comparison between the S-N data of the S690 U-rib stiffened steel decks and the design S-N curves given in IIW, and the comparison on the corresponding fatigue stress limits σ_{lim} are presented in **Table 6.6**. It should be noted that:

- All the S-N data are found to lie above the current design S-N curve for the U-rib stiffened steel decks, i.e. **Class FAT 100**. The value of the fatigue stress limits σ_{lim} of the S690 U-rib stiffened steel decks are found to be about 2 times of the codified value
- A higher design S-N curve, i.e. **Class FAT 125**, is recommended to be adopted for the fatigue assessment on the S690 U-rib stiffened steel decks under transverse cyclic action.

Hence, it is demonstrated that the current design S-N curve given in IIW is conservative for the fatigue life prediction of the high strength S690 U-rib stiffened steel decks under transverse cyclic action. It is proposed that a higher design S-N curve of Class FAT 125 should be adopted to predict their fatigue life accordingly.

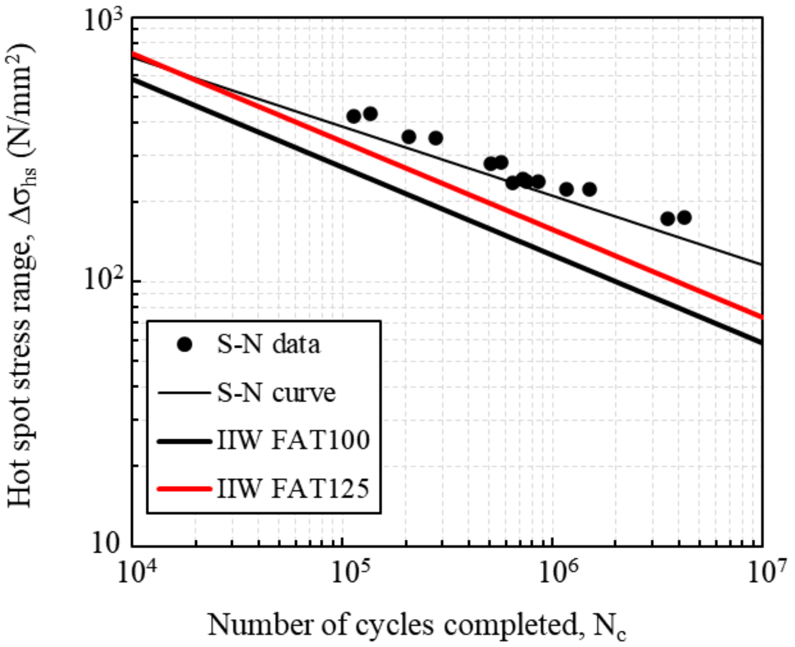

Figure 6.15 S-N curve of S690 U-rib stiffened steel decks

Table 6.6 Comparison of fatigue stress limits

	fatigue stress limit σ_{lim} (N/mm^2)	Ratio
IIW	58.5	*1.0*
S690 U-rib stiffened steel deck	116.8	*2.0*

6.5.4 Comparison with S-N data of S690 welded T-joints

It is interesting to make a comparison on the S-N data, i.e. hot spot stress ranges $\Delta\sigma_{hs}$ and fatigue life N, of different S690 welded T-joints presented in Chapter 4, and also with the S690 rib-to-deck welded joints presented in this Chapter. It should be noted that both the fabrication and the testing processes of these S690 welded joints have been well controlled in a systematic manner, and hence, these S-N data are readily adopted for a direct comparison.

Figure 6.16 presents the S-N data of both the S690 welded T-joints and the S690 U-rib stiffened steel decks, i.e. S-N_Tj and S-N_SD respectively. It is evident that the S-N_Tj data lie very close to the S-N_SD data. Hence, it is determined that the fatigue assessment method based on the hot spot stresses σ_{hs} are readily adopted for these S690 welded joints. In addition, based on these S-N data, a S-N curve_Wj was proposed for the fatigue life prediction of all these S690 welded T-joints and welded rib-to-deck joints on the basis of hot spot stresses σ_{hs} . The corresponding parameters of the S-N curve_Wj are also summarized in **Table 6.7**.

Table 6.7 Parameters of S-N curve of S690 welded joints – S-N curve_Wj

A	m	Fatigue stress limit σ_{lim} (N/mm^2)
15.06	3.90	116.3

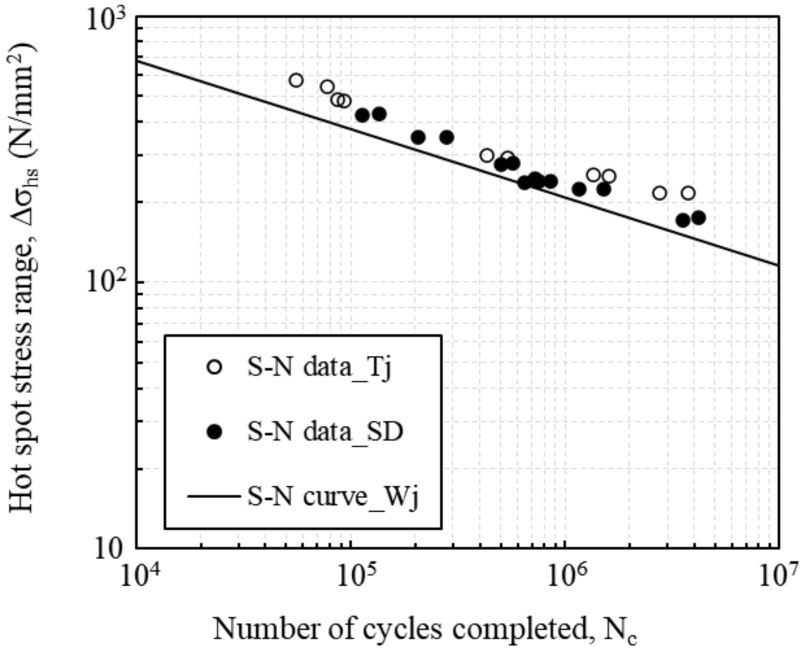

Figure 6.16 S-N data of different S690 welded joints

6.5.5 Fatigue life prediction

Similarly, the $(S\text{-}N)_c$ data obtained from the fatigue tests on the coupons of the S690 welded sections were also adopted to predict the fatigue life of the S690 U-rib stiffened steel decks with the consideration on the effects of stress concentration and the welding-induced residual stresses. Refer to Chapter 4.6 for the details.

Figure 6.17 illustrates a comparison on the S-N data of the S690 U-rib stiffened steel decks and those of the S690 welded sections in term of the equivalent stresses σ_{equ} . It was found that the S_{equ} - N data of the U-rib stiffened steel decks are found to lie slightly below the $(S\text{-}N)_c$ curve when the design fatigue life is larger than 5×10^5 cycles. It is considered to be due to the differences between the welding consumable employed in the welding of the S690 welded sections and the S690 U-rib stiffened decks.

Although there are only dozens of S-N data of both the S690 welded T-joints and the S690 U-rib stiffened steel decks available at present, it is proposed to be worthwhile to further develop this approach of fatigue life prediction for various connections and joints based on $(S\text{-}N)_c$ curves obtained from coupon tests.

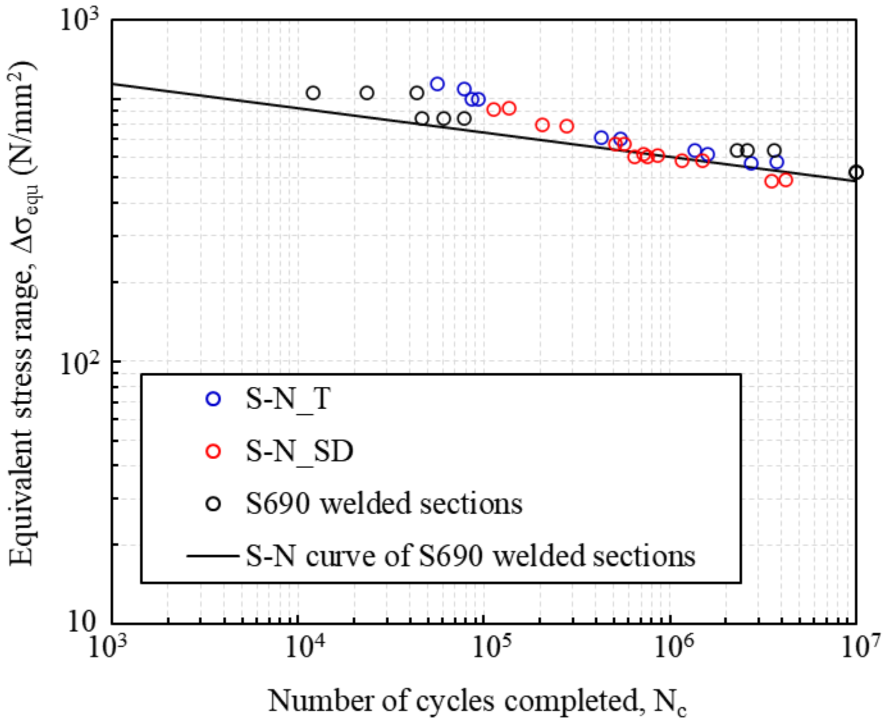

Figure 6.17 Comparison on S690 welded sections and joints

6.6 Conclusions

This Chapter presents a comprehensive experimental investigation into the fatigue behaviour of the S690 U-rib stiffened steel decks under transverse cyclic actions. A total of 14 stiffened steel decks were successfully tested under a wide range of stress levels. With proper instrumentation, the fatigue behaviour in terms of local stress variations and crack initiation and propagation of these U-rib stiffened steel decks were examined in details. Key findings are as follows:

- Local stress variations and crack initiation and propagation of the S690 U-rib stiffened steel decks under transverse cyclic actions are examined throughout the tests. Two typical types of fatigue cracks, i.e. Type WTD – cracks were found to be initiated and propagated from the weld toe of the steel deck, and Type WTR – cracks were found to be initiated and propagated from the weld toe of the rib plate, are identified.
- In addition, two typical stages of fatigue behaviour were identified, namely, i) stable fatigue stage – local degradation in stiffness and strength due to crack initiation and propagation (crack length l_c < 3 mm), and ii) rapid fracture stage – global degradation in stiffness and strength due to significant crack propagation (crack length 3 mm < l_c).
- All the S_{hs}-N data of the S690 U-rib stiffened steel decks are found to lie above the current design S_{hs}-N curve of Class FAT 100 given in IIW. Hence, a higher design S_{hs}-N curve of Class FAT 125 is recommended to be adopted for fatigue assessment on these S690 U-rib stiffened steel decks.
- With the consideration on the effects of stress concentration due to geometrical discontinuities, the S_{hs}-N data of the S690 U-rib stiffened steel decks are found to lie very close to the S_{hs}-N data of the S690 welded T-joints. A S_{hs}-N curve_Wj is thus proposed for

fatigue life prediction to these S690 welded joints.

- With the consideration on the presence of welding-induced residual stresses and also the effects of stress concentration, the $(S\text{-}N)_c$ curve of the S690 welded sections is demonstrated to be able to predict the fatigue life of these S690 U-rib stiffened steel decks in a highly satisfactory manner.

Chapter 7 Conclusions and future plan

7.1 Introduction

In this research project, a comprehensive experimental and numerical investigation into fatigue behaviour of high strength S690 to S960 steel and their welded sections was conducted. This Chapter summarizes key findings of this research project including various outcomes in improved fatigue assessment, and a number of recommendations on future work are also presented.

7.2 Experimental investigations

A comprehensive experimental investigation has been conducted in this research project, and the experimental programme includes:

a) 39 fatigue tests on the coupons of both the S690 and the S960 base plates;
b) another 39 fatigue tests on the coupons of both the S690 and the S960 welded sections;
c) 10 fatigue tests on the welded T-joints between S690 circular hollow sections under in-plane bending;
d) another 10 monotonic tests on the welded T-joints between S690 circular hollow sections under in-plane bending; and
e) 14 fatigue tests on the S690 U-rib stiffened steel decks under axial compression.

Through this experimental investigation, the fatigue performance of various high strength steel and their welded sections and joints are examined in details. Key findings are summarized as follows:

a) Fatigue performance of S690 and S960 base plates

A total of 39 fatigue tests on cylindrical coupons extracted from the S690-QT, the S690-TM and the S960-QT base plates were carried out to obtain their full range fatigue performance. All the S-N data of these high strength steel lie significantly above the design S-N curve given in EN 1993, especially for those design fatigue life larger than 10^6 cycles. **The fatigue stress limits of all these steel are found to be more than 4 times the values given in EN 1993.**

b) Fatigue performance of S690 and S960 welded sections

Another 39 fatigue tests on cylindrical coupons extracted from the S690-QT, the S690-TM and the S960-QT butt-welded sections were also carried out to obtain the full range fatigue performance of these high strength steel after welding. Reductions in the fatigue stress limits of the S690-QT, the S690-TM and the S960-QT welded sections are found to be 37.2%, 21.8% and 29.1% of those of the base plates respectively due to the effects of welding. All the S-N data of these welded sections lie significantly above the design S-N curve given in EN 1993, especially for those design fatigue life larger than 10^6 cycles. **The fatigue stress limits of all these welded sections are also found to be more than 4 times the values given in EN 1993.**

c) Fatigue performance of welded T-joints between S690 circular hollow sections

A total of 10 fatigue tests were carried out on the welded T-joints between S690 circular hollow sections with an identical configuration under cyclic in-plane bending. Deformation characteristics including degradation in strength and stiffness, and propagation of surface cracks along the weld toes of the crowns of the chords of these S690 welded T-joints under cyclic in-plane bending are presented. Both classification method and stress concentration factor method are adopted to assess the effects of stress levels onto the fatigue performance of these S690 T-joints.

All the S_{nom}-N data of the S690 welded T-joints are demonstrated to lie above the design S_{nom}-N curve given in EN 1993-1-9. **After comparison with these data, the design S_{nom}-N curve is recommended to be modified with an appropriate increase in the limiting stress range $\Delta\sigma_{lim}$ by a factor of 1.3 to achieve an effective fatigue assessment on these welded T-joints.**

Similarly, all the S_{hs}-N data of the S690 welded T-joints are also demonstrated to lie above both the design S_{hs}-N curves given in CIDECT-8 and API RP 2A-WSD. **Hence, the design S_{hs}-N curves are recommended to be modified with an appropriate increase in the limiting stress range $\Delta\sigma_{lim}$ by a factor of 1.5 for CIDECT, and 1.8 for API to achieve an effective fatigue assessment on these welded T-joints.**

d) Local stresses of welded T-joints between S690 circular hollow sections

A total of 10 monotonic tests were carried out on the welded T-joints between S690 circular hollow sections with various cross-sectional dimensions in both the braces and the chords under monotonic in-plane bending. Hot spot stresses σ_{hs} and the corresponding stress concentration factors SCF at the weld toes of the crowns of the chords of these S690 welded T-joints under in-plane bending were determined. **Existing design formula given in CIDEC is demonstrated to give rather conservative SCF, and a proposed design formula on SCF for improved accuracy is provided as described in Chapter 7.3a).**

e) Fatigue performance of S690 U-rib stiffened steel decks

A total of 14 fatigue tests were carried out on the S690 U-rib stiffened steel decks with an identical configuration under transverse cyclic actions. Fatigue behaviour in terms of local stress variations and crack initiation and propagation of these U-rib stiffened steel decks were presented.

All the S_{hs}-N data of the S690 U-rib stiffened steel decks are found to lie above the current design S_{hs}-N curve of Class FAT 100 given in IIW. **Hence, the design S_{hs}-N curves are recommended to be modified with an appropriate increase in the limiting stress range $\Delta\sigma_{lim}$ by a factor of about 2 for IIW on these U-rib stiffened steel decks.**

7.3 Numerical investigations

A comprehensive numerical investigation has been conducted in this research project. Key findings are summarized as follows:

a) Structural behaviour of welded T-joints between S690 circular hollow sections

Finite element models with solid elements are established to predict the structural behaviour of welded T-joints between S690 circular hollow sections under in-plane bending. After calibration against test data, the proposed models are demonstrated to be able to predict the overall deformation characteristics and the local stress distributions of these S690 welded T-joints.

Based on the proposed models, a parametric study on a total of 96 welded T-joints with a wide range of geometrical ratios was also conducted to determine SCF of these T-joints. **Through a multiple regression analysis on the predicted values of SCF, an improved design formula for SCF is proposed.**

b) Residual stresses in welded T-joints between S690 circular hollow sections

An advanced coupled thermomechanical modelling approach was adopted to predict the welding-induced residual stresses of the welded T-joints between S690 circular hollow sections. Owing to the presence of large welding-induced residual stresses and strains, the weld toes at the crowns of the brace / chord junctions of these welded T-joints were found to have been yielded after welding. Under the effects of stress concentration, significantly increased mechanical stresses due to applied loads are also found at the weld toes of these welded T-joints, making these locations highly vulnerable to fatigue failure.

With the considerations on the presence of welding-induced residual stresses, effects of stress concentration due to geometry, and different stress ratios during fatigue tests, the $(S\text{-}N)_c$ curve of coupons of the S690 welded sections is demonstrated to be able to predict the fatigue life of these S690 welded T-joints effectively over a practical range of cyclic actions.

7.4 Recommendations for future work

The recommendations for future work are proposed as follows:

- In this research project, effects of stress ratio on fatigue performance are not examined. Fatigue tests under various stress ratios are suggested to be conducted.
- Fatigue behaviour of welded T-joints between S690 circular hollow sections are examined in this research project. Another test programme on welded T-joints between S690 rectangular hollow sections under cyclic in-plane bending is proposed as stress concentration effects are generally considered to be highly critical.

- Welding-induced residual stresses in welded T-joints between S690 CHS have been predicted numerically. It is recommended to adopt X-ray diffraction method to measure welding-induced residual stresses in the S690 welded T-joints with an improved accuracy.
- In this research project, welding-induced residual stresses in the S690 U-rib stiffened steel decks are not studied. Both X-ray diffraction method and numerical modelling method are recommended to determine these welding-induced residual stresses in the S690 U-rib stiffened steel decks to determine critical local stresses accurately for an effective fatigue performance assessment.
- Fracture mechanism approach is suggested to be adopted for further studies on crack initiation and propagation of the S690 welded joints.

References

ABAQUS (2020). Theory Manual 2020, Providence, US: Dassault Systems Simulia Corp.

Abdelbaset, H., & Zhu, Z. (2024). Behavior and fatigue life assessment of orthotropic steel decks: A state-of-the-art-review. In Structures (Vol. 60, p. 105957). Elsevier.

Ahola, A., Lipiäinen, K., Afkhami, S., Lilja, H., & Björk, T. (2022). Fatigue performance of the welded details of an old, demolished steel railway bridge. Engineering Structures, 256, 113966.

AISC. (2010). ANSI/AISC 360-10, Specification for Structural Steel Buildings. American Institute of Steel Construction.

ANSI. (2004). AWS D1.1:2004, Structural Welding Code - Steel. American National Standards Institute.

API. (2002). API RP 2A-WS, Planning, Designing, and Constructing Fixed Offshore Platforms: Working Stress Design. American Petroleum Institute.

ASTM. (2005). Standard Test Method for Strain-Controlled Fatigue Testing. ASTEM E606. ASTM International.

Baumgartner, J. (2017). Review and considerations on the fatigue assessment of welded joints using reference radii. International Journal of Fatigue, 101, 459-468.

CEN. (2005a). BS EN 1993-1-9, Eurocode 3: Design of steel structures, Part 1-9: Fatigue. European Committee for Standardization.

CEN. (2005b). BS EN 1993-1-1, Eurocode 3: Design of steel structures, Part 1-1: General rules and rules for buildings. European Committee for Standardization.

CEN. (2007). BS EN 1993-1-12, Eurocode 3: Design of steel structures Part 1-12: Additional rules for the extension of EN 1993 up to steel grades S700. European Committee for Standardization.

CEN. (2019). BS EN 10025-6, Hot rolled products of structural steels - Part 6: Technical delivery conditions for flat products of high yield strength structural steels in the quenched and tempered condition. European Committee for Standardization.

Chiew, S. P., Zhao, M. S., & Lee, C. K. (2015). Fatigue performance of high strength steel built-up box T-joints. Journal of Constructional Steel Research, 106, 296-310.

Cheng, B., Cao, X., Ye, X., & Cao, Y. (2017). Fatigue tests of welded connections between longitudinal stringer and deck plate in railway bridge orthotropic steel decks. Engineering Structures, 153, 32-42.

Chung, K. F., Ho, H. C., Hu, Y. F., Wang, K., Liu, X., Xiao, M., & Nethercot, D. A. (2020). Experimental evidence on structural adequacy of high strength S690 steel welded joints with different heat input energy. Engineering structures, 204, 110051.

CNS. (2008). GB/T 15248. The Test Method for Axial Loading Constant-Amplitude Low-Cycle Fatigue of Metallic Materials. China Standardization Publishing House Press.

CNS. (2017). GB/T 50017. Standard for Design of Steel Structures. China Standardization Publishing House Press.

CNS. (2018). GB/T 1591. High strength low alloy structural steels. China Standardization Publishing House Press.

Costa, J. D. M., Ferreira, J. A. M., & Abreu, L. P. M. (2010). Fatigue behaviour of butt welded joints in a high strength steel. Procedia Engineering, 2(1), 697-705.

Costa, P. S., Reyes-Valdés, F. A., Saldaña-Garcés, R., Delgado, E. R., & Salinas-Rodríguez, A. (2016). Thermal behavior of an HSLA steel and the impact in phase transformation: Submerged arc welding (SAW) process approach to pipelines. In Characterization of Metals and Alloys (pp. 85-98). Cham: Springer International Publishing.

Dantas, R., Correia, J., Lesiuk, G., Rozumek, D., Zhu, S. P., de Jesus, A., ... & Berto, F. (2021). Evaluation of multiaxial high-cycle fatigue criteria under proportional loading for S355 steel. Engineering Failure Analysis, 120, 105037.

De Jesus, A. M., Matos, R., Fontoura, B. F., Rebelo, C., da Silva, L. S., & Veljkovic, M. (2012). A comparison of the fatigue behavior between S355 and S690 steel grades. Journal of constructional steel research, 79, 140-150.

Eleni Gogou (2012). Use of High Strength Steel Grades for Economical Bridge Design. Masters Thesis Report 2012 April. Delft University of Technology

Fu, Z., Ji, B., Zhang, C., & Li, D. (2018). Experimental study on the fatigue performance of roof and U-rib welds of orthotropic steel bridge decks. KSCE Journal of Civil Engineering, 22(1), 270-278.

Hobbacher, A. (1996). Fatigue design of welded joints and components: Recommendations of IIW Joint Working Group XIII-XV. Woodhead Publishing.

Hu, Y. F., Chung, K. F., Ban, H., & Nethercot, D. A. (2020). Investigations into residual stresses in S690 cold-formed circular hollow sections due to transverse bending and longitudinal welding. Engineering Structures, 219, 110911.

Hu, Y. F., Chung, K. F., Ban, H., & Nethercot, D. A. (2022). Structural testing and numerical modelling of T-joints between cold-formed S690 circular hollow sections under brace in-plane bending. Engineering Structures, 250, 113317.

Hu, Y. F., Ho, H. C., Chung, K. F., Xiao, M., Liu, X., & Nethercot, D. A. (2023). Integrated and coordinated numerical simulations on fabrication processes of high strength S690 cold-formed circular hollow sections. Engineering Structures, 279, 115620.

Huang, Y., Zhang, Q., Bao, Y., & Bu, Y. (2019). Fatigue assessment of longitudinal rib-to-crossbeam welded joints in orthotropic steel bridge decks. Journal of Constructional Steel Research, 159, 53-66.

ISO. (2019). BS EN ISO 6892-1, Metallic Materials – Tensile Testing – Part 1: Method of Test at Room Temperature. International Organization for Standardization.

ISO. (2003). BS EN ISO12107, Metallic Materials – Fatigue Testing – Statistical Planning and Analysis of Data. International Organization for Standardization.

Jiao, H., Mashiri, F., & Zhao, X. L. (2013). Fatigue behavior of very high strength (VHS) circular steel tube to plate T-joints under in-plane bending. Thin-Walled Structures, 68, 106-112.

Jin, H., Zhu, M. F., Hu, Y. F., Ho, H. C., Chung, K. F., Nethercot, D. A., Wang T.H., Liu H.L., & Xie, G. (2024). Investigations into mechanical properties of 50 and 70 mm thick high strength S690 butt-welded sections. Engineering Structures, 314, 118363.

Jin, H., Zhu, M. F., Wang, Y. C., Hu, Y. F., Ho, H. C., Chung, K. F., Nethercot D.A., Wang T.H., Liu H.L., & Xie, G. (2025). Investigation into mechanical properties of heat-affected zones in high strength S690 steel welded sections. Engineering Structures, 331, 119962.

Keindorf, C., Schaumann, P., Ahmed, H., Goes, P., & Vermeulen, M. (2010). High frequency fatigue testing of butt welds with a new magnet resonance machine. In 63rd Annual Assembly & International Conference of the International Institute of Welding (pp. 11-17).

Lan, X., Chan, T. M., & Young, B. (2021). Experimental and numerical studies on stress concentration factors of high strength steel fabricated box X-joints. Thin-Walled Structures, 164, 107858.

Li, M., Suzuki, Y., Hashimoto, K., & Sugiura, K. (2018). Experimental study on fatigue resistance of rib-to-deck joint in orthotropic steel bridge deck. Journal of Bridge Engineering, 23(2), 04017128.

Liu, X., Chung, K. F., Ho, H. C., Xiao, M., Hou, Z. X., & Nethercot, D. A. (2018). Mechanical behavior of high strength S690-QT steel welded sections with various heat input energy. Engineering Structures, 175, 245-256.

Liu, X., Zhang, Y. H., Wang, B., & Sun, X. (2022). Influence of the mean stress on the fatigue life of welded joints under variable amplitude loading. *International Journal of Fatigue*, *163*, 106972.

Mashiri, F. R., Zhao, X. L., & Grundy, P. (2004a). Stress concentration factors and fatigue failure of welded T-connections in circular hollow sections under in-plane bending. International Journal of Structural Stability and Dynamics, 4(03), 403-422.

Mashiri, F. R., Zhao, X. L., & Grundy, P. (2004b). Stress concentration factors and fatigue behaviour of welded thin-walled CHS–SHS T-joints under in-plane bending. Engineering Structures, 26(13), 1861-1875.

Mashiri, F. R., & Zhao, X. L. (2006). Thin circular hollow section-to-plate T-joints: Stress concentration factors and fatigue failure under in-plane bending. Thin-walled structures, 44(2), 159-169.

Matti, F. N., & Mashiri, F. R. (2020). Experimental and numerical studies on SCFs of SHS T-Joints subjected to static out-of-plane bending. Thin-Walled Structures, 146, 106453.

Morrow, J. (1965). Cyclic plastic strain energy and fatigue of metals. In Internal friction, damping, and cyclic plasticity (pp. 45-87). ASTM International.

Paris, P., & Erdogan, F. (1963). A critical analysis of crack propagation laws. Journal of basic engineering, 85(4), 528-533.

Rolfe, S. T., & Barsom, J. M. (1977). Fracture and fatigue control in structures: Applications of fracture mechanics. ASTM International.

Schubnell, J., Discher, D., & Farajian, M. (2019). Determination of the static, dynamic and cyclic properties of the heat affected zone for different steel grades. Materials Testing, 61(7), 635-642.

Schubnell, J., Konidena, S. K., Jung, M., Braun, M., Ehlers, S., Madia, M., ... & Löschner, D. (2024). Approach for the probabilistic fatigue assessment of welded joints based on the local geometry of the weld seam. Fatigue & Fracture of Engineering Materials & Structures, 47(1), 88-107.

Smith, K. (1970). A stress-strain function for the fatigue of metals. Journal of materials, 5, 767-778.

Sun, J., Hensel, J., Klassen, J., Nitschke-Pagel, T., & Dilger, K. (2019). Solid-state phase transformation and strain hardening on the residual stresses in S355 steel weldments. Journal of Materials Processing Technology, 265, 173-184.

Sun, C., Xie, J., Zhao, A., Lei, Z., & Hong, Y. (2012). A cumulative damage model for fatigue life estimation of high-strength steels in high-cycle and very-high-cycle fatigue regimes. Fatigue & Fracture of Engineering Materials & Structures, 35(7), 638-647.

Shao, Y. B., Du, Z. F., & Lie, S. T. (2009). Prediction of hot spot stress distribution for tubular K-joints under basic loadings. Journal of Constructional Steel Research, 65(10-11), 2011-2026.

Shi, Z., Yang, S., Pu, Q., & Zhang, Y. (2019). Fatigue performance of orthotropic steel decks in long-span cable-stayed steel-box girder railway bridges. Journal of Bridge Engineering, 24(5), 04019035.

The Editors of Encyclopaedia Britannica (2024). Tacoma Narrows Bridge. Encyclopedia Britannica. https://www.britannica.com/topic/Tacoma-Narrows-Bridge.

Tong, L., Fu, Y., Liu, Y., & Zhao, X. L. (2014). Stress concentration factors of diamond bird-beak SHS T-joints under brace loading. Thin-Walled Structures, 74, 201-212.

Tong, L., Xu, G., Liu, Y., Yan, D., & Zhao, X. L. (2015). Finite element analysis and formulae for stress concentration factors of diamond bird-beak SHS T-joints. Thin-Walled Structures, 86, 108-120.

Tong, L., Niu, L., Ren, Z., & Zhao, X. L. (2021a). Experimental research on fatigue performance of high-strength structural steel series. Journal of Constructional Steel Research, 183, 106743.

Tong, L., Niu, L., Ren, Z., & Zhao, X. L. (2021b). Experimental investigation on fatigue behavior of butt-welded high-strength steel plates. Thin-Walled Structures, 165, 107956.

Tong, L., Niu, L., Ren, Z., & Zhao, X. L. (2023). Fatigue performance of transverse welded attachment of high-strength structural steel series. Thin-Walled Structures, 182, 110188.

Wardenier, J., Kurobane, Y., Packer, J. A., Van der Vegte, G. J., & Zhao, X. L. (2008). Design guide for circular hollow section (CHS) joints under predominantly static loading. CIDECT Design Guide 1. CIDECT.

Wang, D. Q. Q., Yao, D. D., Wang, Q., Gao, Z. B., Zhang, Z. F., & Li, X. W. (2023). Evaluating the fatigue property of S355J2W steel butt-welded joint: Multiple notch effects. International Journal of Fatigue, 167, 107362.

Willms, R. (2009). High strength steel for steel constructions. In Nordic Steel Construction Conference, Malmo, Sweden.

Xiong, M. X., & Liew, J. R. (2020). Experimental study to differentiate mechanical behaviours of TMCP and QT high strength steel at elevated temperatures. Construction and Building Materials, 242, 118105.

Yamashita, Y., & Murakami, Y. (2016). Small crack growth model from low to very high cycle fatigue regime for internal fatigue failure of high strength steel. International Journal of Fatigue, 93, 406-414.

Zhao X.L., Herion S., Packer J.A., Puthli R.S., Sedlacek G., Wardenier J., Weynand K., van Wingerde A.M. & Yeomans N.F. (2001). Design guide for circular and rectangular hollow section welded joints under fatigue loading, CIDECT Design Guide 8. CIDECT.

Zong, L., Shi, G., & Wang, Y. (2015). Experimental investigation and numerical simulation on fatigue crack behavior of bridge steel WNQ570 base metal and butt weld. Construction and Building Materials, 77, 419-429.